A Thesis Submitted for the Degree of PhD at the University of Warwick

Permanent WRAP URL:

http://wrap.warwick.ac.uk/163992

warwick.ac.uk/lib-publications

Novel electrolytes for high-voltage and high-stability aqueous rechargeable batteries

Shigang Chen

A thesis submitted in fulfilment of the requirements for the degree of Doctor of Philosophy
in the

University of Warwick

Supervised by:
Professor Shanwen Tao

October 2021

Contents

List of Figures

VIII

List of Tables

Acknowledgements

Declaration

This PhD thesis has not been submitted for a degree at another university. The figures and tables in the chapter 2-9 are the original works of the author and have not been published elsewhere except for the following publications. Amongst those, Fig. 2.1 was completed with cooperation of Dr. Mengfei Zhang in University of Warwick; Fig. 4.3 and Table 4.2 were completed by Prof. Shanwen Tao in University of Warwick; Fig. 6.1 (e), Fig. 7.3 and Fig. 8.2 were completed with cooperation of Dr. Pan Sun in University of Chicago. In chapter 1 regarding literature review, Table 1.1, Table 1.2, Fig. 1.1, Fig. 1.3, Fig. 1.7, Fig. 1.11 are plotted by author, while copyrights of Fig. 1.2, Fig. 1.13 (a) and Fig. 1.14 (f, g) are belonged to American Chemical Society; copyrights of Fig. 1.4 (a), Fig. 1.5 (a, c, d), Fig. 1.8 (i), Fig. 1.9 (a-c, e, f), Fig. 1.10 (e), Fig. 1.12 (a, d), Fig. 1.13 (b, c) and Fig. 1.14 (d, e) are belonged to Wiley-VCH Verlag GmbH & Co. KGaA, Weinhem; copyright of Fig. 1.4 (b) is belonged to Chemical Society of Japan; copyrights of Fig. 1.4 (c), Fig. 1.8 (a-f) and Fig. 1.14 (a) are belonged to Royal Society of Chemistry; copyrights of Fig. 1.4 (d), Fig. 1.5 (b), Fig. 1.8 (g), Fig. 1.13 (d) and Fig. 1.14 (b, c) are belonged to Elsevier; copyrights of Fig. 1.6 (a-f), Fig. 1.8 (h), Fig. 1.9 (d), Fig. 1.10 (c, f), Fig. 1.12 (b, c) and Fig. 1.13 (e) are belonged to Nature Publishing Group; copyrights of Fig. 1.10 (a, b) are belonged to AAAS; copyright of Fig. 1.10 (d) is belonged to National Academy of Sciences.

Publication List

1. **Chen, S.**, Lan, R., Humphreys, J., & Tao, S. (2020). Salt-concentrated acetate electrolytes for a high voltage aqueous Zn/MnO_2 battery. *Energy Storage Materials*, *28*, 205-215.

2. **Chen, S.**, Lan, R., Humphreys, J., & Tao, S. (2020). Effect of cation size on alkali acetate-based 'water-in-bisalt' electrolyte and its application in aqueous rechargeable lithium battery. *Applied Materials Today*, *20*, 100728.

3. **Chen, S.**, Lan, R., Humphreys, J., & Tao, S., (2020). Perchlorate based 'oversaturated gel electrolyte' for an aqueous rechargeable hybrid Zn−Li battery. *ACS Applied Energy Materials*, *3* (3), 2526-2536.

4. **Chen, S.**, Sun, P., Sun, B., Humphreys, J., Zou, P., Xie, K., & Tao, S., (2021). Nitrate-based 'oversaturated gel electrolyte' for high-voltage and high-stability aqueous lithium batteries. *Energy Storage Materials*, *37*, 598-608.

5. **Chen, S.**, Sun, P., Humphreys, J., Zou, P., Zhang, M., Jeerh G., & Tao, S., (2021). Acetate-based 'oversaturated gel electrolyte' enabling highly stable aqueous $Zn-MnO_2$ battery. *Energy Storage Materials*, *42*, 240-251.

6. **Chen, S.,** Sun, P., Humphreys, J., Zou, P., Zhang, M., Jeerh G., Sun, B., & Tao, S., (2021). N,N-Dimethylacetamide-diluted nitrate electrolyte for aqueous $Zn//LiMn_2O_4$ hybrid ion batteries, *ACS Applied Materials & Interfaces*, *13* (39), 46636-46643.

7. Irvine, J., **Chen, S.**, Tao, S. et al., (2021). Roadmap on inorganic perovskites for energy applications, *Journal of Physics: Energy*, *3*, 031502.

8. Humphreys, J., Lan, R., **Chen, S.**, Walker, M., Han, Y., & Tao, S., (2021). Cation doped cerium oxynitride with anion vacancies for Fe-based catalyst with improved activity and oxygenate tolerance for efficient synthesis of ammonia. *Applied Catalysis B: Environmental, 285,* 119843.

9. Humphreys, J., Lan, R., **Chen, S.**, & Tao, S., (2020). Improved stability and activity of Fe-based catalysts through strong metal support interactions due to extrinsic oxygen vacancies in $Ce_{0.8}Sm_{0.2}O_{2-\delta}$ for the efficient synthesis of ammonia. *Journal of Materials Chemistry A*, *8*, 16676-16689.

10. Zou, P., **Chen, S.**, Lan, R., & Tao, S. (2019). Investigation of perovskite oxide $SrCo_{0.8}Cu_{0.1}Nb_{0.1}O_{3-\delta}$ as a cathode material for room temperature direct ammonia fuel cells. *ChemSusChem*, *12* (12), 2788-2794.

11. Zou, P., **Chen, S.**, Lan, R., Humphreys, J. Jeerh G. & Tao, S. (2019). Investigation of perovskite oxide $SrFe_{0.8}Cu_{0.1}Nb_{0.1}O_{3-\delta}$ as cathode for a room temperature direct ammonia fuel cell. *International Journal of Hydrogen Energy*. *44* (48), 26554-26564.

12. Zhang, M., Zou, P., Jeerh, G., **Chen, S.**, Shields, J., Wang, H., & Tao, S. (2020). Electricity generation from ammonia in landfill leachate by an alkaline membrane fuel cell based on precious-metal-free electrodes. *ACS Sustainable Chemistry & Engineering*, *8* (34), 12817-12824.

13. Zhang, M., Li, H., Duan, X., Zou, P., Jeerh, G., Sun, B., **Chen, S.**, Humphreys, J., Walker, M., Xie, K., & Tao, S. (2021). An efficient symmetric electrolyser based on bifunctional perovskite catalyst for ammonia electrolysis. *Advanced Science*, *8*, 2101299.

Abstract

Aqueous rechargeable batteries (ARBs) are superior in terms of safety and power density, while facing the challenges of low energy density, short cyclic lifespan, and narrow working temperature windows. The challenges are originated from narrow electrochemical stability windows (ESWs), electrode dissolution/side reaction, and instability upon temperature variation of aqueous electrolytes. Therefore, routes upon ameliorating aqueous electrolytes like additive, pH adjusting, salt concentrating, gelling, solvent hybridizing, interface tuning and beyond concentrating are developed, while salt concentrating is a simply processed and highly effective method for ameliorating aqueous electrolytes.

In this thesis, salt-concentrated electrolytes were developed based on inexpensive salts from acetates, perchlorates to nitrates, which enhanced electrolyte stability thus battery cyclic lifespan, and improved working voltage thus energy density of whole cells. In acetate concentrated system, Zn//MnO$_2$ and VO$_2$//LiNi$_{0.5}$Mn$_{1.5}$O$_4$ redox pairs delivered working voltages of 2.0 (overcharged state for Zn//MnO$_2$) and 2.5 V, coupling cyclic lifespans of 600 and 1200 cycles, respectively. Moreover, "oversaturated gel electrolyte" (OSGE) was proposed to break the limitation of salt solubility, bringing more low-solubility salts into salt-concentrated system, while further extending ESWs in comparison of "room-temperature saturated gel electrolyte" (RTSGE). OSGE endowed Zn//MnO$_2$ and VO$_2$//LiNi$_{0.5}$Mn$_{1.5}$O$_4$ redox couples with high voltages of 2.0 and 2.5 V, and lengthened charge/discharge lifespan to 2000 and 700 cycles, respectively. Furthermore, OSGE enabled the stable operation of correlated ARBs up to 80 °C, which revealed the wide working temperature windows of OSGE-based ARBs. In order to realize stability of ARBs with relatively diluted electrolytes, and simplify battery assembly processing, *N*,*N*-dimethylacetamide (DMA) was employed to dilute nitrate concentrated electrolyte, which obtained desired performance for Zn//LiMn$_2$O$_4$ battery. The overall route of this thesis is from salt concentrating to beyond concentrating, and back to diluting with simple battery assembly procedures, which implement high-voltage and high-stability ARBs with industrially appliable potentials

The research method here can be basically classified into liquid study (especially solvation structure) on electrolytes by spectroscopy and molecular dynamics (MD) simulation; material characterization on electrodes by X-ray, spectroscopy, and

microscope; electrochemical characterization on electrolytes, electrodes and assembled batteries by voltammetry, a.c. impedance and galvanostatic.

Abbreviations

ARAiB	Aqueous rechargeable aluminium-ion battery
ARB	Aqueous rechargeable battery
ARFB	Aqueous redox flow battery
ARLiB	Aqueous rechargeable lithium-ion battery
ARZiB	Aqueous rechargeable Zinc-ion battery
CE	Coulombic efficiency
CEI	Cathode electrolyte interface
CIP	Contact ion pair
CV	Cyclic voltammetry
DFT	Density functional theory
DiB	Dual-ion battery
DIW	Deionized water
DMA	N,N-dimethylacetamide
DSC	Differential scanning calorimetry
E_g	Separation Energy
EDX	Energy-dispersive X-ray spectroscopy
EIS	Electrochemical impedance spectroscopy
ESW	Electrochemical stability window
EV	Electric vehicles
FTIR	Fourier transform infrared spectroscopy
GCD	Galvanostatic charge/discharge
HER	Hydrogen evolution reaction
HiB	Hybrid-ion battery
HME	Hydrate-melt electrolyte
HOMO	Highest occupied molecular orbital
LiB	Lithium-ion battery
LJPP	Lennard-Jones pair potential
LSV	Linear sweep voltammetry
LUMO	Lowest unoccupied molecular orbital
m	molar-salt in kg-solvent
MAB	Metal//air battery
MCB	Metal//chalcogen battery

MD	Molecular dynamics
MiB	Magnesium-ion battery
MOF	Metal organic framework
NMP	1-methyl-2-pyrrolidinone
NMR	Nuclear magnetic resonance
OER	Oxygen evolution reaction
ORR	Oxygen reduction reaction
OSGE	Oversaturated gel electrolyte
OTF	Trifluoromethanesulfonate
PAA	Polyacrylic acid
PB	Proton battery
PBA	Prussian blue analogue
PiB	Potassium-ion battery
PTFE	Polytetrafluoroethylene
PVA	Polyvinyl alcohol
PVDF	Polyvinylidene fluoride
RT	Room temperature
RTSGE	Room-temperature saturated gel electrolyte
SDS	Sodium dodecyl sulfate
SEI	Solid electrolyte interface
SEM	Scanning electron microscope
SHE	Standard hydrogen electrode
SiB	Sodium-ion battery
SSIP	Solvent-separated ion pair
STA	Simultaneous thermal analysis
TFSI	Bis (trifluoromethane sulfonly) imide
TGA	Thermal gravimetric analysis
V_{OC}	Open circuit potential
VMD	Visual molecular dynamics
WiBSE	"water-in-bisalt" electrolyte
WiSE	"water-in-salt" electrolyte
XRD	X-ray diffraction
ZAB	Zinc//air battery

CHAPTER 1 Introduction & literature review

1.1 Background

Climate change draws the attention globally, hence under the UN Paris Agreement, countries committed to restricting global warming to properly below 2 °C and to actively pursue a 1.5 °C limitation [1-3]. That triggered the boom of research and practice towards carbon dioxide mitigation, ranging from carbon avoidance (photovoltaic power station, hydrogen energy), carbon embedding (methanol), to carbon removal (bioenergy crops, carbon capture technology) [4, 5]. The strategy popularizing electric energy in automobiles as electric vehicles (EVs) is able to reduce the overall energy usage through enhancing energy efficiency, thus reduce the carbon emissions, which can be categorized into carbon avoidance as well [4, 6, 7]. Transport is the second largest source of CO_2 emissions at 24% of the total, while the fuel efficiency of the mode of travel can influence transport CO_2 emission largely [8]. Compared with current internal-combustion-engine vehicles, EVs are expected to reduce well-to-wheel emissions by 70–85% by 2030 with virtually zero tailpipe emissions and excellent energy utilization efficiency, which requires the fully popularized EVs in transport sector [8]. The commercialization of EVs, involving full battery electric vehicle (BEVs), hybrid electric vehicles (HEVs) and hybrid plug-in electric vehicles (HPEVs), demands the mature battery technology with the properties of high energy density, high power density and long lifespan, which the currently commercialized batteries especially the lithium-ion batteries (LiBs) fail to satisfy [7, 9, 10].

In fact, the bottleneck of EVs promotion is battery, whilst the bottlenecks of the battery are undesired energy density, low power density and safety issue, which are caused by the relatively low capacity of positive electrode, sluggish electrode kinetics and/or electrode/electrolyte interface kinetics, and flammable organic solvent of electrolytes, respectively [11-15]. The cyclic lifespan of commercialized LiBs (electrode) is acceptable, while the degradation of electrolyte can shorten lifespan of whole cell, and even induce potential safety hazard [13, 14]. Concerning these issues, several new concepts from lithium-air batteries, lithium-sulfur batteries and flow batteries (innovations on the cathodes)

[16-18], to solid-state batteries, quasi-solid-state batteries and aqueous batteries (innovations on the electrolytes) have been proposed and researched intensively [19-21]. Meanwhile, the capacity of positive electrode will be influenced by the interfacial kinetics and mass transportation between electrolyte and positive electrode as well, even the working potential of positive electrode will be lowered attributing to the interfacial polarization thereby lowering the energy density of the whole cell [22, 23]. Therefore, electrolytes are of paramount importance for making batteries with high energy density and excellent safety.
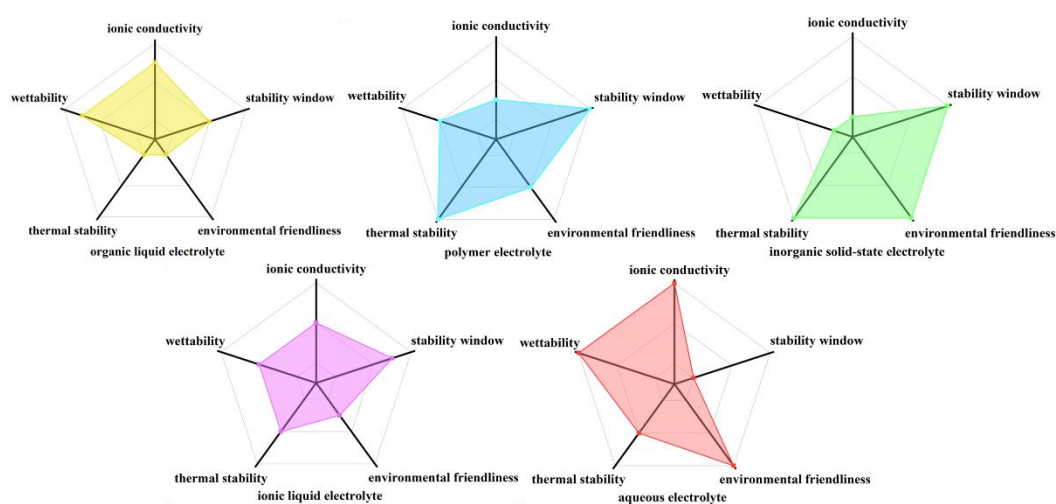
Fig. 1.1 Semi-quantitative comparison of organic liquid electrolyte, polymer electrolyte, inorganic solid-state electrolyte, ionic liquid electrolyte and aqueous electrolyte.

To be an ideal electrolyte material, the properties of electronic insulating, high ionic conductivity, wide electrochemical stability widow, robust mechanical property, thermal stability and safety, facilitated interfacial kinetics, seldom chemical "cross-talk" of electrodes, simple manufacturing process in large-scale, low cost, environmental friendliness and non-toxicity are all expected [24, 25], whilst no currently used electrolytes can meet all these criteria. The conventional electrolytes can be classified into organic liquid electrolytes, polymer electrolytes, inorganic solid-state electrolytes, ionic liquid electrolytes and aqueous electrolytes,

which are semi-quantitatively compared in Fig. 1.1. Among these electrolytes, the aqueous electrolytes are impressive in terms of ionic conductivity, environmental friendliness and interfacial wettability [26-33].

Based on the aqueous electrolytes, aqueous rechargeable batteries (ARBs) move to the forefront, which are destined to avoid the potential flammability and explosion of organic liquid electrolyte-based batteries and exempt the sophisticated (atmosphere controlling) manufacturing process [34, 35]. Furthermore, attributing to the high permittivity and low viscosity of water, the ionic conductivity of aqueous electrolytes is considerably higher than that of organic liquid electrolytes, resulting in excellent rate capability and power density of ARBs [29, 34]. Thanks to those advantages of aqueous electrolytes, the ultrafast charge/discharge energy storage system can be established in grid-scale with ARBs [29, 36]. However, there is a noticeable gap between conventional LiBs and ARBs in energy density, which restricts the large-scale application, and eliminates the benefits of low cost and good safety of ARBs in the EV industry [37, 38].

The relatively low energy density of ARBs is basically derived from the low working voltages which are caused by the narrow electrochemical stability windows (ESWs), which is related to the oxygen evolution in high potential and hydrogen evolution in low potential of aqueous electrolytes [34, 39]. To some extent, the narrow ESWs of aqueous electrolytes is Achilles' heel for improving energy density of ARBs [34, 40]. Furthermore, the issue regarding ESWs can induce the short cyclic lifespan thus higher cost when running energy storage stations based on ARBs [41]. It is noteworthy that the electrode dissolution in aqueous electrolytes can hinder the long-term charge/discharge cycling as well, due to the strong polarity of water molecules [42]. Theoretically, mass dissolution is a thermodynamically favorable process as determined by the Gibbs free energy, regardless acid/alkaline environments of electrolytes in real situations [42, 43]. In spite of narrow ESWs and electrode dissolution, instability can be caused by side reactions of electrodes with water and/or oxygen as well, especially those for LiBs [40]. Moreover, the phase transition of water with temperature variation is able to limit the application of ARBs in elevated or subzero temperatures thereby confining operation temperature windows of aqueous electrolytes [44]. In the

following parts, the methods which can increase energy density, expand cyclic lifespan and extent working temperature windows of ARBs through tailoring aqueous electrolytes are summarized, discussed, and commented. Before that, the design concepts (principles) and historical development of aqueous electrolytes are introduced and summarized as well.

1.2 Principles for electrolytes

A typical liquid electrolyte used in rechargeable batteries, fuel cells, and electrochemical capacitors, is composed of solvent, anion, and solvent-solvated cation. For the organic liquid electrolytes, solid electrolyte interface (SEI) can function as another critical component to equip the electrolytes with both electrochemical and thermal stability and excellent rate capability [45, 46], whilst no such interfaces can be observed in the aqueous electrolytes. Thus, a reasonable design is necessary for aqueous electrolytes, enabling good stability of electrolyte/electrode interfaces.

The design of an electrolyte determines from not only whether the reactants in both sides may be solid, liquid, or gaseous (processing consideration), but also the limiting electrochemical potentials μ_A and μ_C for anode and cathode (their Fermi energies), respectively [47]. The anode and cathode refer to negative electrode with lower electrochemical potential and positive electrode with higher electrochemical potential, respectively, which follow the mainstream definition in battery research area. The working voltage window of electrolyte is derived from separation energy (E_g) of lowest unoccupied molecular orbital (LUMO) and highest occupied molecular orbital (HOMO) of electrolyte [48]. Thus, the thermodynamic stability of battery requires that μ_A and μ_C should locate in the working voltage window of electrolyte as exhibited in the schematic illustration of electron energies of electrode and electrolyte of Fig. 1.2. The open circuit potential (V_{OC}) of battery cell can be defined as presented in the following equation [49]:

$$eV_{OC} = \mu_A - \mu_C < E_g \tag{1.1}$$

, where e is magnitude of electronic charge, while for the organic electrolytes, passivating SEI film offer the kinetic stability to a large V_{OC} with no extra-large of $V_{OC} - E_g$ [49]. Because an anode with a μ_A above the LUMO can reduce the electrolyte unless a passivation layer generates a barrier to electron transfer from the anode to the electrolyte LUMO; likewise, a cathode with a μ_C below the HOMO will oxidize the electrolyte unless a passivation layer blocks electron transfer from the electrolyte HOMO to the cathode [49].
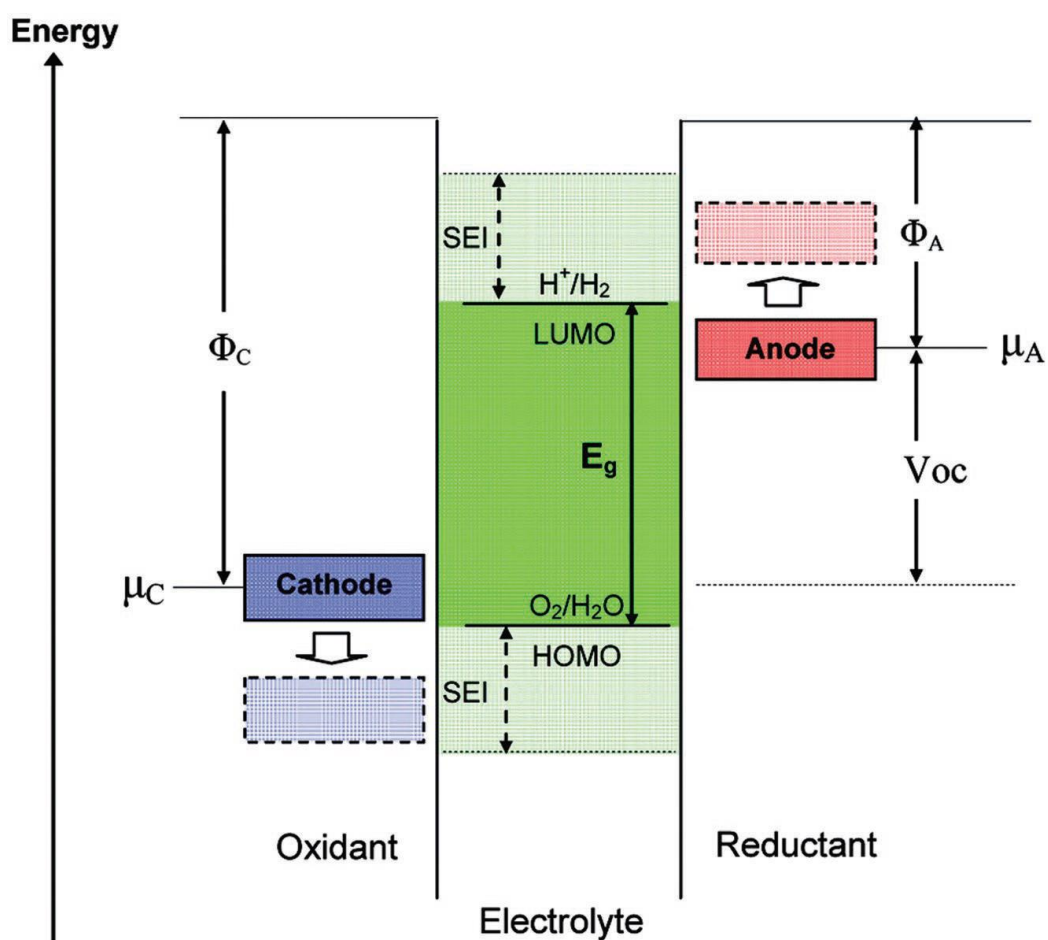
Fig. 1.2 Schematic open-circuit energy diagram of an aqueous electrolyte [49].

Experimentally, the ESW can be determined through standard potentiodynamic approaches such as LSV and CV, despite the diversity of electrochemical environments of electrolytes in actual applications [50, 51]. The restricting reduction and oxidation potentials are assigned to predefined value (reaching decomposition current). The cutoff criteria may be arbitrary in lack of theoretical

significance. In fact, the observed total current of work electrode i_T can be expressed in the sum of two parts as shown in the following equation [51]:

$$i_T = i_{nF} + i_F \tag{1.2}$$

, in which i_{nF} represents the nonfaradaic component (capacitive, interface double layer) and i_F represents the faradaic component (impurity reactions, redox process, and the decomposition of the electrolyte at the interface) [51]. Ideally, i_{nF} should be closed to zero if i_T indicates the ESW of electrolytes exactly. Thus, practically, the i_{nF} should be eliminated when predefining the current level for i_T. Normally, the i_{nF} and i_F can be distinguished by the slope of LSV/CV curve. The lower slope of LSV/CV curve is assigned to i_{nF}, appearing former, whilst the higher one is assigned to i_F, appearing later [52, 53]. And the non-porous electrodes such as Pt and glassy carbon are able to create the circumstance of $i_F \approx 0$ [51].

Conducting ions is the essential requirement of electrolytes, which is able to affect how fast the energy stored in electrodes can be delivered. In liquid electrolytes, the transport of ions is realized by the solvation and dissociation of ionic compounds, and the migration of these solvated ions through the solvent media, successively [54]. In terms of solvation and migration, ionic conductivity can be determined as [55]:

$$\sigma = \sum_i n_i \, \mu_i Z_i e \tag{1.3}$$

, while for most liquid electrolytes, the conductivity results from the overall migration of both anions and cations. And for most batteries, only the portion of current carried by the cation matters, thus the concept of transference number (t_{cation}) is introduced as [55]:

$$t_{cation} = \frac{\mu_{cation}}{\sum_i \mu_i} \tag{1.4}$$

In diluted electrolyte, the transference number of cations is normally 0.2 to 0.4, meaning that the anions are much more mobile than the cations due to the solvation

sheath around cations [54]. The remarkably less than 1 transference number can induce concentration polarization during battery operation through resultant overwhelming anion movement and enrichment near electrode surfaces, which requires relatively "naked" cation with high cation current portion [54].

Meanwhile, the lower viscosity (η) of solvents is able to enhance mobility and ameliorate concentration polarization according to the Stokes-Einstein relation [55]:

$$\mu_i = \frac{1}{6\pi\eta r_i} \tag{1.5}$$

, where r_i is solvation radius. The lower η leads to higher μ_i, while the lower solvation degree of cation (solvation radius) leads to higher μ_i. Besides, the dielectric constant ϵ of solvents is critical as well, which determines charge carrier number (n_i). The higher ϵ, ions can have a higher probability of staying free [56]. Therefore, in terms of ionic conductivity, an ideal solvent should demonstrate high ϵ and low η, which is difficult in organic solvent system, while water can be an optimized option thereby offering desired ionic conductivity to high power-density ARBs.

Based on the design concept, numerous aqueous electrolytes have been developed and applied into various kinds of ARBs. In the following parts, the historic development of aqueous electrolytes is summarized in different types of ARBs, ranging from monovalent-ion battery, multivalent-ion battery, metal//air battery, metal//chalcogen battery, hybrid battery to redox flow battery.

1.3 Historical development of electrolytes for ARBs

1.3.1 Monovalent-ion battery

Among the monovalent-ion batteries, LiB is the most popular and practical, while sodium-ion battery (SiB), potassium-ion battery (PiB), and even proton battery (PB) and ammonium-ion battery began to play an important role in the stage owing

to growingly concern upon lithium resource, twisting the development of corresponding aqueous electrolytes [57]. In 1994, the first aqueous rechargeable lithium-ion battery (ARLiB) was introduced by Jeff Dahn and his co-workers with VO_2//$LiMn_2O_4$ chemistry in 5 M $LiNO_3$ aqueous solution, delivering an energy density of 75 wh·kg^{-1}, which was regarded as a breakthrough in the energy storage system [58]. Up to 2010s, Na_2SO_4 aqueous solutions were employed as the electrolytes for SiBs, coupling $NaTi_2(PO_4)_3$ anode and $Na_4Mn_9O_{18}$ cathode [59, 60]. Compared with Li, Na offers multiple advantages from wide abundance in the crust of earth, dramatically lower cost to even distribution all over the world, hence has attracted a great deal of attention [61, 62]. Meanwhile, a Prussian blue analogue (PBA), nickel hexacyanoferrate was proposed to function as cathode for PiB with 1 M KNO_3 aqueous electrolyte. Its open-framework structure allowed retention of 66% of the initial capacity even at a C rate of 41.7. The high power density, safety, and inexpensive production method make this device an attractive candidate for use in large-scale energy storage to support the electrical grid [63]. Proton insertion/extraction involving electrochemical energy chemistries have been reported as hybrid devices [64], until the discovery of pure proton rocking-chair capacitor with anthraquinone (AQ)//tetrachlorohydroquinone (TCHQ) redox couple and 0.5 M H_2SO_4 aqueous electrolyte [65]. Recently, 62 wt% (9.5 m, molality, molar-salt in kg-solvent) H_3PO_4 was reported as the electrolyte for a high-rate aqueous proton battery, with Mn_2O_3 as anode and CuFe-PBA as cathode. It is noteworthy that the unit of m is unlike the conventional solution concentration unit of M (molarity, molar-salt in liter-solution), because of the evident density variation of solution thus volume change caused by high salt concentration [39, 66, 67]. As a eutectic mixture electrolyte with a low melting point, the 9.5 m H_3PO_4 electrolyte enhanced the low-temperature performance of PBs even at -78 °C [68]. In 2017, the first rocking-chair ammonium-ion battery was demonstrated with ammonium Prussian white analogue cathode, organic solid as anode and 1.0 M $(NH_4)_2SO_4$ aqueous solution as electrolyte. Although, the average working voltage and energy density of that battery was ~1.0 V and ~43 Wh·kg^{-1} respectively, that performance was still encouraging, even was able to inspire research towards ammonia waste utilization [69].

1.3.2 Multivalent-ion battery

The energy density of multivalent-ion battery (MViB) is theoretically higher than that of presently commercialized LiB, due to the higher capacity induced by the multivalent insertion in cathode [70]. Magnesium (Mg), aluminum (Al), calcium (Ca) and Zinc (Zn) ion batteries dominate among the MViBs, while iron (Fe) and copper (Cu) ion batteries also started recently [71-73]. Similar with ARLiBs, the aqueous electrolytes enable the MViBs to become safe and environmentally friendly, even perform better than ARLiBs because of the higher energy density, hence water in MViBs can open doors to new opportunities [74]. Among these, the aqueous rechargeable zinc ion battery (ARZiB) can be further selected as the crown jewel attributing to the features of high abundance, large-scale production, nontoxicity, low redox potential (-0.76 V vs. standard hydrogen electrode (SHE)) and high overpotential for hydrogen evolution reactions (HER, contributing to the thermodynamic stability against aqueous electrolytes) [75, 76]. Alkaline $Zn//MnO_2$ battery with KOH aqueous solution served as the primary battery since 1960s, and the efforts to make that rechargeable were put from 1990s, even expanding the manganese-based cathodes to vanadium-based materials and PBA [77-79]. In recent three years, the ARZiBs got remarkable progress, especially aqueous $Zn//MnO_2$ batteries through the technical routines towards aqueous electrolytes such as hydrogel, high salt concentration, pH-adjusting/decoupling, some representative works are exhibited with employed electrolytes, and compared in energy density and life span (cycling number) in Fig. 1.3 [80-94], in which energy density of various aqueous $Zn//MnO_2$ batteries is unified basing on the mass of MnO_2, and some of them are basically estimated. There is an obvious tendency for aqueous $Zn//MnO_2$ batteries as high-energy storage devices, which are almost ready for further commercialization in large scale, whilst their flexible and stretchable properties enabled by the hydrogel electrolytes, extent the applications from electric grids to daily-used, wearable electronic devices [84, 95].
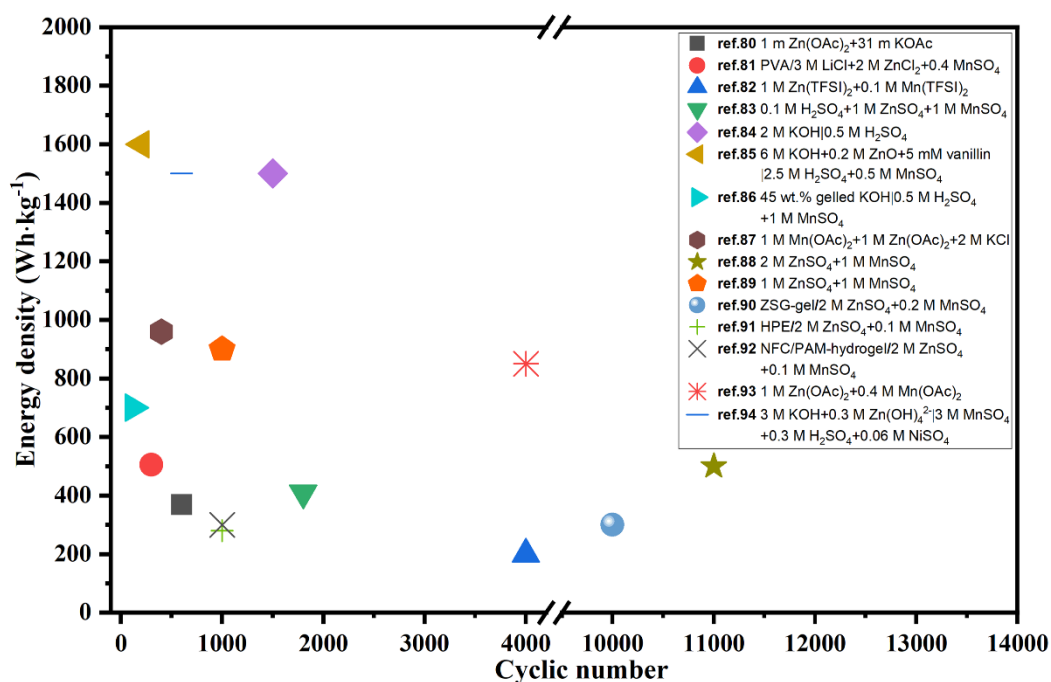
Fig. 1.3 Performance comparison of recently reported Zn//MnO$_2$ batteries based on various aqueous electrolytes in terms of energy density and cycling number.

Except the Zn, Al is also an abundant and cheap element which possesses superior volumetric capacity than Mg and Ca [96]. As early as around 1980, NaCl aqueous solution was used as the electrolyte for Al-alloys//air batteries [97]. In 2012, Liu et al. demonstrated Al ion insertion/extraction in anatase TiO$_2$ electrode with AlCl$_3$ aqueous solution as the electrolyte [98], while it is highly acidic in nature and enhances the dissolution of active material and corrosion of auxiliary battery parts [96]. To overcome this drawback, Al(NO$_3$)$_3$ and Al$_2$(SO$_4$)$_3$ aqueous solutions have been developed as electrolytes for aqueous rechargeable aluminum ion batteries (ARAiBs). However, the corresponding electrochemical activity was weakened in those electrolytes, especially for Al ion insertion/extraction in anatase TiO$_2$ electrode [98]. Therefore, mesoporous nanosized electrodes have been demonstrated to improve electrode and interfacial kinetics thus enhance the discharge capacity [96]. Mg is regarded another alternative to Li, but it suffers a lot from the sluggish kinetics in organic liquid electrolytes. Therefore, water was introduced to the non-aqueous system for better kinetics in electrolytes and cathodes thus the rate capability of whole cells [99]. Since 2013, a lot of works towards aqueous Mg chemistries have been reported in half-cells (mostly using Mg(NO$_3$)$_2$ aqueous solutions as electrolytes) [100, 101], whereas until 2017, Chen

33

et al. reported the full magnesium-ion battery (MiB) based on 1 M MgSO$_4$ aqueous solution with polyimide-nickel hexacyanoferrate redox couple [102]. At the same year, Wang et al. used the 4 m magnesium bis (trifluoromethane sulfonyl) imide (Mg(TFSI)$_2$) concentrated electrolyte to expand the ESW to 2.0 V, enabling poly pyromellitic dianhydride//lithium vanadium phosphate battery chemistry with working voltage of 1.9 V [99].

Likewise, water was introduced into Ca ion battery to improve the electrolyte and electrode/electrolyte kinetics, while an aqueous concentrated electrolyte (8.37 m Ca(NO$_3$)$_2$) was used with CuHCF work electrode in a half-cell system, delivering almost 70 mAh·g^{-1} capacity [103]. In 2017, 2.5 M Ca(NO$_3$)$_2$ aqueous electrolyte was reported, combined with organic polyimide anode and CuHCF cathode as full cell, displaying the 1000 cycles of charge-discharge under 400 mA·g^{-1} current density with 0.5-1.9 cut-off voltage [104]. Among the metal elements used as the cations (charge carriers) of MViBs, Fe element is even more abundant than Zn, Mg and Ca, which is ~46500 ppm in Earth's crust [72]. The reversible Fe plating/stripping was realized in FeSO$_4$ aqueous electrolyte with Fe-based PBA, which exhibit excellent cycling performance of 1000 cycles. The authors also shown that Fe metal anode was able to pair up with a LiFePO$_4$ cathode as hybrid cells, displaying ~155 mAh·g^{-1} discharge capacity [72]. In summary, the Zn and Al-based ARBs are more suitable to be industrialized than the others at this stage, in terms of reliable performance and cost. Particularly, ARZiBs are almost ready in portable electronic devices and large-scale energy storage stations, especially the Zn//MnO$_2$ batteries as shown in Fig. 1.3, while the energy density needs to be improved further for EV applications.

1.3.3 Metal//air battery

Since 1960's and early 1970's, considerable work was carried out on metal//air batteries (MABs) for a variety of applications [105]. MABs are unique compared with other batteries owing to that the electroactive material (oxygen) does not require storage. In this respect, this kind of battery is similar to fuel cells and essentially a fuel cell/battery hybrid, which principally simplifies the battery

design and increases the energy density [105]. Therefore, MABs have attracted much attention as a possible alternative due to their extremely high energy density, compared with that of other batteries, as shown in Fig. 1.4a [106]. The electrolytes utilized for the MABs can be basically classified into aqueous electrolytes (not sensitive to moisture) and non-aqueous electrolytes (water-sensitive system with aprotic solvents). Li and Na are intrinsically suitable for the non-aqueous electrolytes while metals such as Al, Fe and Zn are appropriate for the aqueous system [106]. For the first time, A water-stable Li metal anode with water-stable Li^+-conducting glass ceramics and a lithium-conducting polymer electrolyte was proposed as the anode for a Li//air battery (LAB) with a LiCl aqueous electrolyte at the air electrode in 2008 [107], as the similar cell configuration shown in Fig. 1.4b. Although the nonaqueous electrolyte-based LABs own higher energy density/power density than that of aqueous electrolyte-based ones, the uncertain side reaction in oxygen electrode and aprotic-solvent insoluble Li_2O_2 which usually occur in the former, can be avoid in the latter [108].

Based on the similar design concept, in 2013, a mixed aqueous NaOH/aprotic electrolyte was realized through a separator of $Na_3Zr_2Si_2PO_{12}$ (NASICON) ceramics, and applied into a Na//air battery (SAB), discharging a capacity of ~600 $mAh \cdot g^{-1}$ (energy density of ~1500 $wh \cdot kg^{-1}$) and outputting an areal powder density of 11 $mW \cdot cm^{-2}$ [109]. Unlike LABs and SABs, Zn//air batteries (ZABs) naturally suit aqueous electrolytes, which mostly operated in alkaline media, such as KOH and NaOH, for the sake of higher activity of both the zinc electrode and air electrode since the first invention in 1878 [110]. The structures of cells based on the alkaline aqueous electrolytes are much simpler than those of aqueous LABs and SABs as shown in Fig. 1.4c, because no protection layers are required for Zn metal anodes. For ZABs with open structures, water loss from the aqueous electrolytes is a crucial cause of performance degradation, whereas alkalinity nature of these electrolytes leads to problems of insoluble carbonate precipitation, as well as promoting zinc-dendrite growth and hydrogen evolution, all of them limiting the performance of ZABs [111]. In order to handle these problems through electrolytes, a molten $Li_{0.87}Na_{0.63}K_{0.50}CO_3$ eutectic electrolyte with added NaOH was prepared and employed by a ZAB, which was cycled 110 cycles at 550 ℃, having an average charging potential of ~1.43 V and discharge potential of ~1.04

V [112]. The relevant cell configuration was shown in Fig. 1.4d, as well as the CV curve upon Zn plating/stripping (~1.38 V vs. Ni/Ni(OH)$_2$ for zinc deposition and ~0.7 V vs. Ni/Ni(OH)$_2$ for oxidation of Zn to Zn^{2+}) [112]. Al and Fe are deemed as the first and second most abundant metallic elements in the earth's crust. The theoretical energy density of Al//air batteries (AABs, 8140 wh·kg^{-1}) is much higher than that of ZABs (1350 wh·kg^{-1}), while that of Fe//air batteries (IABs) is 1200 wh·kg^{-1} [113, 114]. Considering these factors, AABs should be more promising; however they suffer a lot from the anode self-corrosion and sluggish kinetics, which demand a rational electrolyte of stability and electrode/electrolyte interface process. At the beginning, NaCl aqueous solution was utilized as the electrolyte for AABs, but the energy density was restricted in that neutral situation, then alkaline system was introduced for not only AABs (KOH) but also IABs (KOH+LiOH) [105, 115].
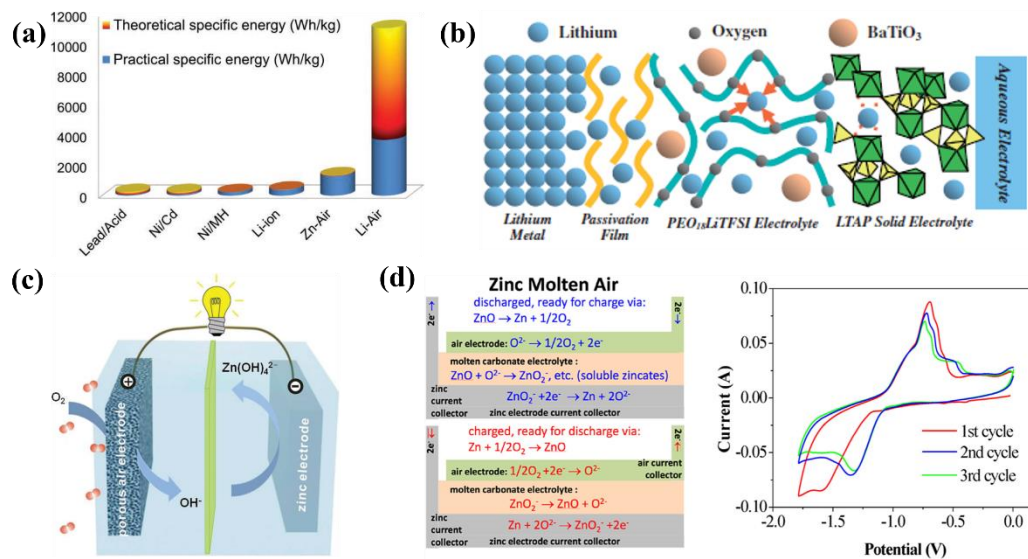
Fig. 1.4 (a) Theoretical and practical energy densities of various types of rechargeable batteries [106]; (b) Schematic diagram of the proposed water stable lithium metal electrode with polymer buffer layer and glass ceramic separator [108]; (c) Schematic principle of operation for ZABs [110]; (d) Schematic representation of the zinc molten air battery and CV curve of Zn redox reaction in that electrolyte with a sweep rate of 100 mV·s^{-1} [112].

1.3.4 Metal//chalcogen battery

Besides MABs, metal//chalcogen batteries (MCBs) are promising alternatives, because they can provide remarkable capacities while using cheaper and more reliable electrodes of sulfur (S), selenium (Se) and tellurium (Te) than air electrodes [116]. The exceptional energy density (for instance, 2600 $Wh \cdot kg^{-1}$ for Li//S batteries, LSBs) of MCBs may be readily sealed, alleviating electrolyte leakage/loss issues, hence making them a safer option. However, this kind of secondary batteries (especially for LSBs) faces the challenges of inferior electrical conductivity of cathodes, polysulfides dissolution and their shuttling between electrodes and considerable volume variation during charge/discharge cycles [116]. In conventional LSBs, ether solvents were mostly used in liquid electrolytes, which can dissolve polysulfides. Traditional carbonate-based LiB electrolytes (carbonates) and ionic liquids, which are either polysulfide incompatible or sparingly polysulfide-soluble, have been adopted in some special cases. Unfortunately, the use of these flammable liquid electrolytes raises the risk of electrolyte fire [117]. Therefore, some research attempted to introduce aqueous electrolytes into metal//chalcogen chemistries [118]. Aqueous Al//S batteries were reported as early as 1993, which used KOH aqueous solution with both K_2S_4 and $In(OH)_2$ additives as electrolyte, while the relevant working voltage was only 1.3 V, and the cyclic performance was even not demonstrated [119]. In 2019, one Fe//S battery was reported with 0.5 M $FeSO_4$ aqueous solution as electrolyte, although the working voltage was even lower (0.6-0.8 V), the cyclic performance was improved to 200 charge/discharge cycles through changing the Fe metal anode midway, and the polysulfide shuttling could be avoided [120]. As for LSBs and Na//S batteries (SSBs), analogous to LABs/SABs, protection layers (membrane electrolytes) were necessary in the metal anode side when introducing aqueous electrolytes. Li et al. integrated a photocatalyst into a hybrid LSB involving 0.01 M Li_2S_4 and 0.2 M LiOH aqueous electrolyte (catholyte) to store the solar energy directly. In the Li anode side, an organic liquid electrolyte of 1 M $LiClO_4$ in ethylene carbonate (EC)/dimethyl carbonate (DMC) was used, coupling $Li_{1.35}Ti_{1.75}Al_{0.25}P_{2.7}Si_{0.3}O_{12}$ (LATP) glass ceramic separator [121]. The structure of this solar energy directly stored LSB and reaction mechanism was shown in Fig. 1.5a. For Na metal anode-based one, 0.25 M Na_2S_4+0.1 M NaOH aqueous electrolyte (catholyte) was matched with 1 M $NaClO_4$ in EC: propylene carbonate (PC)+5% fluoroethylene carbonate (FEC) organic electrolyte (anolyte) with the

assistance of NASICON membrane, as shown in Fig. 1.5b [122]. This configuration for both LSBs and SSBs, not only stabilized Li/Na metal anodes in aqueous electrolytes, but also prevented dendrite formation and polysulfide shuttling, and increased utilization of active matters.
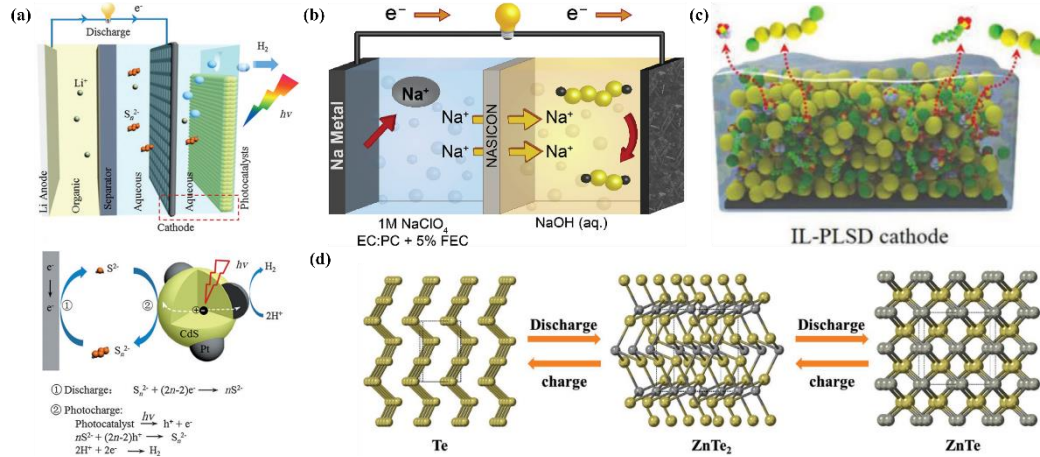
Fig. 1.5 (a) The battery consists of a Li anode with organic electrolyte, a Li-ion conductive LATP glass ceramic separator, and an aqueous Li_2S_n alkalic catholyte containing the Pt/CdS photocatalysts, and corresponding photocharging, discharging processes [121]; (b) Schematic of a sodium-aqueous polysulfide hybrid battery with a sodium-metal anode, organic anolyte, NASICON separator, and an alkaline aqueous polysulfide catholyte [122]; (c) Schematics of PLSD cathodes coated with Zn^{2+}-conducting IL [123]; (d) Schematic representation for phase transformation during discharging (yellow: Te atoms, grey: Zn atoms) [124].

Zn is a highlight among aqueous system, and aqueous Zn//chalcogen batteries are also eye-catching recently, contributed by Zhi group. An aqueous Zn//S battery was initially realized by a "liquid film" comprising ionic liquid encapsulated within a copolymer (working as cathode, as shown in Fig. 1.5c), and a 1 M $Zn(TFSI)_2$ aqueous electrolyte. This Zn//polysulfide system delivered an extraordinary capacity of 1148 mAh·g^{-1} and an overwhelming energy density of 724.7 Wh·kg^{-1} (calculated on the basis of cathode mass, under current density of 0.3 A·g^{-1}) [123]. The same aqueous solution (1 M $Zn(TFSI)_2$) was used as the electrolyte of one Zn//Se battery as well, whilst the performance was not good. Thus, one 2 M $Zn(TFSI)_2$/polyethylene glycol (PEG)/water electrolyte was

prepared, extending the ESW of aqueous electrolyte and enhance battery performance [125]. The overall reaction mechanism of this battery was studied as well, determined as [125]:

$$Zn + Se \leftrightarrow ZnSe \tag{1.6}$$

, which delivered same conversion reaction mechanism in both organic and aqueous electrolyte. Extraordinary capacities in organic system (551 mAh·g^{-1}) and aqueous system (611 mAh·g^{-1}) were achieved, as well as remarkable rate performance and cycling performance. Meanwhile, one aqueous Zn//Te battery was reported by Zhi group as well, utilizing a 1 M ZnSO$_4$ polyamide (PAM) hydrogel as electrolyte, which displayed ultraflat discharge plateau and high volumetric capacity (2619 mAh·cm^{-3} under 0.05 A·g^{-1} current density) [124]. That battery exhibited obvious flat discharge plateaus at about 0.59 and 0.48 V originating from Te reduction. Furthermore, that was proved as two-step solid-to-solid conversion with the successive formation of ZnTe$_2$ and ZnTe obeying the following two equations [124]:

$$2Te + Zn^{2+} + 2e^- \leftrightarrow ZnTe_2 \quad \text{(First step)} \tag{1.7}$$

$$ZnTe_2 + Zn^{2+} + 2e^- \leftrightarrow 2ZnTe \text{ (Second step)} \tag{1.8}$$
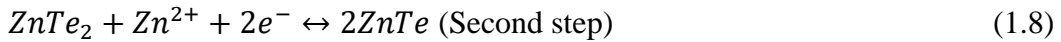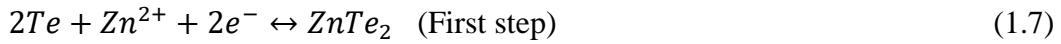
, which was demonstrated in Fig. 1.5d. This work presented a new direction to design conversion-type aqueous MCBs with high capacity, stable output potential, excellent rate capability and good cyclic performance.

1.3.5 Hybrid battery

Aqueous hybrid batteries (AHBs) are new members of ARB family, attracting great interest of researchers, which can be classified into hybrid ion batteries (HiBs), dual ion batteries (DiBs) and capacitor batteries (CBs). Except the CBs integrating battery behaviour in one side and capacitor behaviour in the other side, the mechanism of HiBs and DiBs is similar to that of single-ion ARBs, while their

electrolytes are composed of various electrochemically active ions, diffusing from electrolyte to electrodes simultaneously (for DiBs) or individually (for HiBs) [126]. Compared with the ARBs of single ions, AHBs own several significant benefits, summarized as: (1) enhanced rate performance via combining the ions of sluggish diffusion with those of better kinetics; (2) superior coulombic efficiency (CE) by avoiding ion trapping; (3) high flexibility and adaptability (more options for electrode materials); (4) low cost due to the less occupancy of Li/other costly elements in the whole cell; (5) wide applications (energy storage and Li purification) [127]. HiBs are most popular among AHBs, which can be further divided into monovalent/monovalent ion batteries, monovalent/multivalent ion batteries [126]. In the year of 2013, Xia group initially reported two monovalent/monovalent systems ($Na_{0.22}MnO_2$//$LiMn_2O_4$ and TiP_2O_7//$Na_{0.44}MnO_2$) based on Li_2SO_4+Na_2SO_4 mixed electrolytes, exhibiting specific energy of 17 Wh·kg^{-1} and 25 Wh·kg^{-1} based on the total weight of active electrode materials, respectively [128]. In 2018, a low-cost aqueous Mg-Na battery was proposed as monovalent/multivalent system, employing Mn_3O_4 as cathode of MiB, $NaTi_2(PO_4)_3$ as anode of SiB and 2 M $MgSO_4$+1 M Na_2SO_4 aqueous solution as electrolyte, which avoided the cathode problems of SiBs and anode problems of MiBs [129]. In the monovalent/multivalent system, Zn metal anode based HiBs were reported intensively [126], especially the ones in mild aqueous electrolytes, which can get rid of poor cyclic performance and Zn dendrite in the alkaline condition as the following equation:

$$Zn + 4OH^- \leftrightarrow Zn(OH)_4^{2-} + 2e^- \leftrightarrow ZnO + 2OH^- + H_2O + 2e^- \qquad (1.9)$$
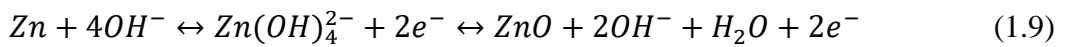
In 2012, Chen et al. proposed Zn metal anode based HiBs for the first time, which employed $LiMn_2O_4$ as cathode and 3 M $LiCl$ + 4 M $ZnCl_2$ solution (pH = 4) [130]. Afterwards, aqueous Zn//$LiMn_2O_4$ batteries were investigated frequently, while the relevant reaction mechanism was determined as:

Negative: $Zn^{2+} + 2e^- \leftrightarrow Zn$ $\qquad (1.10)$

Positive: $LiMn_2O_4 \leftrightarrow Li_{1-x}Mn_2O_4 + xLi^+ + xe^-$ $\qquad (1.11)$
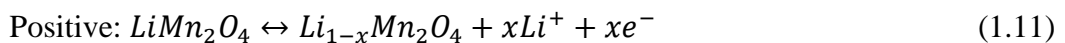
In 2018, Wang group made a breakthrough upon aqueous $Zn//LiMn_2O_4$ batteries via using 1 m $Zn(TFSI)_2$+20 m LiTFSI highly concentrated electrolyte, which was cycled for 4000 cycles under 4 C rate. In that work, Zn//Zn symmetrical cell based on the highly concentrated electrolyte was cycled for 500 cycles (~170 h) under a current density of 0.2 mA·cm^{-2} without any dendrite and ZnO observed [131].

The ions in HiBs participating in electrode reaction are only cations, while both cations and anions are involved in DiBs, which need to be considered as active matter. The typical cathodes of DiBs are graphitic carbons, metal organic frameworks (MOFs), organic cathodes or electroactive polymers and MXene, among which graphitic carbon cathodes are likely the most suitable candidates for practical applications due to its unique layered structure, environmentally friendliness, and low cost [132, 133]. The aqueous DiB using 1 M $(NH_4)_2SO_4$ aqueous solution as the electrolyte was reported by Zhang et al. in 2019, in which n-type polyimide anode reacted with NH_4^+ while the p-type radical polymer reacted with SO_4^{2-} to obtain a large cell voltage of 1.9 V [120]. Whilst, Ji group made contributions to the aqueous DiBs by using concentrated $ZnCl_2$ aqueous solutions (30 m) with $ZnCl_4^{2-}$-insertion molecular solid of ferrocene as anode, Zn-insertion PBA as cathode. This electrolyte not only minimized the dissolution of ferrocene anode, but also widened the voltage of full cell by 0.35 V, compared with a dilute $ZnCl_2$ electrolyte [134].

Both cations and anions contribute to capacity in CBs, which is basically like DiBs, while the cations are involved in redox-active oxide cathode, and anions are absorbed/desorbed by an inert activated carbon (AC) anode in CBs. Therefore CBs is one kind of relatively new device that is intermediate in energy between batteries and supercapacitors, whilst principally offering supercapacitor-like power and cyclability values [135]. The high ionic conductivity of aqueous electrolytes is able to induce high capacitance of electrical double layer (EDL) in the active carbon anode-electrolyte interfaces, hence can be a good option for CBs [29]. Li_2SO_4 aqueous solution was assembled with $LiMn_2O_4$ cathode and AC anode as a Li ion capacitor by Wang and Xia in 2005 [136], before that $Ni(OH)_2$ cathode was demonstrated as a good cathode for aqueous system with AC anode in alkaline aqueous electrolyte (KOH) [137]. Brousse et al. prepared a Na ion capacitor based

on Na$_2$SO$_4$ aqueous solution with AC anode, while MnO$_2$ was utilized as cathode for Na$^+$ intercalation/deintercalation in the bulk as the equation below [138]:

$$MnO_2 + Na^+ + e^- = MnOONa \tag{1.12}$$

, while the surface redox could be enhanced once the cathode was nanosized as the following:

$$(MnO_2)_{surface} + Na^+ + e^- = (MnOONa)_{surface} \tag{1.13}$$
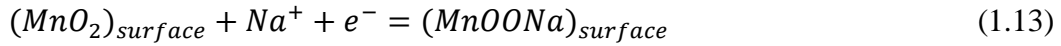
Recently, a Zn ion capacitor was innovatively proposed by Kang et al., in which AC, Zn metal and ZnSO$_4$ aqueous solution served as cathode, anode and electrolyte, respectively. A metric of 121 mAh·g^{-1} capacity (84 Wh·kg^{-1} energy density), 14.9 kW·kg^{-1} power output and an excellent cycling stability (over 10000 cycles with 91% capacity retention) was exhibited [139]. Numerous works towards Zn ion capacitors have been reported since then, indicating another feasible route to improve electrochemical energy storage system.

1.3.6 Redox flow battery

Redox flow batteries (RFBs) are novel electrochemical energy storage devices, storing electrical energy in two redox-active matters with distinct redox potentials. The redox species are usually dissolved or suspended in the electrolyte tanks (negolyte and posolyte in Fig. 1.6a). Electrochemical charge-transfer reactions occur on the electrode stack, consisting of a pair of porous electrodes separated by an ion-conducting membrane. The capacity of the RFB scales with available charges stored in the electrolyte tank whilst the current output of the RFB is determined by the rate of the electrochemical reaction on the electrode stack. This unique configuration enables design flexibility in decoupling energy and power, which is critical for large-scale energy storage and energy distribution [140]. Aqueous redox flow batteries (ARFBs) are one of the most important candidates for large-scale energy storage, which can be applied over a wide power range with long lifetimes over a flexible discharge duration. Moreover, the natural scalability

induced by their unique design of decoupled power and energy is deemed as the most prominent advantage.

Since the first ARFB invented by NASA in 1970s with Fe (III)/Fe (II) and Cr (III)/Cr (II) as the active matters, and $FeCl_2$ and $CrCl_3$ added HCl solution as electrolyte, a vast number of ARFBs have been invented, classified as vanadium (V)-, Zn-, Fe-, polysulfide (PS)-based (inorganic) and organic-based ARFBs [141]. In 1985, a V (III)/V(II) redox couple was introduced as the first V-based ARFB with VCl_3 dissolved HCl/H_2SO_4 solution as electrolyte, while there was a considerable room for ameliorating the reversibility of the redox reactions [142]. Furthermore, V-based ARFBs face the challenges of low thermal stability, crossover of V-species, and limited kinetics which are basically correlated to the electrolyte issues, and porous nanofiltration-ameliorated Nafion membranes (perfluorinated cation exchange membranes) as shown in Fig. 1.6b can be the effective solutions [143, 144]. Beside V-based ARFB, Zn-based ones are massively reported due to the high adaptability of Zn metal anodes towards aqueous system, and Zn//Br$_2$ systems were literally first reported among Zn-based species, in which the KCl/NH$_4$Cl added ZnBr$_2$ concentrated solutions served as electrolytes [145]. However, Br$_2$ is deemed as the hazardous substrate and corresponding redox potential exceeds the ESW of water. Hence, Li et al. introduced the Zn//I$_2$ species with the scheme of battery structure shown in Fig. 1.6c, involving Nafion membrane and ZnI$_2$ solution as electrolyte. The redox mechanism was revealed as [146]:

Anode: $Zn \leftrightarrow Zn^{2+} + 2e^-$ $\qquad E^0 = -0.7626\,V\,vs.\,SHE$ (1.14)

Cathod: $I_2(s) + I^- \leftrightarrow I_3^-$
$\qquad\qquad I_3^- + 2e^- \leftrightarrow 3I^-$ $\qquad E^0 = 0.5360\,V\,vs.\,SHE$ (1.15)

Overall: $Zn + I_3^- \leftrightarrow Zn^{2+} + 3I^-$ $\qquad E = 1.2986\,V$ (1.16)
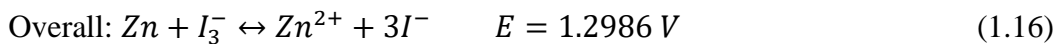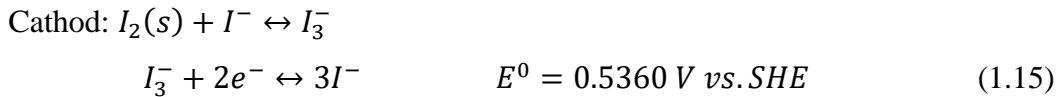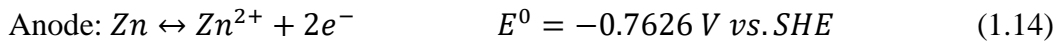
, with relevant CV curve shown in Fig. 1.6d. ZnI$_2$ electrolytes with various concentrations were investigated in that case, and the concentration of 3.5 M was

selected for further cyclic performance test due to the optimum CE, energy efficiency (EE) and voltage efficiency (VE) dependent on that condition, whereas ethanol was further added for expanding the stable electrolyte temperature window to from -20 to 50 ℃ [146]. Similar to Zn-based ones, Fe-based ARFBs were widely studied and applied. As mentioned above, the initially studied ARFB was Fe-based one with Fe^{3+}/Fe^{2+} and Cr^{3+}/Cr^{2+} as the active matters, and HCl solution as electrolyte, which has been limited by the sluggish reaction kinetics of Cr^{3+}/Cr^{2+}, parasitic HER, and the crossover of active materials. The management towards electrolyte pH was chosen as an effective strategy to mitigate those challenges [141], which will be discussed in detail in next section.

The first PS-based ARFB was invented by Regenesys Ltd. in 1991 with NaBr on positive side and Na_2S_4 on negative side as electrolyte [147], extending the utilization of PS from MCBs to ARFBs. Analogous to Zn-based ARFBs, the Br^-/Br_3^- chemistry was replaced by I^-/I_3^- in the PS system, demonstrating higher solubility, faster kinetics and a lower vapour pressure [148]. That cell was comprised by KI and K_2S_2+KOH aqueous solution and Nafion 115/117 membranes with the cell structure shown in Fig. 1.6e and CV curves of redox matters shown in Fig. 1.6f. Compared with inorganic-based ARFBs, organic-based ARFBs can demonstrate large earth abundance and high tunability through functionalization. In 2009, Xu et al. innovatively reported the concept of the organic-based ARFB by adopting 1,2-dihydrobenzoquinone-3,5-disulfonic acid (BQDS) or 1,4-dihydrobenzoquinone-2-sulfonic acid (BQS) as cathode and conventional $PbSO_4$ in tiron-added aqueous H_2SO_4 solution as anolyte, which delivered an average CE of 99% and EE of 70% over 100 cycles. The obtained high performance indicated that soluble quinones were promising positive materials for ARFBs [149]. Lately, one reversible ketone hydrogenation and dehydrogenation was realized as organic-based ARFB using molecular structure design of 9-fluorenone (FL) as the example. An ARFB consisting of a ferro/ferricyanide catholyte and 1.36 M 4-carboxylic-7-sulfonate fluorenol (4C7SFL)/1 equiv. NaOH anolyte (equivalent to 2.72 M electron transfer) was subjected to current density testing and extended cycling, which delivered 1000 charge-discharge cycles at 25 ℃ (75% capacity retention) and 780 cycles (70% capacity retention) at 50 ℃ [150].

44
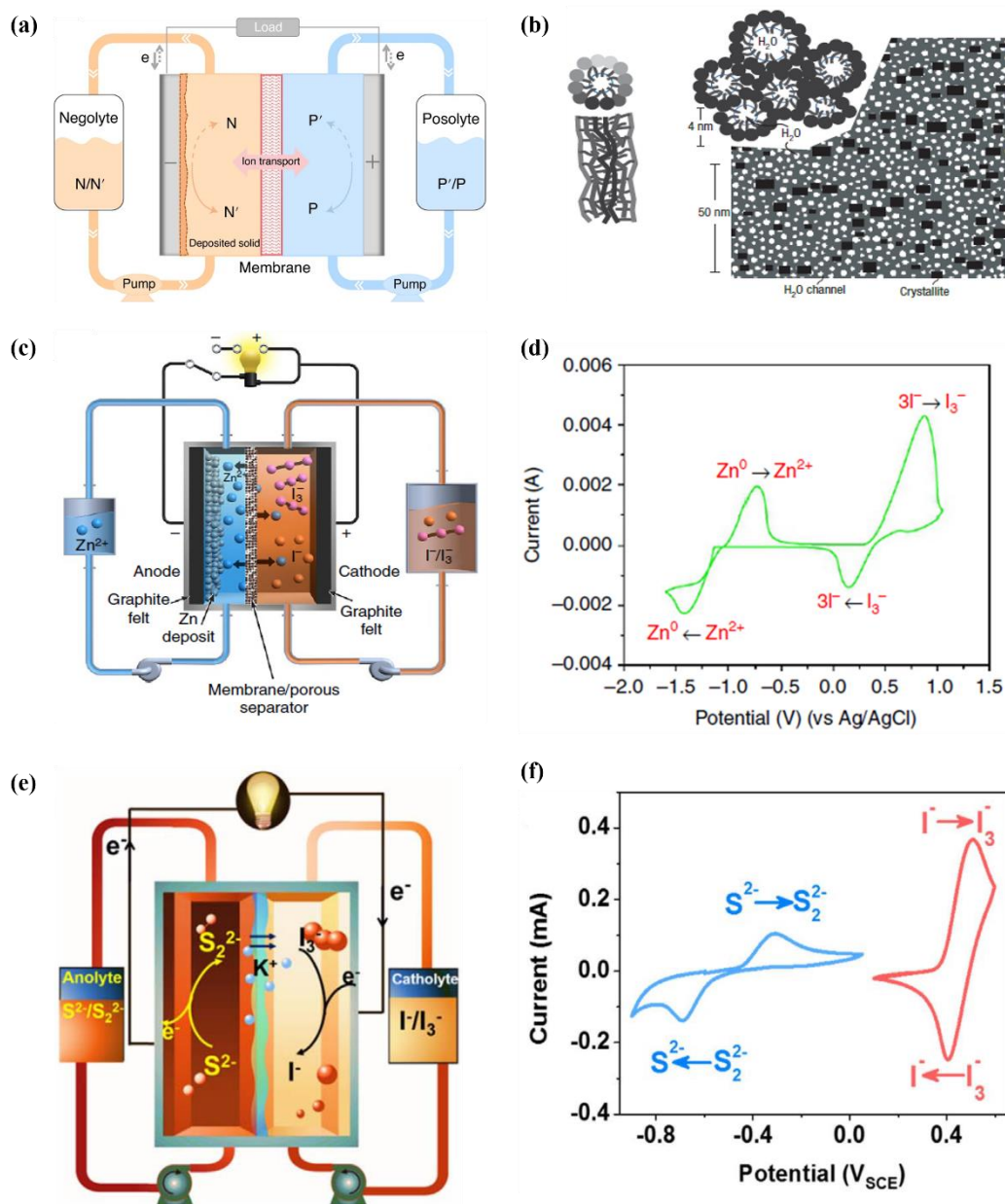
Fig. 1.6 (a) A schematic representation of a general RFB cell. The solid and dashed curly arrows represent the charging and discharging process, respectively. N/N′, negolyte in oxidized/reduced state; P/P′, posolyte in oxidized/reduced state [140]; (b) Two views of an inverted-micelle cylinder and schematic diagram of the approximately hexagonal packing of several inverted-micelle cylinders [144]; (c) Schematic representation of the proposed Zn//I$_2$ system [146]; (d) CV curves of 0.085 M ZnI$_2$ on a glassy carbon electrode at the sweep rate of 50 mV·s^{-1} [146]; (e) A schematic illustration of the proposed aqueous polysulfide/iodide redox flow batteries [151]; (f) CV curves of 5 mM K$_2$S$_2$-0.5 M KCl solution (blue) and 5 mM KI-0.5 M KCl solution (red) at 5 mV·s^{-1} on a gold electrode [151].

Overall, the historical development of aqueous electrolytes for ARBs in various species were briefly introduced with the timelines of representatively innovative works summarized in Fig. 1.7. The flourishment of aqueous electrolytes facilitated the all-around development of ARBs, while the challenges of low energy density, poor cyclic stability and narrow working temperature window towards ARBs were exposed during practice. From the perspective of electrolytes, the narrow ESWs, electrode dissolution/side reaction, and phase transition/instability of water at different working temperatures are the challenges of ARBs. Therefore, it is critical to cultivate more mature aqueous electrolytes via developing new concepts.
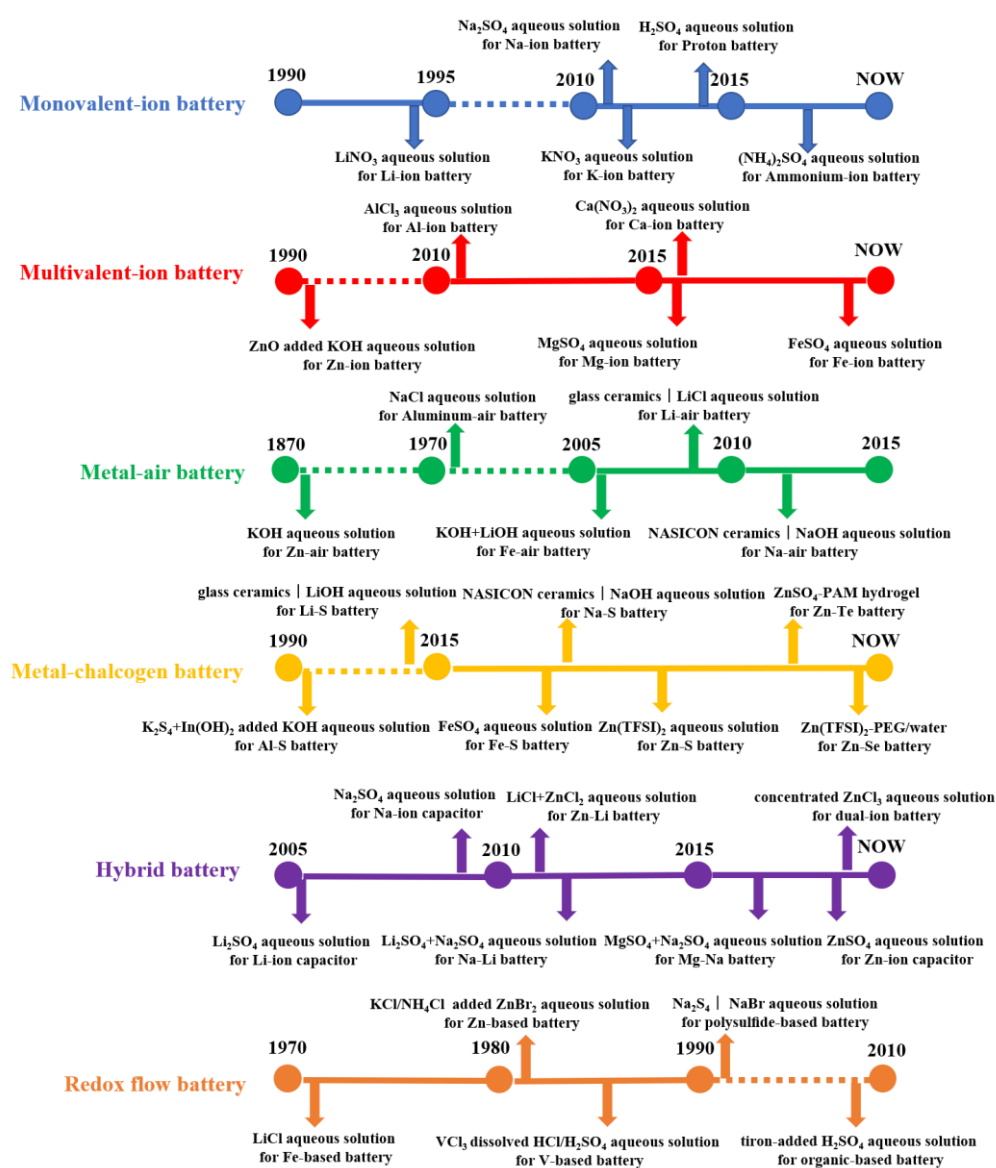
Fig. 1.7 Historical development of aqueous electrolytes with representatively innovative works for various ARBs

46

1.4 New concepts for better electrolytes of ARBs

Electrolytes in any battery systems have been tailored to the specific chemistry and structure of the electrodes and reactions present in the cell [46]. Although the requirements vary with the electrodes, there are still some common demands towards electrolytes such wide ESW, high ionic conductivity, desired thermal stability and wide working temperature range, while negligible electrode dissolution/side reaction aims at aqueous electrolytes [152]. The recently developed new concepts for better aqueous electrolytes can be categorized into electrolyte additive, salt-concentrated electrolyte, gelled electrolyte, solvent-hybrid electrolyte, electrode/current collector-electrolyte interface tuning, beyond salt-concentrated electrolyte which are common strategies for liquid phase electrolytes, except pH management (including two-pH decoupling electrolyte) which is unique strategy for aqueous electrolytes.

1.4.1 Electrolyte additive

For conventional LiBs, using electrolyte additives is one of the most economic ways to improve performance. Usually, the amount of an additive in the electrolyte is no more than 5% either by weight or by volume, but significantly improves reversibility and cycle life of LiBs [153]. The strategy of electrolyte additives is appropriate to ARBs as well, which was intensively reported in ARZiBs in recent five years. The additives added to the aqueous electrolytes can be classified into ion, metal, organic and inorganic, offering the function of enhancing ion transportation, manipulating ESWs, tuning electrode surfaces/interfaces [154]. One typical work for widening ESWs of aqueous electrolyte was adding sodium dodecyl sulfate (SDS) to the 1 M Na_2SO_4+1 M $ZnSO_4$ aqueous electrolyte, which equipped the HiB of Zn//$Na_2MnFe(CN)_6$ with 2.0 V operation voltage and a capacity retention of 75% over 2000 cycles. In that research, the surfactant additive could effectively suppress the oxygen evolution reaction (OER) thus extended the ESW to 2.5 V, attributing to SDS adsorption layer which was theoretically confirmed by density functional theory (DFT) calculation as shown in Fig. 1.8a-f [155]. Beside SDS, Mn ion additive was proved to suppress the OER to broaden the ESW through the competition mechanism of the dissolution/deposition

reaction of MnO_2/Mn^{2+} and OER in solvent [83]. The above-introduced two additives expanded ESWs through suppressing OER, while additives like $PbSO_4$, diethyl ether (Et_2O) and sodium dodecyl benzene sulfonate (SDBS) were used for inhibiting corrosion and suppressing dendrite of Zn metal anode thence enhancing cyclability. The $PbSO_4$ was added to 1 M Li_2SO_4+2 M $ZnSO_4$ electrolyte gelled by 5% fumed silica until saturation, which provided 20% lower corrosion current density on the Zn anode. The Zn metal anode in the tested $Zn//LiMn_2O_4$ HiB with $PbSO_4$ added electrolyte was determined as dendrite-free morphology through SEM characterization [156]. In $Zn//MnO_2$ system, 2 vol.% Et_2O was added in 3 M $Zn(CF_3SO_3)_2$+0.1 M $Mn(CF_3SO_3)_2$ electrolyte, which was believed to be absorbed near the tip of metal anode substrate surface inducing an electrostatic shield, and suppressing the dendrite formation by maintaining a smooth deposition layer as shown in Fig. 1.8g [157]. SDBS was reported to improve the electrochemical behaviors of a $Zn//LiFePO_4$ HiB. With the assistance of this additive, Zn ions were deposited smoothly on the surface of the Zn metal instead of participating in the vertical growth of flake-shaped Zn dendrites. Simultaneously, the Li^+ diffusion coefficient was increased from 1.78×10^{-11} to 8.22×10^{-11} $cm^2 \cdot s^{-1}$ by ameliorating the wettability of the $LiFePO_4$ cathode, contributing to the high power density of whole cell [158].

In LiBs, additives are used intensively for engineering interfaces, especially engineering SEIs, which were employed to tailor interfaces of ARBs as well. Recently, Wang and Xu groups reported trimethylethyl ammonium trifluoromethanesulfonate ($Me_3EtNOTf$) as an additive to fluorinate interface between Zn metal anode and aqueous zinc trifluoromethanesulfonate ($Zn(OTf)_2$) electrolyte, which enabled the stable cycling of both $Zn//VOPO_4$ full cell (136 $Wh \cdot kg^{-1}$ and retains 88.7% of its capacity for >6000 cycles) and $Zn//O_2$ cell (325 $Wh \cdot kg^{-1}$ for >300 cycles). The ZnF_2-rich composition in that interface was caused by the additive, while $ZnCO_3$, $ZnSO_3$ and poly-species could also be discovered there (Fig. 1.8h). DFT calculation suggested that downstream reactions resulting from alkylammonium decomposition were responsible for the formation of $ZnCO_3$ [159]. In another work, ZnF_2 was added to a 2 M $ZnSO_4$ electrolyte directly for the formation of stable F-rich interfacial layer. The F-rich interfacial layer could not only regulate the growth orientation of zinc crystals, but also serve as an inert
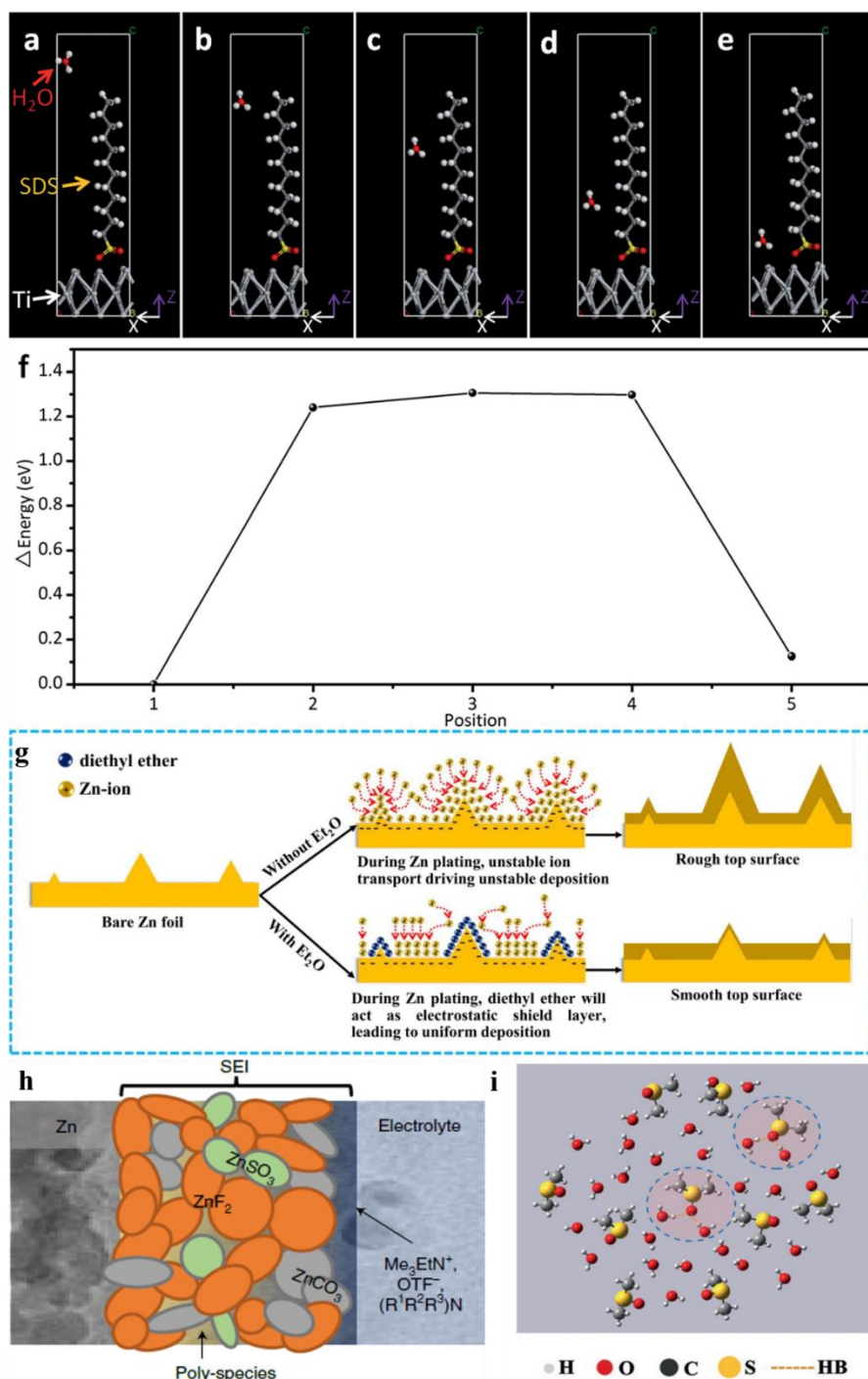
Fig. 1.8 (a-e) Models of density functional theory calculations, showing a water molecule passing through the SDS adsorption interlayer at different positions [155]; (f) The tendency of the energy change at different positions [155]; (g) Schematics of morphology evolution for Zn metal anodes in mild aqueous electrolyte with and without Et$_2$O additive during Zn stripping/plating [157]. (h) Cartoon of proposed Zn^{2+}-conducting SEI, characterized by small nodular particles embedded in a polymeric framework [159]. (i) Local structure of the χ_{DMSO}=0.3 system from MD simulations [44].

protection layer against side reactions such as HER. Under the protection of that interfacial layer, Zn stripping/plating was stably repeated for 600 h, and one anode-free Zn//LiMn$_2$O$_4$ HiB was realized [160]. Except for the interfaces between Zn metal anode and aqueous electrolytes, addictive can also function on cathode. In 2016, Wang group constructed a cathode electrolyte interphase (CEI) between LiCoO$_2$ cathode and LiTFSI aqueous electrolyte through electrochemical oxidation of tris(trimethylsilyl) borate. The LiCoO$_2$ cathode was stabilized at a high cut-off voltage corresponding to 0.7 e^- electron charge transfer, which delivered 2.5 V working voltage and 120 Wh·kg^{-1} energy density [161].

To widen the working temperature windows of ARBs, some efforts towards tailoring solvation sheath were made, which adjusted correlated ARBs to the frozen environments. Dimethyl sulfoxide (DMSO), a highly polar aprotic solvent, can form strong H bonds with water molecules and significantly change the original H-bond structure of water molecules [162]. According to the previous studies, HER of water molecules is a competitive process with the H-bond formation process in the solution [163], hence DMSO is an effective additive to suppress HER. DMSO was added into an aqueous solution of 2 M NaClO$_4$ with molar fraction of 0.3 (2M-0.3 electrolyte). The 2M-0.3 electrolyte exhibited sufficient ionic conductivity of 0.11 mS·cm^{-1} at -50 °C. The Raman and FTIR spectra proved that H bonds were stably formed between DMSO and water molecules, facilitating the operation of the electrolyte at ultra-low temperatures, while the molecular dynamics (MD) modeling in Fig. 1.8i demonstrated the consistent result [44]. In ARFB system, additives are employed as well for widening working temperature windows. 10 vol% ethanol served as additive in one near-neutral 5 M ZnI$_2$ electrolyte of Zn//I$_2$ ARFB, enabling the stable battery running at the temperature range of -20 to 50 °C. Nuclear magnetic resonance (NMR) study and DFT-based simulation along with flow test data illustrated that the addition of ethanol induced ligand formation between oxygen on the hydroxyl group and the zinc ions, which not only extended the stable electrolyte temperature window but ameliorated the interface of zinc metal anode [146]. In PB system, anions such as BF$_4^-$ and SO$_4^-$ were discovered that enhanced the adaptability of relevant aqueous electrolytes towards frozen conditions. In one work of PB, FTIR, Raman and NMR analyses synergistically demonstrated that the introduction of

BF_4^- anions efficiently break the H-bond networks of original water molecules, resulting in ultralow freezing point. Therefore, the alloxazine//MnO_2 redox couple could run regularly even at -90 °C and display a high specific discharge capacity of 85 mAh·g^{-1} [164]. In the same way, the H bonds between water molecules in electrolyte could be remarkably damaged by modulating the interaction between SO_4^{2-} and water molecules, lowering the freezing point of electrolyte. As the result, the p-chloranil//reduced graphene oxide redox couple of proton insertion mechanism, delivered extraordinary electrochemical performance even at -70 °C. [165] Basically, the electrolyte additive strategy can be a feasible route to improve stability and widen working temperature windows of ARBs. However, some additives probably fail to become a universal way for better main aqueous electrolytes. Furthermore, the electrolytes additives just function as minor revision to some cases rather than fundamentally transition, while solvents and salts affect more in aqueous electrolytes.

1.4.2 pH management & two-pH decoupling electrolyte

In aqueous electrolytes, pH value can make a considerable impact on ESWs by thermodynamically affecting HER and OER. Furthermore, the pH and H_2O in aqueous electrolytes with or without O_2 can influence the stability and working potential of electrodes in ARLiBs as [40]:

$$Li(intercalated) + \frac{1}{4}O_2 + \frac{1}{2}H_2O \leftrightarrow Li^+ + OH^-$$
(1.17)
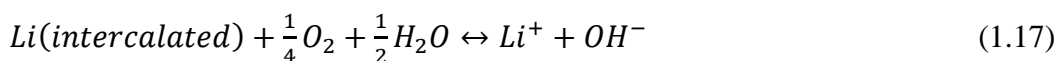
Based on the chemical potential of intercalated Li in electrode ($\mu_{LI}^{int}(x)$) and Li in Li metal (μ_{LI}^0), the working potential of electrode ($V(x)$) can be derived as [166]:

$$V(x) = 4.268 - 0.059\, pH\ (V)$$
(1.18)

, while the x here for both $\mu_{LI}^{int}(x)$ and $V(x)$ is the amount of intercalated Li in lithium-ion intercalated compounds. Through equation (1.18), the $V(x)$ in equilibrium condition is determined as 3.85 V at pH 7 and 3.50 V vs. Li/Li$^+$ at pH 13, which signifies that the reduction state of all usual anode materials in ARLiBs

would theoretically be chemically oxidized by the O_2 and H_2O rather than undergoing the electrochemical redox process. However, after eliminating O_2 in aqueous electrolytes, the reaction is [167]:

$$Li(intercalated) + H_2O \leftrightarrow Li^+ + OH^- + \frac{1}{2}H_2 \tag{1.19}$$
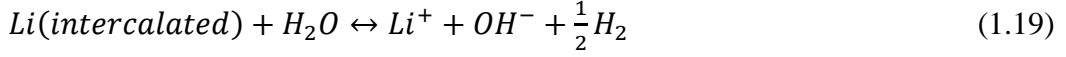
, and correlated $V(x)$ can be further determined as [40]:

$$V(x) = 3.039 - 0.059\,pH\ (V) \tag{1.20}$$

, revealing that H_2O can also chemically oxidize some reduction-state anodes in ARLiBs.

Theoretically, pH value of aqueous electrolytes can serve as a benchmarking to determine whether the electrodes are stable against corresponding aqueous electrolytes. Practically, pH adjusting can be another route to manipulate the stability of ARBs [40]. Basing on that idea, Cui group used 1 M KH_2PO_4 (pH=1) solution as electrolyte for a PiB with copper hexacyanoferrate cathode and a AC/polypyrrole hybrid anode, which had zero-capacity loss after 1000 deep-discharge cycles [36]. Xie el al. adjusted the pH value of 5 M $LiNO_3$ aqueous electrolyte by controlling concentration of LiOH, and found that when pH was ~8.5, the ARLiB with CuV_2O_5//$LiMn_2O_4$ redox couple demonstrated optimum cyclic performance [168]. pH management upon aqueous electrolytes is also a popularly used strategy to stabilize ARFBs. For example, Xie et al. utilized a 1.5 M HAc/NaAc buffer electrolyte to maintain pH value of negative electrolyte in a Zn//Fe based ARFB in the range of 2.0-6.0. The chemical reaction of Zn species with proton species was very insignificant, while the electroreduction of proton on the negative electrode was significantly suppressed at this pH range [169]. In PS-based ARFB system, PS could be stabilized in alkaline electrolyte through avoiding the formation of H_2S in the conditions of neutral and acidic. The equilibrium potential of PS was pH-dependent for pH < 11.5, while remained at -0.51 V vs. SHE when pH > 11.5. The reaction of PS in water was as follows [170]:

$$S_2^{2-} + 2H_2O + 2e^- \leftrightarrow 2HS^- + 2OH^- \qquad E^0 = -0.51\,V\,vs.\,SHE \qquad (1.21)$$
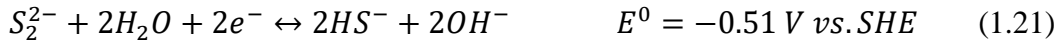
In one Zn//I$_2$ ARFB, fast overcharge self-protection ability was demonstrated with a smart pH-responsive electrolyte. Once overcharged, the electrolyte pH would be increased, induced by HER as well as the consequent irreversible formation of insulating ZnO at anode side and soluble Zn(IO$_3$)$_2$ at cathode side, which could rapidly switch off the Zn//I$_2$ ARFB with capacity degrading to 6% of the initial capacity, thereby avoiding continuous battery damage. Noticeably, that stimulus-responsive ARFB could be switched on with nearly 100% of capacity recovery by re-adjusting the electrolyte pH, delivering excellent stability [171].

Besides stability, pH management even can improve the energy density of ARBs, especially for Zn//MnO$_2$ system, in which the cathode mechanism can be classified into proton-participated conversion in mild/strong alkaline environment [151, 172], reversible Zn ion insertion/extraction in neutral/mild acidic aqueous electrolyte [79, 173], proton and Zn ion coinsetion in mild acid condition [174], and cathode dissolution/deposition mechanism under strong acid circumstance [83, 175]. Various cathode mechanisms generate different working potential of cathode, among which the one of dissolution/deposition mechanism is highest. Therefore, pH value of 1 M ZnSO$_4$+1 M MnSO$_4$ aqueous electrolyte was ajusted by H$_2$SO$_4$ for creating strong acid environment, while 0.1 M was chosen as optimized concentration of H$_2$SO$_4$ for balancing between high working voltage and desired cyclic stability. The discharge profiles of the Zn//MnO$_2$ battery with pH-adjusted electrolyte exhibited three discharge regions: D1 (2.0–1.7 V), D2 (1.7–1.4 V), and D3 (1.4–0.8 V), which represented MnO$_2$ dissolution, proton insertion, and Zn ion insertion, respectively (Fig. 1.9a). The average out-put voltage of that cell was 1.95 V, together with ~570 mAh·g^{-1} capacity (active matter of both cathode and anode), exhibiting ~409 Wh·kg^{-1} energy density [83]. On the basis of dissolution/deposition mechanism of MnO$_2$, one membrane-free Zn//MnO$_2$ ARFB was proposed for large-scale energy storage with correlated schematic illustration, and digital picture, cross-section schematic of the cell shown in Figs. 1.9b and 1.9c, respectively [89]. Actually, aqueous electrolytes pH not only affect working mechanism of MnO$_2$ cathode but Zn metal anode as well. The redox potential of Zn stripping/plating is -0.76 V vs. SHE, while that of Zn/Zn(OH)$_4^{2-}$ conversion in

alkaline environment can be extended to -1.199 V vs. SHE [86]. Thus, decoupling the working conditions of the MnO_2 cathode and Zn anode to enable both acidic MnO_2 and alkaline Zn redox reactions in a single cell, can break 2.0 V barrier of aqueous $Zn//MnO_2$ battery. One design (Fig. 1.9d) used both an alkaline (6M KOH+0.2 M ZnO+5 mM vanillin) and an acidic (3 M H_2SO_4+0.1 M $MnSO_4$) electrolyte in two chambers separated by a neutral (0.1 M K_2SO_4) electrolyte to avoid their neutralization. The neutral electrolyte chamber was encapsulated by two membranes (cation-exchange or bipolar membrane) with ion selectivity on each side. Based on this design, the decoupled $Zn//MnO_2$ battery exhibited an exceptionally high open-circuit voltage of 2.83 V and a specific energy density of 1621.7 Wh·kg^{-1} (on the active matter mass of MnO_2) [85]. The three-chamber structure was sophisticated to some extent, hence one work attempted to construct this kind of decoupled $Zn//MnO_2$ battery into a ARFB with one anolyte of 2.4 M KOH+0.1 M $Zn(CH_3COO)_2$, and one catholyte of 0.5 M H_2SO_4+1.0 M $MnSO_4$, separated by a bipolar membrane (Fig. 1.9e) [84]. Recently, one polyacrylate-based alkaline hydrogel and PAM-cellulose-based acid hydrogel were prepared and employed as two-pH decoupling electrolyte. The commonly used cellophane worked as a separator, effectively solving the problem of neutralization of electrolyte caused by diaphragm ruptures. The flexible $Zn//MnO_2$ battery displayed high working voltage of 2.7 V, high areal capacity of 2.63 mAh·cm^{-2}, and acceptable cyclic stability of 86.7% capacity retention after 400 cycles [176].

The alkaline/acid decoupling electrolytes were designed for aqueous $Zn//MnO_2$ battery, whereas alkaline/mild ones were proposed by Wu Group as well for Zn-Li HiBs. In that system, 5 M $LiNO_3$ and 5 M LiOH+1 M $Zn(OAc)_2$ aqueous solutions were selected as the cathodic and anodic electrolytes, respectively, coupling the waste Nafion NR117 membrane treated with 3 wt% H_2O_2 and 1 M H_2SO_4 as separator (Fig. 1.9f). Before that, the same membrane was employed in an aqueous $Zn//MnO_2$ battery, and an aqueous Li-ion capacitor with alkaline/mild electrolytes, showing the feasibility and validity as a separator [177, 178]. While in the Zn-Li HiB, Zn anode in alkaline solution and $LiMn_2O_4$ cathode in mild solution together equipped the whole cell with above 2.3 V working voltage. This battery system delivered a steady energy density of 208 Wh·kg^{-1} (based on the
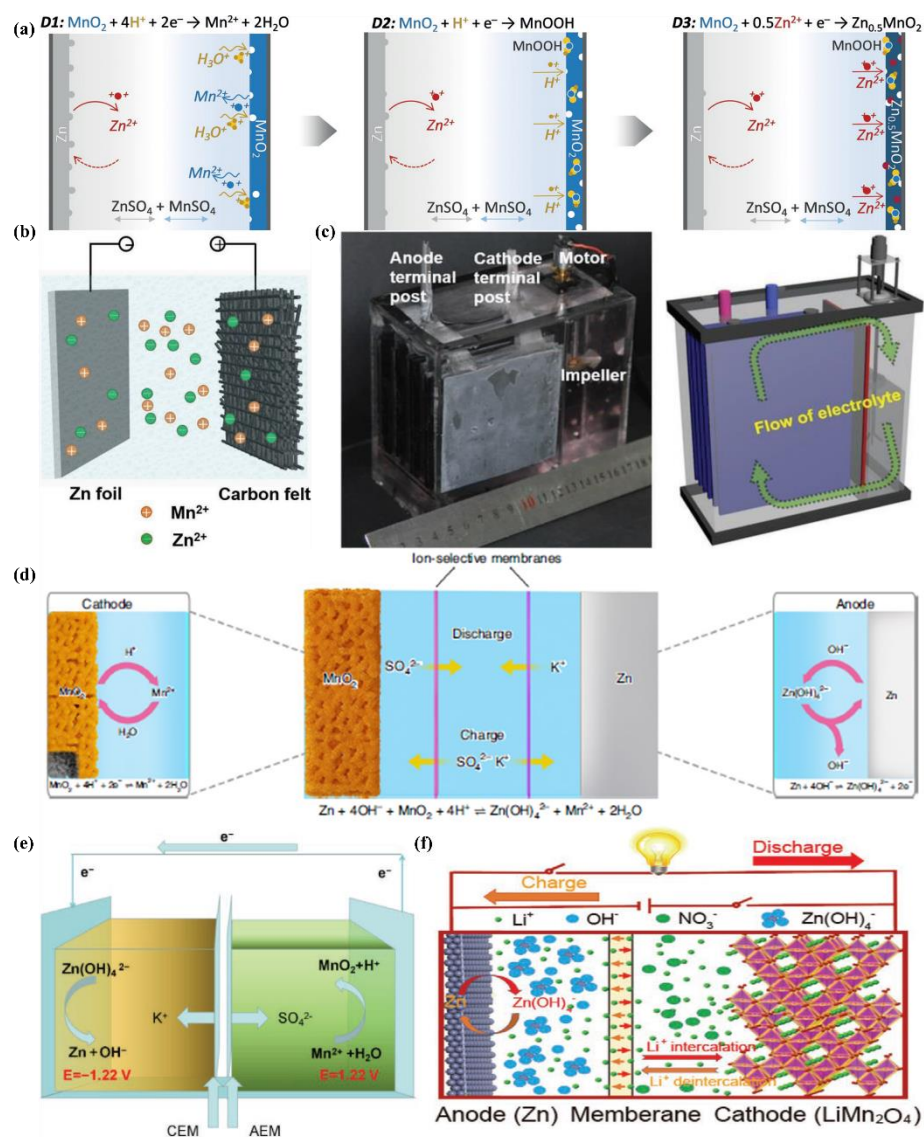
Fig. 1.9 (a) Schematic representation and charge storage mechanism of the aqueous Zn//MnO$_2$ battery in H$_2$SO$_4$ adjusted 1 M ZnSO$_4$+1 M MnSO$_4$ electrolyte [83]; (b) Configuration of a membrane-free Zn//MnO$_2$ ARFB [89]; (c) The digital picture and cross-section schematic of the cell, where the electrolyte flow propelled by the impeller is indicated by green arrow [89]; (d) Schematic diagram of the cell structure and chemical reactions at the cathode and anode during the discharge and charge based on decoupled reactions in acidic and alkaline electrolytes separated by a neutral electrolyte in the central chamber [85]; (e) The schematic illustration and mechanism of Zn//MnO$_2$ ARFB battery using an acid/alkaline decoupling electrolyte [84]; (f) Schematic representation of the structure and working mechanism of the assembled Zn-Li HiB with alkaline/mild decoupling electrolyte [179].

55

total weight of active materials) at 1.69 C with a high average output voltage up to 2.31 V, cycled for over 1000 cycles with an average CE of >98% [179]. In summary, aqueous electrolyte pH can influence redox potential and even reaction mechanism of electrodes thereby influencing the stability and working voltages of whole cells, which is an important mitigation towards disadvantages of ARBs. However, managing pH of aqueous electrolytes may fail to shift the electrode redox potential considerably according to equations (1.18) and (1.20). Whereas, for two-pH decoupling electrolytes, the complicated cell structures probably restrict their application and popularization in ARBs, twined with the unheeded HER and OER in electrode-electrolyte interfaces under high working voltage. Therefore, the ways of pH management and two-pH decoupling electrolyte need more studies and further optimization to maturely enhance stability and working voltage/energy density of ARBs.

1.4.3 Salt-concentrated electrolyte

Liquid electrolytes are the groups of solvents and salts, while salt concentration is a critical parameter, impacting ESWs, ionic conductivity, electrode/electrolyte interfaces through solvation structures, viscosity, ionic mobility and overall electrolyte structure (morphology) [54, 180]. Originating from that, salt concentration manipulation is an easy and effective way to tailor corresponding liquid electrolytes. Increasing the salt concentration in liquid electrolytes will result in enhanced interactions between cations and anions/solvents as well as a decrease in the content of free-state solvent molecules, which will demonstrate unusual physicochemical and electrochemical properties that are remarkably distinct from a conventional dilute electrolyte [180]. In 2015, one significant breakthrough was made by Wang and Xu groups, proposing one concept of "water-in-salt" electrolyte (WiSEs) which ushered salt-concentrated electrolytes and ARBs into new era [39]. The salt-concentrated electrolytes in ARBs can be categorized into WiSEs, hydrate-melt electrolytes (HMEs) and regular super-concentration electrolytes (RSCEs), which engender wide ESWs then high energy density. The definition of WiSEs is that salt outnumbers the solvent in binary system by both weight and volume, leading to an anion-containing Li^+ solvation sheath (Fig. 1.10a) and the formation of a dense interphase on the anode surface

(mainly arising from anion reduction, Fig. 1.10b). Combined with the substantially reduced electrochemical activity of water at a WiSE of 21 m LiTFSI, an ESW of ~3.0 V was provided, which equipped one full ARLiB (Mo_6S_8//$LiMn_2O_4$) with 2.3 V working voltage and 1000 charge/discharge cycles [39]. Since that, WiSEs demonstrated all-round versatility in raising energy density, enhancing stability and widening working temperature windows of ARBs. In terms of energy density enhancement, Wang and Xu groups applied the WiSE to one ARLiB with halogen conversion–intercalation chemistry in graphite (Fig. 1.10c), delivering capacity of 243 mAh·g^{-1} (for the total weight of the electrode) at an average potential of 4.2 V vs. Li/Li^+. Pairing up with graphite anode with artificial SEI, a 4-V class ARLiB was created with the energy density of 460 Wh·kg^{-1} [66]. Furthermore, Wang and Xu groups employed the WiSE in ZAB chemistry with porous carbon air cathode, demonstrating an energy density of 1000 Wh·kg^{-1} (based on the mass of cathode) within 200 cycles [131]. Meanwhile, in the LAB system, WiSEs provided the necessary functionalities to support aprotic Li//O_2 operations via reversible Li_2O_2 formation and decomposition. The lack of organic solvent molecules was a highlight there, eliminating the known reaction pathways towards by-product formation in organic electrolyte systems [181]. In another theoretically high energy density system of LSB, WiSE played a role as well, coupling sulfur anode with solid–liquid two-phase, and $LiMn_2O_4$/$LiCoO_2$ cathode, delivering working voltage of 1.8/2.24 V (Fig. 1.10d). The capacity of sulfur anode was tested as 1327 mAh·g^{-1}, while the energy density of full cell was determined as 200 Wh·kg^{-1} (total electrode mass) for >1000 cycles at ~100% CE [182].

The stability brought by WiSEs is also significant among ARBs, not only suppressing HER/OER of water but also the electrodes dissolution in aqueous electrolytes. In the above-mentioned LSB system, the excellent cyclic stability was induced by the solid–liquid two-phase reaction pathway, where the liquid polysulfide phase in the sulfide electrode was thermodynamically phase-separated from the WiSE [182]. The phenomenon of negligible polysulfide dissolution in WiSEs, can also be discovered in SiB chemistry. Yue et al. investigated concentration-controlled cathode dissolution through a $Na_3V_2(PO_4)_3$ cathode, whose time-, cycle-, and state-of-charge-dependent dissolution was evaluated by multiple electrochemical and chemical methods. In that study, a novel mechanism

of interface concentrated confinement was proved with WiSEs, which enhanced the cyclic stability of $NaTi_2(PO_4)_3$//$Na_3V_2(PO_4)_3$ full cell. The high viscosity, low vanadium ion diffusion, low polarity of solvated water and and scarce solute-water dissolving surfaces in WiSEs (9 m NaOTf+22 m tetraethylammonium triflate, TEAOTf), remarkably decreased the thermodynamic-controlled solubility, the dissolving kinetics, and physical space local mass interfacial confinement (Fig. 1.10e) [43]. The WiSEs were discovered that could reduce O_2 solubility in water, and the kinetics of oxygen reduction reaction (ORR) through slowing down O_2 diffusion [183]. Hence, WiSE-based cells were able to work with open configuration which obtained superior ability to dissipate heat and pressure, and eliminated the risk of explosion [183]. Except stability, WiSEs can also expand the working temperature widows of ARBs. One WiSE of 22 m KCF_3SO_3 (KFSI) was prepared for one PiB, matched with Fe-substituted Mn-rich PBA $K_{1.85}Fe_{0.33}Mn_{0.67}[Fe(CN)_6]_{0.98} \cdot 0.77H_2O$ (KFeMnHCF-3565) cathode, and 3,4,9,10-perylenetetracarboxylic diimide (PTCDI) anode. Beside the impressive performance of 80 Wh·kg^{-1} and superior capacity retention of 85% at 20 C after more than 10000 charge-discharge cycles at RT, that full PiB was assembled in a pouch cell, demonstrating superior performance at a wide temperature range of -20 to 60 °C [184]. In the study reported by Reber et al., a key factor limiting WiSE application in low temperatures was recognized as salt crystallization tendency even near RT. Thus, 10 m sodium (fluorosulfonyl)(trifluoromethylsulfonyl)imide (NaFTFSI) with asymmetric anions was introduced into 25 m NaFSI with symmetric anions. After that, a SiB based on the asymmetric anion optimized WiSE in combination with a $NaTi_2(PO_4)_3$ anode and a $Na_3(VOPO_4)_2F$ cathode, demonstrated excellent capacity retention and high energy density down to temperatures of -10 °C [185]. In the WiSE, the expensive organic salts were widely used, which increased the cost of the whole cells. Some research attempted to use cost-effective salts as substitutions, and obtained some achievements, especially the ones based on acetates and chlorates [80, 134, 186, 187]. Ji group applied potassium acetate (KOAc) into WiSE, which was capable of cycling relevant PiBs to 11000 cycles under a current density of 1 A·g^{-1} with a ESW of ~3.2 V [188]. Through blending with LiOAc and Zn(OAc)$_2$, this acetate-based WiSE could be used in ARLiBs and Zn//MnO_2 systems with desired performance and potentials on large-scale practice [80, 187]. Meanwhile, Ji group reported $ZnCl_2$-based WiSE

(30 m ZnCl$_2$), enabling dendrite-free Zn metal anode with high CE, and one novel DiB with high reversibility [134, 186].
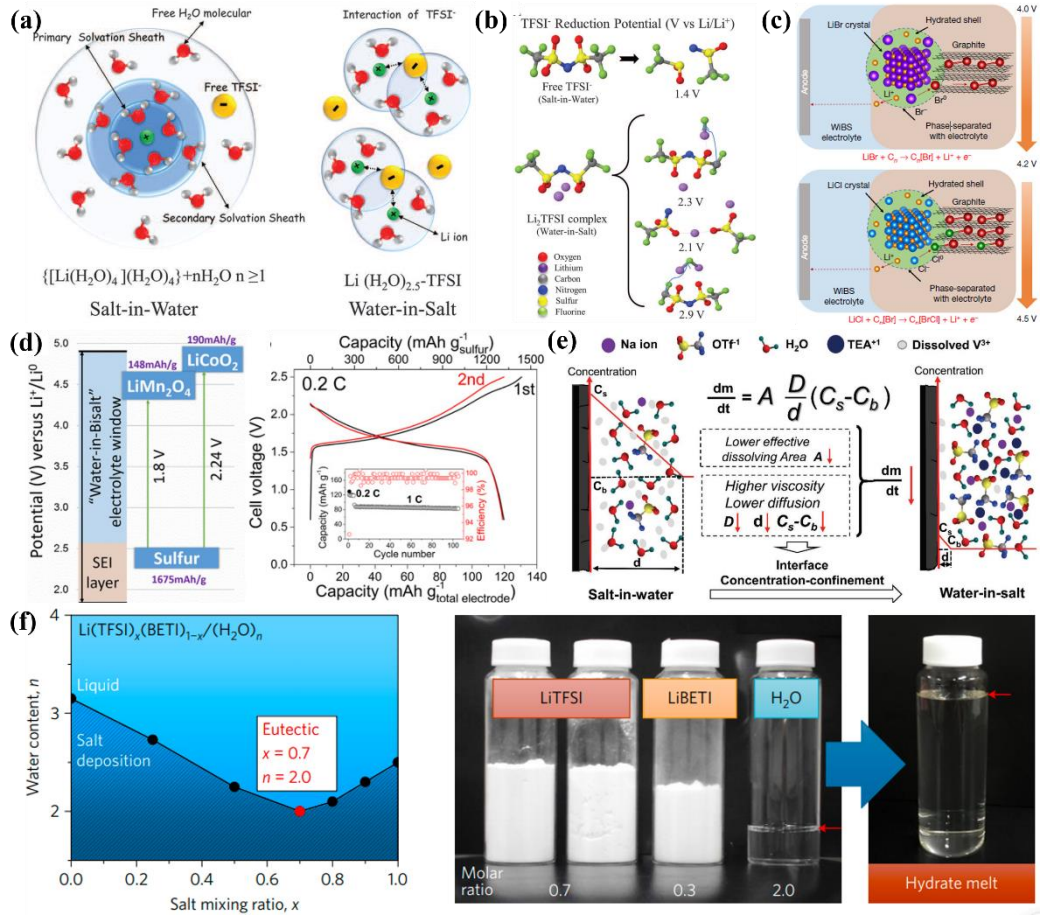
Fig. 1.10 (a) Illustration of the evolution of the Li-ion primary solvation sheath in diluted and WiSE [39]; (b) Predicted reduction potentials of Free and complex TFSI$^-$ from G4MP2 quantum chemistry calculations [39]; (c) Schematic drawing of the conversion-intercalation mechanism occurring in (LiBr)$_{0.5}$(LiCl)$_{0.5}$-graphite during its oxidation in the WiSE. The two-stage reactions involved the oxidation of Br$^-$ (~4.0 V) and Cl$^-$ (~4.2 V) and their subsequent intercalation into graphitic structure [66]; (d) Illustration of S-LiMn$_2$O$_4$ and S-HV-LiCoO$_2$ full cell in WiSE with expanded ESW. Voltage profiles of S-HV-LiCoO$_2$ full cell in WiSE at rate of 0.2C. (Inset) Capacity stability and CE during cycling [182]; (e) Schematic illustration of vanadium dissolution according the Noyes-Whitney equation [43]; (f) Liquidus line of Li(TFSI)$_x$(BETI)$_{1-x}$ salt–water mixtures and stoichiometric amounts of LiTFSI, LiBETI and water used to prepare a Li(TFSI)$_{0.7}$(BETI)$_{0.3}$·2H$_2$O hydrate melt. The red arrows indicate the liquid levels [189].

Among the salt-concentrated system, another significant electrolyte was reported as HMEs, which utilized the eutectic system. LiTFSI and $LiN(SO_2C_2F_5)_2$ (LiBETI) salts were firstly selected for HMEs, because these anions were weakly Lewis basic and only interacted with Li^+ weakly, thereby promoting the solvation of the Li^+ by water molecules rather than the abundant formation of ion pairs. Furthermore, the anions exerted a 'plasticizing' effect, avoiding the crystallization of salts and hydrates. Fig. 1.10f demonstrates the miscibility limits of blended LiTFSI-LiBETI salts in water at RT, while a eutectic composition of $Li(TFSI)_{0.7}(BETI)_{0.3}$ with highest miscibility was determined, forming a stable, transparent liquid with an extremely low water content ($H_2O:Li^+ = 2.0$ in molar ratio), equaling to a water molar concentration of 10.1 $mol·L^{-1}$ (Fig. 1.10f). Because of this low water concentration, the water molecules could be isolated from each other by the bulky anions, thus suppressed water activity by decreasing the opportunity for the formation of clusters of free water molecules. That HME equipped $Li_4Ti_5O_{12}//LiNi_{0.5}Mn_{1.5}O_4$ redox couples with upper limitation of working voltage of 3.1 V and energy density of >130 $Wh·kg^{-1}$ within 100 cycles [189]. Besides, the concept of HME was applied into SiB and PiB as well, employing $Na(PTFSI)_{0.65}(TFSI)_{0.14}(OTf)_{0.21}·3H_2O$ and $K(PTFSI)_{0.12}(TFSI)_{0.08}(OTf)_{0.8}·2H_2O$ hydrate melts with ternary anions including $TFSI^-$, OTf^- and especially asymmetric $N(SO_2CF_3)(SO_2C_2F_5)^-$ ($PTFSI^-$) anion, which significantly expanded the ESWs to 2.7 and 2.5 V respectively. Na(PTFSI) and K(PTFSI) with asymmetric anions normally owned high solubility attributing to their high vibrational mobility and flexibility offered by asymmetric structure, realizing Na and K hydrate melts at super-high concentration [190]. The HMEs were also appropriate in LABs, coupling LiSICON glass ceramic-protected Li metal anode and Ketjen Black (KB) cathode, which shown a low charge potential of ~3.16 V, a high discharge capacity of 38 $mAh·cm^{-2}$, and a stable cyclic ability of 50 cycles with capacity limitation of 1000 $mAh·g^{-1}$ under current density of 500 $mA·g^{-1}$ [191]. After substituting into $ZnCl_2·2.33 H_2O$, the HME could work with Zn metal anode and Pt/C cathode as a ZAB, delivering a reversible capacity of 1000 $mAh·g^{-1}$ (based on catalyst) over 100 cycles [192]. In WiSE system, one similar concept to HME was proposed as "water-in-bisalt" electrolyte (WiBSE), which could dissolve another unhydrated salt of similar chemical properties and form binary salt systems in the molten state with higher cation/water ratios. In the

typical WiBSE of 21 m LiTFSI+7 m LiOTf, one more compact SEI than that in WiSE was created, allowing a 2.5 V TiO_2//$LiMn_2O_4$ full LiB with an average discharge voltage of 2.1 V and an energy density of 100 $Wh \cdot kg^{-1}$ (total electrode mass) [67]. Additionally, the acetate was able to replace the organic FSI^- anion based salts in WiBSEs, while the cation-size effect on ESWs in acetate system was further investigated [193].

Normally, the cation/water ratio of WiSEs and HMEs can go beyond 2.0, for those aqueous electrolytes with high salt concentration but fail to approach that ratio or meet the definitions of WiSEs/HMEs, can be categorized as RSCEs. Pan et al. investigated thermodynamic and kinetic contributions to ESW of $LiNO_3$-based RSCE ($LiNO_3$:H_2O=1:2.5) through MD simulation and spectral analysis. One local structure of intimate Li^+-water interaction was discovered at super-concentration, inducing $(Li^+(H_2O)_2)_n$ polymer-like chains rather than the ubiquitous hydrogen bonding between water molecules, thereby extending the ESW to 2.55 V [194]. Basing on RSCEs, one universal strategy was proposed to improve specific energy, reversibility and safety of MViBs, which took $Ca(NO_3)_2$-based electrolytes for example, driving the Ca-ion/sulfur-metal oxide full cell stably [195]. 3 M $Zn(FSI)_2$ aqueous electrolyte was employed by Chen group for Zn//$ZnMn_2O_4$ battery, which exhibited excellent stability by suppressing Mn dissolution (capacity retention of 94% over 500 cycles under a high current density of 500 $mA \cdot g^{-1}$) [173]. After that, the same group optimized concentration of $ZnCl_2$ to 7.5 m, which achieved ultralow solid-liquid transition temperature via breakage of H bonds, thence an ultra-wide temperature window from -90 to 60 °C [196]. Xue et al. introduced super-concentrated sugars into 2 M $NaNO_3$ to reduce the free water molecules and destroy the tetrahedral structure, thus expanding the ESW to 2.812 V by breaking the H bonds. As results, LiBs, SiBs, PiBs and supercapacitors with excellent electrochemical performances were derived from the sugar-based electrolytes [197]. In a word, salt-concentrated electrolytes can be a universal strategy to improve energy density, cyclic stability and widen working temperature windows of ARBs, which have been practiced intensively and extensively as summarized in Table 1.1 [39, 43, 66, 67, 80, 131, 134, 173, 181-203]. However, cost probably impedes their large-scale applications because of the large amount of salt in that system, although desired performance was obtained. The unit prices

of some representative salts utilized in salt-concentrated electrolytes are compared in Fig. 1.11, in which corresponding information was collected from the Sigma-Aldrich in USA, Sinoreagent in China and Alfa Aesar in UK. Concluded from Fig. 1.11, some organic salts are exceptionally expensive but only a little better in electrolyte performance than the cost-effective salts ranging from nitrites, perchlorates, chlorates to acetates, hence it is of importance for us to strike a balance between the electrolyte property and cost in real applications.

Table 1.1 A summary of recently representative works upon salt-concentrated electrolytes for ARBs.

Electrolyte	Electrode	ESW	Energy density	Cyclic stability	Working temperature	Reference
$LiNO_3 \cdot 2.5H_2O$	$AC//LiMn_2O_4/Li\ Ni_{1/3}Mn_{1/3}Co_{1/3}O_2$	2.55 V	n/a	n/a	RT	[194]
8.37 m $Ca(NO3)_2$-PVA	S｜C//$Ca_{0.4}MnO_2$	2.6 V	110 $Wh \cdot kg^{-1}$ (total electrode)	150 cycles (0.2 C)	RT	[195]
2 M $NaNO_3$/66.7 wt% sucrose	AC//PBA	2.8 V	n/a	2000 cycles (2 $A \cdot g^{-1}$)	-50 to 80 ℃	[197]
7.5 m $ZnCl_2$	Zn//Polyaniline	n/a	n/a	2000 cycles (0.2 $A \cdot g^{-1}$)	-90 to 60 ℃	[196]
$ZnCl_2 \cdot 0.03KBr \cdot 2H_2O$	Zn//graphite	n/a	~440 $Wh \cdot kg^{-1}$ (cathode)	100 cycles (0.25 $A \cdot g^{-1}$)	RT	[198]

30 m $ZnCl_2$	Zn//Zn symmetrical cell	2.3 V	n/a	600 hours (~1800 cycles, 0.2 $mA·cm^{-2}$)	RT	[186]
30 m $ZnCl_2$	Fc-C//PBA	2.3 V	n/a	2000 cycles (5 C)	RT	[134]
$ZnCl_2·2.33\ H_2O$	Zn//Pt/C	n/a	n/a	100 cycles (0.1 $A·g^{-1}$)	30 ºC	[192]
30 m KOAc	$KTi_2(PO_4)_3$//AC	3.2 V	n/a	11000 cycles (1 $A·g^{-1}$)	RT	[188]
8 m LiOAc+32 m KOAc	TiO_2//$LiMn_2O_4$	~3.0 V	n/a	50 cycles (0.5 C)	RT	[187]
7 m LiOAc+45 m CsOAc	VO_2//$LiNi_{0.5}Mn_{1.5}O_4$	~3.0 V	114.8 $Wh·kg^{-1}$ (total electrode)	1200 cycles (4 C)	RT	[193]

1 m Zn(OAc)2+31 m KOAc	Zn//MnO$_2$	3.1 V	232.7 Wh·kg^{-1} (activated electrode and electrolyte)	600 cycles (C/3)	RT	[80]
4 M KOH+16 M KOAc	Al alloy//Mn$_x$O$_y$@Ag	2.2 V	436.1 Wh·kg^{-1} (activated electrode and electrolyte)	2300 min (~30 cycles, 25 mA·cm^{-2})	RT	[199]
17 m NaClO$_4$	NaTi$_2$(PO$_4$)$_3$//Na$_4$Fe$_3$(PO$_4$)$_2$(P$_2$O$_7$)	2.7 V	36 Wh·kg^{-1} (total electrode)	>200 cycles (1 C)	RT	[202]
21 m LiTFSI	Mo$_6$S$_8$//LiMn$_2$O$_4$	~3.0 V	84 Wh·kg^{-1} (total electrode)	1000 cycles (4.5 C)	RT	[39]
21 m LiTFSI	LICGC｜Li//Ru/TiSi$_2$	~3.0 V	n/a	300 cycles (0.05 A·g^{-1})	RT	[181]

9.26 m NaOTf	$NaTi_2(PO_4)_3$//$Na_{0.66}[Mn_{0.66}Ti_{0.34}]O_2$	2.5 V	31 Wh·kg^{-1} (total electrode)	>1200 cycles (1 C)	RT	[200]
22 m KFSI	PTCDI//KFeMnHCF-3565	~3.0 V	80 Wh·kg^{-1} (total electrode)	10000 cycles (100 C)	-20 to 60 ℃	[184]
3 M ZnFSI	Zn//$ZnMn_2O_4$	n/a	~202 Wh·kg^{-1} (total electrode)	500 cycles (0.5 A·g^{-1})	RT	[173]
21 m LiTFSI+7 m LiOTf	C/TiO_2//$LiMn_2O_4$	~3.1 V	100 Wh·kg^{-1} (total electrode)	100 cycles (0.5 C)	RT	[67]
21 m LiTFSI+7 m LiOTf-PEO/PVA	passivated graphite//$(LiBr)_{0.5}(LiCl)_{0.5}$-graphite	~3.1 V	460 Wh·kg^{-1} (total electrode)	~250 cycles (0.08 A·g^{-1})	RT	[66]

21 m LiTFSI+7 m LiOTf-PVA	S-KB//LiMn$_2$O$_4$/LiCoO$_2$	~3.1 V	200 Wh·kg^{-1} (total electrode)	>1000 cycles (1 C)	RT	[182]
21 m LiTFSI+7 m LiOTf (open battery configuration)	Al$_2$O$_3$@LiTi$_2$(PO$_4$)$_3$//LiMn$_2$O$_4$	~3.1 V	170 Wh·kg^{-1} (total electrode)	1000 cycles (5 C)	RT	[183]
42 m LiTFSI + 21 m Me$_3$EtN·TFSI	Li$_4$Ti$_5$O$_{12}$//LiMn$_2$O$_4$	3.25 V	145 Wh·kg^{-1} (total electrode)	150 cycles (0.2 C)	RT	[201]
1 m Zn(TFSI)$_2$+20 m LiTFSI	Zn//LiMn$_2$O$_4$	n/a	180 Wh·kg^{-1} (total electrode)	4000 cycles (4 C)	RT	[131]
1 m Zn(TFSI)$_2$+20 m LiTFSI	Zn//Super P	n/a	300 Wh·kg^{-1} (total electrode)	200 cycles (0.05 A·g^{-1})	RT	[131]
9 m NaOTf+22 m TEAOTf	NaTi$_2$(PO$_4$)$_3$//Na$_3$V$_2$(PO$_4$)$_3$	n/a	n/a	100 cycles (1 C)	RT	[43]

25 m NaFSI+10 m NaFTFSI	$NaTi_2(PO_4)_3$//$Na_3(VOPO_4)_2F$	2.7 V	64 Wh·kg^{-1} (total electrode)	500 cycles (C/5, 1 C)	-10, 10, 30 ℃	[185]
Li(TFSI)$_{0.7}$(BETI)$_{0.3}$·2H$_2$O	$Li_4Ti_5O_{12}$//$LiNi_{0.5}Mn_{1.5}O_4$	3.8 V	>130 Wh·kg^{-1} (total electrode)	100 cycles (6.8 C)	RT	[189]
Na(PTFSI)$_{0.65}$(TFSI)$_{0.14}$(OTf)$_{0.21}$·3H$_2$O	$NaTi_2(PO_4)_3$//$Na_3(VOPO_4)_2F$	2.7 V	77.9 Wh·kg^{-1} (total electrode)	500 cycles (5 C)	RT	[190]
Li(TFSI)$_{0.7}$(BETI)$_{0.3}$·2H$_2$O	LiSICON｜Li//KB	3.8 V	950 Wh·kg^{-1} (activated electrode and electrolyte)	50 cycles (0.5 A·g^{-1})	RT	[191]
Zn(ClO$_4$)$_2$·6H$_2$O- succinonitrile	Zn//Poly(2,3-dithiin-1,4-benzoquinone)	2.55 V	n/a	3500 cycles (0.3 C)	-20, -10 ℃, RT	[203]
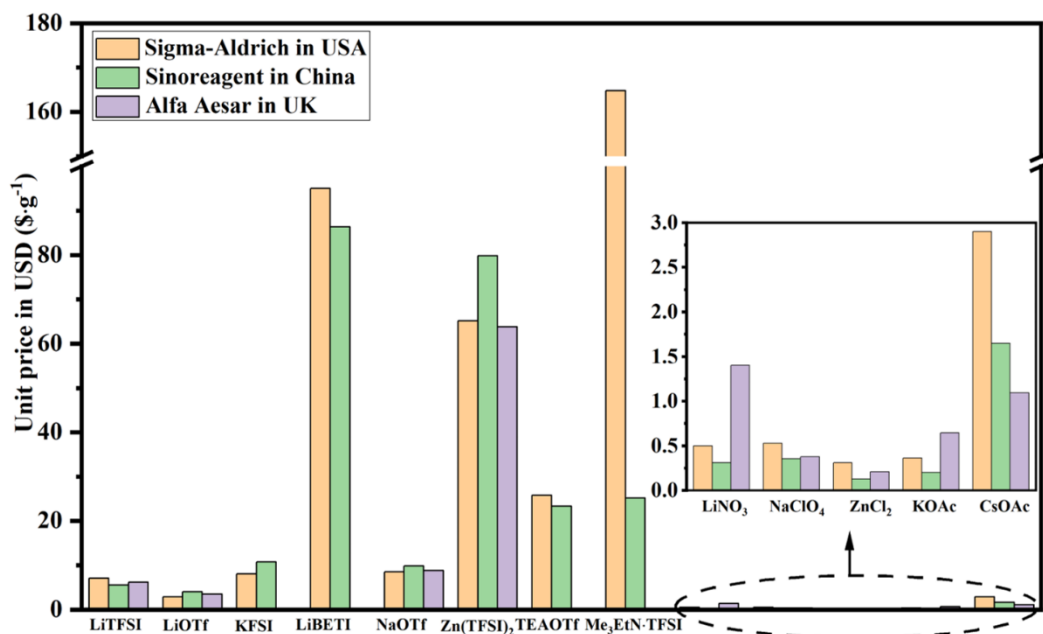
Fig. 1.11 The comparison upon unit price of various representative salts utilized in salt-concentrated electrolytes.

1.4.4 Gelled electrolyte

The gelled aqueous electrolyte can be deemed as hydrogel electrolyte, consisting of a crosslinked network of polymer chains with interstitial spaces filled with solvent water, which endows the aqueous electrolyte with quasi-solid state and flexible property. Hydrogel electrolyte can be fabricated and applied into flexible and stretchable ARBs not only because of the physical property but also highly available and tunable polymer chemistries. The hydrogel-based ARBs with self-healing, shape memory and stretchability enable wearable devices for health care, implantable device, soft electronics, and strain sensors [95, 204]. The frequently used polymer host materials in hydrogel electrolyte are polyvinyl alcohol (PVA), PAA, PAM, gelatin, alginate, agarose, chitosan, poly(ethylene oxide)-*block*-poly(propylene oxide)-*block*-poly(ethylene oxide) (PEO-PPO-PEO) and poly(*N*-isopro-pylacrylamide-*co*-acrylamide) (PNIPAM/AM), which possess various features, functional groups, crosslinking/gelation methods (Fig. 1.12a), and cooperate with aqueous solutions of different cations, anions and pH value [204]. The original function of hydrogel electrolytes based on these polymers was donating ARBs with quasi-solid properties [205], while additional functions were discovered as well to mitigate the challenges of ARBs. In a 5 M LiCl-PVA

hydrogel electrolyte for supercapacitor, PVA could prevent the chemical dissolution of V_3O_7 electrode by minimizing the water content, providing a neutral pH medium, and serving as an elastic coating [206]. In development, PVA was found that could further extend the ESW of $LiClO_4$ aqueous solution, hence bring higher energy density and cyclic stability to Zn-Li HiBs [207]. Through integrating PVA with currently popular WiSE (21 m LiTFSI), one flexible and wearable symmetrical ARLiB was developed with energy densities of 141 $Wh \cdot kg^{-1}$ during 4000 cycles, using a single $LiVPO_4F$ as both anode and cathode. In that cell, high energy and power density, and flexibility were realized mutually in the attendance of PVA [208]. Beside PVA, carboxymethyl cellulose (CMC) was added into one acetate-based WiSE (20 m KOAc) in a small amount (2 wt.%) for gelling, which maintained similar ESW of 32 m KOAc WiSE with less salt dissolved. The existence of CMC reduced the Mn and Fe dissolution in KMHCF cathode, then enhanced the cyclic stability of this PiB to 400 cycles [193]. In 2020, one significant work was reported by Lu group with LiTFSI salt and poly(ethylene glycol) (PEG) polymer, basing on a common phenomenon of molecular crowding in living cells, which changed the hydrogen-bonding structure in water molecules thence reduced the activity of water solvent. That molecular crowding electrolyte was optimized to 2 m LiTFSI-94% PEG-6% H_2O, delivering a ESW of 3.2 V, especially excellent stability against HER (Fig. 1.12b), which endowed $Li_4Ti_5O_{12}$//$LiMn_2O_4$ full cell with energy density ranging from 75 to 110 $Wh \cdot kg^{-1}$ over 300 charge-discharge cycles (Fig. 1.12c) [209]. Another similar work was reported in 2021 as "water-in-gel" electrolyte, which was consisted by water, NaCl, $ZnCl_2$ and sodium alginate (SA), expanding ESW to 2.72 V. A "pass-way" for cation transportation was built within that electrolyte through coordinate bonds between the carboxylate groups of SA and Na/Zn ions. And due to random coil conformation of alginate chains affected by dissolved ions, the 3D-fibrilar, porous polymer network will assure the uniform distribution and efficient transportation of Na/Zn ions in aqueous environment. One Zn-Na hybrid battery on basis of that electrolyte was proposed, achieving a high extraction voltage of Na^+ (2.1 V vs. Zn/Zn^{2+}) and a high capacity retention of 96.8 % after 450 cycles [210].

Except for wide ESWs, the quasi-solid state and poor fluidity of hydrogel electrolytes contribute to high energy density of ARBs as well, based on

decoupling structure. As noted above, one PAA-based alkaline hydrogel and PAM-cellulose-based acid hydrogel were prepared for two-pH decoupling electrolyte, enabling a high working voltage of $Zn//MnO_2$ battery (2.7 V) thence high energy density. Compared with liquid decoupling electrolytes, hydrogel-based ones simplify three-chamber into two-chamber structure thus improve relevant processibility [176]. One gelled decoupling electrolyte with gelatin/$ZnSO_4$ analyte, gelatin/$CuSO_4$ catholyte, and anion-exchange separator was proposed, in which decoupling charge carriers of anolyte and catholyte simultaneously endowed the Zn anode and S cathode with optimal redox chemistry as follows [211]:

Cathode: $S + 2Cu^{2+} + 4e^- \leftrightarrow Cu_2S$ (1.22)

Anode: $Zn \leftrightarrow Zn^{2+} + 2e^-$ (1.23)

Deriving from that, the theoretical volumetric energy density of this flexible HiB was regarded as 3868 Wh·L^{-1}, while that battery delivered a stable output voltage (releasing 92% of its full capacity within a small voltage drop of 0.15 V) and an ultrahigh reversible capacity of 2063 mAh·g^{-1} (on mass of S) under current density of 100 mA·g^{-1} [211]. Hydrogel electrolyte also possesses anti-freezing function, which guarantees the stable operation of ARBs at low temperatures. A new type of zwitterionic polymer hydrogel electrolyte was fabricated, achieve high conductivity without sacrificing flexibility of hydrogels at subzero temperatures. The anionic and cationic counterions on zwitterionic chains facilitate the dissociation of LiCl salt, while salt concentration significantly affected the conductivity and anti-freezing performance of the electrolytes. A direct hopping migration mechanism of hydrated Li^+ through the channel of zwitterion groups was further proposed (Fig. 1.12d). The ultrahigh ionic conductivity of 12.6 mS·cm^{-1} at -40 °C, owning to the synergistic effects including the electrostatic interactions between zwitterionic groups and Li^+ as well as the formation of $Li^+(H_2O)n$ hydration structure [212]. Furthermore, one borax-crosslinked PVA/glycerol hydrogel electrolyte with freezing point of below -60 °C was developed, in which glycerol could strongly interact with PVA chains thereby effectively prohibiting the formation of ice crystals within the whole gel network. This kind of hydrogel

electrolyte with 10.1 mS·cm^{-1} at -35 °C, drove one Zn//MnO$_2$ battery to charge/discharge over 2000 cycles with around 90 % capacity retention at that temperature [213]. In fact, hydrogel electrolyte is a solvent strategy to solidify/inactivate water for wider ESWs, higher stability, and wider working temperature range, which is effective and economic for better ARBs. In next part, another method about solvent manipulation, named as hybrid solvent will be reviewed as well.
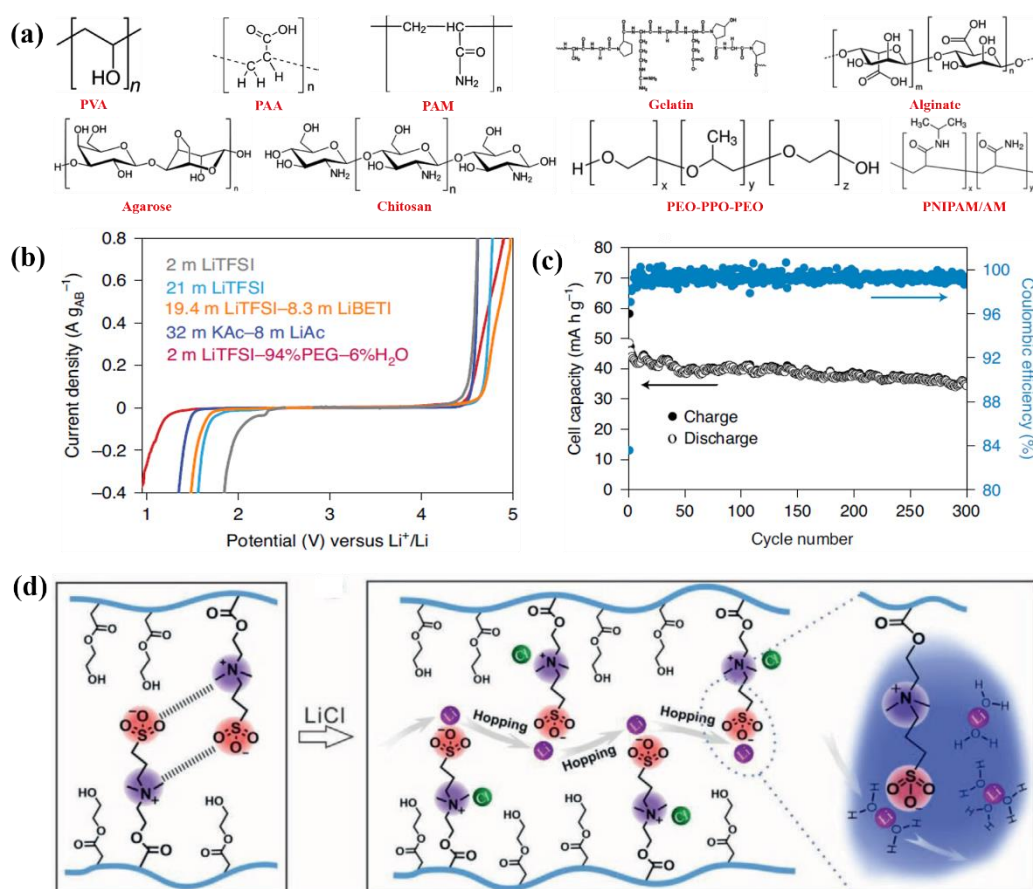
Fig. 1.12 (a) Molecular structure of frequently used polymer host materials for hydrogel electrolytes [204]; (b) Comparison of ESWs between molecular crowding electrolyte and other salt-concentrated electrolytes [209]; (c) Cyclic stability and CE of Li$_4$Ti$_5$O$_{12}$//LiMn$_2$O$_4$ cell based on molecular crowding electrolyte under 1 C rate [209]; (d) Schematic diagram of electrostatic interaction between anionic and cationic groups without salts, and proposed Li$^+$ migration mechanism in zwitterionic polymer hydrogel electrolyte [212].

1.4.5 Hybrid-solvent electrolyte

The SEIs formed in WiSEs were found to be predominantly inorganic metal fluorides originating from the reduction of salt anions of TFSI⁻ or OTf⁻. However, the formation of this anion-originated SEI faces a severe ''cathodic challenge'' as result of the repulsion of anions by negatively polarized anode surfaces, making the expansion of cathodic limits extremely difficult [214]. Therefore, a new class of electrolytes by hybridizing aqueous and non-aqueous solvents was reported, which inherited the intrinsic merits of each system, and successfully resolved the conflicts among performance, cost, interfacial chemistry, ambient controlling, and environmental concerns. Dimethyl carbonate (DMC) was blended with LiTFSI WiSE, introducing a secondary ingredient (alkylcarbonate) to the protective interphase on the anode in addition to the LiF from anion reduction. This hybrid interphase, consisting of LiF and alkylcarbonate, stabilized the electrolyte down to 1.0 V vs. Li/Li⁺, allowing a 3.2 V Li-ion cell chemistry of $Li_4Ti_5O_{12}$ anode and $LiNi_{0.5}Mn_{1.5}O_4$ cathode [214]. After that, the LiTFSI-DMC/water hybrid-solvent electrolyte was applied for DiBs, in which Li⁺ intercalation/deintercalation occurred on $Li_4Ti_5O_{12}$ side, while intercalation/deintercalation occurred on graphite side [215]. Furthermore, DMC was introduced into LiTFSI+LiOTf WiBSE with both broad ESW and excellent safety, assembled with KS6 graphite cathode and Nb_2O_5 anode as a DiB, which exhibited good comprehensive performance including capacity, cycling stability, rate performance, and medium discharge voltage [216]. Except Li⁺-based chemistries, the hybrid solvent concept suits SiBs as well. 7 m NaOTf aqueous solution was mixed with 8 m NaOTf propylene carbonate (PC) solution. Through Raman spectra characterization, the intensified cation-anion association in that electrolyte was observed, which benefited the formation of an interphase at electrode/electrolyte interface thereby stabilizing water molecules against the reducing surfaces of the electrodes. The Na⁺-based solvent-hybrid electrolyte offered a ESW up to 2.8 V and enabled the $NaTi_2(PO_4)_3$//$Na_3V_2(PO_4)_3$ redox pair [217]. The above-mentioned DMC and PC are regular organic solvents for conventional LiBs, while some ionic liquids were mixed with aqueous solutions in some studies as well [218, 219]. Ionic liquids exhibit unique properties such as flame-retardant ability, non-volatility, and high thermal stability, while its high viscosity may hinder further applications. Therefore, a ''water in salt/ionic liquid'' electrolyte composed of a salt of LiTFSI and a molten salt of 1-ethyl-3-methylimidazolium bis(trifluoromethanesulfonyl)

73

imide (EMIM-TFSI), was mixed with extremely small amount of water (water/LiTFSI/EMIM-TFSI molar ratio is 1:1:2). In such electrolyte, ESW was considerably widened without sacrifice of ionic conductivity, allowing the accessibility of full capacity of commercial Nb_2O_5 material at a low potential window (-1.6 V vs. Ag/AgCl) [219]. Meanwhile, deep eutectic solvents (DESs), generally obtained by simply mixing Lewis acids and bases in the eutectic molar ratio, have emerged as attractive alternatives to ionic liquids due to the high degree of design freedom. 6 wt.% water was added into one urea-based DES, endowed Zn anode with unusual reversibility and durability. The intensified water-DES interactions significantly suppressed the water reactivity while the merits of aqueous system on the ionic conductivity and viscosity were conserved [218].

Some organic solvents possessing low freezing points can be employed to enhance the low-temperature performance of ARBs by hybridizing aqueous electrolytes. For instance, the freezing point of acetonitrile (AN) is -48 °C, together with the properties of high dielectric constant (35.9), high oxidation stability (> 5 V vs Li^+/Li), and high miscibility with water, enabled one ARLiB of $Li_4Ti_5O_{12}$//$LiMn_2O_4$ redox pair with high capacity at both RT and 0 °C [220]. In addition, ethylene glycol (EG) has been widely used as antifreeze in engine coolant owing to its high boiling point and relatively low freezing point (-12 °C). When mixing with water, the freezing point can be further reduced (even to -40 °C), while the solvation interaction of Zn^{2+} with H_2O is partly reduced by the introduction of EG, contributing to fewer side reactions such as HER on the Zn anode side. In one reported work by Li group, the portion of EG in the mixture was optimized to 40% in volume, considering both ionic conductivity and ESW, which drove the Zn//PANI-V_2O_5 battery to more than 250 cycles under current density of 0.2 Ag^{-1} at -20 °C [221]. Qiao group proposed one route by using low-cost antisolvents, which for example added methanol into $ZnSO_4$ aqueous electrolyte to weaken Zn^{2+} solvation sheath and minimize water activity through strengthening the interaction between free and coordinated water molecules with antisolvents. Zn reversibility was significantly boosted in antisolvent electrolyte of 50 % methanol in volume (Anti-M-50 %) at low or elevated temperatures. Basing on the Anti-M-50% electrolyte, the merits of Zn//PANI coin cell/pouch cell were impressive, even repeatedly charged/discharged to 2000 cycles at -10 °C

[222]. Hybridizing solvents was applied into ARFBs as well by Yu at el., who systematically studied a wide range of salts (LiCl, Li_2SO_4 and LiTFSI) and solvents (dimethoxyethane, DME; tetraethylene glycol dimethyl ether, TEGDME; Acetonitrile, AN; dimethylformamide, DMF). Finally, 1.5 M LiI in DMF/water was chosen because of the 2.8 V ESW and retained ionic conductivity at low temperatures, which enabled successful operation of Zn//LiI ARFBs at -20 °C for 150 cycles with nearly no capacity loss [223]. The merits of the works involving hybrid-solvent electrolytes are summarized (Table 1.2) on basis of representatively published papers [214-225]. And depending on the merits, we can conclude that the strategy of hybridizing solvents is promising if the balance point between wide ESW, high ionic conductivity, low freezing point and cost can be found.

Table 1.2 A summary of recently representative works upon hybrid-solvent electrolytes for ARBs.

Electrolyte	Electrode	ESW	Energy density	Cyclic stability	Working temperature	Reference
14 M LiTFSI in DMC/water	$Li_4Ti_5O_{12}$//$LiNi_{0.5}Mn_{1.5}O_4$	4.1 V	165 Wh·kg^{-1} (total electrode)	>1000 cycles (6 C)	RT	[226]
14 M LiTFSI in DMC/water	$Li_4Ti_5O_{12}$//graphite	4.1 V	n/a	50 cycles (0.2 A·g^{-1})	RT	[215]
9.25 m LiTFSI+3.1 LiOTf in DMC/water	Nb_2O_5//graphite	4.0 V	n/a	300 cycles (0.2 A·g^{-1})	RT	[216]
Li_4(TEGDME)(H_2O)$_7$	$Li_4Ti_5O_{12}$//$LiMn_2O_4$	4.2 V	120 Wh·kg^{-1} (total electrode)	500 cycles (3 C)	RT	[224]
50 wt% Li(LiOH)PAA	TiO_2/$LiTi_2(PO_4)_3$// $LiMn_2O_4$/$LiNi_{0.5}Mn_{1.5}O_4$	2.7 V	142.2 Wh·kg^{-1} (total electrode)	100 cycles (0.5 C)	RT	[225]
Mixture of 7 m NaOTf in water and 8 m NaOTf in PC	$NaTi_2(PO_4)_3$//$Na_3V_2(PO_4)_3$	2.8 V	45 Wh·kg^{-1} (total electrode)	100 cycles (10 C)	RT	[217]

LiTFSI+Zn(TFSI)$_2$ (Li$^+$:Zn^{2+}=20 in molar) in DES/water	Zn//LiMn$_2$O$_4$	>2.5 V	224.6 Wh·kg^{-1} (cathode)	600 cycles (0.1, 0.5, 1 C)	RT	[218]
LiTFSI/H$_2$O/(EMIM-TFSI)$_{2.0}$	Nb$_2$O$_5$//AC	4.7 V	51.9 Wh·kg^{-1} (total electrode)	3000 cycles (1 A·g^{-1})	RT	[219]
15.3 LiTFSI in AN/water	Li$_4$Ti$_5$O$_{12}$//LiMn$_2$O$_4$	4.5 V	173 Wh·kg^{-1} (total electrode)	1000 cycles (5 C)	RT, 0 °C	[220]
2 M ZnSO$_4$ in EG/water	Zn//PANI-V$_2$O$_5$	2.8 V	1700 Wh·kg^{-1} (cathode)	>250 cycles (0.2 A·g^{-1})	-40 °C to RT	[221]
2 M ZnSO$_4$ in Anti-M-50%	Zn//PANI	~2.5 V	n/a	2000 cycles (5 A·g^{-1})	RT, -10 °C	[222]
1.5 M LiI in DMF/water	Zn//LiI	2.8 V	n/a	2000 cycles (0.2 mA·cm^{-2})	RT, -20 °C	[223]

1.4.6 Electrode/current collector-electrolyte interface tuning

Interface tuning is a common strategy for all kinds of electrolytes, while the goals of tuning can be generally classified into thermodynamics (chemical and thermal stability) and kinetics (charge and mass transportation). Aqueous electrolytes own superior interfacial kinetics and wettability, thus it is more importance to cover the shortage in thermodynamics. SEI can kinetically stabilize electrolytes at potentials far beyond their thermodynamic stability limits, so that cell reactions are proceed reversibly. However, it even fails to occur in aqueous electrolytes until the discovery of WiSE. The formation mechanism of SEI in WiSE are possibly contributed by two pathways: (1) reduction of anion complexes or clusters; and (2) reduction of O_2 and CO_2 dissolved in the electrolyte (Fig. 1.13a) [227], implied by combining various spectroscopic, electrochemical and computational techniques. This in-situ constructed SEI not only enabled a series of high voltage/energy density ARLiBs with unprecedented stability, but also brought high flexibility and even "open configurations" that have been hitherto unavailable for any LiB chemistries [39, 67, 183]. Whereas, in Zn^{2+}-based aqueous system, severe HER during Zn plating/stripping, hitherto makes the in-situ formation of SEI impossible. As mentioned in electrolyte addictive strategy, some additives were added for facilitating the formation of SEI in ARZiBs. Wang at el. used 0.5 m $Me_3EtNOTF$ addictive to build a fluorinated and hydrophobic interphase that conducts Zn^{2+} while suppressing HER through alkylammonium decomposing [159]. Meanwhile, the same group developed inorganic ZnF_2-$Zn_5(CO_3)_2(OH)_6$-organic bilayer SEI on basis of low-concentration aqueous $Zn(OTF)_2$-$Zn(NO_3)_2$ electrolyte, mutually considering Zn^{2+} diffusion (inorganic inner layer) and water inactivation (organic outer layer). $Zn_5(OH)_8(NO_3)_2 \cdot 2 H_2O$ layer was initially formed on Zn anode surface via self-terminated chemical reaction of NO_3^- with Zn^{2+} and OH^-, and then it converted into Zn^{2+} conducting $Zn_5(CO_3)_2(OH)_6$, promoting the formation of ZnF_2 as the inner layer. Whilst the organic-dominated outer layer was generated by the reduction of OTf^- [228]. Another interfacial engineering is beforehand coated SEI/protective layer, which is more mechanically robust than in-situ grown SEI. In WiSE system, one pre-coated anode-protected layer was prepared by adding 0.5 M LiTFSI and 10 wt.% PEO into the mixture of 1,1,2,2-

tetrafluoroethyl-2',2',2'-trifluoroethyl ether (HFE) and DMC (95:5 in volume), vigorously heated and stirred at 75 °C, which stabilized graphite anode in a WiBSE and guaranteed one full cell with 4.0 V working voltage [229]. The HFE-PEO protective gel was applied to another graphite anode in the same WiBSE, paired up with the cathode of halogen conversion–intercalation chemistry, which not only provided more than 4.0 V working voltage but also considerably high capacity of 243 mAh·g^{-1} (for total electrode mass) [66].

Besides ARLiBs, pre-coated protective layers were massively used on the surface of Zn metal anodes on the purpose of dendrite-controlling [230]. One layer of sieve-element function (selective channel of Zn^{2+}) and uniform-pore distribution (≈3.0 nm) of a kaolin was prepared and coated on Zn metal anode for alleviating dendrite and corrosion issues. Owing to the selective channel of Zn^{2+} and narrow distribution pore diameter of kaolin (Fig. 1.13b), homogeneous Zn^{2+} migration confined by this channel was achieved with dendrite-free deposition. Moreover, the coated KL-Zn anode harvested a long-time stability (800 h under current density of 1.1 mAh·cm^{-2}) and accordingly suppressed side reactions on anode surface/interface. This property was further verified by kaolin-Zn//MnO$_2$ cell with high initial specific capacity and good capacity retention as well as a reasonably well-preserved morphology characterized by SEM [231]. A porous nano-CaCO$_3$ coating was discovered as owning the ability to guide uniform and position-selected Zn stripping/plating on the nano-CaCO$_3$-layer/Zn metal anode interfaces. This Zn-deposition-guiding ability was mainly ascribed to the porous nature of the nano-CaCO$_3$-layer, since the discovery of similar functionality (even though relatively inferior) in Zn metal anodes coated with porous acetylene black or nano-SiO$_2$ layers. The coated Zn anode was matched with CNT-MnO$_2$ cathode in ZnSO$_4$+MnSO$_4$ electrolyte, showing a 42.7% higher discharge capacity than bare Zn metal anode (177 vs 124 mAh·g^{-1} at 1 A·g^{-1}) after 1000 cycles [232]. Compared with SEI, CEI was not popularly reported, while it is still worthy to be investigated and practiced for improving the stability of cathode-electrolyte interface against side reactions and cathode dissolution. One general strategy to construct CEI for suppressing vanadium-based cathodes dissolution in aqueous electrolytes and beyond was proposed, which introduced Sr ion into vanadium oxide layers as a sacrifice guest, leaching out from the vanadium-based cathode as an in-situ CEI

coating layer on the surface (Fig. 1.13c) [233]. In ARLiBs, it is generally accepted that CEIs can only be formed in super-concentrated electrolytes containing fluorine-based organic anions (TFSI⁻, OTf⁻, etc.), while in traditional nitrite-based aqueous electrolyte (pH-adjusted saturated $LiNO_3$), CEI was initiatively discovered on the surface of $LiNiO_2$ cathode with composition of Li_2CO_3 and LiOH demonstrated by transmission electron microscopy (TEM) and X-ray photoelectron (XPS). Under protection of CEI, the capacity retention of $LiNO_2$ was significantly enhanced, in comparison with that in 1 M $LiNO_3$+LiOH (pH 10) aqueous electrolyte after 50 cycles [234].
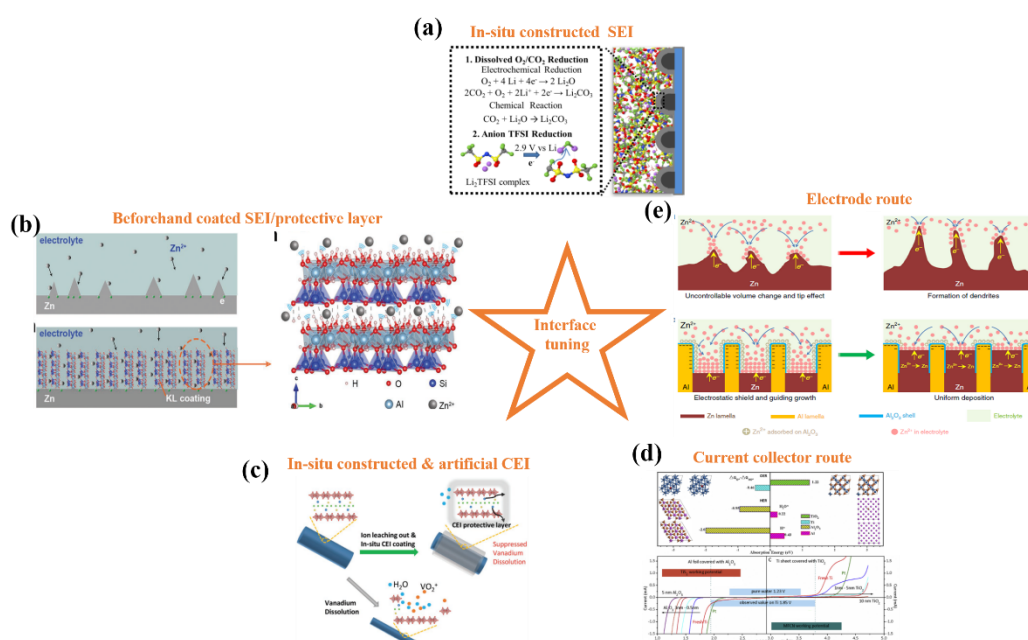
Fig. 1.13 (a) SEI formation mechanisms in WiSE [227]; (b) Schematic diagrams of Zn deposition process on bare Zn and KL-Zn with a detailed schematic diagram of confined Zn^{2+} transmission in kaolin [231]; (c) Illustration of the in situ CEI layer strategy design [233]; (d) Stability of Al and Ti current collectors in 15 m $NaClO_4$ aqueous electrolyte [235]; (e) Schematic illustration of eutectic strategy for dendrite and crack suppression [236].

In the study regarding HME of $Li(TFSI)_{0.7}(BETI)_{0.3}\cdot 2H_2O$, the effect from current collector to ESW was confirmed, which could further expand observed ESW when changing cathode current collector into Ti, and anode one into Al [189]. Zhu et al. reported that oxidizing Al current collector to Al_2O_3 (3 nm thickness surface) for anode and Ti one to TiO_2 (5 nm thickness surface) for cathode could expand ESW

of 15 M NaClO$_4$ aqueous electrolyte to 3.5 V (Fig. 1.13d). That wide ESW enabled TiS$_2$ anode of SiBs with low working potential (1.5 V vs. Na/Na$^+$) for the first time. Thus, a full cell coupling TiS$_2$ anode with PBA cathode in 15 M NaClO$_4$ aqueous electrolyte demonstrated a working voltage of 2.6 V, and cyclic life up to 1000 times (30 C rate) with high energy density of 100 Wh·kg^{-1} [235]. In Zn metal anode-based ARBs, the substrates (current collectors) can also affect Zn stripping/plating. Archer group found that graphene with a low lattice mismatch for Zn, was shown to be effective in driving deposition of Zn with a locked crystallographic orientation relation. The resultant epitaxial Zn anodes achieved exceptional reversibility in 2 M ZnSO$_4$ aqueous electrolytes (10000 cycles), and 1000 cycles of full-cell charging/discharging together with α-MnO$_2$ cathode [237]. In aqueous supercapacitor system, tuning electrode itself was reported as a method to widen ESW as well. In that work, W atoms in WO$_3$ crystal was partially replaced by Mo atoms thence introduced oxygen vacancy. The negative limitation of ESW was tunable between -0.4 and -1.2 V vs. SHE in 1 M Li$_2$SO$_4$ aqueous electrolyte owning to the consolidation process-customized band gap and HER overpotentials of Mo-substituted WO$_3$ electrode [238]. Zn alloying is another electrode route pertaining interface, especially alloying with Al. Eutectic-composition alloying of Zn and Al as an effective strategy substantially tackled irreversibility issues of Zn metal anodes by making use of their lamellar structure composed of alternating Zn and Al nano lamellas. The lamellar nanostructure not only promoted Zn stripping from precursor eutectic Zn$_{88}$Al$_{12}$ (at.%) alloys, but produced core/shell Al/Al$_2$O$_3$ interlamellar nanopatterns in situ to in turn guide subsequent growth of zinc (Fig. 1.13e), enabling dendrite-free Zn stripping/plating for more than 2000 h in oxygen-absent aqueous electrolyte of 2 M ZnSO$_4$ [236]. Zn-Al alloying was also employed in one ARAiB which consisted of an Al$_x$MnO$_2$ cathode, a Zn substrate-supported Zn-Al alloy anode, and an Al(OTf)$_3$ aqueous electrolyte. The featured alloy interface layer could effectively alleviate the passivation and suppress the dendrite growth, ensuring ultralong-term stable Al stripping/plating. The relevant architected cell exhibited a record-high discharge voltage plateau near 1.6 V and specific capacity of 460 mAh·g^{-1} for over 80 cycles [239]. Generally, interface tuning can be another universal method for ameliorating aqueous electrolyte and any other electrolytes, which is worthy to be dug out more deeply.

1.4.7 Beyond concentrated electrolyte

The benefits of salt-concentrated electrolytes towards ARBs have been intensively claimed here, while this kind of electrolyte has to use the salts with high solubility, restricting its applications in scale and scope. Therefore, the routes concerning breaking ceiling of salt solubility thereby introducing more cost-effective salts with relatively low solubility, and further broadening ESW come out, which can be classified into de-solvation/salting-out, and solubility enhancement. Zhou group found a new liquid electrolyte for Li metal batteries with de-solvated Li^+ ("Li^+ de-solvated electrolyte"), which merely composed of inactive "frozen-like" solvent and crystal-like salt solute [240]. Addition of salts into concentrated electrolytes could effectively eliminate the abundance of free solvents in electrolytes and make the concentrated electrolytes more aggregative than their original counterparts: electrolyte configuration evolved from solvent-separated ion pair (SSIP)-dominated structures to contact ion pair (CIP)-dominated structures (Fig. 1.14a) [241]. This kind of beyond concentrated electrolyte was even more aggregative than the saturated state and composed of only crowded solvent-depleted CIPs without any free solvents [241]. Tao group introduced this concept into aqueous electrolytes with inexpensive inorganic salts. One "oversaturated gel electrolyte" (OSGE) was simply prepared with PVA and saturated $LiNO_3$ at 95 ℃. The excess salt was then crystallized at room temperature, which was dispersed equally by the continuous room-temperature saturated gel (RTSG), forming the heterogeneous morphology (Fig. 1.14b). The continuous ion pathway ensured the considerable ionic conductivity of OSGE, regardless the existence of ion-insulated crystallized salt, while ESW was further expanded compared with that of RTSGE due to the further compacted CIPs (Fig. 1.14c). Moreover, the stability window of OSGE was still wide enough at elevated temperatures even at 80 ℃, ensuring the desired elevated temperature performance of ARLiBs [53]. Meanwhile, one perchlorate OSGE (1 m $Zn(ClO_4)_2$+10 m $LiClO_4$-PVA) was also employed for Zn-Li HiBs by same group, which shown one almost dendrite-free morphology with better cyclic stability [207]. Yan et al. applied this strategy for the electrolytes of low-temperature Zn-ion capacitors, which possessed superior ionic conductivity (even $1.3×10^{-3}$ $S·cm^{-1}$ at -60 ℃) based on $Zn(ClO_4)_2$ salty ice, attributing to the unique 3D ionic transport channels inside such ice [242]. Beside de-

solvation/salting-out, solubility increasing route was attempted as well. $ZnCl_2 + ZnBr_2 + Zn(OAc)_2$ aqueous electrolyte with a record super-solubility up to 75 m was reported, which broke through the physical solubility limit, attributing to the formation of acetate-capped water-salt oligomers (WSOs) bridged by Br^- /Cl^--H and Br^-/Cl^-/O-Zn^{2+} interactions (Fig. 1.14d and 1.14e). This supersoluble electrolyte drove one high-performance DiB to display a reversible capacity of 605.7 mAh·g^{-1} (corresponding energy density of 908.5 Wh·kg^{-1}) [243]. One 63 m "water-in-hybrid-salt" (WiHS) electrolyte (42 m LiTFSI + 21 m $Me_3EtN·TFSI$) was prepared, which doubled solubility of LiTFSI due to the inert salt based on an asymmetric ammonium cation of Me_3EtN^+. the FTIR spectrum in Fig. 1.14f revealed that the hydrogen bonding network of WiHS electrolyte was severely disrupted, leading to a further broadened ESW (Fig. 1.14g) [201]. Basically, the mechanism behind beyond concentrated electrolytes still needs more studies, especially more fundamental studies, although some excellent works about this electrolyte tuning strategy were reported.
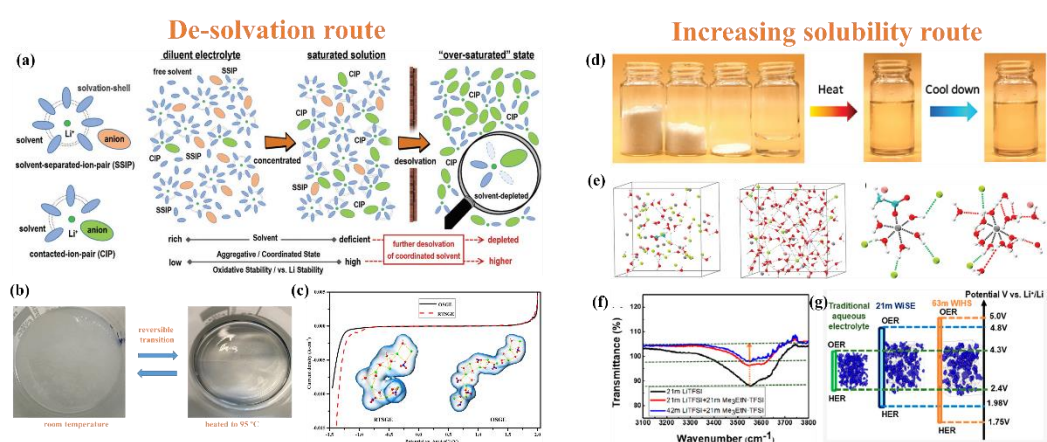
Fig. 1.14 (a) Design idea of further depleting solvent molecules within the Li^+ solvation sheath [241]; (b) Optical images of top view of OSGE at RT and 95 °C [53]; (c) Comparison of ESW and Li^+ solvation sheath between OSGE and RTSGE [53]; (d) $WSOE_{45}$-1 prepared by stoichiometric amounts of $ZnCl_2$, $ZnBr_2$, $Zn(OAc)_2$, and water [243]; (e) Snapshots and extracted typical molecules conformations of MD simulation on $WSOE_{45}$-1 and 5 m $ZnBr_{0.5}Cl_{1.5}$ aqueous solution [243]; (f) FTIR spectra of WiSE, 42 m WiHS, and 63 m WiHS electrolytes [201]; (g) MD simulation results and ESWs of traditional aqueous electrolyte, WiSE and WiSH electrolyte [201].

1.5 Summary

To mitigate the challenges of narrow ESW, electrode dissolution/side reaction and temperature-variation instability to aqueous electrolytes, various strategies on electrolyte additive, pH management, salt concentration, electrolyte gelling, solvent and interface tuning, and breaking through salt solubility limitation were reported intensively during past five years, which have formed a dense network with different working mechanisms and different specific routes. In this thesis, the salt-concentrated route was selected because of simple processing and high efficiency. The working mechanism of salt-concentrated electrolyte is breaking free H-bond network thus suppressing HER/OER activity. There are two ways to realize that. One is to create intimate interaction between cation and water molecules by acetate salt-concentrated electrolyte, and the other one is to induce contacting cation-anion pair in water molecules-based solvation structure. Both routes can lead to disorder distribution of water molecules and aggregation of H-bond, thus impede HER/OER thermodynamically (reaction potential) and kinetically (electron transfer across interface). To generate contacting cation-anion pair, the attempts were not only confined in OSGE with excellent elevated-temperature stability, but also went beyond diluted electrolytes by low-permittivity organic solvent.

CHAPTER 2 Research aim & methodology

2.1 Research aims and objectives

As discussed above, ARBs have been developed in monovalent-ion battery, multivalent-ion battery, metal//air battery, metal//chalcogen battery, hybrid battery and redox flow battery, while main challenges for ARBs such as low energy density, undesired cyclic stability, and narrow working temperature windows, can be mitigated through tackling electrolytes (expanding ESWs, suppressing electrode dissolution/side reaction and enhancing electrolyte stability upon temperature variation). The electrolyte manipulations can be summarized into seven routes of additive, pH management, salt concentration, gelling, solvent hybridizing, interface tuning and beyond concentrated electrolyte as shown in Fig. 2.1. Whilst, salt-concentrated route was chosen in this thesis, which can address issues of electrolytes by simply increasing salt concentration (changing solvation structures). The cost-effective salts of acetates, perchlorates and nitrates were utilized to suit industrial practice, while the effect of cation size in alkali acetate system was investigated. Moreover, one concept of "oversaturated gel electrolyte" (OSGE) was originally proposed by us, which is saturated with salt and polymer as sol above RT, then crystalizing a part of salt as gel at RT thereby inducing de-solvation and breaking free H-bond networks within water molecules [207]. This sort of electrolyte breaks through the limitation of salt solubility and introduces more salts into salt-concentrated system with wide ESW for high-energy and high-stability ARBs. Finally, the feasibility of diluting salt-concentrated electrolytes by organic solvent for retained or even better electrochemical stability was testified. The overall design ideas are from salt-concentrated to salting-out, and back to relatively diluted electrolytes. A general description of procedures and methodology is as following:

- Firstly, synthesize electrolyte and electrode materials via a designed technique, such as sol-gel, solid-state reaction, and chemical co-precipitation etc.
- Secondly, characterize physical properties of the obtained materials with a variety of methods, including X-ray diffraction (XRD), scanning electron microscope (SEM), energy-dispersive X-ray spectroscopy (EDX), Raman

spectroscopy, Fourier transform infrared spectroscopy (FTIR), simultaneous thermal analysis (STA).

- Next, prepare electrodes: blend the active materials with conducting reagent and binder, and then coat them onto a conductive substrate; directly use the self-support (binder-free) electrodes.

- Evaluate the electrochemical behaviours of the prepared electrolyte/electrode materials by linear sweep voltammetry (LSV), cyclic voltammetry (CV), galvanostatic charge/discharge (GCD) and electrochemical impedance spectroscopy (EIS).

- Finally, further test the practical energy storage device (full cell) with a two-electrode configuration. Measure corresponding CV, GCD and cyclic stability performances.
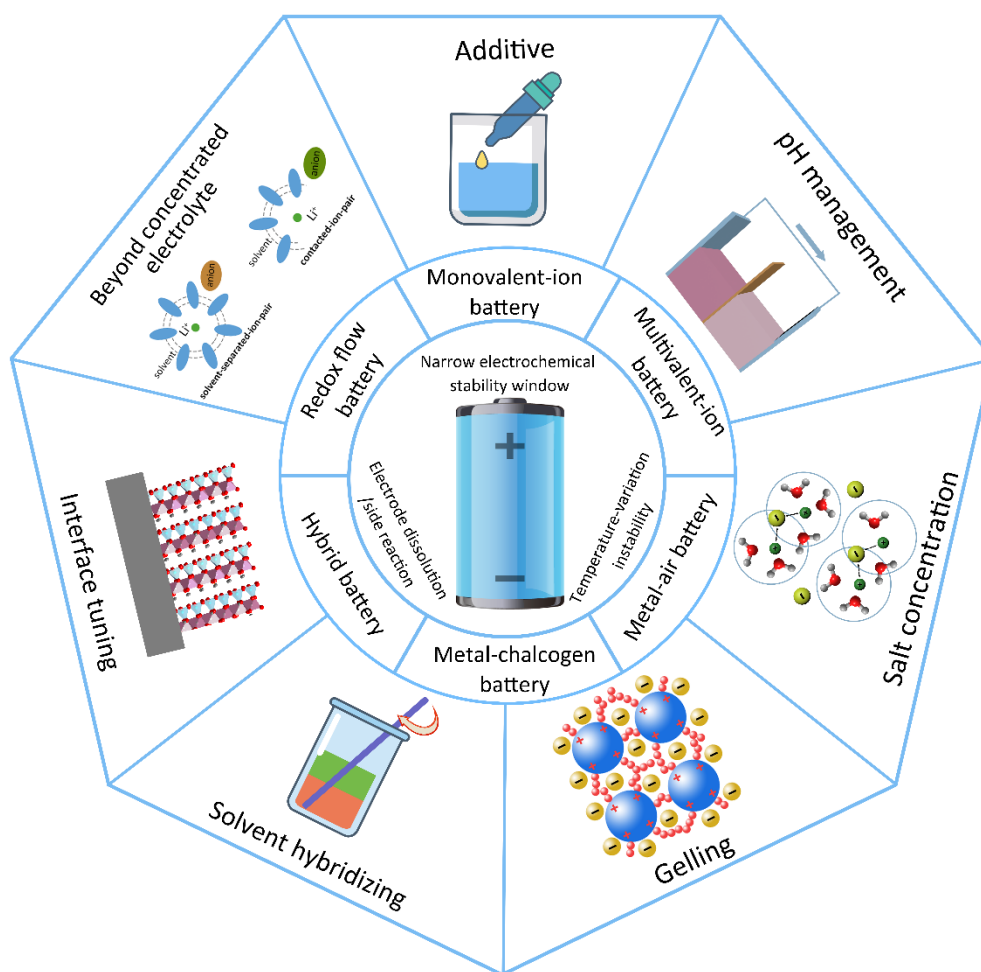
Fig. 2. 1 Challenges, application and improving strategy upon aqueous electrolytes of ARBs.

2.2 Organization of the thesis

The structure of this thesis is summarized as follows.

Chapter 1 provides the background information and reviews principles, historical development, and new concepts (additive, pH management, salt concentration, gelling, solvent hybridizing, interface tuning and beyond concentrated electrolyte) of electrolytes for ARBs.

Chapter 2 provides research aims and methodology (experimental) of this thesis.

Chapter 3 focuses on acetate salt-concentrated electrolyte for aqueous $Zn//MnO_2$ battery, which delivers excellent cyclic stability under overcharging.

Chapter 4 investigates the effect of cation size towards alkali acetate salt-concentrated electrolytes and applies the optimum electrolyte into $VO_2//LiNi_{0.5}Mn_{1.5}O_4$ system, which runs stably under high working voltage.

Chapter 5 proposes one concept of OSGE, introducing perchlorates with relatively low solubility to salt-concentrated system, which delivers wide ESWs from room temperature (RT) to elevated temperatures.

Chapter 6 expands application of OSGE to nitrate system, exhibiting wide ESWs and high ionic conductivity from RT to elevated temperatures, which enables stable charge/discharge of $VO_2//LiNi_{0.5}Mn_{1.5}O_4$ redox couple under high working voltage, and $VO_2//LiMn_2O_4$ one at elevated temperatures.

Chapter 7 further expands application of OSGE to acetate system, which not only stabilizes aqueous $Zn//MnO_2$ battery in conditions of overcharge and elevated temperatures, but also induces a hybrid charge storage mechanism.

Chapter 8 testifies the feasibility of utilizing *N,N*-Dimethylacetamide diluted nitrate concentrated electrolyte for high-stability aqueous $Zn//LiMn_2O_4$ battery without O_2 eliminating.

Chapter 9 summarises the significance of this thesis and compares property of various electrolytes. Future works for electrolytes of ARBs are suggested based on present study.

2.3 Methodology

2.3.1 Preparation of electrolytes

The liquid electrolytes were prepared by dissolving salts in deionized water (DIW) at RT until forming a transparent aqueous solution. OSGEs were prepared by dissolving salts in DIW to saturated state at 95 °C (chapters 5 and 6) or at 75 °C (chapter 7) to get transparent solution, which was followed by adding 10 wt.% poly(vinyl alcohol) (PVA, Sigma-Aldrich, 99+% hydrolyzed) (chapters 5 and 6) or 12 wt.% polyacrylic acid (PAA, Sigma-Aldrich, average Mv. 450000) (chapter 7) vs. DIW, and vigorous stirring for more than 3 hours as homogeneous aqueous sol. This was cooled down to RT as quasi-solid-state hydrogel. Finally, the heated OSGE with mobility was poured on glass microfibre (Whatman) substrate located on glass plate, then the doctor blade was manually moved to one direction thereby dispersing OSGE evenly on the substrate. Both sides of glass microfibre substrate were coated by OSGE successively. The overall thickness of perchlorate OSGE (chapter 5) was set as 0.4 mm, while that for nitrate (chapter 6), and acetate (chapter 7) OSGEs was set as 0.8 mm through doctor blade control.

The RTSGEs were prepared via dissolving salts in DIW based on their solubility at RT. This was followed by the addition of 10 wt.% PAV at 95 °C (chapters 6 and 6) or 12 wt.% PAA (chapter 7) at 75 °C vs. DIW. The chemical reagents for electrolyte salts were lithium acetate dihydrate (Alfa Aesar, 99%), sodium acetate anhydrous (Alfa Aesar, 99%), potassium acetate (Alfa Aesar, 99%), caesium acetate (Alfa Aesar, 99%), zinc acetate dihydrate (Sigma Aldrich, ACS, 98.0-101.0%), lithium perchlorate (Alfa Aesar, 98%), zinc perchlorate hexahydrate (Alfa Aesar, Reagent Grade), lithium nitrate anhydrous (Alfa Aesar, 99%) and zinc nitrate hexahydrate (Alfa Aesar, 99%, metals basis). The ratios of salts against

DIW in all these electrolytes were based on molality (m, molar-salt in kg-solvent) because of the evident density variation of solution under high salt concentration.

2.3.2 Preparation of electrodes

For synthesizing the self-supported MnO_2-TiN/TiO_2 cathode in chapter 3, TiN/TiO_2 porous substrate was prepared with titanium powder (Alfa Aesar, -200 mesh, 99.5%), potassium chloride (Alfa Aesar, 98%), polyethylene glycol (Alfa Aesar, PEG 1500), poly methyl methacrylate (Alfa Aesar, PMMA) and stearic acid (Alfa Aesar, Reagent Grade) by hot press at 150℃ at first to become pellets then calcination under N_2 at 1200 ℃ for 2 hours [244]. To grow nanosized MnO_2 on porous TiN/TiO_2 substrate, 0.04 g SDS (Sigma-Aldrich, ACS reagent) was dissolved in 10 mL deionized water, then 20 ml of 0.02 $g \cdot mL^{-1}$ potassium permanganate (Sigma-Aldrich, ACS reagent) solution was added dropwise and stirred for 15 min to gain a homogeneous solution. Subsequently, the mixed solution was transferred into a 40 mL polytetrafluoroethylene (PTFE) liner. The TiN/TiO_2 porous substrate was transferred to the PTFE liner. The sealed autoclave was kept at 130℃ for 10 h. The autoclave was then cooled to the room temperature and the prepared electrode was washed by deionized water several times before drying in a vacuum oven at 50℃ for 24 h. Finally, the sample was annealed in 99.99% Ar (BOC) at 400℃ for 2 hours to achieve a better crystallized phase [245]. While the MnO_2 nanosized particles in chapter 7 were synthesized by the same hydrothermal and annealing processes without any substrate.

In order to prepare VO_2 nanobelts as the active matter of the anode in chapters 4 and 6, 9.0 g vanadium oxide powder (Alfa Aesar, 99.5%) was dispered into 200 mL ethonal by sonicating, then 200 mL DIW was added into the mixture via strong magnetic stirring for at least one hour. The above suspension was divided and tranferred into two 250 mL stainless steel autoclaves equally. The autoclaves were sealed and maintained at 180℃ for 48 h and then cooled down to RT naturally [246]. After that, the obtained powder sample was washed centrifugally with DIW and 2-propanol several times to remove any possible residual produced in hydrothermal reaction finally it was dried in the vacuum oven at 75℃ for 8 hours.

To obtain $LiNi_{0.5}Mn_{1.5}O_4$ hollow microspheres as the active matter of cathode in chapters 4 and 6, 10 mmol of manganese sulphate monohydrate (Sigma Aldrich, $\geq99.0\%$) and 100 mmol of ammonium hydrogen carbonate (Alfa Aesar, 99%) were separately dissolved in 700 mL of DIW. 70 mL of ethanol and the NH_4HCO_3 solution were then added to the $MnSO_4$ aqueous solution successively under stirring. The mixture was kept under stirring for 1 hour at room temperature and then centrifuged, washing with DIW and 2-proponal several times. The as-obtained intermediates were dried at 80 ºC and fired at 400 ºC for 5 hours. Furthemore, the fired intermediates, nickel nitrate hexahydrate (Alfa Aesar, 98%) and lithium hydroxide monohydrate (Sigma Aldrich, $\geq98\%$) were dispersed in 15 mL of ethanol. The ethanol was evaporated slowly at RT under stirring. Finally the mixture was ground manually for more than 10 minutes and then calcined at 800 ºC for 20 hours in air to become $LiNi_{0.5}Mn_{1.5}O_4$ hollow microspheres [247]. While the $LiMn_2O_4$ hollow microspheres in chapter 6 were prepared by the same processes without nickel nitrate hexahydrate as orignical chemical.

$LiMn_2O_4$ power used in chapters 5 and 8 was synthesized by dispersing calculated amounts of manganese oxide (Alfa Aesar, 99.9%) and lithium hydroxide (Sigma Aldich, 99%) in ethanol. The ethanol was slowly evaporated at RT under stirring. The obtained mixture was manually ground in an agate mortar and pestle for 10 minutes and then put in an alumina crucible and calcined under atmosphere at 800 ºC for 20 hours [247]. $LiMn_2O_4$ nanorods used in chapter 8 were synthesized by two steps, firstly formed as β-MnO_2 by hydrothermal reaction, secondly lithiated by wet-chemistry method. Manganese acetate tetrahydrate (Alfa Aesar, Mn 22%, typical) and sodium peroxydisulfate (Alfa Aesar, 98%) were dissolved in DIW at RT with a molar ratio of 1:1, magnetic stirring up to a homogeneous clear solution, then transferred into Teflon-lined stainless-steel autoclave and heated at 120 °C for 12 h in a preheated electric oven. After that hydrothermal reaction, the as-obtained precipitated product was centrifugally washed by DIW and 2-propanol in succession. The cleaned powder was then dried at 100 °C for 12 h under atmosphere. Lithium hydroxide monohydrate (Sigma-Aldrich, ACS 98%) was dispersed in 2-propanol with as-synthesized β-MnO_2 with molar ratio of 1:2, which was dried at RT and manually ground in mortar for 10 minutes. Finally, the mixture was calcined at 700 °C under atmosphere for 10 h. [248, 249]

2.3.3 Battery assembly

Commercial zinc foil was polished by zinc powder (Alfa Aesar, median 6-9 micron, 97.5%) for approximately 10 min, then washed with soap and deionized water, rinsed with 2-proponal and dried at 60℃ in vacuum oven for 3 h [156]. The processed Zn foils were Zn metal electrodes utilized in chapters 3, 5, 7 and 8. To prepare the electrode slurry in chapters 4 and 6, 80 wt.% active material powders (VO_2 or $LiNi_{0.5}Mn_{1.5}O_4$), 7% polytetrafluoroethylene (PTFE, Sigma Aldrich, 60 % in H_2O) binder suspension (10%), and Super P (TIMCAL) powder (10%) were mixed with 2-propanol until a homogenous slurry was formed. The slurry was brushed onto a surface of Ti mesh (thickness of 0.1 mm) with mass loading of ~2.0 mg·cm^{-2} for the anode and ~3.0 mg·cm^{-2} for the cathode, which were dried in vacuum oven at 60 °C for more than 2 hours. For applying in three-electrode system, activated carbon (AC) electrodes were prepared as the counter electrodes in chapters 4, 6 and 7. The AC electrodes were obtained by mixing the AC (Black Pearl 2000, Cabot) and PTFE at a mass ratio of 95: 5 similar with the above-mentioned process. The as-prepared $LiMn_2O_4$ in chapter 5 was mixed with Super Pnand PTFE with the mass ratio of 85:10:5, then brushed on Ti mesh (thickness of 0.1 mm). The active mass was controlled to 5.0-6.0 mg.

In chapter 7, MnO_2 slurry was prepared by mixing the MnO_2 nanorods, Super P and 5 wt.% polyvinylidene fluoride (PVDF, Solef 5130) in a weight ratio of 75:20:5 in 1-methyl-2-pyrrolidinone (NMP, Alfa Aesar, 99+%) solvent. The slurry was then brushed on Ti mesh (thickness of 0.1 mm) with a loading mass of ~2.5 mg·cm^{-2} and dried in a vacuum oven at 80 °C for at least 2 hours. In chapter 8, $LiMn_2O_4$ slurry was obtained by blending $LiMn_2O_4$ nanorods, Super P and PVDF in a weight ratio of 85:10:5 in NMP solvent, then processed with same process (loading mass of ~3 mg·cm^{-2}). After that, all the prepared electrodes and zinc metal electrodes were cut into round shape discs with a diameter of 12 mm using a precision disc cutting machine (Kejing, MSK-T10), whilst the OSGE coated on glass microfiber filter was cut into a 16 mm-diameter disc as separator. The anode and cathode were assembled in CR2016 or CR2032 coin cells using the hydraulic crimping machine (Kejing, MSK-110). In chapters 3 and 5, the cells were assembled in CR2016, and the others were in CR2032. In chapter 3, the cathode

substrate TiN/TiO$_2$ (thickness 0.2 mm) was fragile because of porous morphology, thus the leaf spring in the cathode side was not used as CR2016 style. In chapter 5, the thickness of OSGE was 0.4 mm, thinner than the OSGEs with 0.8 mm thickness in chapters 6 and 7. The amount of liquid electrolyte (chapters 3, 4 and 8) assembled in coin cells was controlled in the range from 200 to 300 μL. The loading mass was controlled by brushing active material with certain mass on the substrate with calculated area.

2.3.4 Material characterization

XRD data was collected on the Panalytical X-Pert Pro MPD diffractometer equipped with a focussing Johanson monochromator on the incident beam optics, giving high-resolution pure Cu K$_{\alpha 1}$ radiation. Reflection/transmission spinner stage worked as the sample stage of powder, while Z-translation stage functioned as the sample stage for thin film. To collect the XRD data of MnO$_2$ nanoparticles (in chapters 3 and 7), Panalytical Empyrean equipped with a Co target was employed to avoid the fluorescence. For both XRD devices, absolute scans in the 2θ range of 10–90° with step sizes of 0.0167° were used during data collection. Wide-angle X-ray scattering (WAXS) was utilized for phase of MnO$_2$-TiN/TiO$_2$ cathode in chapter 3 before and after charge-discharge reaction with a 5m Xenocs Xeuss 2.0 SAXS instrument, equipped with Mo sources and a Pilatus 300K hybrid photon counting detector. The Rietveld refinement of the structure of the oxide electrode materials in chapter 4 was carried out by GSAS+EXPGUI [250, 251].

FTIR measurements were carried out on a Bruker Vertex 70V IR spectrometer (chapter 3) or Bruker Alpha II ATR spectrometer (chapters 4 and 5). All the liquid samples were dropped on CaF$_2$ window substrate with same amount of 100 μL. The number of scans was set as 32, while the background was based on CaF$_2$ window substrate under atmosphere, which was deducted for every measurement. In FTIR, transmittance (T) is usually for qualitive analysis, while absorbance (A) is used for quantitative analysis. The relationship between T and A is:

$$A = -\log{(T)} \tag{2.1}$$

Hence, only A can demonstrate the positive correlation between FTIR peak intensity and concentration of samples as Lambert-Beer law:

$$A = \varepsilon c l \tag{2.2}$$

In this thesis, FTIR analysis was used to discover the relationship between concentration/composition and solvation structure of aqueous solution, therefore the shift and shrink of FTIR peak should be caused by the transition of solvation structure only. The strong positive correlation between concentration and A can affect the result largely, which need to be eliminated. And that is the reason why transmittance was chosen as the y-axis for the aqueous electrolyte samples. Raman spectra were recorded on a Renishaw inVia Reflex Raman Microscope equipped with a DPSS laser at 532 nm (10% power nominally 2 mW) and Renishaw CCD detector. A grating of 1800 l/mm, objective of X50 LWD and acquisition time of 10 seconds per energy pixel were employed during testing. Automated sample stage for depth (z) and surface (xy) mapping was utilized during Raman mapping, as well as spectrum range from 400 to 4000 cm^{-1}.

SEM measurements were carried out on a ZEISS SUPRA 55-VP Field Emission Scanning Electron Microscope equipped with Oxford Instruments EDX spectrometer for elemental composition analysis with a detection limit of approx. 0.5 at.%. STA was conducted in a NETZSCH STA 449 F3-Jupiter Thermal Analyser through heating from RT to 600 °C in air, with a heating rate of 10 °C·min^{-1} and a flow rate of compressed air of 50 mL·min^{-1}. The viscosity of various electrolytes at different temperatures was recorded by an IKA Rotavisc lo-vi advanced viscometer equipping with VOL-SP-6.7 spindle. Thermo Scientific STAR A214 pH meter was employed to test pH values of different aqueous solutions.

2.3.5 Molecular dynamics simulation

MD simulations were performed with the program GROMACS, version 4.50 using OPLS-AA force field [252, 253]. Water molecules in the system was described by using TIP3P model [254]. The force-field parameters and geometry parameters of Li^+ and NO_3^- for chapter 6 were taken from the works reported in other literature [254]. The force-field parameters of Zn^{2+} and K^+ in chapter 7 were taken directly from the OPLS-AA force field [253], while those of of acetate were taken from the works reported in other literature [255]. Moreover, PAA was simplified to a PVA oligomer with a chain of 30 repeating units and its force-field parameters were taken from other literature [256]. The force-field parameters of Zn^{2+} and Li^+ in chapter 8 were taken directly from the OPLS-AA force field [253], while those of DMA were taken from the works reported in other literature [257]. The components of simulated electrolytes are given in the Table 2.1, Table 2.2 and Table 2.3. The densities in Table 2.1 were determined by the simulations after inputting the molecule specie, number, and size of simulation box. The simulations were started by minimizing the energies of the initial configuration using the steepest descent algorithm. After energy minimization, a 10 ns constant-NPT simulation (time step 1 fs) was performed to obtain the reasonable size of solutions box. Then, a 1 ns constant-NVT simulation (time step 1 fs) was performed to pre-equilibrium the system. Finally, 100 ns constant-NVT simulation were then carried out to obtain the equilibrium state. Periodic boundary conditions were employed for all xyz directions. The temperature was controlled at 298 K with Langevin thermostat [258]. The pressure was kept at 1 atm using Langevin barostat [259]. The particle mesh ewald summation technique was used to calculate the long-range electrostatic interactions [259]. The nonbonded interactions were calculated based on Lennard-Jones pair potentials (LJPPs) which assumed the interaction occurred between two bodies [260]. LJPPs were evaluated within a cut-off of 1.2 nm. The cross-interaction parameters were obtained from the Lorentz-Berthelot rules [261]. Trajectory analysis was partly done with the use of visual molecular dynamics (VMD) and partly with home-developed programs [262].

Table 2.1 Components of simulated electrolytes in chapter 6 for MD simulations.

LiNO$_3$:H$_2$O ratio	Number of H$_2$O	Number of LiNO$_3$	Size of simulation box (Å^3)	MD, density at 298 K (g·cm^{-3})
15:55	800	216	38.2×38.2×38.2	1.289
33:55	800	475	33.5×33.5×33.5	1.404

Table 2.2 Components of simulated electrolytes in chapter 7 for MD simulations.

Concentration of KOAc (m)	Number of H$_2$O	Number of Zn(OAc)$_2$	Number of KOAc	Number of PAA chain
0	1000	18	0	0
31	1000	18	562	20
40	1000	18	727	20

Table 2.3 Components of simulated electrolytes in chapter 8 for MD simulations.

Dilution time by DMA	Number of H$_2$O	Number of Zn(NO$_3$)$_2$	Number of LiNO$_3$	Number of DMA
0	1110	32	174	0
4	1110	32	174	860
9	555	16	87	971

2.3.6 Electrochemical measurements

Solartron 1470E multichannel cell test system was employed to test both CV, determining the redox peaks of the anodes and cathodes, and LSV curves, determining ESWs of electrolytes. For LSV, two Ti foils which had been ultrasonically washed before, were utilized as working electrode and counter electrode, while Ag/AgCl was used as the reference electrode. Unlike conventional LiBs, in aqueous system, Li metal electrode cannot be used as reference, while if taking Zn metal electrode with standard potential of -0.72 V vs. SHE as reference, the Zn deposition will appear on reference electrode at first before onset of HER in salt-concentrated electrolytes. Meanwhile, the same device was employed for obtaining the charge/discharge curves of the anode/cathode under a current density of 20 mA·g^{-1} in the three-electrode system with AC-Ti mesh as the counter electrode and Ag/AgCl as reference electrode. The results were used for matching the capacity of the anode and cathode in a full cell (chapters 4 and 6). EIS was employed to obtain the total conductivity of various electrolytes through an integrated Solartron 1455A frequency response analyzer with 10 mV bias and 100 kHz-0.1 Hz frequency range. To estimate the transference number of Zn^{2+} in various electrolytes (chapters 3, 5, 7 and 8), a current interrupt method was utilized with 1.0 V vs. Zn/Zn^{2+} voltage to Zn//Zn symmetric cell. Based on that, the Zn^{2+} conductivity can be estimated. The steady current in the current interrupt test was caused by the Zn^{2+} transportation only, while the longer time (normally several hours) the current is recorded, the higher accuracy will be shown [263]. Although the test time was no more than 2 minutes here, it still can demonstrate the range or variation trend of transference number.

In chapters 5-7, the cells based on the OSGE were heated at 50 ℃ for 2 hours to improve the electrode-electrolyte interfacial wettability. After coin cells assembly, they were relaxed under open circuit for 8 hours, while the cells were connected to the battery tester, the OCV of which are recorded as well. GCD cycling and rate capability measurements with corresponding potential limitation were carried out using 8-channel Land CT2001A battery tester at RT (controlled by air conditioner in lab). The capacity and energy density of cells were calculated based on the active mass of cathodes (chapters 3, 5, 7 and 8) or total active mass of electrodes (chapters 4 and 6). The mass of active material in chapter 3 was got by comparing the mass of TiN/TiO$_2$ substrate before and after MnO$_2$ growing through

hydrothermal reaction. While in chapters 4-8, the active material was brush on the current collector directly. The active mass of single electrode cut into disc was determined by area ratio with pristine current collector. There are two significant figures for mass of active material, according to the accuracy of weighing balance (Fisher Scientific) in our lab (0.1 mg). Therefore, there are two significant figures for capacity as well. Three figures are kept in the value of capacity, capacity retention, CE and energy density, the last digits of which were bracketed for showing the uncertainty. After that, RT-GCD cycling, Land BT3001A and home-made graphite bath (water bath kettle filled with graphite) were employed for testing cells at elevated temperatures (chapters 6 and 7). The energy density was obtained through integrating the discharge curve in Origin software with the equation below:

$$E = \int_0^{C_{sd}} V(C)\, dC \qquad\qquad (2.3)$$

In this thesis, SHE was utilized for expressing standard electrode (theoretical) potential, while those of using Zn/Zn^{2+} are for two-electrode system (coin cell) with Zn metal electrode as both counter and reference electrode. In chapter 4 and chapter 6 regarding ARLiBs, although the observed potentials of cathodes/anodes were determined in there-electrode with Ag/AgCl reference electrode, the potential value was also converted into against Li/Li^+ (standard electrode potential of which is -3.05 V vs. SHE) for comparing with reported works on LiBs. All the conversions can be done based on the standard electrode potential against SHE.

CHAPTER 3 Acetate concentrated electrolyte for high-voltage Zn//MnO₂ battery

3.1 Abstract

Although wide ESWs for aqueous electrolytes have been achieved on the expensive organic salts, the high cost could be a potential obstacle for large-scale application of these electrolytes. Therefore, in terms of cost, aqueous electrolytes based on inexpensive salts would be a better choice. Aqueous solutions of salts such as $LiNiO_3$ and KOAc have been investigated as the potential electrolytes for ARBs [58, 187, 188, 264]. Based on a similar strategy, in this study, we developed aqueous Zn^{2+}-conductors with wide ESWs to be used as electrolytes for high voltage Zn//MnO₂ batteries. Both $Zn(OAc)_2$ and KOAc were dissolved in water at room temperature to form a 1 m $Zn(OAc)_2$ + 31 m KOAc aqueous solution. The as-formed salt-concentrated aqueous electrolyte also meets the definition of WiBSE [39]. The ESW at RT of the 1m $Zn(OAc)_2$ + 31 m KOAc electrolyte was around 3.4 V. That electrolyte was assembled with a self-supported α-MnO₂-TiN/TiO₂ cathode (nanosized α-MnO₂ particles grown on the porous TiN/TiO₂ substrate directly via a hydrothermal reaction) and polished zinc foil as the anode, completing the Zn//MnO₂ battery. The Zn//MnO₂ battery was demonstrated as a hybrid battery, in which Zn^{2+} was stripped/deposited on the Zn foil anode and proton insertion in the MnO₂ cathode. Through the electrochemical characterization, the Zn//MnO₂ battery delivered a discharge capacity of 30(5) $mAh\cdot g^{-1}$ and an energy density of 36(9) $Wh\cdot kg^{-1}$ (based on the 1.2 mg MnO₂ mass) on the first cycle, and a discharge capacity of 24(3) $mAh\cdot g^{-1}$ and an energy density of 27(7) $Wh\cdot kg^{-1}$ at the 600th cycle, with capacity retention of 79.(7)% when charged/discharged at a current density 100 $mA\cdot g^{-1}$. The cut-off voltage was 2 V which is higher than the normally reported values 1.8 V or 1.6 V [81, 172, 174, 265, 266]. Dendrite was not observed at the Zn foil anode after cyclic and rate performance, attributing to the superiority of salt-concentrated electrolytes.

3.2 Results and discussion

3.2.1 Property of acetate concentrated electrolyte

In order to investigate the relationship between the salt concentrations and ESWs of acetate aqueous system, 1 m $Zn(OAc)_2$, 1 m $Zn(OAc)_2$+5 m KOAc, 1 m $Zn(OAc)_2$+10 m KOAc, 1 m $Zn(OAc)_2$+20 m KOAc and 1 m $Zn(OAc)_2$+31 m KOAc were tested, respectively via LSV at a sweep rate of 1 mV·s^{-1}. The measured ESWs are shown in Fig. 3.1a. Clearly, the ESW becomes wider with increased salt concentration, from 2.6 V for 1 m $Zn(OAc)_2$ to 3.4 V for 1 m $Zn(OAc)_2$+31 m KOAc (Table 3.1). In the investigated samples, 1 m $Zn(OAc)_2$+31 m KOAc exhibits the widest stability window thus is selected as the electrolyte for an aqueous $Zn//MnO_2$ battery. On the LSV curves shown in Fig. 3.1a, the onsets (rapid accelerating) of the negative side (Zn plating/HER) can be differentiated easily, whereas onsets at the positive sides (OER), especially for those of samples 1 m $Zn(OAc)_2$+5 m KOAc and 1 m $Zn(OAc)_2$+10 m KOAc, 1 m $Zn(OAc)_2$+20 m KOAc and 1 m $Zn(OAc)_2$+31 m KOAc, are very difficult to distinguish. Therefore, Tafel curves in high polarization areas were used to study OER kinetics of Ti foil electrodes in these four electrolytes. The Tafel curves derived from the corresponding LSV curves within the potential ranging from 1.95 to 2.0 V were converted into vs. SHE with *IR* eliminated as shown in Fig. 3.1b. The standard electrode potential of Ag/AgCl is 0.222 V vs. SHE [267]. As all LSV result was obtained at room temperature, the potential value vs. SHE was converted through potential value vs. Ag/AgCl plus 0.222 V. As for the *IR* part, *R* means serial resistance of electrolyte, the value of which was determined through EIS test in Fig. 3.2, while *I* means current density at various potential during LSV test. Therefore, both the value of *IR* and potential-*IR* was varied, which could be obtained after inputting the fixed value of *R* of every electrolyte in Origin. The Tafel slopes of 1 m $Zn(OAc)_2$+5 m KOAc, 1 m $Zn(OAc)_2$+10 m KOAc, 1 m $Zn(OAc)_2$+20 m KOAc and 1 m $Zn(OAc)_2$+31 m KOAc electrolytes are calculated as 114.9, 136.1, 141.1 and 147.6 mV·dec^{-1} respectively, indicating decreased OER kinetics from 1 m $Zn(OAc)_2$+5 m KOAc to 1 m $Zn(OAc)_2$+31 m KOAc (the larger the slope, the lower the activity [268]). The high concentration supresses the OER reaction thus extends the ESW.
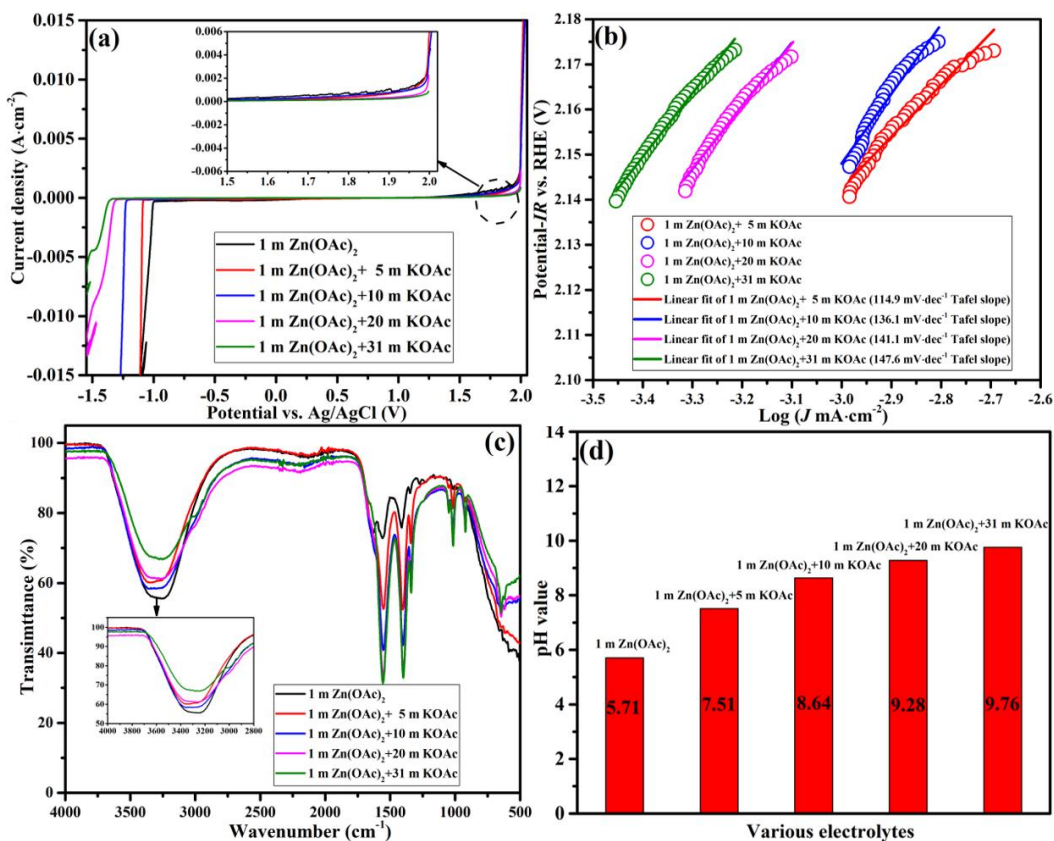
Fig. 3.1 (a) ESW test on the acetate salt-concentrated electrolytes under $1 \ mV \cdot s^{-1}$ sweep rate; (b) Tafel curves of acetate salt-concentrated electrolytes regarding OER; (c) FTIR spectra of the acetate salt-concentrated electrolytes; (d) pH value of the acetate salt-concentrated electrolytes at RT.

According to previous reports, a local structure of intimate Li^+-water interaction will be enhanced at high salt concentrations in the Li-ion aqueous electrolytes, generating $(Li^+(H_2O)_2)n$ polymer-like chains, solidifying as the hydrates melt and induce wider stability windows [194]. Similar situations may happen on the salt-concentrated 1 m $Zn(OAc)_2$+31 m KOAc electrolyte. FTIR was used to characterize the liquid structure of these aqueous electrolytes to confirm the relationship between their structures and ESW. The FTIR spectra of these aqueous electrolytes are exhibited in Fig. 3.1c. The peaks observed from ca. 2900-3600 cm^{-1} represent the O-H stretching vibration bands involved in the hydrogen bonding [269], which gradually decrease when the concentration of salts in the aqueous electrolytes are increased. The peaks of ca. 1560, 1390 and 1330 cm^{-1} are assigned to asymmetric and symmetric stretching vibrations of the carboxylate group from the acetate anions. CH$_3$ asymmetric deformation [269] is increased and sharpened,

100

with the increased concentration of the solution. Both changes indicate the phase out of hydrogen bonds and semi-solidification of salt-concentrated electrolytes [194]. For ARBs, the pH value of aqueous electrolytes can significantly affect their performance [40]. As for Zn//MnO$_2$ systems, depending on their pH value, there are various kinds of reaction mechanisms, specially Zn^{2+} ion insertion/desertion for neutral or mild acidic electrolytes and proton insertion/desertion for alkaline electrolytes [174, 265]. Therefore, the pH value of those aqueous electrolytes was measured by a Thermo Scientific STAR A214 pH meter (Fig. 3.1d). The pH value of 1 m Zn(OAc)$_2$ is 5.71, which gradually increases with the increased concentration of alkaline KOAc solution, reaching 9.76 for the sample 1 m Zn(OAc)$_2$+31 m KOAc. This is a mild alkaline condition, which may induce proton-involved electrode reaction [270].

The ionic conductivity of these electrolytes was measured by EIS, utilizing 0.1 m KCl aqueous solution (the conductivity of 0.1 M KCl aqueous solution is 1.28×10^{-2} S·cm^{-1} at RT [271]) with the same dimensions (20 mL) and same set-up as the calibration sample. The recorded a.c. impedance spectra are shown in Fig. 3.2a. The ionic conductivity is 1.53×10^{-2} S·cm^{-1} for 1 m Zn(OAc)$_2$, to 2.96×10^{-2} S·cm^{-1} for 1 m Zn(OAc)$_2$+31 m KOAc (Table 3.1). To get an accurate tendency of ionic conductivity with the raising of KOAc concentration, ionic conductivity of 1 m Zn(OAc)$_2$+3 m KOAc (8.68×10^{-2} S·cm^{-1}), 1 m Zn(OAc)$_2$+7 m KOAc (1.11×10^{-1} S·cm^{-1}), 1 m Zn(OAc)$_2$+15 m KOAc (7.57×10^{-2} S·cm^{-1}) and 1 m Zn(OAc)$_2$+25 m KOAc (2.43×10^{-2} S·cm^{-1}) were tested by EIS as well, while the relevant tendency is shown in Fig. 3.2b. With increased KOAc concentration, the ionic conductivity increases at first achieving a maximum at 1 m Zn(OAc)$_2$+7 m KOAc due to the raising of charge carriers in the electrolytes, then decreases due to the soaring of viscosity of electrolytes [272]. It is noteworthy that, the conductivity measured by EIS is the total conductivity which included the conductivity of all the charge carriers such as Zn^{2+}, K$^+$, OAc$^-$, H$^+$ and OH$^-$ ions. Therefore, to confirm the ions interaction effect caused by ions other than the Zn^{2+} ion, the transference number of Zn^{2+} ($T_{Zn^{2+}}$) of various electrolytes was tested by the current interrupt method. This was carried out in a Zn//Zn symmetric cell with various electrolytes using Zn foils working as Zn^{2+} reversible electrodes, while also serving as blocking

electrodes for other ions. $T_{Zn^{2+}}$ can be determined by the initial current (I_o) and final steady-state current (I_s) of current interrupt method with the following equation [263]:

$$T_{Zn^{2+}} = \frac{I_s}{I_o} \tag{3.1}$$

As shown in Fig. 3.2c, after applying 1.0 V vs. Zn/Zn^{2+}, the current of all the Zn//Zn symmetric cells with various electrolytes drops except the cell with 1 m Zn(OAc)$_2$ electrolyte, the current of which is kept around 0.025 A. In Fig. 3.2d, $T_{Zn^{2+}}$ decreased with the increased concentration of KOAc, from 1 for 1 m Zn(OAc)$_2$ to 0.38 for 1 m Zn(OAc)$_2$+31 m KOAc. The activity of Zn^{2+} ions in the electrolyte is suppressed under high concentration of KOAc. From the current interrupt method, Zn^{2+} conductvity can be estimated by comparing the resistance of Zn//Zn symmetric cells with 1 m Zn(OAc)$_2$+31 m KOAc electrolyte, and that of 0.1 M KCl standard solution with the same set-up and dimension. The ohmic resistance caused by Zn^{2+} migration can be calculated as 83.3 Ω, hence the ionic conductivity of Zn^{2+} can be estimated as 7.80×10^{-3} S·cm^{-1}. The Zn^{2+} ionic conductivity is high enough to be used as an electrolyte for a Zn^{2+} ion batteries.

Table 3.1 Summary on ESWs and ionic conductivity of various electrolytes.

Sample	ESW (vs. Ag/AgCl) at 1 mV·s^{-1} (V)	Ionic conductivity (S·cm^{-1})
1 m Zn(OAc)$_2$	-1 to 1.6	1.53×10^{-2}
1 m Zn(OAc)$_2$+5 m KOAc	-1.1 to 1.7	1.01×10^{-1}
1 m Zn(OAc)$_2$+10 m KOAc	-1.3 to 1.7	9.70×10^{-2}
1 m Zn(OAc)$_2$+20 m KOAc	-1.4 to 1.95	5.29×10^{-2}
1 m Zn(OAc)$_2$+31 m KOAc	-1.45 to 1.95	2.96×10^{-2}
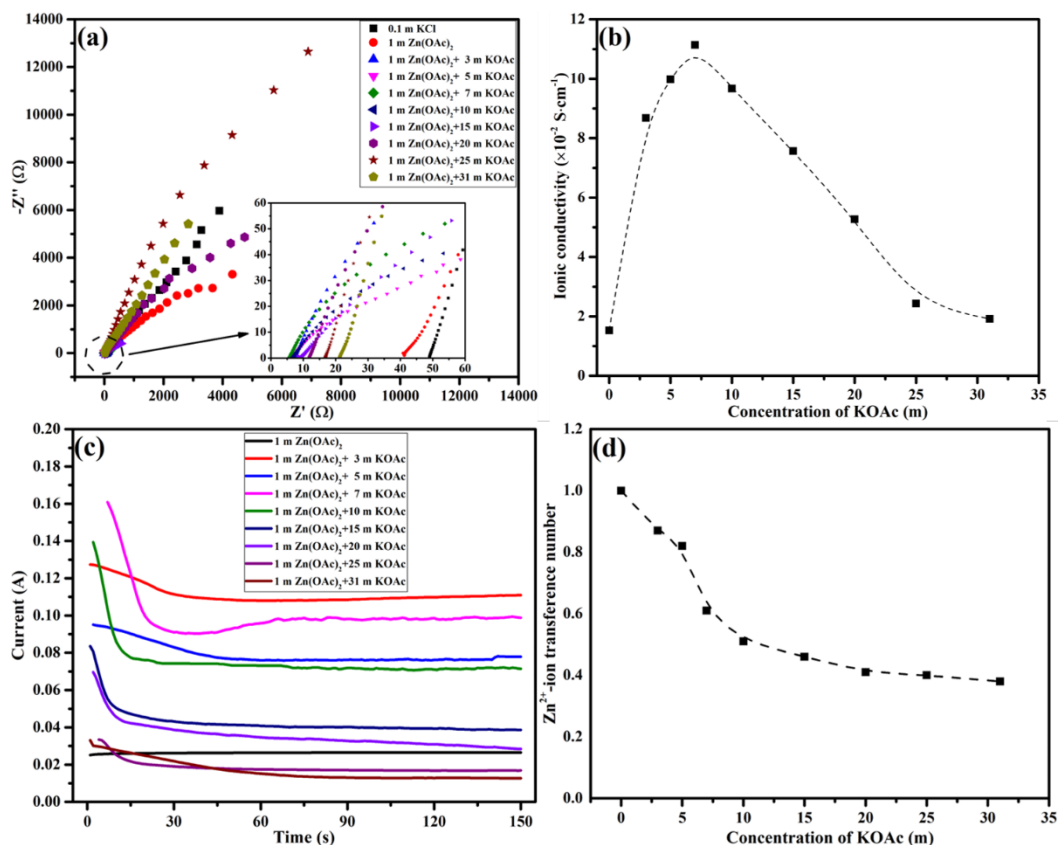
Fig. 3.2 (a) EIS of various electrolytes with different salt concentrations at RT; (b) Relationship between ionic conductivity and KOAc concentration in various electrolytes; (c) The current interrupt test on Zn//Zn symmetrical cells with various electrolytes under 1 V vs. Zn/Zn^{2+} applied voltage; (d) The relationship between Zn^{2+} transference number and KOAc concentration in various electrolytes.

3.2.2 Working mechanism and reversibility of Zn anode

To study the working mechanism and reversibility of Zn anode, Zn//Ti coin cell was prepared based on various electrolytes to discover the influence from KOAc concentration to CE of Zn stripping/plating. CV tests were carried out within the potential range of -0.6 to 0.6 V vs. Zn/Zn^{2+}, at a sweep rate of 1 mV·s^{-1}. The CV curves and relevant chronocoulometry curves of Zn//Ti coin cell with 1 m $Zn(OAc)_2$+31 m KOA electrolyte are shown in Fig. 3.3a and 3.3b, respectively. In the first CV cycle, the redox peaks are at 0.26 and -0.22 V vs. Zn/Zn^{2+} coupling with 82.1% CE derived from chronocoulometry curves, while the peaks shifted to 0.2 and -0.2 V versus Zn/Zn^{2+} in the second CV cycle and stayed at that position in the following cycles. This indicates that the Zn stripping/plating reaction is achieved in this mildly alkaline electrolyte [131]. Meanwhile, the CEs increase

103

from 91.2% in the second CV cycle to 99.0% in the 5th CV cycle, which demonstrates the feasibility and reversibility of Zn stripping/plating (Fig. 3.3b). To confirm the reversibility and stability of Zn in the 1 m $Zn(OAc)_2$+31 m KOAc electrolyte, Zn//Zn symmetric cell was made and tested for 200 cycles (ca. 2000 min) under galvanostatic condition with a current density of 5 $mA \cdot cm^{-2}$. In Fig. 3.3c, the charge/discharge curves are displayed with potential limitation of -0.2 to 0.2 V vs. Zn/Zn^{2+} according to the position of redox peaks on CV curves [131], and CE of every cycle is shown in its inset figure, in which the CE of the first cycle is 64.2% increasing to 99.1% in the 19th cycle. The CEs maintains around 99.0% in the following cycles until the 200th cycle (99.2% CE). This delivers the desired reversibility and stability. The average capacity for the capacity of Zn stripping/plating is about 0.8 $mAh \cdot cm^{-2}$ which is enough to assemble a full cell with our α-MnO_2-TiN/TiO_2 cathode (no more than 0.5 $mAh \cdot cm^{-2}$ capacity), while that Zn stripping/plating capacity is still considerable according to the previous reports [131, 218]. According to the previous report, Zn prefers to react with OH^- and form ZnO in strong alkaline environment [265]. However, the pH value of 1 m $Zn(OAc)_2$+31 m KOAc is only 9.76, which is regarded as a mild alkaline condition. To further investigate the reaction mechanism, the capacity limit of 2 $mAh \cdot cm^{-2}$ is set for cycling test on the Zn//Zn symmetric cell under various current densities from 0.5 (5 cycles with 2 activation cycles), 1 (5 cycles), 2 (5 cycles) to 5 (10 cycles) $mA \cdot cm^{-2}$ respectively with 94 h test time in total (Fig. 3.3d). After the symmetrical cell measurements, the tested Zn foils were characterized by SEM and XRD (Fig. 3.3d). No obvious dendrite was observed on Zn foil while the small peak of ZnO (202, ICDD: 01-075-1526) can be found, attributing to the possible slight reaction between Zn and OH^-, while the main reaction between the Zn and electrolyte should still be Zn stripping/depositing because of the limited amount of OH^- ions in this salt-concentrated electrolyte.
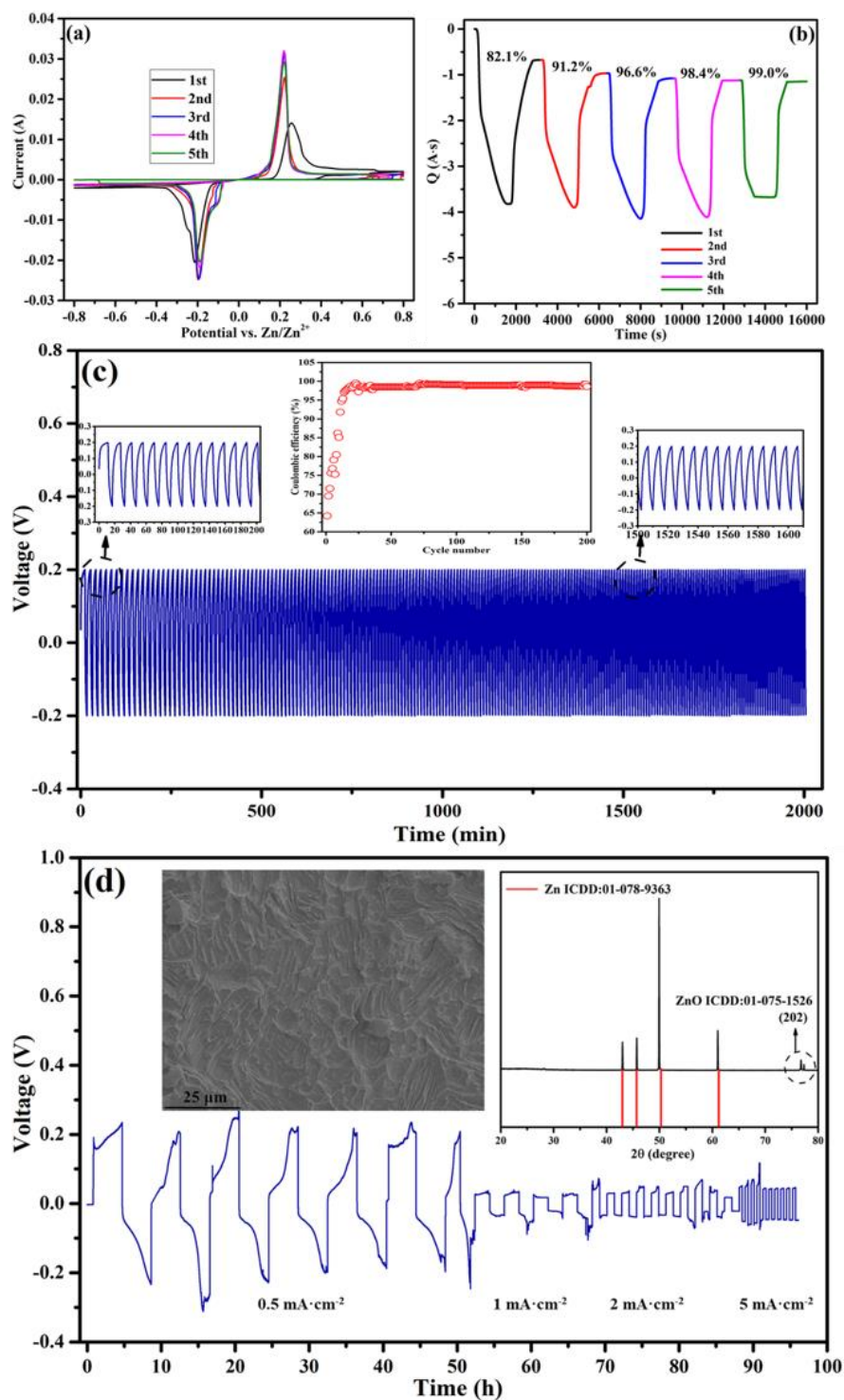
Fig. 3.3 (a) CV curves of Zn plating/stripping in Zn//Ti cell under 1 mV·s^{-1} sweep rate; (b) Chronocoulometry curves derived from the CV curves of that Zn//Ti coin cell; (c) Galvanostatic Zn stripping/plating in a Zn//Zn symmetrical cell under 5 mA·cm^{-2} current density with -0.2 to 0.2 voltage limitation; (d) Galvanostatic Zn stripping/plating in a Zn//Zn symmetrical cell under 0.5, 1, 2 and 5 mA·cm^{-2} current density with 2 mAh·cm^{-2} capacity limitation.

3.2.3 Cathode characterization and battery performance

In this study, MnO_2 was directly grown on a home-made TiN/TiO_2 porous substrate which has been utilized in LSBs with excellent redox stability [273]. The morphology of the as-prepared TiN/TiO_2 substrate is shown in Fig. 3.4a. It is composed of TiO_2 phase (ICDD: 03-065-1119) and TiN phase (ICDD: 04-069-8169) (Fig. 3.4b). XRD analysis on the deposited powders after hydrothermal reaction indicates α-MnO_2 (ICDD: 04-005-4884) was successfully grown on the TiN/TiO_2 porous substrate (Fig. 3.4c). The morphology and elements of MnO_2-TiN/TiO_2 cathode are characterized by SEM/EDX (Fig. 3.5). In Fig. 3.5a, the image with 50 μm resolution displays the morphology of nanosized MnO_2 particles on porous substrate whilst peaks for Ti, O, N, Mn and Si (caused by the conductive polymer film used to stick samples to the sample stage of SEM device), as exhibited in the inset EDX analysis. The particle size of this MnO_2 is less than 100 nm (Fig. 3.5 b). The corresponding element mappings are shown in Fig 3.5c-f for elements Mn, O, N and Ti, respectively. Element Mn is distributed in the same location as the nanoparticles while elements N and Ti are evenly distributed on the whole substrate.

The CV curves of both the Zn anode and MnO_2-TiN/TiO_2 cathode were collected respectively, which were recorded at a sweep rate of 1 mV·s^{-1} in a three-electrode cell separately. 1 m $Zn(OAc)_2$+31 m KOAc electrolyte was sued as the electrolyte, Ti foil as counter electrode, and Ag/AgCl as reference electrode. In the CV curves of Fig. 3.6a, both Zn anode and MnO_2-TiN/TiO_2 cathode, exhibit a pair of redox peaks happening at ~-0.95 and ~-1.1 V vs. Ag/AgCl (~0.03 and ~-0.12 V vs. Zn/Zn^{2+}), representing for the Zn plating/striping [173]. Meanwhile, the other pair of redox peaks at ~0.6 and ~0.3 V vs. Ag/AgCl (~1.58 and ~1.28 vs. Zn/Zn^{2+}) is due to the reversible conversion between MnO_2 and MnOOH caused by the proton insertion in the alkaline environment [172, 266], which will be proven by charge/discharge curves and material characterization on the cathode after electrochemical measurements. For the full cell test, the cyclic charge/discharge test was carried out under galvanostatic condition with 100 mA·g^{-1} current density, within the potential range between 2.0 and 0.8 V vs Zn/Zn^{2+} (Fig. 3.6b). Its specific discharge capacity (based on the 1.2 mg active matter) in the first cycle is

31(0)/30(5) mAh·g^{-1} with 99.(0) % CE which is further improved to 99.(9)% after the 14th cycle and maintained until the 340th cycle, after which it slowly decreased to ~ 98.(0)% for the last 260 cycles. The capacity is significantly higher than the theoretical capacity of 308 mAh g^{-1} for MnO_2, based on the molecular weight of MnO_2 and one electron transfer [174]. This extra storage capacity could be related to the nanosized α-MnO_2 cathode prepared in this study. This kind of interfacial ion storage mechanism has been observed in LIBs [274, 275]. However, it cannot be ruled out that a tiny amount of Zn^{2+} may also react with MnO_2 to realise two electron transfer leading to higher capacity. The specific discharge capacity of the 600th cycle is 24(8)/24(3) mAh·g^{-1} with 98.(2)% CE, which displays 79.(7)% capacity retention, compared to the capacity of the first cycle. The slightly decreased CE after the 340th cycle could be related to side reactions which need further investigation, however that was still good enough under high working voltage with 600 charge/discharge cycles. The relevant charge-discharge curves of the cyclic test are shown in Fig. 3.6c. The corresponding capacity is consistent with the values shown in Fig. 3.6b. The charge/discharge capacity areas are ~1.4-~1.7 and ~1.2-~1.55 V vs. Zn/Zn^{2+} respectively, which are consistent with redox couple of CV curve on MnO_2-TiN/TiO$_2$ cathode shown in Fig. 3.6a. This is believed to be due to the proton insertion in MnO_2 electrode [276]. While the inclined capacity areas of relevant charge/discharge curves indicate that capacitive behaviour cannot be eliminated. That requires kinetic CV test to tell contribution ratio of battery behaviour and capacitive behaviour, respectively, which will be investigated in chapter 7. The corresponding energy density is calculated via integrating the discharge curves in Fig. 4c, which is 36(9), 36(4), 36(1), 35(2), 32(1), 30(2) and 27(8) Wh·kg^{-1} for first, 5th, 10th, 20th, 100th, 200th, 400th and 600th charge-discharge cycles, respectively. In this work, the cell voltage was further extended to 2.0 V, taking advantage of the wide electrochemical stability window of the salt-concentrated 1 m $Zn(OAc)_2$+31 m KOAc used as the electrolyte. The energy density of that cell was therefore improved to 36(9) Wh·kg^{-1} in the first cycle, which is comparable to some recently published papers about Zn/MnO_2 batteries in alkaline, neutral and mild acid environments based on MnO_2 cathodes, [172, 174, 277-279] In reported works, the typical discharge/charge voltage range is 1.8/1.6 V-1.0 V for aqueous Zn-MnO_2 batteries with proton insertion

mechanism [172, 278, 279]. Taking the advantage of the wide ESW of the salt-concentrated electrolyte, our Zn//MnO$_2$ battery still exhibits good stability at a discharge-charge voltage of 2.0 V to 0.8 V. Compared to the reported aqueous Zn//MnO$_2$ batteries, this is a kind of over-charge/discharge. From this point of view, aqueous Zn//MnO$_2$ batteries based on this electrolyte displayed high stability.
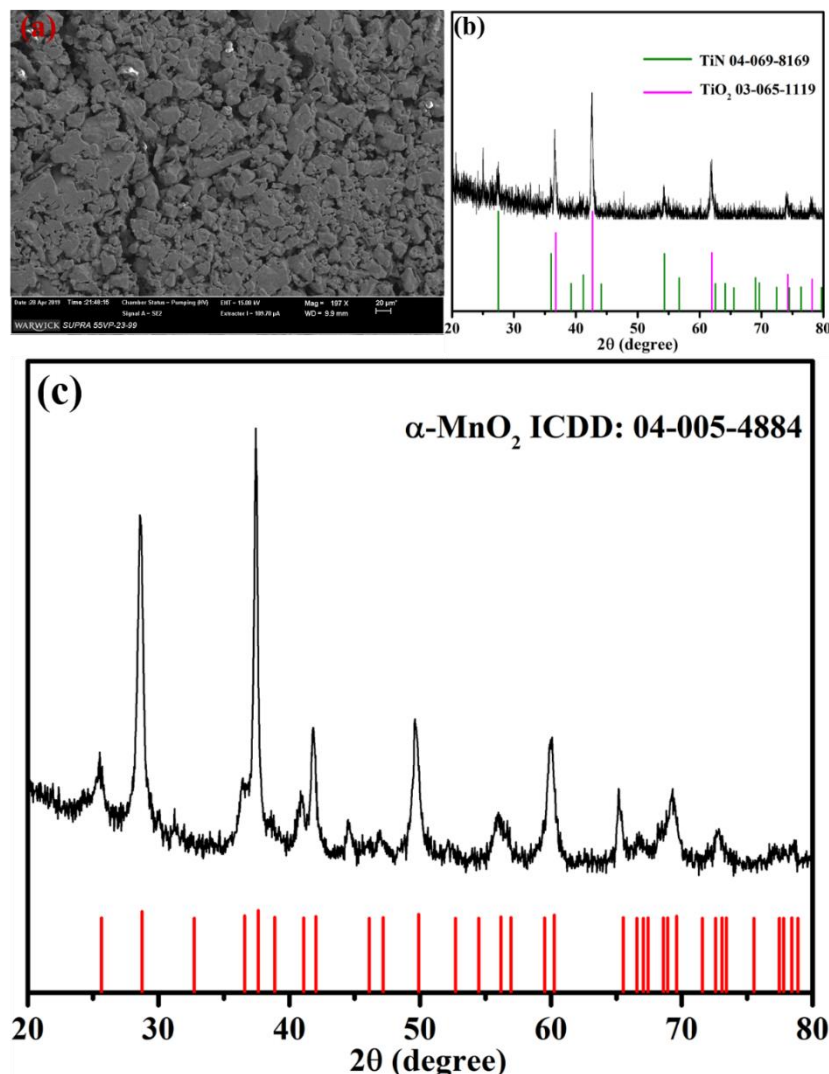
Fig. 3.4 (a) SEM image of TiN/TiO$_2$ porous substrate; (b) XRD analysis on TiN/TiO$_2$ porous substrate; (c) XRD analysis on α-MnO$_2$ nanosized particles.

The rate performance of the Zn//MnO$_2$ coin cell was tested under current densities of 100, 200, 400, 800, 1600 mA·g^{-1} respectively. Accordingly, the specific discharge capacity of the last cycle for each current density was determined as 24(0)/23(8), 22(0)/21(7), 19(1)/18(8), 16(0)/15(7) and 12(1)/11(7) mAh·g^{-1} respectively (Fig. 3.6d). It has been reported that, at mild acidic conditions, the

stability of Zn//MnO$_2$ battery at low rate is poor because of the irreversible conversion reaction at ~ 1.26 V, whilst the battery is much more stable at high rate [278]. In our Zn//MnO$_2$ coin cell, the electrolyte is a weak basic, the cycling stability of the battery at a current density of 100 mA·g^{-1} (~ C/3) is still quite good (Fig. 3.6b). This may be related to the different reaction mechanisms in different reaction environments, which are discussed below.
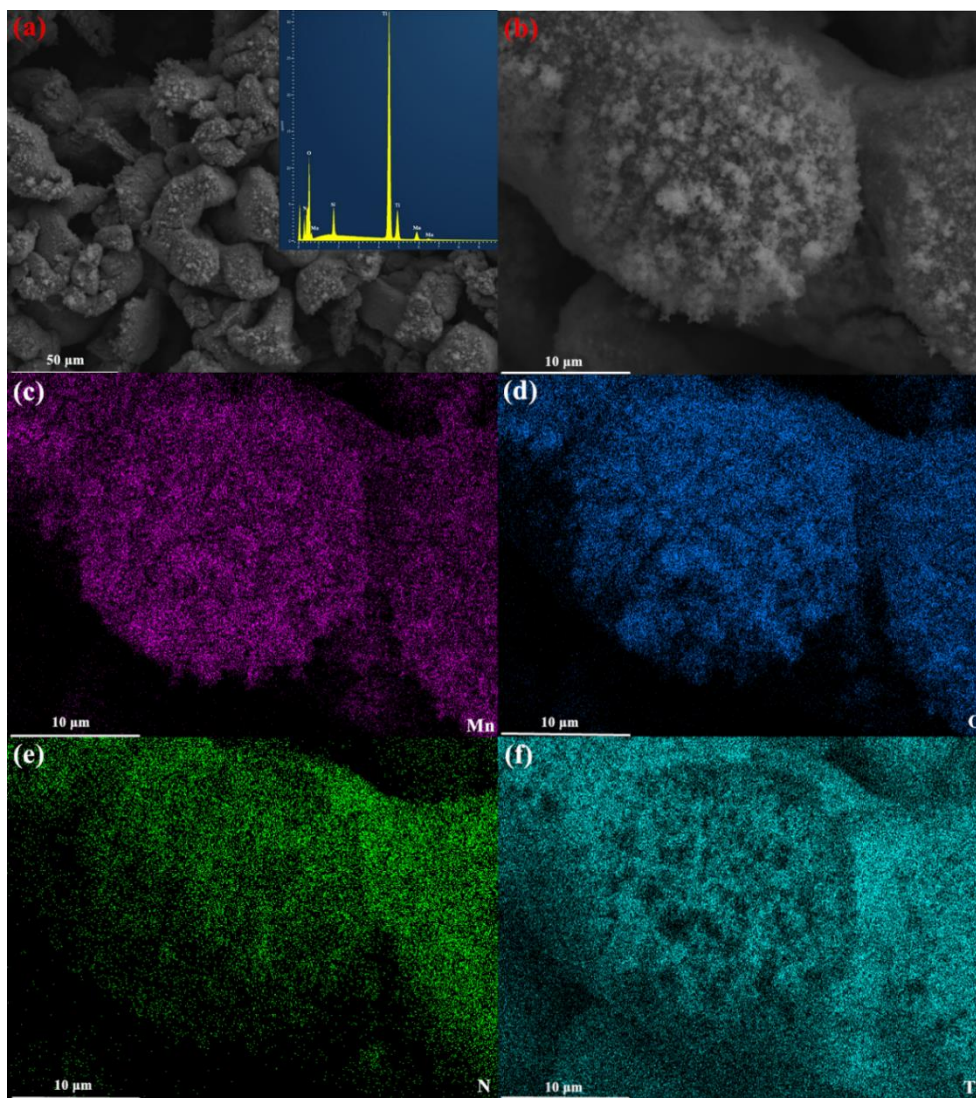
Fig. 3.5 (a) SEM image of self-supported MnO$_2$-TiN/TiO$_2$ cathode under 50 μm resolution with EDX element analysis as inset. (b) SEM images of self-supported MnO$_2$-TiN/TiO$_2$ cathode under 10 μm resolution and according EDX mappings of (c) Mn, (d) O and (e) N and (f) Ti elements.
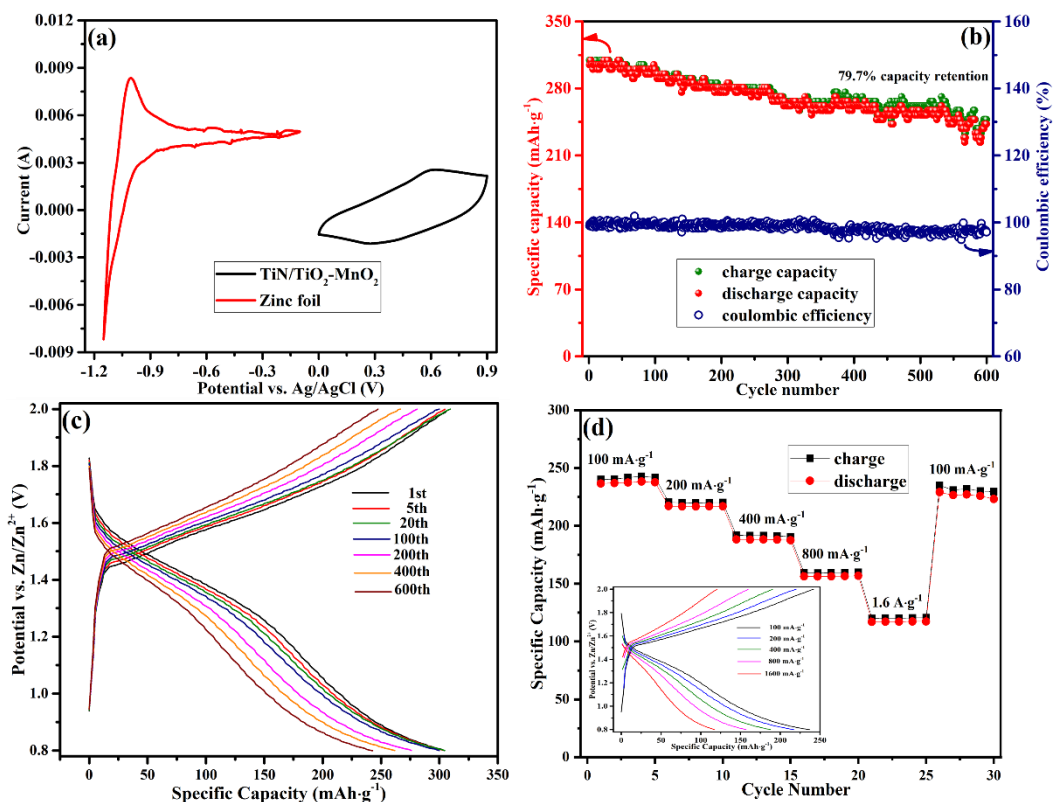
Fig. 3.6 (a) CV curves of Zn and MnO$_2$-TiN/TiO$_2$ cathode with Ti foil as counter electrode and Ag/AgCl as reference; (b) GCD cycling of Zn//MnO$_2$ battery under 100 mA·g^{-1} current density between 0.8 and 2.0 vs. Zn/Zn^{2+} within 600 cycles; (c) Charge/discharge curves of Zn//MnO$_2$ battery between 0.8 and 2.0 V vs. Zn/Zn^{2+}. (d) Rate performance of Zn//MnO$_2$ battery under various current density with the according charge/discharge curves shown in the inset.

3.2.4 Working mechanism of cathode and post-mortem analyses

To investigate the reaction mechanism of the cathode in 1 m Zn(OAc)$_2$+31 m KOAc electrolyte further, 31 m KOAc electrolyte adjusted by acetic acid to have similar pH value with that of 1 m Zn(OAc)$_2$+31 m KOAc electrolyte, was utilized as electrolyte in the three-electrode system with CV sweep range of 0.2 to 1.1 V. As shown in Fig. 3.7a, the redox couple around 0.6/0.3 V vs. Ag/AgCl, which coincides with the redox couple of MnO$_2$-TiN/TiO$_2$ cathode in the 1 m Zn(OAc)$_2$+31 m KOAc electrolyte (Fig. 3.6a). The presence or absence of Zn^{2+} has little effects on the redox reaction at the MnO$_2$-TiN/TiO$_2$ cathode, indicating that Zn^{2+} may not participate in the reaction of MnO$_2$-TiN/TiO$_2$ cathode in our salt-concentrated electrolyte. Therefore, Zn^{2+} takes part in the Zn plating/stripping

110

reaction on the anode side while H_2O in the aqueous electrolyte is the source of proton for insertion in MnO_2 with the generation or depletion of OH^- ions on cathode side. Unlike the traditional 'rocking-chair' cathode for LiBs which works based on the migration of Li^+ between cathode and anode, this $Zn//MnO_2$ battery can be regarded as a HiB, while the total concentration of mixed ions should be fixed to ensure the charge neutrality of the electrolytes [280]. After the electrochemical tests, both the cathode and anode were taken apart for post-mortem analyses. The FTIR spectra of the MnO_2-TiN/TiO$_2$ cathodes before and after the cycling are shown in Fig. 3.7b. The additional peaks at 645 and 1620 cm$^-$ ^{1} on the spectrum for the cathode after-cycling tests are attributed to the bands of the Mn-O vibrations and OH bending mode, respectively, indicating the possible presence of MnOOH [281, 282]. However, the typical peaks of MnOOH at round 1100, 1140 and 1180 cm^{-1} standing for γ-OH, δ-2-OH and δ-1-OH bending modes cannot be observed in Fig. 3.7b [281, 282].

Meanwhile, WAXS was employed to detect the phase transformation of that cathode before and after charge-discharge reaction (Fig. 3.7c). The groutite MnOOH (ICDD: 04-010-4787) [283] was detected although the signal was quite weak. This indicates that, in our aqueous $Zn//MnO_2$ battery, the cathode reaction on discharge is [172],

$$MnO_2 + H_2O + e^- \leftrightarrow MnOOH + OH^- \tag{3.2}$$
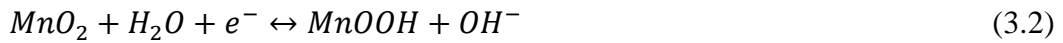
However, in the real process, it is intercalation of protons into the MnO_2 to form MnOOH, even the strong alkaline solution such as mixed KOH-LiOH was used as the electrolyte [266]. As the proton comes from active water, total mass of active electrode and electrolyte is employed as well for calculating energy density. The active mass of water and Zn participated in reaction can be estimated based on their reaction mechanism as:

$$m_{active\ water} = m_{MnO_2} \times \frac{M_{H_2O}}{M_{MnO_2}} \tag{3.3}$$

$$m_{active\ Zn} = m_{MnO_2} \times \frac{M_{Zn}}{M_{MnO_2}}/2 \tag{3.4}$$

Derived from these, the relevant energy density can be calculated as 23(3) Wh·kg^{-1}.
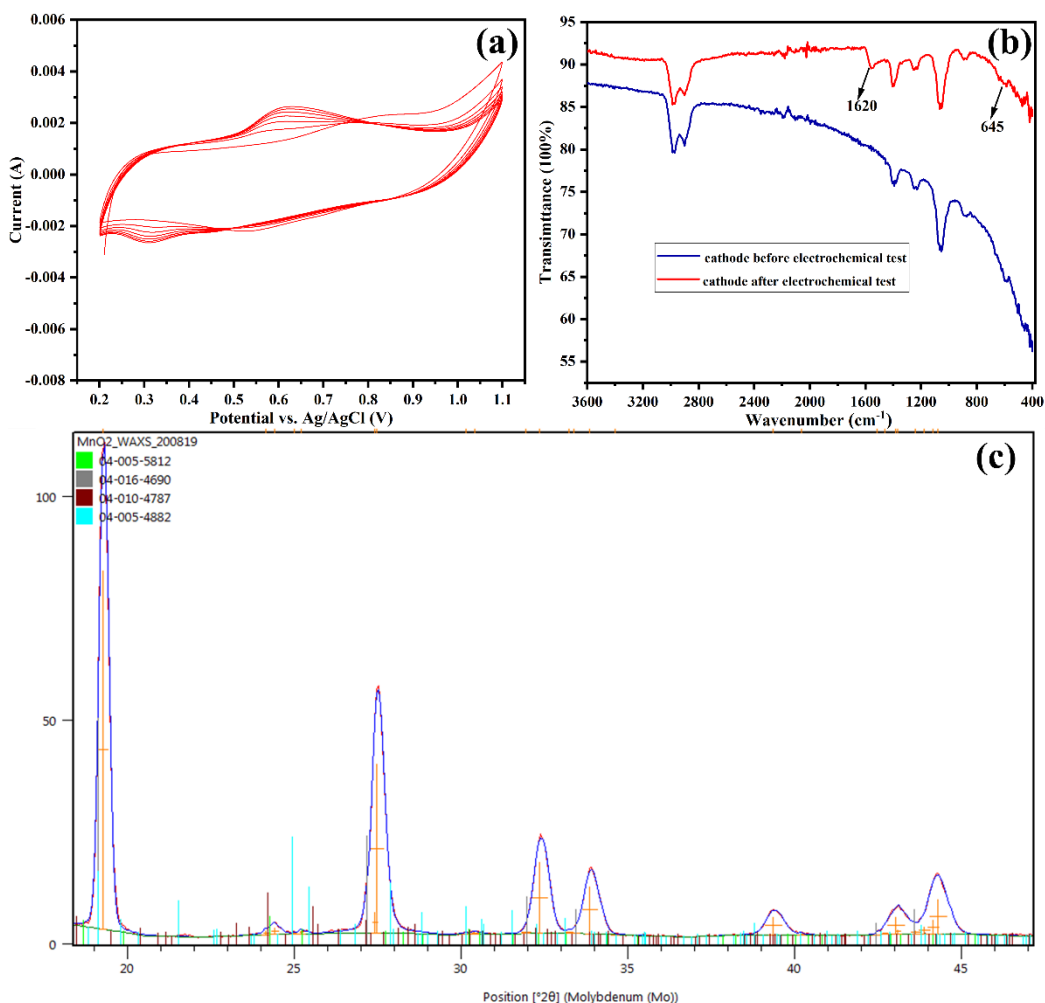
Fig. 3.7 (a) CV curves of MnO$_2$-TiN/TiO$_2$ cathode in 31 m KOAc salt-concentrated electrolyte in three-electrode cell under 1 mV·s^{-1} sweep rate within 5 cycles; (b) FTIR spectra of MnO$_2$-TiN/TiO$_2$ cathode before and after GCD cycling; (c) WAXS analysis on MnO$_2$-TiN/TiO$_2$ cathode after GCD cycling.

XRD spectra of Zn anodes before and after cycling are compared (Fig. 3.8a). No obvious difference in morphology was observed. For Zn anode before and after the test, it is composed of Zn (ICDD: 01-078-9363) with a couple of weak peaks of ZnO (ICDD: 04-020-0364) due to the slow oxidation of Zn anode under atomphere or slight reaction with OH$^-$. The cross-section SEM image of Zn anode after cycling is shown in Fig. 3.8b. The SEM image and corresponding layer mapping of Zn and O elements are shown in Fig. 3.8c and 3.8d respectively.

Dendrite was not observed on the Zn anode after the cyclic test. For rechargeable batteries with metal anodes, dendrites induced by the uneven metal deposition can lead to thermal runaway and explosion hazards, which may limit their applications. The use of salt-concentrated 1 m $Zn(OAc)_2$+31 m KOAc electrolyte in our Zn//MnO_2 battery enhances the threshold of critical current density for cations depletion in the electrolyte thus suppresses the formation of zinc dendrites [284].
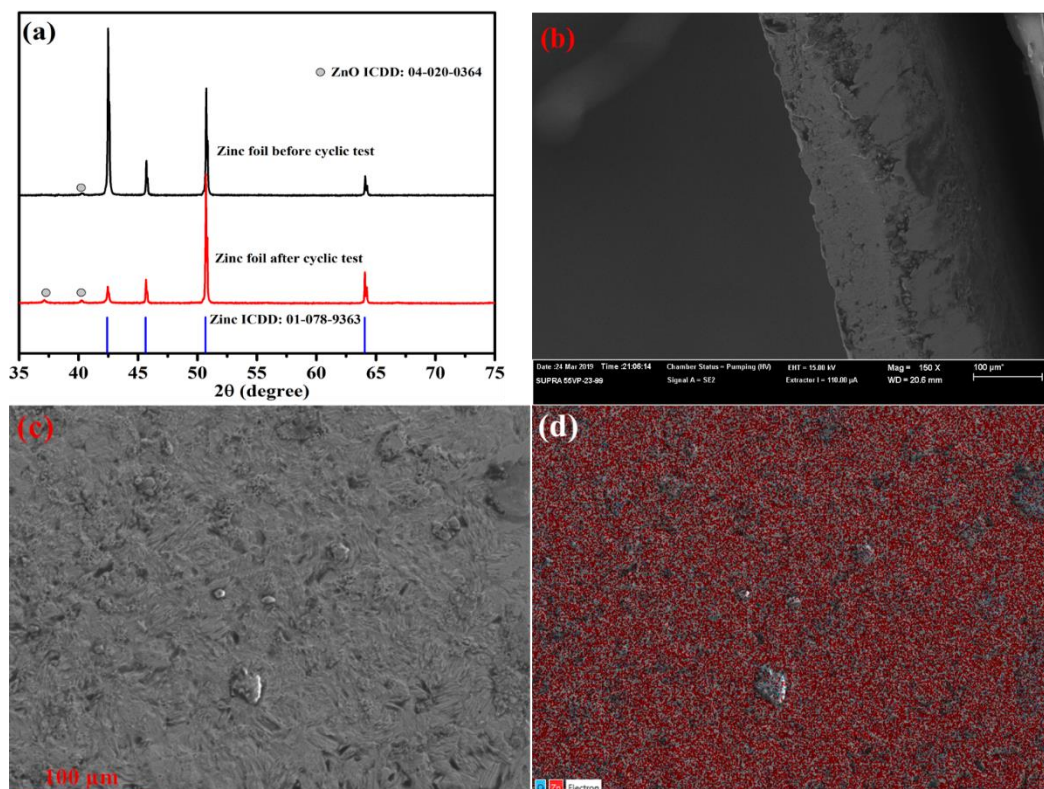
Fig. 3.8 (a) XRD on the Zn metal anodes before and after GCD cycling; (b) Cross-section SEM image of Zn metal anode after GCD cycling; (c) SEM image on the surface and (d) corresponding layer mapping of Zn and O elements on Zn metal anode after GCD cycling.

3.3 Conclusion

In this study, a new salt-concentrated 1 m $Zn(OAc)_2$+31 m KOAc electrolyte has been developed. It has an ESW of 3.4 V. At RT, the mixed ionic conductivity of 1 m $Zn(OAc)_2$+31 m KOAc aqueous solution is 2.96×10^{-2} S·cm^{-1}, while the ionic conductivity of Zn^{2+} measured by current interrupt method is 7.80×10^{-3} S·cm^{-1}, which is high enough to be used as the electrolyte for batteries. Compared with

other expensive organic salts, the acetate concentrated electrolyte has low cost and reduced toxicity. LSV, Tafel curves, EIS, FTIR and pH value tests were employed to investigate the properties of salt-concentrated 1 m $Zn(OAc)_2$+31 m KOAc electrolyte. A CR2016 coin cell using 1 m $Zn(OAc)_2$+31 m KOAc electrolyte, Zn metal anode and MnO_2-TiN/TiO_2 cathode was assembled. The battery can be charged to 2.0 V, taking advantage of the wide ESW of electrolyte. The reaction and storage mechanisms of both anode and cathode were investigated in detail. The reaction mechanism of the investigated $Zn//MnO_2$ battery is a hybrid one with both Zn^{2+} and proton insertion involved due to the mild alkaline environment of this electrolyte. The $Zn//MnO_2$ battery is characterized by cyclic and rate performance test, which delivers desired stability, energy density and rate capability. Dendrite-free Zn metal anode is confirmed after cycling, attributing to the improved threshold critical current density for cations depleting in the new acetate-based salt-concentrated electrolyte. While, through the charge/discharge curves, the capacitive behaviour cannot be eliminated, which will be investigated detailly in following chapters. In summary, the $Zn//MnO_2$ battery based on acetate concentrated electrolyte demonstrates excellent stability among the ones with same proton insertion mechanism. It can be cycled to 600 times with working voltage range of 0.8-2.0 V, the normal up limit of which is 1.8 V. Although its cyclic life and energy density still have room for enhancement, compared with $Zn//MnO_2$ batteries with different electrode mechanisms in Fig. 1.3, the acetate concentrated electrolyte still play the protective function with wide ESW under overcharged state, showing the practicability in real application.

CHAPTER 4   Cation-size effect in alkali-acetate concentrated electrolytes for aqueous rechargeable lithium-ion batteries

4.1 Abstract

In this chapter, a systematic investigation on the ESWs of alkali acetates was carried out, with the exception of rubidium and francium, which are regarded as rare and even radioactive elements [285]. The aqueous electrolytes consisting of different alkali metal acetates were investigated at the same concentration. Amongst these alkali metal acetates, caesium acetate (CsOAc) was demonstrated as the optimum and was therefore prepared as a room-temperature saturated aqueous solution (45 m), which exhibited an ESW of 3.4 V. Although Cs is not an abundant resource, employing CsOAc in aqueous electrolytes is still affordable in terms of cost, as seen when comparing the price of CsOAc [286] to that of popularly used LiTFSI in WiSE [287]. When 45 m CsOAc was further blended with 7 m LiOAc as a mixed-cation acetate concentrated electrolyte, a ESW of 2.95 V was achieved, which can be further widened to 3.3 V under sweep rate of 50 mV·s^{-1}. Finally, this 45 m CsOAc+7 m LiOAc WiBSE was assembled with a Ti mesh-VO$_2$ nanobelt anode (VO$_2$ loading ~2.0 mg·cm^{-2}) and a Ti mesh-LiNi$_{0.5}$Mn$_{1.5}$O$_4$ (LiNi$_{0.5}$Mn$_{1.5}$O$_4$ loading ~3.0 mg·cm^{-2}) cathode to form a full ARLiB with a working voltage of 2.5 V. This full cell delivered its highest specific discharge capacity of 68.(1) mAh·g^{-1} (calculated on 2.1 mg anode and 3.6 mg cathode active matter) under 1 C (1 C=110 mA·g^{-1}), while a desired cyclic stability with 86.(5)% capacity retention after 1200 charge/discharge cycles was displayed under a 4 C rate with about 99.(0)% CE even reaching near 10(0)% at certain cycles. It is worth noting that the working mechanism may be a hybrid charge storage one, comprised by both battery behaviour and capacitive behaviour. And the capacitive behaviour here probably is extrinsic pseudocapacitance, enhanced by nanosized electrodes [288, 289], which will be studied in the future.

4.2 Results and discussion

4.2.1 Property comparison of various acetate concentrated electrolytes

To investigate the ESWs of LiOAc, NaOAc, KOAc and CsOAc aqueous solutions, all the acetate aqueous solutions were prepared at the same concentration (7 m was chosen as it is the concentration for RT saturated LiOAc aqueous solution and LiOAc has the lowest solubility among the investigated acetates). As shown in Fig. 4.1a, the ESWs of those acetate-based electrolytes were obtained by LSV at a sweep rate of 1 mV·s^{-1}. Meanwhile, in this work, the onset of the accelerated current increasing in the LSV curves is determined as the limit of ESW [39]. The dash lines in Fig. 4.1a, d and Fig. 4.2b indicate the onsets for HER/OER (limits of ESWs). As shown in Fig. 4.1a, the ESW is 2.3 V (-1.0 to 1.3 V vs. Ag/AgCl) for 7 m LiOAc; 2.2 V (-1.0 to 1.2 V vs. Ag/AgCl) for 7 m NaOAc, 2.5 V (-1.2 to 1.3 V vs. Ag/AgCl) for 7 m KOAc and 2.5 V (-1.2 to 1.3 V vs. Ag/AgCl) for 7 m CsOAc. The main tendency is that the large-size cations (CsOAc and KOAc) show wider ESW than that of small-size ones (LiOAc and NaOAc). These values are listed in Table 4.1 for comparison. Normally, the explanation regarding wider stability window is related to the activity of water [39, 52, 290], while according to one previous report, a local structure of intimate Li^{+}-water interaction will be raised at high salt concentrations in the Li-ion aqueous electrolytes, generating (Li^{+}(H$_2$O)$_2$)n polymer-like chains and expanding ESWs [194]. However, to the best of our knowledge, the effect of cation size on the polymer-like chains has not been studied before. Normally, in the dilute aqueous solutions of alkali metal acetates, the larger radius of cations may lead to weaker interaction between the cations and water molecules [291], whereas in high concentration solutions of alkali metal acetates, the interaction between cations and water molecules is analogous to the weak covalent interaction which may be enhanced with the increasing radius and mass of cations [292, 293]. The cation in the polymer-like chains is similar to the central atom in polymers, which can weaken the inner interaction of branch chains like the H bond in water through enhancing weak covalent interactions between the central atom and branch chain [294]. Therefore, the ordered free H-bond network is changed into relatively disordered one with aggregation of H bond, and then supress the HER/OER kinetically and thermodynamically [295].

To demonstrate the relationship between cation, interaction of cation and water molecule, and corresponding ESW, FTIR and Raman spectra were carried out. The results are shown in Fig. 4.1b and 4.1c respectively. In the FTIR results shown in Fig. 4.1b, for LiOAc to CsOAc, the peaks at wavenumbers ranging from 3320 to 3390 cm^{-1} corresponding to O_H-H stretching vibrations are decreased, which are attributed to the aggregation of water molecules and H bonding of H_2O [131]. To further demonstrate a higher strength of the polymer-like chains (the interaction between cations water molecules is analogous to polymer chains [194]) from LiOAc to CsOAc aqueous solution, the corresponding Raman spectra were collected in the range of 400 to 4000 cm^{-1} (Fig. 4.1c). The increased peak intensity from LiOAc to CsOAc aqueous solutions appeared at the Raman shift ranges, from 920 to 940, 1420 to 1430 and 2950 to 2970 cm^{-1}, indicating ν (C-C), ν_s (COO) and ν_1 (C-H) stretching respectively [296], whereas the peak standing for O_H-H bond (3320 to 3500 cm^{-1}) is decreased in intensity from LiOAc to CsOAc aqueous solution. Moreover, the peak moves to higher Raman shift from LiOAc to CsOAc aqueous solution, which is caused by the change of peak area ratio between free and donor-acceptor O_H-H bond (the peak area of donor-acceptor O_H-H bond is increased) [194, 297]. As the concentrations and anions of these aqueous solutions are totally same, these changes are introduced by the cation difference. All the observed transitions of Raman spectra indicate a waned free O_H-H bond and enhanced interaction between cation and water molecule, thus break the free H-bond network [296]. It should be noted that, at RT, the solubility of acetates in water increases from LiOAc to CsOAc [298]. At RT, the saturated concentration is roughly 7 m for LiOAc, 13 m for NaOAc, 31m for KOAc and 45 m for CsOAc respectively, amongst which, only 31 m KOAc and 45 m CsOAc meet the definition of WiSE [39]. The ESWs of these RT-saturated aqueous solutions were studied by LSV. As shown in Figure 4.1d, the ESWs under a sweep rate of 1 mV·s^{-1} can be defined as 2.3 V (-1 to 1.3 V vs. Ag/AgCl) for 7 m LiOAc, 2.6 V (-1.15 to 1.45 V vs. Ag/AgCl) for 13 m NaOAc, 2.95 V (-1.25 to 1.7 V vs. Ag/AgCl) for 31m KOAc and 3.4 V (-1.6 to 1.8 V vs. Ag/AgCl) for 45 m CsOAc. The optimum ESW of 3.4 V is obtained in 45m CsOAc one.
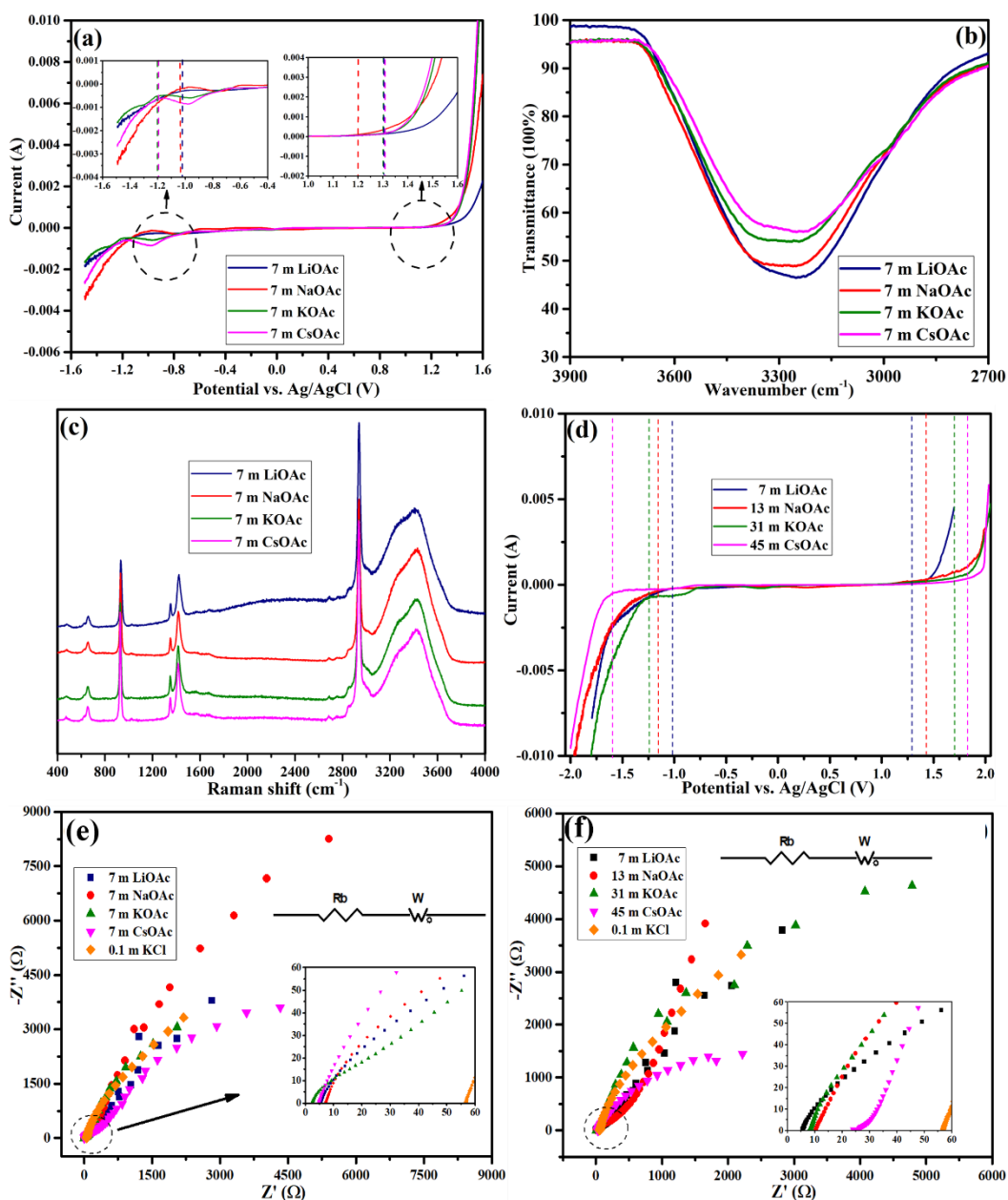
Fig. 4.1 (a) ESW test on 7 m acetate-based aqueous electrolytes with various cations under 1 mV·s^{-1}; (b) FTIR spectra of 7 m acetate-based aqueous electrolytes with various cations; (c) Raman spectra of 7 m acetate-based aqueous electrolytes with various cations; (d) ESW test on 7 m LiOAc, 13 m NaOAc, 31 m KOAc and 45 m CsOAc aqueous electrolytes under 1 mV·s^{-1}; (e) EIS plot of 7 m acetate-based aqueous electrolytes with various cations; (f) EIS plot of 7 m LiOAc, 13 m NaOAc, 31 m KOAc and 45 m CsOAc aqueous electrolytes.

Besides wide ESWs, sufficient ionic conductivity is an essential requirement for battery electrolytes. The ionic conductivity of all the mentioned acetate based aqueous electrolytes was measured through EIS, using 0.1 M KCl aqueous solution

(conductivity 1.28×10^{-2} S·cm^{-1} at RT) as the calibration solution [271]. Based on the EIS data shown in Fig. 4.1e, an equivalent circuit with a bulk resistance (R_b) of electrolyte connected with a Warburg impedance (Z_w) in series is proposed to fit the relevant EIS result. Ti foil was utilized as the electrodes for the EIS test, functioning as blocking electrodes for all the ions in the acetate system, thus no ionic charge transfer occurred and only the signals of R_b and Z_w were detected. The ionic conductivity of all these acetate solutions is higher than 10^{-2} S·cm^{-1}, which is not negatively affected by the high salt concentration.

4.2.2 Property of mixed Cs-Li acetate concentrated electrolytes

Considering the wide ESWs among the studied acetates discussed above, 45 m CsOAc electrolyte was chosen to be mixed with LiOAc to prepare Cs-Li acetate concentrated electrolytes, which can be used for ARLiBs. The FTIR of 7, 14, 28, 45 m CsOAc, 45 m CsOAc + 3 m LiOAc and 45 m CsOAc+7 m LiOAc aqueous solutions are shown in Fig. 4.2a. The peaks within wavenumber range of 3100-3600 cm^{-1} in Fig. 4.2a are decreased in intensity when the CsOAc concentration is increased (especially when the CsOAc concentration is above 28 m when it can then be regarded as WiSE), indicating the gradual phase out of O$_H$-H bonds. Accordingly, at a sweep rate of 1 mV·s^{-1}, the ESWs increased from 2.5 V (-1.2 to 1.3 V vs. Ag/AgCl) to 3.4 V (-1.6 to 1.8 V vs. Ag/AgCl) when the concentration of CsOAc increased from 7 m to 45 m (Fig. 4.2b). A slight shrink in ESW was observed for 3 m LiOAc + 45 m CsOAc WiBSE and 7 m LiOAc+45 m CsOAc WiBSE, compared to that of 45 m CsOAc. It is 2.8 V (-1.3 to 1.5 V vs Ag/AgCl) for 3 m LiOAc + 45 m CsOAc WiBSE, and 2.95 V (-1.35 to 1.6 V vs. Ag/AgCl) for 7 m LiOAc+45 m CsOAc WiBSE. The decrease in ESW of WiBSE has previously been observed in 32 m KOAc + 8 m LiOAc electrolyte, which was considered to be the limitation of LiOAc ESW [187]. This may be due to the same reason for the decreased ESW of 7 m LiOAc+45 m CsOAc WiBSE observed in our study. Mixing two types of salt together in order to widen the ESW furthermore only occurs in the eutectic systems like LiTFSI and LiBETI [299].
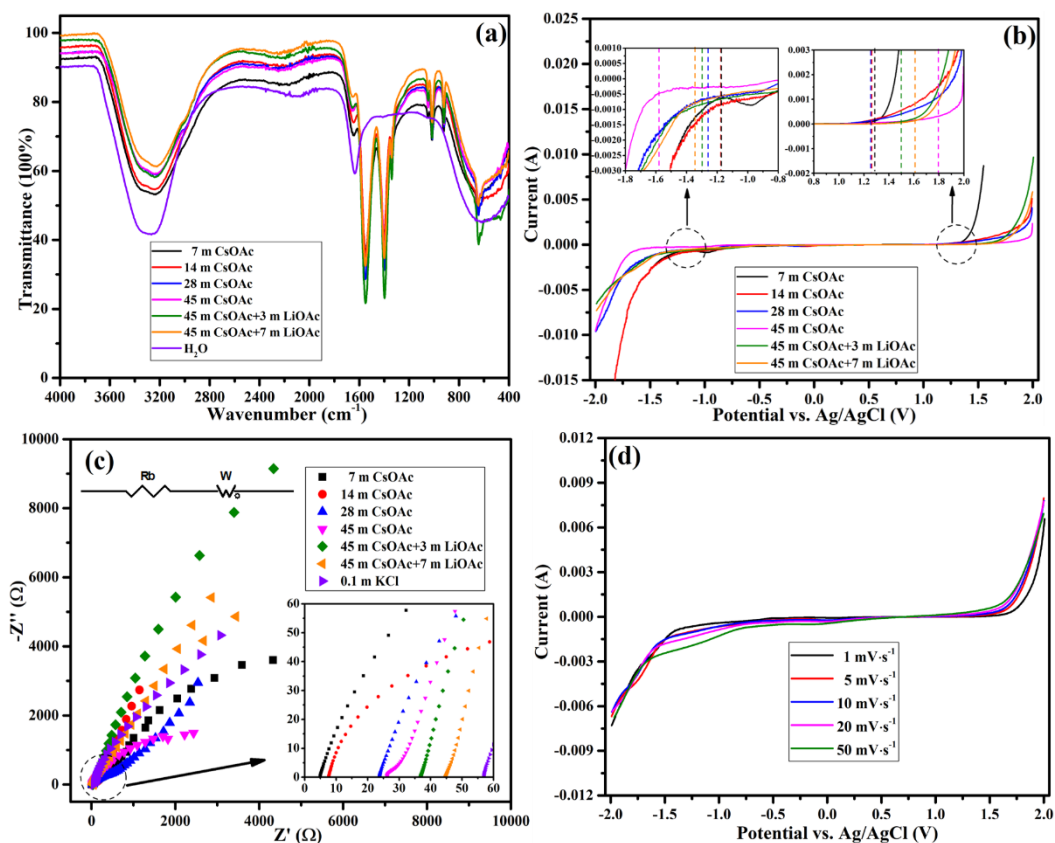
Fig. 4.2 (a) FTIR spectra of CsOAc-based aqueous electrolytes with various concentrations; (b) ESW test on CsOAc-based aqueous electrolytes with various concentrations under 1 mV·s^{-1}; (c) EIS plots of CsOAc-based aqueous electrolytes with various concentrations; (d) ESW test on 45 m CsOAc+7 m LiOAc electrolyte under different sweep rates from 1 to 50 mV·s^{-1}.

The corresponding ionic conductivity of CsOAc-based aqueous electrolytes with various concentrations was studied by EIS as well, in the same set-up using the same geometric factor and under the same ambient conditions. The EIS plots and equivalent circuit of one bulk resistance (R$_b$) of electrolyte connected with one Warburg impedance (Z$_w$) in series are displayed in Fig. 4.2c. The corresponding ionic conductivity is listed in Table 4.1. It is obvious that, the ionic conductivity decreases with increased concentration due to enhanced viscosity and polymer-like chains [194, 272]. The ionic conductivity of 7 m LiOAc+45 m CsOAc is 1.98×10^{-2} S·cm^{-1} at RT. In the work of Cui and Bao groups, the viscosity of 27 m KOAc and 32 m KOAc+8 m LiOAc electrolytes were tested as 32 and 374 mPa·s^{-1}, respectively. The higher concentration and bigger size of hydrated molecules will generate the higher viscosity of liquid electrolytes, hence the viscosity of 45

m CsOAc+7 m KOAc and 45 m CsOAc is envisaged to be higher than that of 32 m KOAc+8 m LiOAc and 27 m KOAc respectively. Meanwhile, there are interactions between various hydrated molecules, which will raise the viscosity as well, that is the reason why the viscosity of 32 m KOAc+8 m LiOAc is much higher than that of 27 m KOAc in the previous report [187]. And it is expected that the viscosity of 45 m CsOAc+7 m KOAc will be higher than that of 45 m CsOAc, which will be experimentally verified in the future.

Table 4.1 The summary of properties (ESW and ionic conductivity) of different electrolytes.

Samples	Stability potential (vs. Ag/AgCl) under 1 mV·s^{-1} (V)	ESW under 1 mV·s^{-1} (V)	Conductivity (S·cm^{-1})
7 m LiOAc	-1.0 to 1.3	2.3	1.30×10^{-1}
7 m NaOAc	-1.0 to 1.2	2.2	9.81×10^{-2}
13 m NaOAc	-1.15 to 1.45	2.6	2.32×10^{-1}
7 m KOAc	-1.2 to 1.3	2.5	7.10×10^{-2}
31 m KOAc	-1.25 to 1.7	2.95	8.99×10^{-2}
7 m CsOAc	-1.2 to 1.3	2.5	1.49×10^{-1}
14 m CsOAc	-1.25 to 1.3	2.55	9.42×10^{-2}
28 m CsOAc	-1.35 to 1.3	2.65	4.03×10^{-2}
45 m CsOAc	-1.6 to 1.8	3.4	3.06×10^{-2}
45 m CsOAc+3 m	-1.3 to 1.5	2.8	2.51×10^{-2}
45 m CsOAc+7 m	-1.35 to 1.6	2.95	1.98×10^{-2}

Following the physiochemical properties, the effect of desired rate capability on the ESWs of 45 m CsOAc+7 m LiOAc WiBSE is demonstrated by LSV test under sweep rates ranging from 1 to 50 mV·s^{-1} (Fig. 4.2d), correlated to charge/discharge rates of 0.9 to 45 C. The OER side remains basically unchanged whilst there is a slight difference in the HER side (even raised from 1.35 to 1.7 V vs. Ag/AgCl responding to scanning rates from 1 to 50 mV·s^{-1}) indicating excellent rate performance of this WiBSE. It is anticipated that good rate performance of the full cell can be achieved. At a sweep rate of 50 mV s^{-1}, the ESW extends to 3.3 V (Fig. 4.2d). The increased ESW at higher sweep rate may be caused by the increased over-potential of OER and HER, which needs further investigation.

4.2.3 Electrode material characterization and battery performance

Among all the investigated aqueous electrolytes, 45 m CsOAc + 7 m LiOAc WiBSE was selected as the electrolyte for $VO_2//LiNi_{0.5}Mn_{1.5}O_4$ ARLiBs because of the wide ESW and the capability of Li-ion transportation. In this research, nanobelt VO_2 (B) with theoretical capacity of 320 mAh·g^{-1} is used as the anode [300, 301]. Whilst, $LiNi_{0.5}Mn_{1.5}O_4$ hollow microspheres are synthesized and used as the cathode to overcome the limit of the bulk material and ameliorate the rate capability of $LiNi_{0.5}Mn_{1.5}O_4$, thereby improving the performance of the full cell [247, 302]. The phase and morphology of both electrode materials are characterized by XRD (Fig. 4.3) and SEM/EDX (Fig. 4.4). In the XRD plot of the cathode and anode, the phases of $LiNi_{0.5}Mn_{1.5}O_4$ (ICDD: 04-018-2271) and VO_2 (ICDD: 04-014-1695) can be indexed by the Highscore software respectively, with no obvious impurity detected in either electrode material. Both XRD pattern and corresponding crystal diagrams of $LiNi_{0.5}Mn_{1.5}O_4$ and VO_2 are shown in Fig. 4.3a-d. The $LiNi_{0.5}Mn_{1.5}O_4$ is cubic spinel structure, space group $Fd\bar{3}m$ (227), $a =$ 8.1824(1) Å; $V = 547.827$ (2) Å^3. This is fairly close to the reported a = 8.2178(1) Å for $LiNi_{0.5}Mn_{1.5}O_4$ [303]. The XRD patterns for VO_2 can be indexed by the listed peaks for VO_2 (B) with ICDD card 04-014-1695 (Fig. 4.3e), which was reported by Jiang and Dahn [304]. The listed lattice parameters for the VO_2 (B) phase are, space group C2/m (12), $a = 12.0673$ Å, $b = 3.6892$ Å, $c = 6.4212$ (Å), $\beta = 106.97$ °.
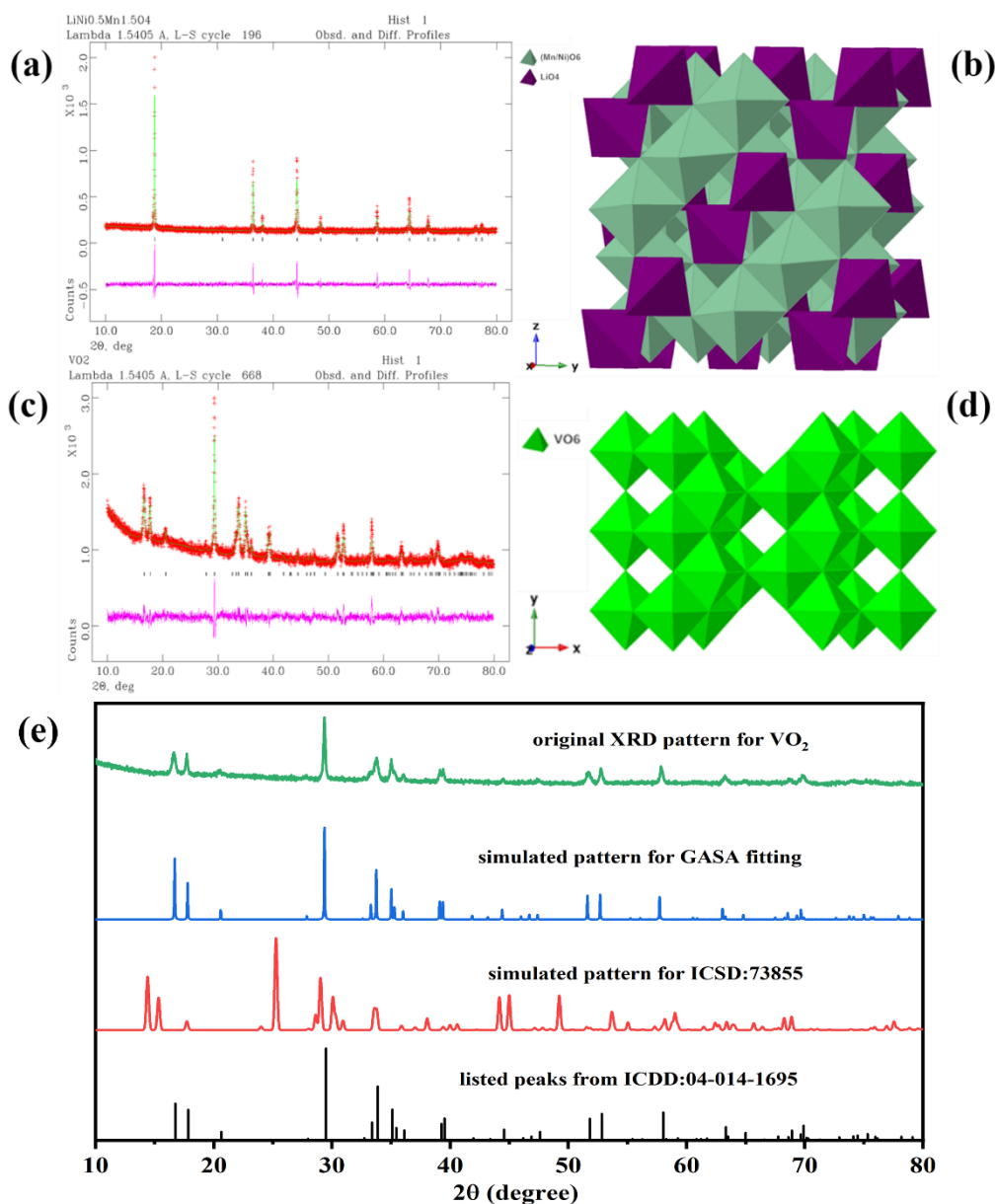
Fig. 4.3 (a) Refined XRD pattern and (b) crystal diagram of LiNi$_{0.5}$Mn$_{1.5}$O$_4$ hollow microspheres after Rietveld refinement fitting; (c) Refined XRD pattern and (d) crystal diagram of VO$_2$ nanobelts after Rietveld refinement fitting; (e) Comparison of XRD patterns for monoclinic VO$_2$ from different sources.

To the best of our knowledge, the first crystal structure of VO$_2$ (B) was reported by Oka et al., with lattice parameters of space group C2/m (12), $a = 12.093(1)$ Å, $b = 3.7021(2)$ Å, $c = 6.4330(5)$ (Å), $\beta = 106.97(1)$ ° (ICSD No. 73855) [305]. As the atomic positions for the V and O atoms are not available in the ICDD cards, we use the reported lattice parameters and atomic positions for VO$_2$ (B) reported by Oka to generate a simulated XRD pattern, which is displayed in Fig. 4.3e. As displaying, the simulated pattern is very different from the listed peaks for VO$_2$(B)

in the ICDD card 04-014-1695. This means XRD peaks simulated from the listed space group and lattice parameters in this card are inconsistent with those of the listed peaks in the same card. In most reported XRD patterns for $VO_2(B)$, there is a strong peak at 2θ around 25°, while in our VO_2 and the listed peaks from ICDD card 04-014-1695, the strongest peak is at 2θ around 29° and there is no peak at 2θ around 25° (Fig. 4.3e). The differences between these two patterns are obvious. However, in reported papers, XRD for $VO_2(B)$ phase with a strong peak at 2θ around 29° was also observed although there is no detailed structure data [306]. Using the reported lattice parameters by either Dahn or Oka to refine the structure of this VO_2 was unsuccessful, which is not unexpected. If carefully observing the listed and simulated peaks for VO_2 (the bottom two in Fig. 4.3), the listed peaks in the ICDD card are all shifted to the right with smaller d-values, compared to the simulated peaks. This implies that the VO_2 here has the same symmetry as the reported structure for VO_2 (B), with space group of C2/m (12), but with reduced lattice parameters [307, 308]. After applying this strategy, the refinement was successfully carried out and the refined lattice parameters are: Space group *C2/m* (12); *a* = 10.3945(8) Å, *b* = 3.1829(2) Å, *c* = 5.5358(7) Å, β = 106.947(14)°, V = 175.197 Å^3, which are listed in Table 4.2. As the VO_2 is not well crystallised, the thermal factors for O2-O4 are not refined. It is noticed that all the lattice parameters are smaller than the conventional values for $VO_2(B)$ phase, although the β value does not change so much. To the best of our knowledge, VO_2 phase with this structure has not been reported before. In order to differ it from the existing $VO_2(B)$ phase, we call it $VO_2(B1)$ phase. $VO_2(B1)$ phase share the same symmetry to $VO_2(B)$ phase but with reduced lattice parameters. Through the refined crystal structure data of $VO_2(B1)$ phase, it was found that the simulated pattern from our refined data matches with that listed in the ICDD card 04-014-1695 (Fig. 4.3e). This indicates that Dahn might mix up the observed peaks and the lattice parameters from different samples in that ICDD card 05-014-1695 [304]. The final refined pattern and the crystal structure for sample VO_2 are listed in Table 4.2 and shown in Fig. 4.3c and 4.3d. The morphology of hollow microsphere $LiNi_{0.5}Mn_{1.5}O_4$ and nanobelt VO_2 is determined by the SEM image with 5 and 2.5 μm resolutions in Fig. 4.4a and 4.4c, respectively. The size of hollow microspheres ranges from 2 to 5 μm whilst that of the nanobelt can be determined as 1.5-4 μm

in length, 70-180 nm in width and 20-30 nm in thickness according to the previous report using the same method for VO_2 synthesis [309]. The EDX layered images of $LiNi_{0.5}Mn_{1.5}O_4$ and VO_2 are displayed in Fig. 4.4b and 4.4d, which clearly indicate the distribution of elements.
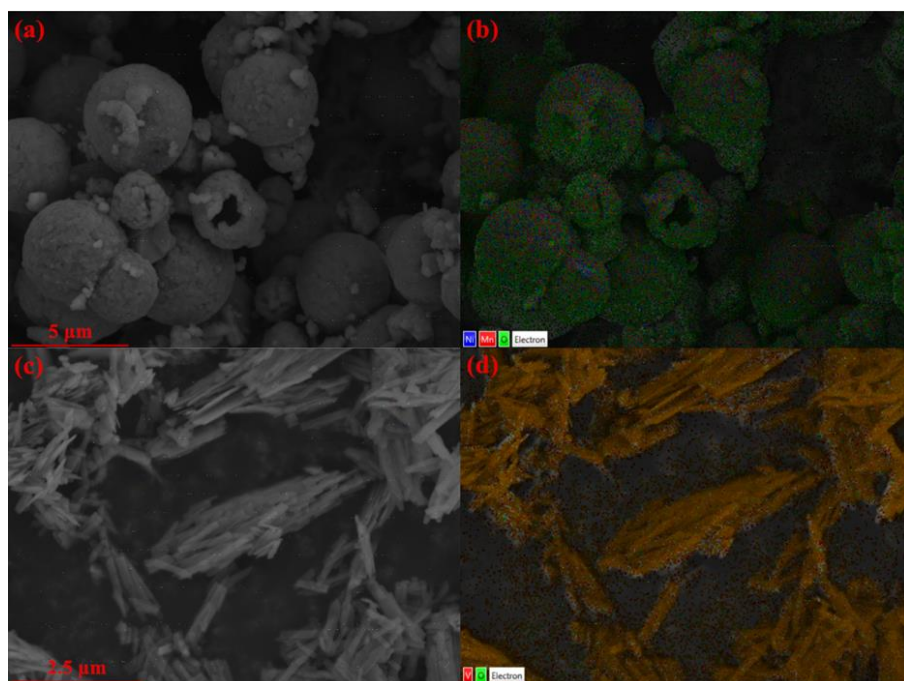
Fig. 4.4 (a) SEM image of $LiNi_{0.5}Mn_{1.5}O_4$ hollow microspheres with 5 μm resolution; (b) Corresponding EDX layer image of $LiNi_{0.5}Mn_{1.5}O_4$ hollow microspheres; (c) SEM image of VO_2 nanobelts with 2.5 μm resolution; (d) According EDX layer image of VO_2 nanobelts with 2.5 μm resolution.

Table 4.2 Structure and lattice parameters of VO_2 (B1).

atom	site	occupancy	x	y	z	$U_{iso}(\text{Å}^2)$
V1	4i	1	0.2998(7)	0	0.7121(13)	0.0257(32)
V2	4i	1	0.3985(8)	0	0.3185(16)	0.0018(24)
O1	4i	1	0.3624(21)	0	0.998(5)	0.006(6)
O2	4i	1	0.2301(21)	0	0.323(4)	0.025
O3	4i	1	0.4511(31)	0	0.676(5)	0.025
O4	4i	1	0.1190(18)	0	0.695(4)	0.025

Space group *C2/m* (12); $a = 10.3945(8)$ Å, $b = 3.1829(2)$ Å, $c = 5.5358(7)$ Å, $\beta = 106.947(14)°$, $V = 175.197$ Å^3, $Z = 8$, density: 6.2890 g·cm^{-3}. $R_{wp} = 4.17\%$, $R_p = 3.18\%$, $\chi^2 = 1.722$. Note: thermal factor for O2 to O4 are not refined.

Before assembly of the full cell, 45 m CsOAc+7 m LiOAc WiBSE was used as the electrolyte in a three-electrode system for CV to determine the redox potentials of Ti mesh-VO_2 anode and Ti mesh-$LiNi_{0.5}Mn_{1.5}O_4$ cathode, in which Ti mesh-VO_2 anode and Ti mesh-$LiNi_{0.5}Mn_{1.5}O_4$ electrodes functioned as the work electrodes, Ti mesh-AC as the counter electrode and Ag/AgCl as reference the electrode. As shown in Fig. 4.5a, the oxidation/reduction peaks of the Ti mesh-VO_2 anode are defined as -0.4/-1.0 V vs. Ag/AgCl (2.6/2.2 V vs. Li/Li^+), while the redox couple of Ti mesh-$LiNi_{0.5}Mn_{1.5}O_4$ cathode can be determined as 1.5/1.1 V vs. Ag/AgCl (4.7/4.3 V vs. Li/Li^+). Insertion of Cs ions in VO_2 and $LiNi_{0.5}Mn_{1.5}O_4$ is negligible due to the size of the larger Cs ions, which was proved by reported work [193]. The active mass of these two electrodes are controlled via average loading mass on current collector of ~2.0 mg·cm^{-2} for the anode and ~3.0 mg·cm^{-2} for the cathode to match the capacity of anode and cathode in the VO_2/ $LiNi_{0.5}Mn_{1.5}O_4$ full cell [310].

A CR2032 coin cell with 2.1 mg active material for the anode and 3.6 mg active material for the cathode, was then assembled and delivered for GCD testing under 1 C (110 mA·g^{-1}) rate and from 0.8 to 2.5 V vs. Li/Li^+ (converted from that vs. Ag/AgCl) within 200 cycles (Fig. 4.5c). The first, 5th, 10th, 50th, 100th and 200th cycles of charge/discharge curves of this full cell are shown in Fig. 4.5b with specific charge/discharge capacity of 65.(5)/57.(8) mAh·g^{-1} (88.(2)% CE) for first cycle calculated on the active materials on both electrodes. In the 6th cycle, that cell delivers its highest discharge capacity of 68.(1) mAh·g^{-1} with a corresponding energy density of 11(5) Wh·kg^{-1} (based on the active mass of both anode and cathode), which is impressive among the WiSE and WiBSE based ARLiBs [67, 187, 311, 312]. While, it is noticeable that the charge/discharge curves in Fig. 4.5b are not typical ones [53, 247], owning narrow platueas. That phenomenon may be caused by the nanosized electrodes with enhanced extrinsic pseudocapacitance, which requires more fancy physical characterization such as in-situ magnetometry for verification [313]. To demonstrate the cyclic stability and rate capability of this full cell, 4 C was employed for repeated GCD tests towards another coin cell with 2.2 mg anode active matter and 3.9 mg cathode active mass, which was cycled for 1200 cycles. The discharge capacity is 45.(8) mAh·g^{-1} in the first cycle and 39.(6) mAh·g^{-1} in the last cycle with 86.(5)% capacity retention (Fig. 4.5d). Meanwhile,

its CE is increased with continuous charge-discharge reactions, which can reach above 99.(0)% after 300 cycles and even near 10(0)% at certain cycles after 500 cycles. This increased CE at 4 C is consistent with the wider ESW of this WiBSE at high sweep rates (Fig. 4.2d) due to the increased ohmic and concentration polarization thus the increased over-potential of OER and HER under high charge/discharge rate.
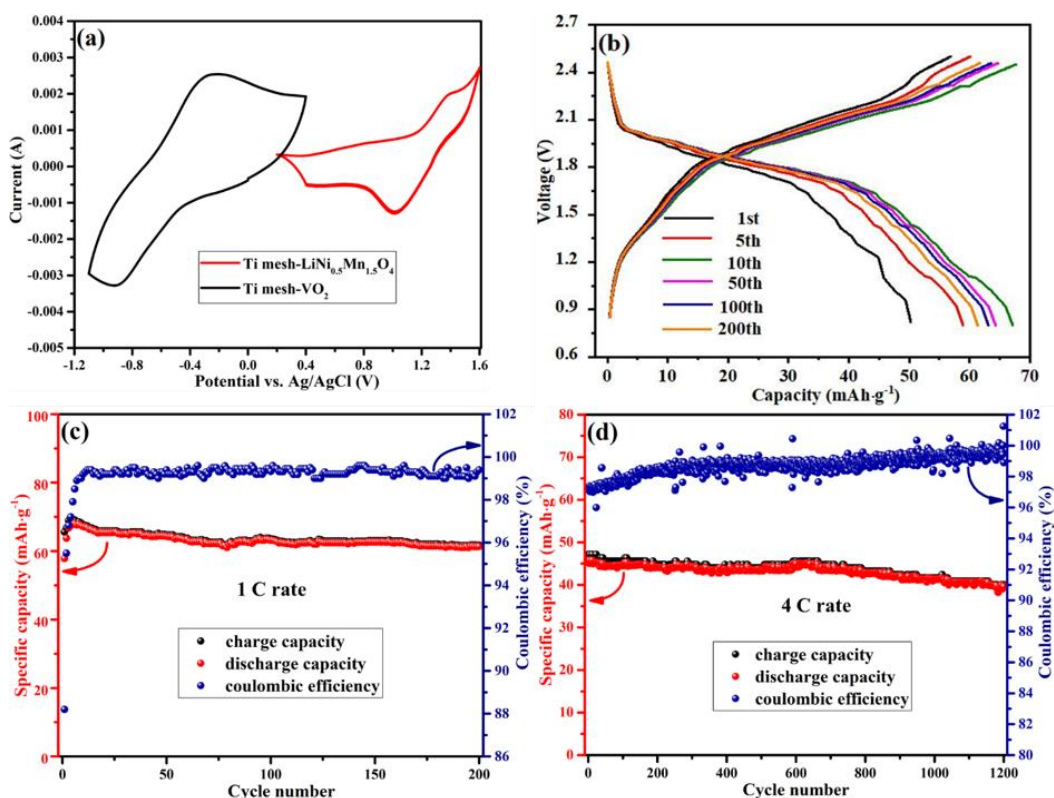
Fig. 4.5 (a) CV curves of Ti mesh-VO$_2$ anode and Ti mesh-LiNi$_{0.5}$Mn$_{1.5}$O$_4$ cathode under 1 mV·s^{-1} sweep rate. (b) charge/discharge curves of VO$_2$// LiNi$_{0.5}$Mn$_{1.5}$O$_4$ coin cell under 1 C rate. (c) Cycling performance of VO$_2$// LiNi$_{0.5}$Mn$_{1.5}$O$_4$ full cell under 1 C rate within 200 cycles. (d) Cycling performance of VO$_2$//LiNi$_{0.5}$Mn$_{1.5}$O$_4$ full cell under 4 C rate within 1200 cycles.

4.3 Conclusions

In this research, alkali metal acetates including LiOAc, NaOAc, KOAc and CsOAc, are systematically studied to investigate the influence of cations on ESWs. It has been found that acetates with large cations tend to have a wider ESW. Through Raman and FTIR spectra characterization, the enhanced polymer-like chains were

detected, and H bonds become weaker from LiOAc to CsOAc aqueous solutions, which account for the broadened ESWs from LiOAc to CsOAc. Amongst the investigated acetates, 45 m CsOAc WiSE was selected as it has the widest ESW (3.4 V) and was thereby blending with 7 m LiOAc to form a mixed cation WiBSE for ARLiBs. Finally, CR2032 coin cells were assembled with 45 m CsOAc + 7 m LiOAc WiBSE, Ti mesh-VO_2 anode and Ti mesh-$LiNi_{0.5}Mn_{1.5}O_4$ cathode with an operation voltage of 2.5 V. The battery exhibits a desired discharge capacity (considering active mass of both anode and cathode) and energy density under a rate of 1 C, while the excellent cyclic stability is also displayed under 4 C rate with above 99% and near 100% CE at certain cycles. This research suggests a new strategy of choosing acetate salts with large cations for better salt-concentrated electrolytes. Whereas it is necessary to figure out the hybrid charge storage mechanism induced by nanosized electrodes, with more advanced physical characterization in the future.

CHAPTER 5   Perchlorate "oversaturated gel electrolyte" for aqueous Zn//LiMn$_2$O$_4$ hybrid ion battery

5.1 Abstract

In reported papers on salt-concentrated electrolytes, the aqueous electrolytes were prepared at RT [39, 131, 188, 189, 264]. The wide ESW of these electrolytes is closely related to the suppressed water activity. From this point of view, a processable crystal-type gel electrolyte for the application of supercapacitor with high working voltage attributing to crystallization of salt and hydrophilic polymer, was reported [314]. Hereon, using a salting-out aqueous solution, coupling PVA for a gel electrolyte, which can also be referred to as OSGE. The water activity could be further reduced in OSGE through crystallizing the dissolved salts and solidifying the electrolytes, hence the ESW is expected to be even wider. In this study, both RTSGE and OSGE using inorganic salt LiClO$_4$ were investigated.

An ESW of 2.7 V was observed for the 6 m LiClO$_4$-PVA RTSGE whilst the ESW was further expanded to 3.3 V for the 10 m LiClO$_4$-PVA OSGE, when the saturated LiClO$_4$ sol was prepared at 95 °C then slowly cooled down to RT. The ESW of that OSGE varied from 3.3 to 2.5 V when the temperature increased from RT to 80 °C, which demonstrated its potential capability as the electrolyte in ARBs operated at elevated temperatures. The crystals were observed at RT in the OSGE but high ionic conductivity of 1.32×10^{-2} S·cm^{-1} at RT is still high enough as electrolyte for battery. The addition of PVA facilitates the homogeneous distribution of the un-ionised LiClO$_4$ in the OSGE when cooled down to lower temperatures, which is analogous to dispersed phase, compared with dissolved LiClO$_4$ and PVA involved hydrogel (continuous phase), therefore maintained the desired conductivity while reduced the activity of water. The ESW was basically retained at 3.0 V when 1 m Zn(ClO$_4$)$_2$ was added into this OSGE to introduce the Zn^{2+} conductivity, which was estimated as 5.31×10^{-3} S·cm^{-1} by current interruption method. Based on novel inexpensive 1 m Zn(ClO$_4$)$_2$+10 m LiClO$_4$-PVA OSGE, a HiB was assembled, with zinc metal as anode, LiMn$_2$O$_4$ on Ti mesh as cathode. During GCD cycling, the CEs were nearly 10(0) % at the first 30 cycles then retains at around 99.(0)% in the following cycles. A discharge capacity of

11(7) mAh·g^{-1} (based on mass of LiMn$_2$O$_4$) and an energy density of 18(3) Wh·kg^{-1} for first cycle were delivered, which became 93.(5) mAh·g^{-1} and 13(8) Wh·kg^{-1} with 79.(1) % capacity retention after 300 cycles.

5.2 Results and discussion

5.2.1 Property of OSGE

When investigated as a salt of electrolytes for Li//O$_2$ batteries, LiClO$_4$ usually perform better (greater discharge capacity) than LiTFSI-containing electrolytes. This is attributed to the better solvent viscosity, oxygen solubility and stability against oxygen [272, 315, 316]. However, for ARBs, LiClO$_4$ or any other perchlorates are seldom used as the salts in electrolytes due to safety and toxicity concerns [272]. For this reason, PVA-containing hydrogel in quasi-solid state is utilized by us to handle the corresponding issues caused by perchlorates [206]. To demonstrate the advantages of the OSGE, the ESWs of 1 m (unsaturated), 6 m (RTSGE) and 10 m (OSGE) LiClO$_4$-PVA are shown in Fig. 5.1a. The ESW for unsaturated 1 m LiClO$_4$-PVA gel electrolyte is 2.3 V (-0.6 to 1.7 V vs. Ag/AgCl). With further concentration increasing until saturated at room temperature (6 m), the ESW increased to 2.7 V (-0.9 to 1.7 V vs. Ag/AgCl). Finally, the OSGE of 10m LiClO$_4$-PVA OSGE is 3.3 V (-1.4 to 1.9 V vs. Ag/AgCl), which is 0.6 V higher than that of RTSGE. Fig. 5.1b shows the ESW of 10 m LiClO$_4$-PVA OSGE at different sweep rates. When the sweep rate is increased from 1 to 50 mV·s^{-1}, the cut-off potential for both HER and OER sides can be basically maintained. However, at OER side, the current at low sweep rate of 1 mV s^{-1} is much smaller than those at sweep rates at or above 5 mV s^{-1}. Although the observed current at the OER onset in Fig. 5.1b increases with the raise of sweep rate, that is believed due to the reversible non-faradaic (capacitive) current which owns relatively low influence to stability window than the faradaic current [317]. The variation of ESW of 10 m LiClO$_4$-PVA OSGE vs. temperature from RT to 80 °C is recorded in Fig. 5.1c, which exhibits the ESWs as 3.3 V (-1.4 to 1.9 V vs. Ag/AgCl) at RT, 3.0 V (-1.3 to 1.7 V vs. Ag/AgCl) at 40 °C, 2.8 V (-1.2 to 1.6 V vs. Ag/AgCl) at 60 °C and 2.5 V (-1.0 to 1.5 V vs. Ag/AgCl) at 80 °C. The reduced ESW could be caused by the decreased over-potential for HER and OER on the two electrodes at elevated

temperatures. In the Fig. 5.1d, the optical image of reversible transition between sol and gel state for the OSGE at 95 °C and RT can be observed, further demonstrating the wide working temperature window of this OSGE.
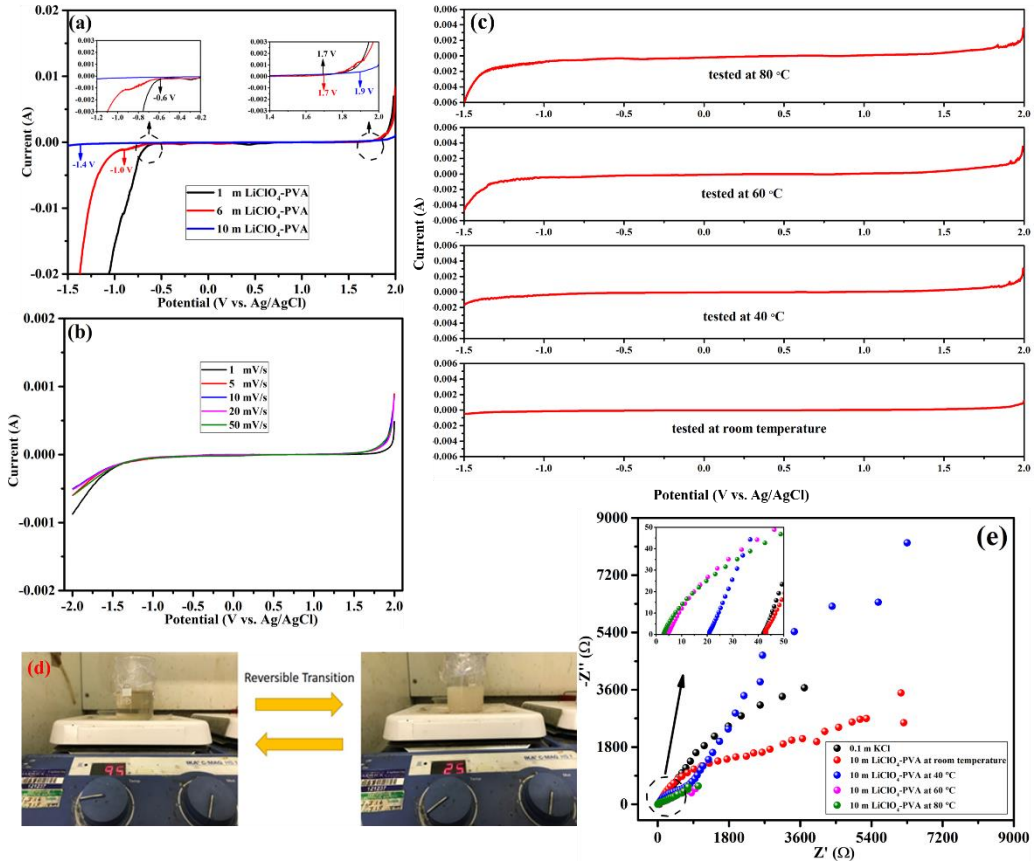
Fig. 5.1 (a) ESW test on 1, 6 and 10 m LiClO$_4$-PVA electrolyte under 1 mV·s^{-1}; (b) ESW test on 10 m LiClO$_4$-PVA OSGE under different sweep rates; (c) ESW test on 10 m LiClO$_4$-PVA OSGE at various temperatures; (d) Optical image on reversible transition between sol and gel state of 10 m LiClO$_4$-PVA OSGE; (e) EIS test on 10 m LiClO$_4$-PVA OSGE at various temperatures.

Besides wide ESW, sufficient ionic conductivity is another important parameter for battery electrolytes. Therefore the ionic conductivities of 10 m LiClO$_4$-PVA OSGE was measured by EIS using 0.1 M KCl aqueous solution (conductivity 1.28×10^{-2} S·cm^{-1} at RT) as the calibration solution [271], the impedance response of which is shown in Fig. 5.1e, with the corresponding ionic conductivity of 1.32×10^{-2} S·cm^{-1} at RT. PVA in OSGE helps the homogenous distribution of the crystallized LiClO$_4$, which is usually utilized as the disperser for sol-gel processing to disperse the crystals evenly and realize the reversible transition between sol and

gel state [318]. Crystalized LiClO$_4$ as ionic insulator can slightly decrease ionic conductivity of OSGE by lengthening ion transport pathway [319]. The lower ionic conductivity of OSGE is mainly induced by the increased viscosity because of the high salt concentration and PVA. However, the oversaturated situation really can lower the transference number of Li$^+$/Zn^{2+} due to the contact cation-anion pairs [53, 320], thus lower the Li$^+$/Zn^{2+} conductivity. In addition, the ionic conductivity of 10 m LiClO$_4$-PVA OSGE increases from 1.32×10^{-2} to 1.86×10^{-1} S·cm^{-1}, when the temperature increases from RT to 80 °C (Fig. 5.1e), which is an advantage for operating at evaluated temperatures.
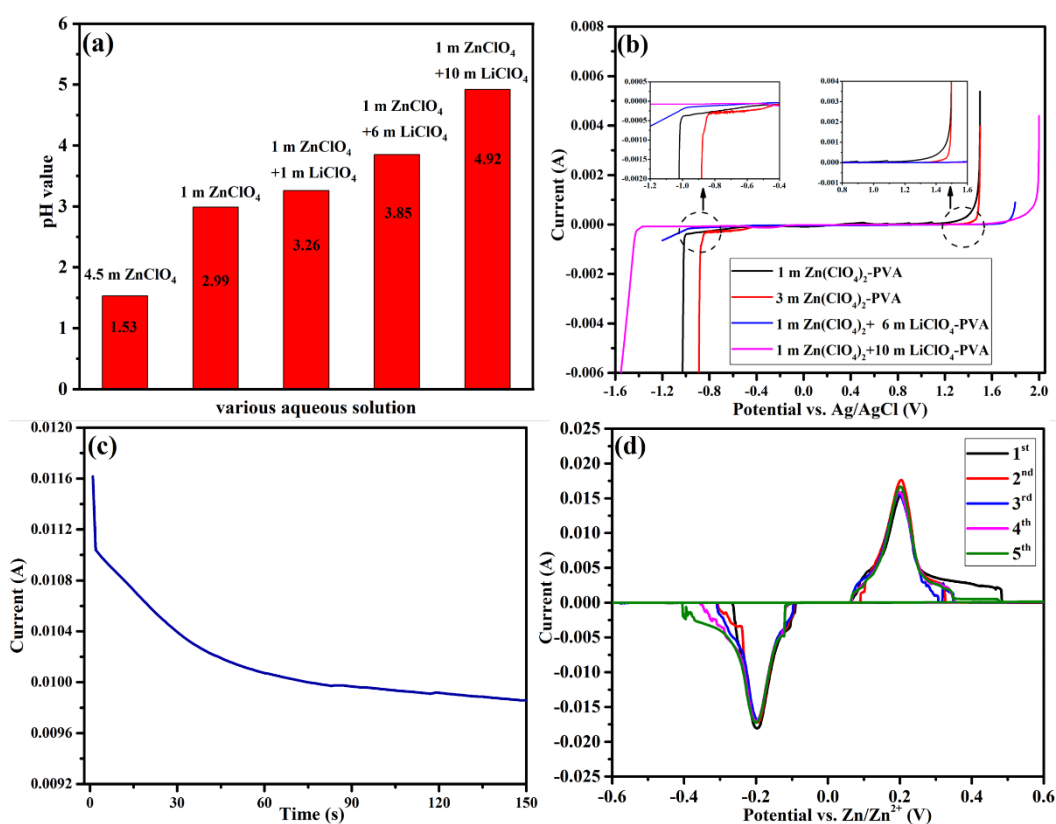
Fig. 5.2 (a) pH value of various electrolytes with optical images of pH meter as inset; (b) ESW test on four different electrolytes (1 m Zn(ClO$_4$)$_2$-PVA, 3 m Zn(ClO$_4$)$_2$-PVA, 1 m Zn(ClO$_4$)$_2$ + 6 m LiClO$_4$-PVA and 1 m Zn(ClO$_4$)$_2$+10 m LiClO$_4$-PVA); (c) The current interrupt test on Zn//Zn symmetrical cell based on 1 m Zn(ClO$_4$)$_2$+10 m LiClO$_4$-PVA OSGE under 1.0 V vs. Zn/Zn^{2+} applied voltage; (d) CV curves of Zn//Zn symmetrical cell basing on the 1 m Zn(ClO$_4$)$_2$ + 10 m LiClO$_4$-PVA OSGE under 1 mV·s^{-1} sweep rate.

In order to use the 10 m $LiClO_4$-PVA OSGE in an aqueous HiB using Zn metal as the anode, it is necessary to introduce Zn^{2+} conduction. Owing to the similar chemical properties with $LiClO_4$, $Zn(ClO_4)_2$ was added to induce Zn^{2+} and combine with $LiClO_4$ to form an OSGE (over-saturated for $LiClO_4$ and unsaturated for $Zn(ClO_4)_2$). However, according to previous reports, the pH values of aqueous electrolytes can significantly affect their performance [321]. It is therefore necessary for us to optimize the compositions based on the pH values of aqueous solutions. In Fig. 5.2a, the pH value of RT-saturated $Zn(ClO_4)_2$ (3 m) and 1 m $Zn(ClO_4)_2$ aqueous solution are 1.02 and 3.44 respectively. The acidic environment caused by hydrolysis of Zn^{2+} ($Zn(OH)_4^{2-}$), enhances the activity towards the HER [321]. However, with the increase in $LiClO_4$ concentration, the pH value increases accordingly and finally reaches 5.38 for 1 m $Zn(ClO_4)_2$ + 6 m $LiClO_4$, which is a weak acid. With the addition of PVA, the RTSGE approaches neutrality with a pH value of 6.25. Although, the pH meter employed in our lab cannot detect the pH value of OSGE with quasi-solid state, it is believed that the pH value can approach neutrality due to the addition of more $LiClO_4$, suppressing the hydrolysis of Zn^{2+}. Therefore the activity for the HER will be further decreased [321]. The pH value is higher when a lower concentration of $Zn(ClO_4)_2$ was added, hence the concentration of $Zn(ClO_4)_2$ in 10 m $LiClO_4$-PVA OSGE was fixed to 1 m. To further demonstrate the advantages of 1 m $Zn(ClO_4)_2$+10 m $LiClO_4$-PVA OSGE, 1 m $Zn(ClO_4)_2$-PVA, 3 m $Zn(ClO_4)_2$-PVA, 1 m $Zn(ClO_4)_2$ + 6 m $LiClO_4$-PVA and 1 m $Zn(ClO_4)_2$+10 m $LiClO_4$-PVA electrolytes were prepared for comparison. As shown in Fig. 5.2b, 1 m $Zn(ClO_4)_2$+10 m $LiClO_4$-PVA OSGE is stable within the potential range of -1.3 to 1.7 V vs. Ag/AgCl under an sweep rate of 1 $mV \cdot s^{-1}$. However, the other three electrolytes show relatively narrow ESWs of -1.0 to 1.1, -0.8 to 1.4 and -1.0 to 1.6 V vs. Ag/AgCl respectively.

The measured conductivity by EIS is the total conductivity, including conductivity of all the charge carriers such as Li^+, Zn^{2+}, ClO_4^- ions. To estimate the Zn^{2+} conductivity, current interrupt method was employed in the same set-up and dimension of 0.1 M KCl standard solution using Zn foils as both the work and counter electrodes. These Zn foils are reversible electrodes for Zn^{2+} while they are blocking electrodes for other ions. As shown in Fig. 5.2c, after applying 1.0 V vs. Zn/Zn^{2+} voltage, the current drops because of the blocking effect from Zn metal

electrodes to other ions except for Zn^{2+} in OSGE, then the current remains stable around 9.8 mA to the end. The steady current is caused by the Zn^{2+} transportation only. Through comparing the initial current (I_o) and steady current (I_s), the transference number of Zn^{2+} can be estimated as follows:

$$T_{Zn^{2+}} = \frac{I_s}{I_o} \tag{5.1}$$

Hence the Zn^{2+} conductivity in 1 m $Zn(ClO_4)_2$+10 m $LiClO_4$-PVA OSGE can be estimated as 5.31×10^{-3} $S \cdot cm^{-1}$, which is high enough to be used as an electrolyte for ARZiBs and ARHiBs. Considering both the ESW and ionic conductivity, 1 m $Zn(ClO_4)_2$+10 m $LiClO_4$-PVA OSGE is a suitable electrolyte for Zn-Li HiBs. To demonstrate the feasibility of Zn plating/stripping with OSGE, Zn//Zn symmetrical cell was assembled in CR2016 coin cells and tested by CV under 1 $mV \cdot s^{-1}$ sweep rate within the potential range of -0.6 to 0.6 V vs. Zn/Zn^{2+}. As shown in Fig. 5.2d, the symmetric peaks of oxidation and reduction of Zn//Zn symmetrical cell with 1 m $Zn(ClO_4)_2$+10 m $LiClO_4$-PVA electrolyte from the 1st to 5th CV sweep can be observed around 0.2 and -0.2 V, which demonstrates the stable Zn plating/stripping. The polarization for Zn stripping/plating shifts relevant CV peaks from 0 to ± 0.2 V.

In order to materially characterize 1 m $Zn(ClO_4)_2$+10 m $LiClO_4$-PVA OSGE, FTIR was employed to identify its composition and liquid structure (Fig. 5.3a). The peaks in the curve of all the electrolytes in reflects the peaks of all the original chemicals. 1 m $LiClO_4$-PVA, 6 m $LiClO_4$-PVA and 10 m $LiClO_4$-PVA electrolytes have been characterized by FTIR on the purpose of explaining the further extended ESW of OSGE than RTSGE. Noticeably, in the curve of OSGE, the peak of H bond around 3310 cm^{-1} shrinks and the two peaks at ~3550 and 3590 cm^{-1} corresponding to $LiClO_4$ become sharper, compared with the RTSGE and indicating the solidification of OSGE, which can suppress the active of water attributing to the hydrophilic polymer and quasi-solid state, thence widen ESW [194]. Thermal gravimetric analysis (TGA) and differential scanning calorimetry (DSC) analysis were utilized to characterize the thermal property of the 1 m $Zn(ClO_4)_2$+10 m $LiClO_4$-PVA OSGE (Fig. 5.3b). The first peak of the DSC curve

occurs at ~110 °C, this corresponds to the phase transition of electrolyte from quasi-solid state to liquid state, before that the weight loss in TGA curve is mainly due to the evaporation of water. After that, the acceleration of weight loss in TGA curve was observed due to the decomposition of PVA. A further, faster weight loss and another peak of DSC curve around 220 °C is likely engendered by the decomposition of perchlorates [322]. To demonstrate the appearance of that OSGE furthermore, the optical image of OSGE cast on glass microfiber filter and cut into a round disc with 16 mm diameter is shown in Fig. 5.3c, which displays quasi-solid state. The SEM image of that electrolyte is shown in Fig. 5.3d. There are some dents on the surface of OSGE, which could be attributed to the loss of water under the high vacuum of the SEM measurement environment.
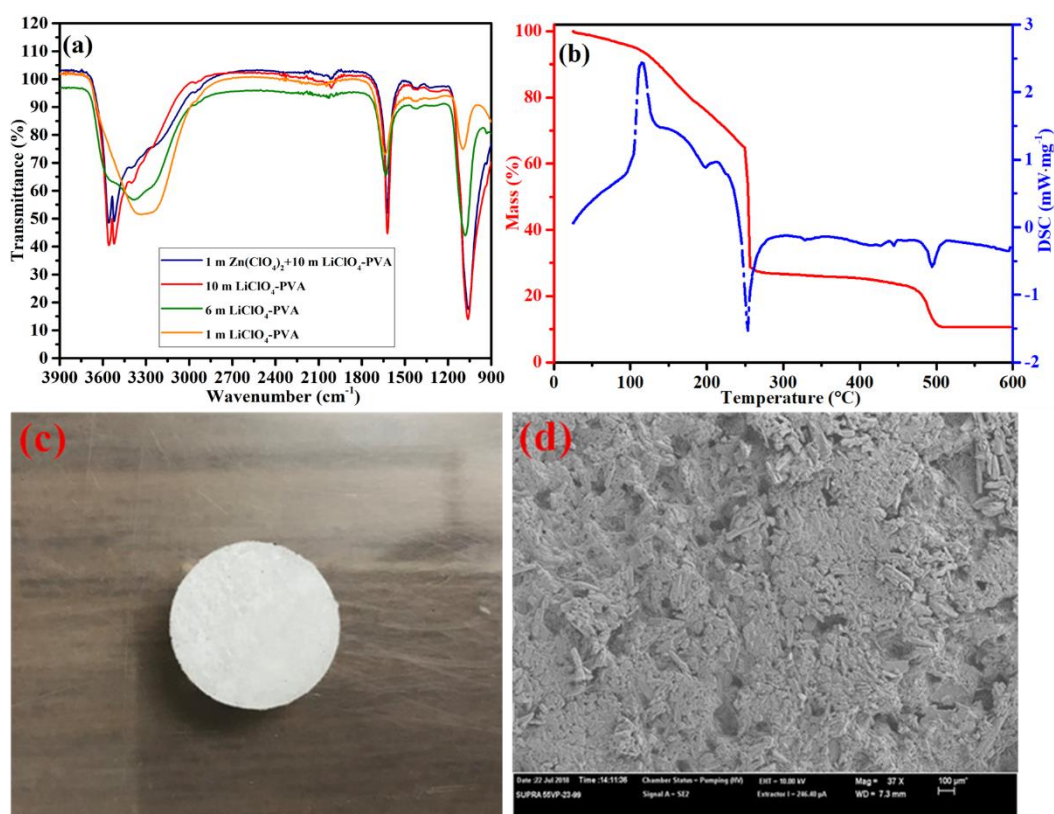
Fig. 5.3 FTIR spectra of various electrolytes (a); TGA analysis on the 1 m Zn(ClO$_4$)$_2$+10 m LiClO$_4$-PVA electrolyte from room temperature to 600 ℃ (b); Optical image of 1 m Zn(ClO$_4$)$_2$+10 m LiClO$_4$-PVA electrolyte after tape casting on the glass microfiber filter (c); SEM image regarding surface of 1 m Zn(ClO$_4$)$_2$+10 m LiClO$_4$-PVA electrolyte with 100 μm resolution (d).

5.2.2 Performance of aqueous Zn//LiMn$_2$O$_4$ HiB based on OSGE

As the 1 m Zn(ClO$_4$)$_2$+10 m LiClO$_4$-PVA OSGE can conduct both Li$^+$ and Zn^{2+}, we are able to take advantage of both Li$^+$ and Zn^{2+} conduction to make Zn-Li HiB. In the HiB of Zn|1 m Zn(ClO$_4$)$_2$+10 m LiClO$_4$-PVA|LiMn$_2$O$_4$-Ti mesh, the well-established Li$^+$ insertion/extraction happens at the LiMn$_2$O$_4$ cathode in a highly reversible manner, whereas Zn stripping/plating at the Zn metal anode. The corresponding XRD pattern of prepared LiMn$_2$O$_4$ powder for the cathode is shown in Fig. 5.4a, which exhibits the single phase of LiMn$_2$O$_4$ (ICDD: 01-070-8343). In Fig. 5.4b, two pairs of oxidation/reduction peaks occur at ~1.0/~0.90 V vs. Ag/AgCl (4.3 and 4.2 V vs. Li/Li$^+$) and ~ 0.90/~0.75 V vs. Ag/AgCl (4.2 and 4.0 V vs. Li/Li$^+$) respectively, indicating the insertion/extraction reaction of Li$^+$ ions in LiMn$_2$O$_4$ [323]. The other pair of redox peaks happen at ~-0.75 and ~-1.1 V vs. Ag/AgCl (~0.23 and ~-0.12 V vs. Zn/Zn^{2+}), representing the Zn plating/striping [174]. In Fig. 5.4d, GCD cycling test of 300 cycles was obtained under 1 C (148 mA·g^{-1}) charge/discharge rate within the voltage range of 0.8 to 2.0 V vs. Zn/Zn^{2+}, while the corresponding GCD curves are exhibited in Fig. 5.4c. In the first cycle, the charge and discharge capacity of the cell is 11(8) and 11(7) mAh·g^{-1} respectively (calculated on 5.6 mg LiMn$_2$O$_4$) and its CE can be determined as 98.(7)%. After that, during the continuous charge/discharge process, its CE is retained nearly 10(0)% for the first 30 cycles and about 99.(0)% in the following cycles to 98.(8)% at the 300th cycle, with 94.(6) mAh·g^{-1} charge capacity, 93.(5) mAh·g^{-1} discharge capacity and 79.(1)% capacity retention in the last cycle compared to the first cycle (also the cycle with highest capacity). The around 99% CE is desired for ARBs, while for conventional LiBs above 99.96% CE is required for more than 80% capacity retention after 500 charge/discharge cycles [324]. The difference of CE requirement between ARBs and LiBs is caused by the SEIs in LiBs, which can track and consume Li ion irreversibly.

Compared with Zn//LiMn$_2$O$_4$ HiBs based on the other electrolytes, the maximum capacity of our Zn//LiMn$_2$O$_4$ cell (11(7) mAh·g^{-1}) is impressive, higher than those of reported values under same charge/discharge rate (~95 mAh·g^{-1} for pyrazol-added gel electrolyte; 115.6 mAh·g^{-1} for fumed silica-based gel electrolyte) [325-327]. However, a fast capacity decay was observed for the initial 30 cycles, which

136

may be caused by the phase transition from cubic I to cubic II of $LiMn_2O_4$ [328] or/and the agglomeration of $LiMn_2O_4$ particles, being demonstrated in the SEM characterization in Fig. 5.6. Its energy density (obtained by integrating the discharge curve) can be calculated as 18(3) $Wh \cdot kg^{-1}$ for the first cycle and 13(8) $Wh \cdot kg^{-1}$ for 300th cycle. Furthermore, the rate performance of the same coin cell was tested under 1, 2, 4, 6 and 8 C, respectively (Fig. 5.4e), with corresponding specific charge/discharge capacity of last cycle under certain current density determined as 94.(0)/92.(9), 81.(8)/81.(1), 68.(7)/68.(3), 53.(8)/53.(3) and 41.(5)/41.(2) $mAh \cdot g^{-1}$. After the charge/discharge rate was returned to 1 C, the charge/discharge capacity became 88.(5)/87.(8) $mAh \cdot g^{-1}$ at the last charge/discharge cycle. The rate capability is not excellent, which probably is attributed to poor electrode kinetics and mass transportation of micro-sized $LiMn_2O_4$.
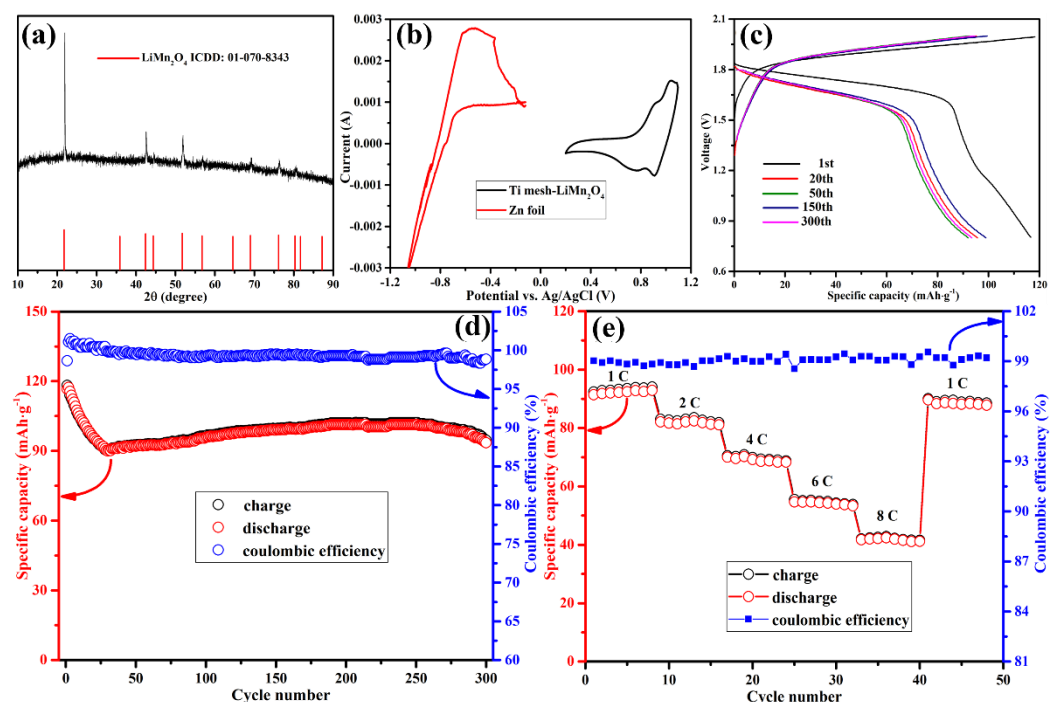
Fig. 5.4 (a) XRD plot of as-obtained $LiMn_2O_4$ powder; (b) CV curves of Zn and Ti mesh-$LiMn_2O_4$ electrodes with Ti foil as counter electrode and Ag/AgCl as reference electrode; (c) Cyclic performance of Zn//$LiMn_2O_4$ HiB under 1 C rate between 0.8 and 2.0 V vs. Zn/Zn^{2+} within 300 cycles; (d) Accordingly charge/discharge curves of Zn//$LiMn_2O_4$ HiB between 0.8 and 2.0 V vs. Zn/Zn^{2+}; (e) Rate performance of Zn/$LiMn_2O_4$ full cell under various rates.

5.2.3 Material characterization on electrolytes and electrodes before/after electrochemical measurements

After the electrochemical test, the coin cell was separated, with the optical images of different components shown in Fig. 5.5a, 5.5b and 5.5c. FTIR spectra of the OSGE before and after electrochemical test are shown in Fig. 5.5d, which can be basically maintained. While the H-bond peak locating at 3000-3800 cm^{-1} shrinks after test, especially the part (3000-3350 cm^{-1}) standing for free H bond. That change probably was caused by further de-solvation due to water loss.
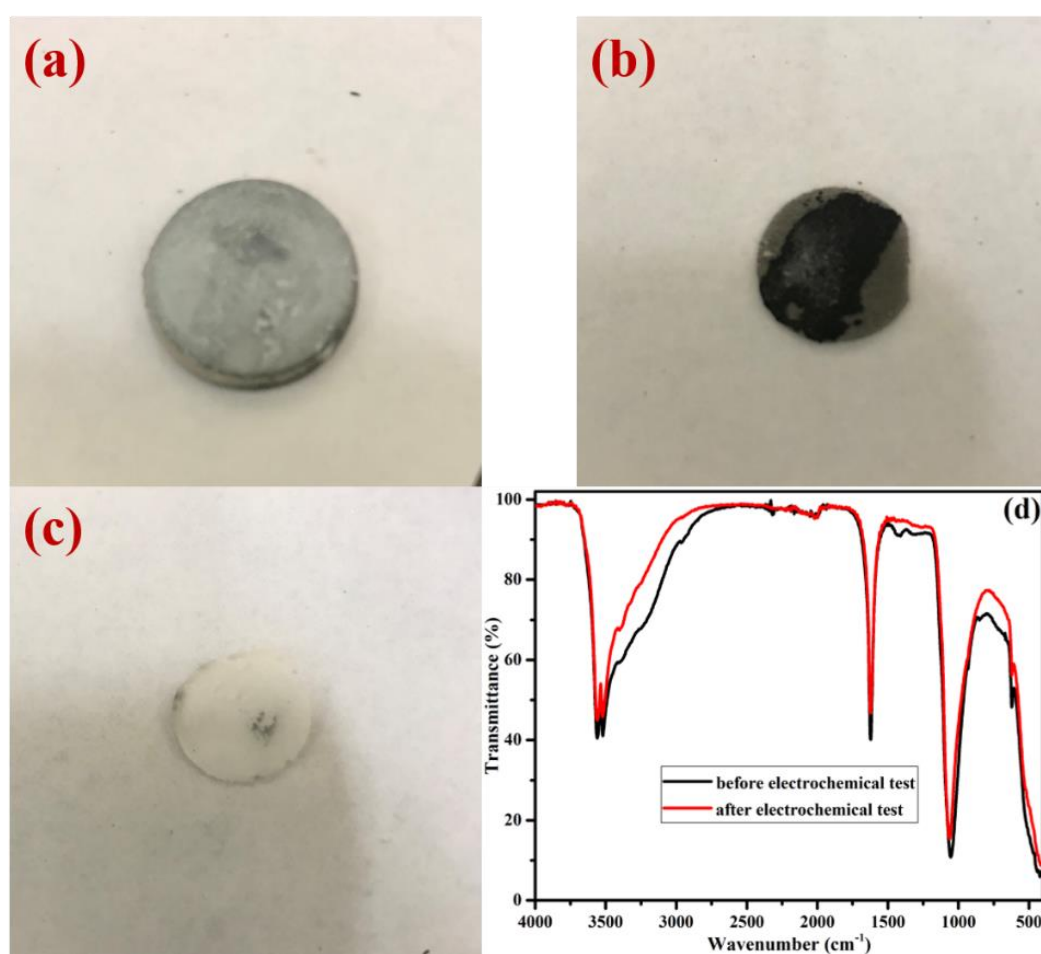
Fig. 5.5 Optical images of (a) Zn metal anode; (b) Ti mesh-LiMn$_2$O$_4$ cathode; (c) OSGE after GCD cycling; (d) FTIR of OSGE before and after GCD cycling.

In Fig. 5.6a, the layered EDX mapping of $LiMn_2O_4$-Ti mesh electrode before and after electrochemical test are compared. The increased particle size of $LiMn_2O_4$ after electrochemical test has been observed. The agglomeration of $LiMn_2O_4$ particles may affect the insertion/desertion of Li^+, leading to the decreased capacity during the charge/discharge process. The existence of elements Zn and Cl in the layered mapping of the $LiMn_2O_4$ electrode after cycling test is due the contact with perchlorate based OSGE. In Fig. 5.6b, the XRD patterns of the $LiMn_2O_4$ electrodes (striping from current collectors by sonication) before and after electrochemical test are compared as well. The $LiMn_2O_4$ (ICDD: 01-070-8343) can be detected in both XRD patterns as main phase. The peaks of carbon can be found in both patterns due to the existence of carbon conductivity addition (Super P), while $Zn(ClO_4)_2$ can only be observed in the sample after the electrochemical test. In Fig. 5.6c, the XRD patterns of Zn metal anode before and after electrochemical test are compared, both are composed of Zn (ICDD: 04-008-6027). The cross-section SEM image of Zn metal anode after cycling is shown in Fig. 5.6d, combining with the layered EDX mapping of Zn anode in Fig. 5.6e. No dendrite can be observed on the Zn metal anode. For ARBs with Zn metal electrodes, dendrites induced by the uneven metal deposition on the anode can lead to thermal runaway and explosion hazards, which is an obstacle for commercialisation of the battery [284]. In this HiB, the high salt concentration can increase the threshold critical current density for cations becoming depleted in the electrolyte thus suppressing the formation of Zn dendrites [284], which significantly improves the safety and stability of this battery.
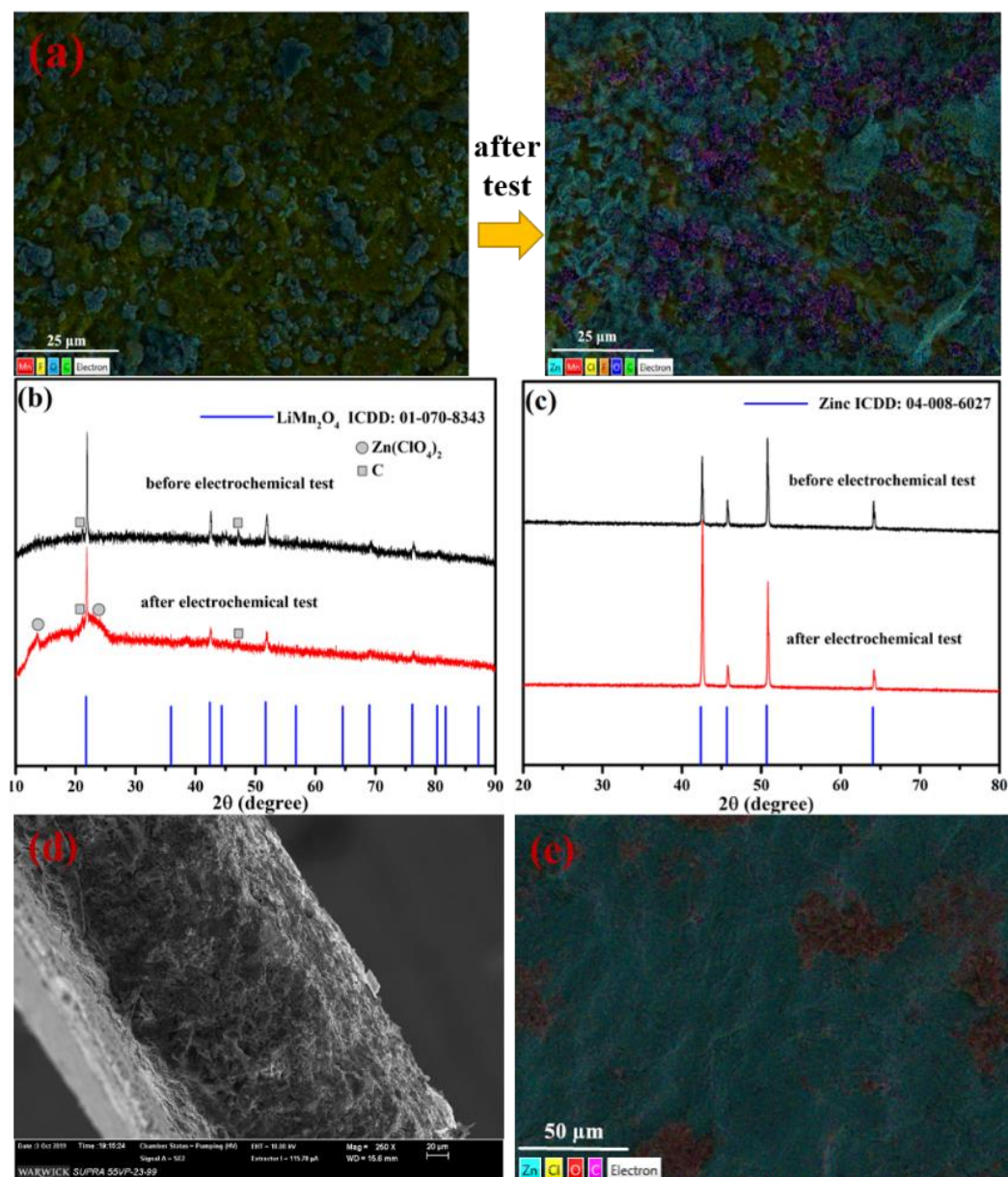
Fig. 5.6 (a) EDX layered mapping of Ti mesh-LiMn$_2$O$_4$ electrode before and after GCD cycling; (b) XRD patterns of Ti mesh-LiMn$_2$O$_4$ electrode before and after GCD cycling; (c) XRD patterns of Zn metal anode before and after GCD cycling; (d) SEM image of Zn metal anode after GCD cycling; (e) Layered mapping of Zn metal anode after GCD cycling.

5.3 Conclusions

In this study, the use of OSGE further expanded the ESW for higher energy-density ARBs. The ESW of 6 m LiClO$_4$-PVA RTSGE reached 2.7 V, while it was extended to 3.3 V, when the electrolyte was prepared in 95 °C saturated state and then cooled down to RT as 10 m LiClO$_4$-PVA OSGE. With the addition of PVA,

the un-ionised LiClO$_4$ crystals are homogeneously dispersed in the gel electrolyte. The properties of this OSGE at elevated temperatures were investigated as well. It had a stable ESW of 2.5 V and ionic conductivity of 1.86×10^{-1} S·cm^{-1} at 80 °C. To optimize the composition of OSGE containing LiClO$_4$ and ZnClO$_4$ for HiBs, pH value, ESW and ionic conductivity were jointly investigated on electrolytes with various Zn(ClO$_4$)$_2$/LiClO$_4$ ratios. Through mild acid environment, 3.0 V ESW and 5.31×10^{-3} S·cm^{-1} Zn^{2+} conductivity, 1 m Zn(ClO$_4$)$_2$+10 m LiClO$_4$-PVA OSGE was regarded as a good electrolyte for aqueous Li-Zn HiBs. Zn metal anode and LiMn$_2$O$_4$-Ti mesh cathode with OSGE were assembled together in a coin cell with working voltage of 2.0 V. It delivered discharge capacity and energy density as 11(7) mAh·g^{-1} and 18(3) Wh·kg^{-1} (calculated on the 5.6 mg active mass of LiMn$_2$O$_4$) respectively at first cycle, becoming 93.(5) mAh·g^{-1} and 13(8) Wh·kg^{-1} for 300 cycles with close to nearly 10(0) % at first 30 cycles then retained to about 99.(0)% CE in the following cycles. After cycling, the anode, cathode and OSGE were materially characterized, whilst the Zn metal anode was dendrite-free. Agglomeration of LiMn$_2$O$_4$ particles was observed after electrochemical test, which probably was related to the slow decrease in capacity. The above attempt demonstrates a viable route to apply OSGE in ARBs, with the potential to be operated above RT. However, the mechanism behind the wider OSGE than RTSGE need to be explained more fundamentally as well as the microsize structure (morphology), which will be implemented in the following chapters.

CHAPTER 6 Nitrate "oversaturated gel electrolyte" for high-voltage and high-stability aqueous rechargeable lithium-ion battery

6.1 Abstract

In a previous study, it was reported that an ESW of 2.55 V was observed for a super-concentrated aqueous solution of $LiNO_3$ as a potential electrolyte for ARLiBs [194]. To maximise the ESW, in this study, $LiNO_3$ was used as the salt in OSGE, demonstrating a further improvement in battery performance over the perchlorate OSGE and $LiNO_3$ concentrated solution. 33 m $LiNO_3$ was dissolved in DIW with PVA at 95 ℃ to a saturated state, after crystalizing the excess $LiNO_3$ at RT, the ESW of $LiNO_3$ OSGE reached 3.2 V (-1.25 to 1.95 V vs. Ag/AgCl), which is 0.1 V higher than that of $LiNO_3$ based RTSGE, and 0.65 V higher than the previously reported $LiNO_3$ concentrated solution [194]. In addition, the ESW of the OSGE, especially the cathodic side of LSV curve was basically maintained as operating temperature increased, while the gap of ESW between OSGE and RTSGE increases to 0.25 V at 80 ℃. A $VO_2//LiNi_{0.5}Mn_{1.5}O_4$ full battery was assembled with this $LiNO_3$ OSGE, delivering the working voltage of 2.5 V and maximum energy density of 17(6) $Wh \cdot kg^{-1}$ (calculated on the active mass of both electrodes) under 1 C rate (110 $mA \cdot g^{-1}$). The $VO_2//LiNi_{0.5}Mn_{1.5}O_4$ battery was repeatedly charged/discharged to 700 cycles under 3 C rate, the CE of which reached 99.(0)% after 500 cycles. The performance of $VO_2//LiMn_2O_4$ full battery with 2.0 V working voltage was characterized at RT, 40, 60 and 80 ℃, respectively. We choose 60 ℃ as the optimal temperature to test elevated-temperature stability of this battery, indicating the potential applications of $LiNO_3$ OSGE in the ARBs operating at elevated temperatures. Overall, except the enhanced ESW and battery performance, OSGE can ensure stable running of ARBs under the circumstances of elevated temperatures and high working voltage, prove the feasibility of employing inhomogeneous electrolytes into battery systems and utilize the inexpensive inorganic salts with relatively low solubility in water into salt-concentrated electrolytes.

6.2 Results and discussion

6.2.1 Property of OSGE

In order to verify whether the ESW increases with salt concentration, and whether OSGE can further expand the ESW in comparison of RTSGE, LSV is utilized here to determine the ESWs of 1 m, 8 m, 15 m $LiNO_3$ aqueous solutions, and 15 m $LiNO_3$-PVA RTSGE and 33 m $LiNO_3$-PVA OSGE, respectively (Fig. 6.1a). As expected, the ESW increases from 2.5 V (-0.9 to 1.6 V vs. Ag/AgCl) for 1 m $LiNO_3$ to 3.2 V (-1.25 to 1.95 V vs. Ag/AgCl) for OSGE. The ESW of $LiNO_3$ RTSGE is 3.1 V (-1.15 to 1.95 V vs. Ag/AgCl), which is 0.1 V lower than that of OSGE, meaning the further expanded ESW of OSGE. All ESWs here are determined through eliminating non-faradic current which is distinguished by lower slopes around onset points for HER/OER [317]. Besides wide ESWs, sufficient ionic conductivity is another important parameter for battery electrolytes, which can ensure the desired charge and mass transportation within electrolyte and electrode-electrolyte interface. Therefore, the ionic conductivity of above-mentioned electrolytes is measured by EIS at RT using 0.1 M KCl aqueous solution (1.28×10^{-2} $S \cdot cm^{-1}$ conductivity at RT) as the calibration solution (Fig. 6.1a) [39, 207]. The ionic conductivity increased with the concentration of $LiNO_3$ at first, then reached a maximum of 1.88×10^{-1} $S \cdot cm^{-1}$ when the concentration reached 8 m. After that, the ionic conductivity decreased with increased concentration, till 2.51×10^{-2} $S \cdot cm^{-1}$ for 33 m (OSGE). The decreased ionic conductivity is generated by enhanced viscosity with the raised $LiNO_3$ concentration (Fig. 6.2a), which grows from 86 $mPa \cdot s^{-1}$ for 1 m $LiNO_3$ to 1211 $mPa \cdot s^{-1}$ for RTSGE (15 m $LiNO_3$-PVA), then experiences a dramatic surge to 11986 $mPa \cdot s^{-1}$ for OSGE (33 m $LiNO_3$-PVA) due to the quasi-solid state. Although the ionic conductivity of OSGE is lowest among the tested samples, it is still comparable with the previously reported values for solid-state, polymer organic-liquid and even aqueous salt-concentrated electrolytes, which is high enough to be used as an electrolyte for battery [187, 329-331]. Theoretically, the ionic conductivity of OSGE will be lowered by the crystallized salt and significantly enhanced viscosity. However, in OSGE, crystalized salts can be dispersed equably with the aid of PVA as in most sol-gel

synthesis processes, which means that the Li$^+$-conduction RTSGE can still form a continuous phase with high ionic conductivity.
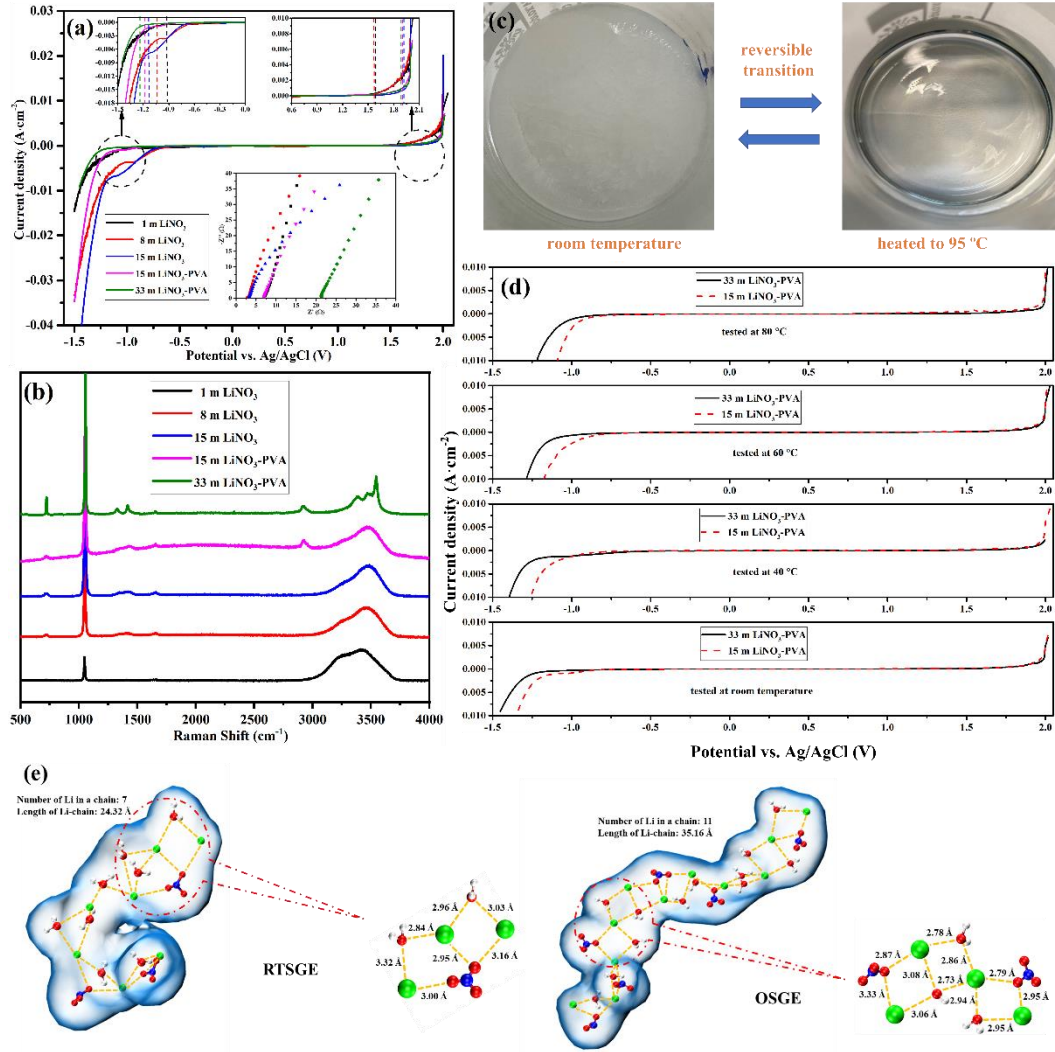
Fig. 6.1 (a) LSV curves of the LiNO$_3$-based aqueous electrolytes under 1 mV·s^{-1} sweep rate with relevant EIS test as insert graph. (b) Raman spectra of the LiNO$_3$-based aqueous electrolytes with 400-4000 cm^{-1} test range. (c) Optical images of top view of OSGE at RT and 95 °C. (d) ESWs variation of both OSGE and RTSGE vs. temperature under 1 mV·s^{-1} sweep rate. (e) Li$^+$ primary solvation sheath evolution from RTSGE to OSGE.

To verify the interaction between Li$^+$ and water molecules, along with solidifying of electrolyte and increased salt concentration, Raman spectrum test is employed, with results shown in Fig. 6.1b. A strong peak at ~3460 cm^{-1} together with a shoulder at 3100-3250 cm^{-1} can be observed in the Raman spectrum of 1 m LiNO$_3$,

which is assigned to O-H stretching vibration of water molecules. The broad O-H peak indicates that more free H bonds than donor-acceptor/donor-donor-acceptor H bonds within water molecule networks [297]. With increased $LiNO_3$ concentration, the shoulder disappears, while a new peak appears at ~3500 cm^{-1} in the Raman spectrum of OSGE. This transition indicates the diminishing population of free water molecules at such extreme concentrations [194]. Moreover, the intensity of peaks at ~1056 and ~721 cm^{-1} attributed to symmetrical and unsymmetrical stretching vibration of NO_3^- respectively are increased at higher $LiNO_3$ concentrations, with the higher intensity ratio between the peaks for NO_3^- and that for O-H vibration [332]. The change of NO_3^--correlated peaks reveals the solidification of the electrolytes (intrinsically the de-solvation which will be demonstrated in MD simulation) [131, 194], while the shrink of free H bonds (3100-3250 cm^{-1}) indicates the waned free H-bond networks thereby suppressing the electrolysis of water thermodynamically (reaction potential) and kinetically (electron transfer across interface), and broadening the ESWs of electrolytes [295]. On the purpose of fundamental explanation on the wider ESW of OSGE than that of RTSGE, MD simulation was employed with Li^+ solvation sheaths shown in Fig. 6.1e. Through the simulation result, the average coordination number of Li^+ and water molecules in OSGE is found to be slightly reduced (no more than 0.5) than that in RTSGE after 4 Å. Moreover, the average distance between Li^+ and NO_3^- is shortened as well, from around 3.0 for RTSGE to 2.8 Å for OSGE. According to the published papers, at over-saturated situations, electrolyte configuration evolves from solvent-separated ion pair (SSIP)-dominated structures to contact ion pair (CIP)-dominated structure (shown in Fig. 1.14a). This situation of electrolytes is merely composed of inactive ''frozen-like'' solvent, de-solvated Li^+ constituted crystal-like lithium salt solute which is proved by the Raman test in the Fig. 6.1b as well, hence more aggressive electrolyte is obtained with even wider ESW. However, the liquid structure of OSGE hinders the free mitigation of charge carriers, thus lowers the ionic conductivity of OSGE.
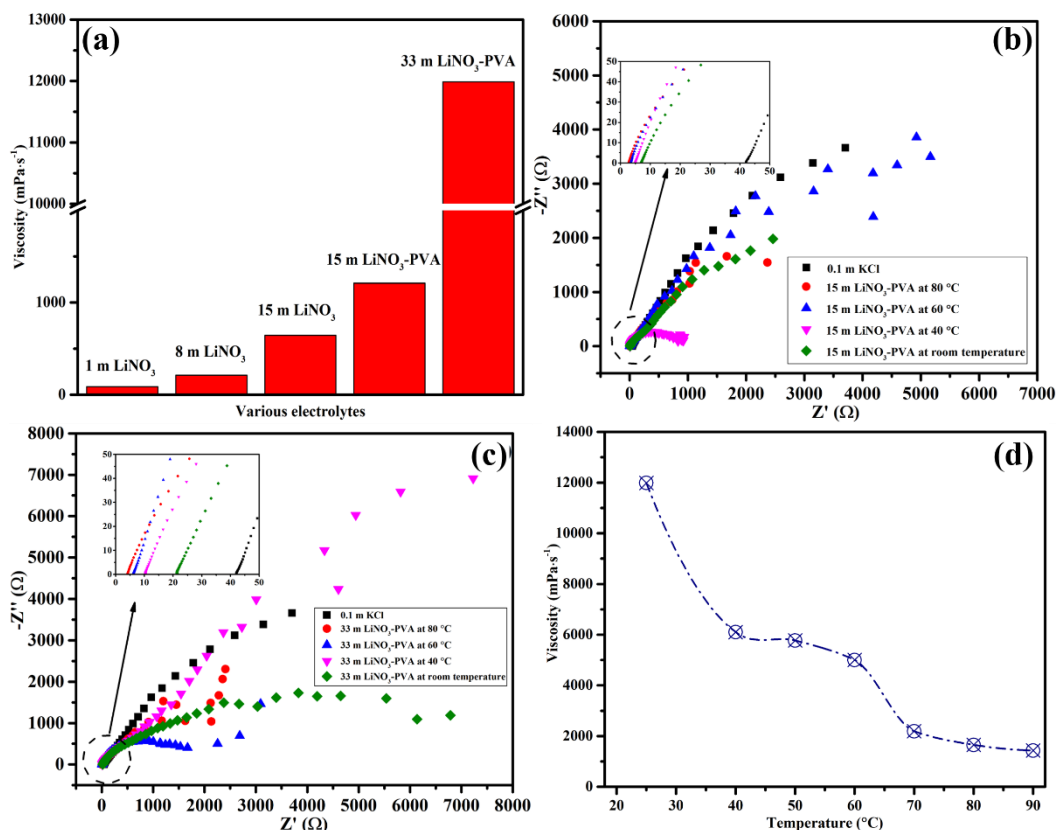
Fig. 6.2 (a) Viscosity of electrolytes with different concentration; (b) EIS plot of RTSGE obtained at various temperatures; (c) EIS plot of OSGE obtained at various temperature; (d) Relationship between viscosity of OSGE and temperature.

As a good commercial battery, a wide working temperature window is another key parameter for working against extreme climates and responding to situations such as mechanical damage, overheating and overcharging [333, 334]. Thus, the ESWs of OSGE were collected at RT, 40, 60 and 80 ℃ respectively with those of RTSGE for comparison. Before that, the top-view optical images of OSGE at versus temperatures are recorded in Fig. 6.1c regarding the sample at RT and heated at 95 ℃ (the temperature used for preparing OSGE). The appearance of OSGE is changed from white gel at RT to transparent sol at 95 ℃ (Fig. 6.1c), which is reversible. It is believed by us that this kind of change is regarded as glass transition, which will be demonstrated by STA later. The LSV curves of OSGE and RTSGE obtained at different temperatures under 1 mV·s^{-1} sweep rate is shown in Fig. 6.1d. The ESW of RTSGE is slightly decreased with increased temperature, from 3.1 V (-1.15 to 1.95 V vs. Ag/AgCl) at RT to 2.8 V (-0.9 to 1.9 V vs. Ag/AgCl) at 80 ℃, while the corresponding ESW of OSGE decreases from 3.2 V (-1.25 to

146

Table 6.1 Summary on ESWs and ionic conductivity of various electrolytes.

Sample	ESW vs. Ag/AgCl at 1 mV·s^{-1} (V)	Ionic conductivity (S·cm^{-1})	Test temperature (°C)
1 m LiNO$_3$	2.5 (-0.9 to 1.6)	7.65×10^{-2}	RT
8 m LiNO$_3$	2.65 (-1.05 to 1.6)	2.40×10^{-1}	RT
15 m LiNO$_3$	3.05 (-1.1 to 1.95)	1.68×10^{-1}	RT
15 m LiNO$_3$-PVA	3.1 (-1.15 to 1.95)	7.63×10^{-2}	RT
15 m LiNO$_3$-PVA	3.0 (-1.05 to 1.95)	1.06×10^{-1}	40 °C
15 m LiNO$_3$-PVA	2.85 (-0.95 to 1.9)	1.58×10^{-1}	60 °C
15 m LiNO$_3$-PVA	2.8 (-0.9 to 1.9)	1.94×10^{-1}	80 °C
33 m LiNO$_3$-PVA	3.2 (-1.25 to 1.95)	2.51×10^{-2}	RT
33 m LiNO$_3$-PVA	3.15 (-1.2 to 1.95)	5.18×10^{-2}	40 °C
33 m LiNO$_3$-PVA	3.05 (-1.1 to 1.95)	8.66×10^{-2}	60 °C
33 m LiNO$_3$-PVA	3.0 (-1.05 to 1.95)	1.28×10^{-1}	80 °C

1.95 V vs. Ag/AgCl) to 3 V (-1.05 to 1.95 V vs. Ag/AgCl), determined by the faradic current with higher slope (compared with slope of the non-faradic area) in the LSV curves. It has been noticed that the onset of OER in the LSV curve of OSGE maintains at various temperatures, indicating the high stability of OSGE against elevated temperatures, while the narrowed ESW is mainly from HER at

the negative side. The high concentration of LiNO$_3$ salt can effectively suppress the OER but less effective towards the HER at elevated temperatures. The ionic conductivity of both LiNO$_3$ RTSGE and OSGE increased at elevated temperature, reaching 1.94 S·cm^{-1} (RTSGE) and 1.28 S·cm^{-1} (OSGE) at 80 ℃, respectively (Fig. 6.2b and 6.2c), originating from the decreased viscosity at elevated temperatures (Fig. 6.2d). There are two drastic viscosity transition in the viscosity-temperature curve, the one from 11986 to 6102 mPa·s^{-1} between RT and 40 ℃ is caused by the dissolution of LiNO$_3$ salt, the other one from 5005 to 2190 mPa·s^{-1} between 60 to 70 ℃ is due to the glass transition of OSGE, which will be further demonstrated in STA test. The ESWs and ionic conductivity of all tested electrolytes at all temperatures are summarized in Table 6.2.
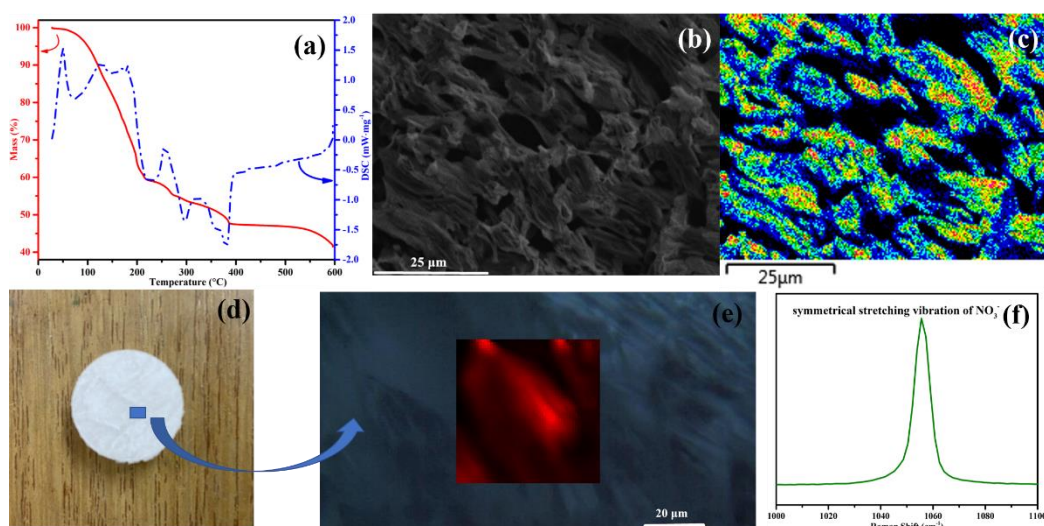
Fig. 6.3 (a) TGA and DSC curves of OSGE from room temperature to 600 °C; (b) SEM image of OSGE with 25 μm resolution; (c) Corresponding EDX mapping of carbon element in OSGE; (d) Optical image of OSGE casted on the glass microfiber substrate; (e) Raman mapping within 50×50 μm area, generated through point intensity selection; (f) Peak used for Raman point intensity selection.

The ESW and ionic conductivity of the LiNO$_3$ OSGE have been investigated in detail above, while STA is further employed to study stability and phase transition of OSGE at elevated temperatures (Fig. 6.3a). The mass of OSGE generally maintains constant within 100 ℃ (only ~ 5% mass loss up to 100 ℃), indicating the desired water retention in the LiNO$_3$ OSGE. There is an endothermic peak at ~45 ℃ in the DSC curve, which could be the dissolution of the RT-crystallized

LiNO$_3$. Through the cross point of the tangent lines for both endothermic and exothermic area, the glass transition point of OSGE is determined as ~65 ºC, after which the viscosity is significantly lowered, indicating the gel-sol transition (consistent with the viscosity change from 5005 to 2190 mPa·s^{-1} among the temperature range from 60 to 70 ºC in Fig. 6.2d). There are two endothermic peaks in the DSC curve at ~131 and ~180 ºC, respectively, together with the dramatic mass loss in the 100 to 200 ºC region on TGA curve indicating the water loss and possible decomposition of PVA and LiNO$_3$ [335, 336]. Finally, the remaining mass is ~42% at 600 ºC, attributing to the mass of lithium oxides and nitrites, after turning that into the mass of LiNO$_3$, it is believed that LiNO$_3$ occupies the major mass ratio (~70 wt%) of original OSGE at RT. The morphology of LiNO$_3$ OSGE was characterized by SEM/EDX (Fig. 6.3b and 6.3c). Some micron sized pores are observed, which are due to the loss of water under the high vacuum during the SEM measurement environment. Carbon in PVA is chosen as the element to show the dispersed salts and continuous hydrogel (Fig. 6.3c). The dark area of EDX mapping is not only introduced by the pores, but also by the crystallized LiNO$_3$. Furthermore, to demonstrate the morphology of OSGE more clearly by eliminating the interference from high vacuum environment of SEM, Raman mapping was employed. The optical image of OSGE coated on the glass fibre substrate is shown in Fig. 6.3d. A 50×50 μm selected area on the sample was characterized by Raman mapping with the spectrum range from 400 to 4000 cm^{-1}. The Raman mapping image in Fig. 6.3e was generated by peak intensity selection with the peak at ~1056 cm^{-1} standing for symmetrical stretching vibration of NO$_3^-$ (Fig. 6.3f). The intensity range of the Raman mapping is from 10000 to 26000 counts, varying from dark red to bright red as shown in Fig. 6.3e, which represents the continuous gel area and dispersed crystallized LiNO$_3$ area, respectively. Although the inhomogeneous morphology was observed, the LiNO$_3$ OSGE is still a good Li$^+$ conductor, as the ion-insulated LiNO$_3$ salt is isolated while there are continuous pathways for ions in gel area.

6.2.2 RT performance of ARLiBs based on LiNO$_3$ OSGE
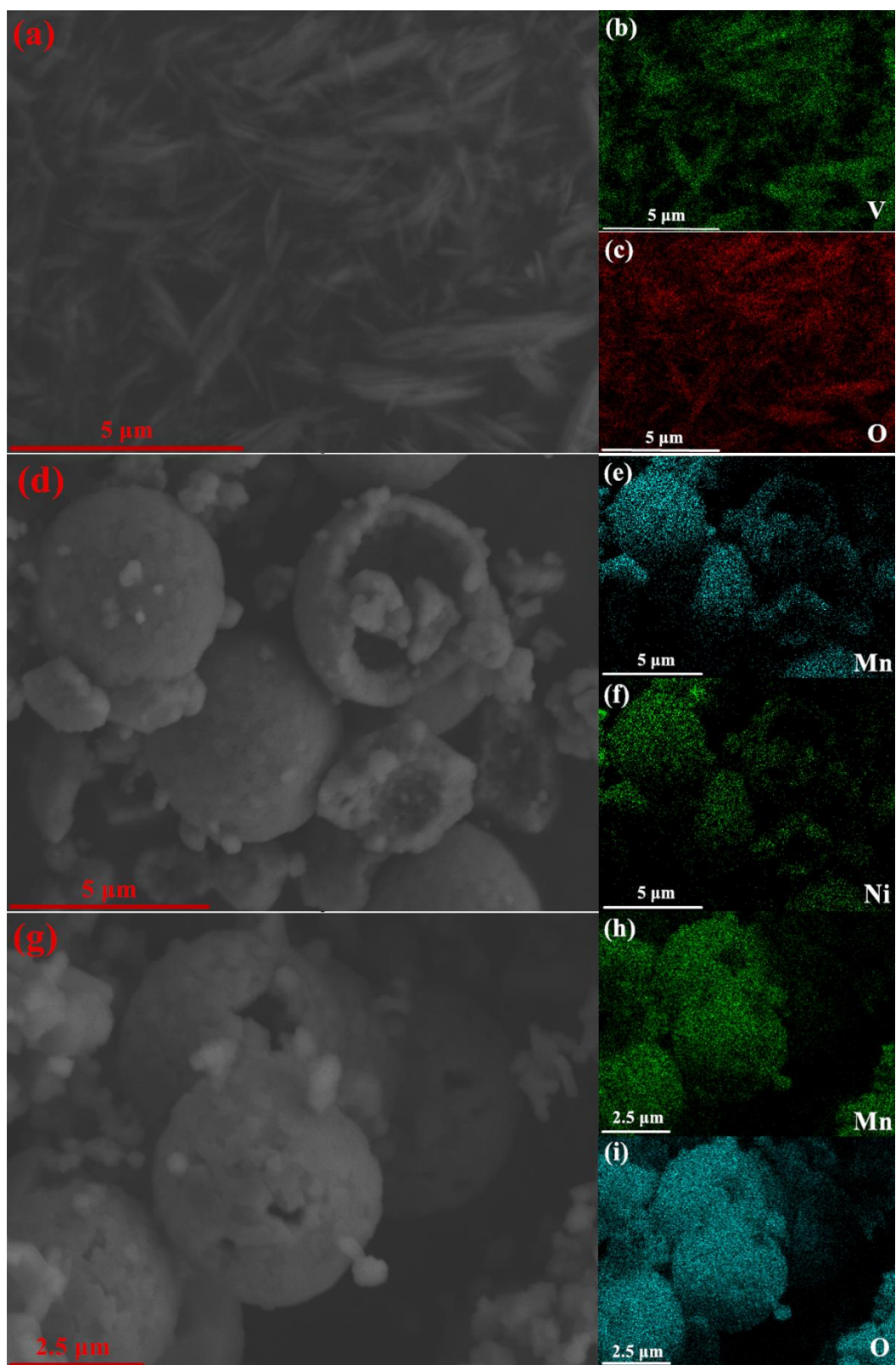
Fig. 6.4 (a-c) SEM image of VO_2 powder with relevant element mapping; (d-f) SEM image of $LiNi_{0.5}Mn_{1.5}O_4$ powder with relevant element mapping; (g-i) SEM image of $LiMn_2O_4$ powder with relevant element mapping.
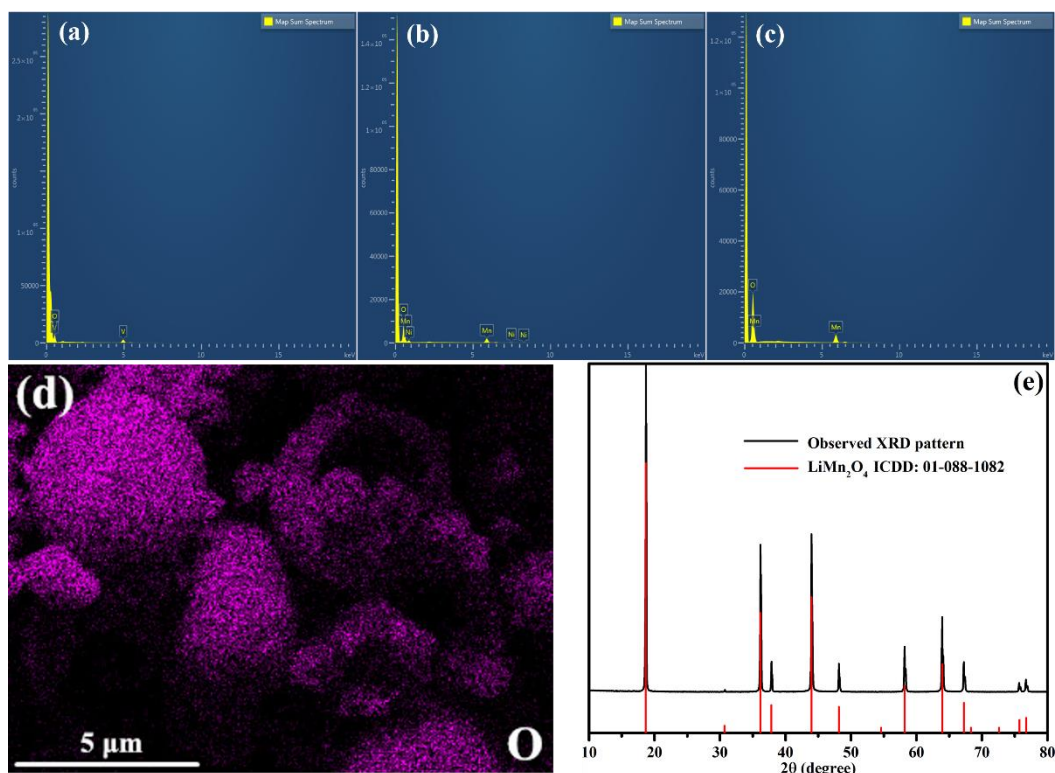
Fig. 6.5 (a, b, c) EDX elements analysis towards VO_2, $LiNi_{0.5}Mn_{1.5}O_4$ and $LiMn_2O_4$ powder; (d) EDX mapping on oxygen element of $LiNi_{0.5}Mn_{1.5}O_4$ powder; (e) XRD plot of $LiMn_2O_4$ powder.

In this study, VO_2 and $LiNi_{0.5}Mn_{1.5}O_4$ were selected as the anode and cathode respectively, and assembled with $LiNO_3$ OSGE as a CR2032 coin cell for battery performance measurement at RT. The cathode was changed to $LiMn_2O_4$ with higher bulk and surface stability for the measurements at elevated temperatures. The morphology of the three electrode powders is shown in Fig. 6.4. Single phase monoclinic VO_2 (ICDD: 01-084-7141, space group: C2/m), cubic $LiNi_{0.5}Mn_{1.5}O_4$ (ICDD: 04-018-2271, space group: Fd-3m) has been proved in previous work [193], while cubic $LiMn_2O_4$ (ICDD: 01-088-1082, space group: Fd-3m) was confirmed by XRD analysis (Fig. 6.5). The morphology of nanobelt VO_2 (Fig. 6.4a), hollow microsphere $LiNi_{0.5}Mn_{1.5}O_4$ (Fig. 6.4d) and $LiMn_2O_4$ (Fig. 6.4g) is determined by the SEM image with 5 and 2.5 μm resolution respectively. It is believed that the nanobelt morphology is able to improve electronic conductivity in the grain boundary of VO_2 thereby improving electrode kinetics [337]. The hollow microsphere of the $LiNi_{0.5}Mn_{1.5}O_4$ and $LiMn_2O_4$ cathodes can prevent the volume change of the electrode particles during repeated charging/discharging,

thus improving the cyclability [338]. The corresponding EDX analysis is shown in Fig. 6.5a-b, which delivers the peaks of O and V for VO_2, O, Mn and Ni for $LiNi_{0.5}Mn_{1.5}O_4$, and O and Mn for $LiMn_2O_4$, respectively. Meanwhile the mapping of these elements is shown in Fig. 6.4 (except O element of $LiNi_{0.5}Mn_{1.5}O_4$, shown in Fig. 6.5d), the relevant elements are homogeneously distributed within the nanobelts and hollow microspheres.
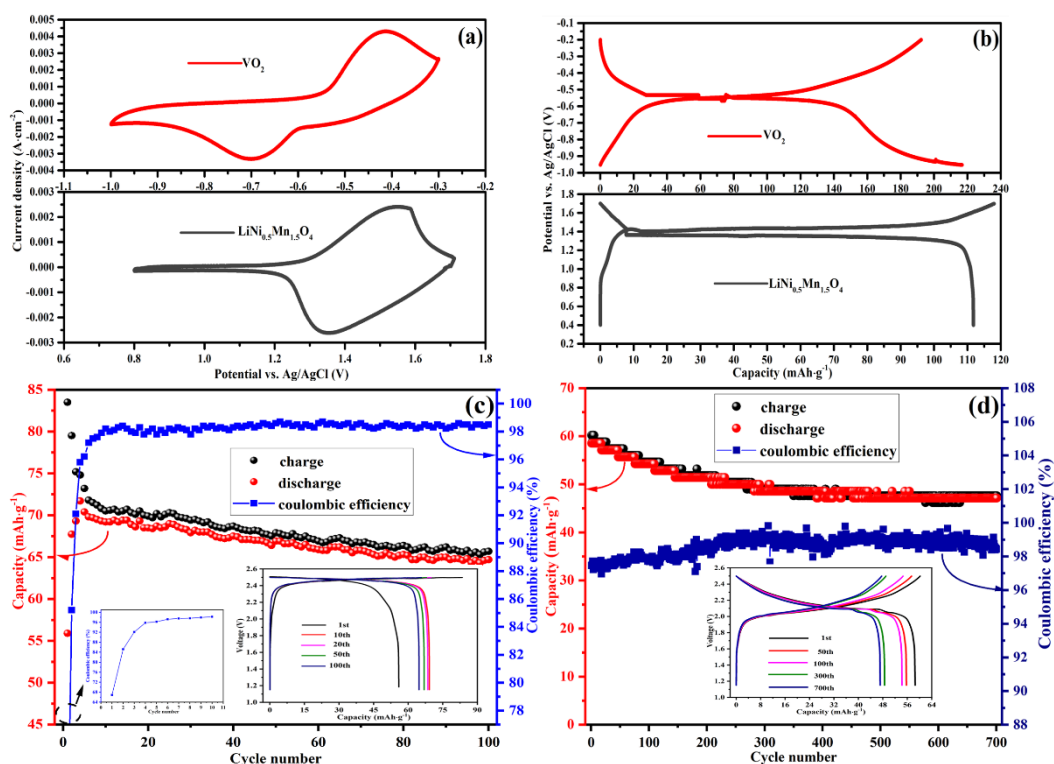
Fig. 6.6 (a) CV curves of VO_2 and $LiNi_{0.5}Mn_{1.5}O_4$ in three-electrode cell with OSGE under 1 $mV·s^{-1}$ sweep rate; (b) Charge/discharge curves of VO_2 and $LiNi_{0.5}Mn_{1.5}O_4$ in three-electrode cell with OSGE under 50 $mA·g^{-1}$ current density; (c) Cyclic performance of VO_2//$LiNi_{0.5}Mn_{1.5}O_4$ full cell under 1 C charge/discharge rate with according charge/discharge curves shown in the inset; (d) Cyclic performance of VO_2//$LiNi_{0.5}Mn_{1.5}O_4$ full cell under 3 C charge/discharge rate with according charge/discharge curves shown in the inset.

In order to demonstrate that $LiNO_3$ OSGE enables high voltage ARBs, $LiNi_{0.5}Mn_{1.5}O_4$ with high working potential was chosen as the cathode while VO_2 was chosen as the anode for the assembly of an ARLiB. Before full cell assembly, the working potential and capacity of VO_2//$LiNi_{0.5}Mn_{1.5}O_4$ in OSGE was

determined in three-electrode cells with VO_2 or $LiNi_{0.5}Mn_{1.5}O_4$ as the work electrode, AC as the counter electrode and Ag/AgCl as the reference electrode. The CV curves of VO_2 and $LiNi_{0.5}Mn_{1.5}O_4$ obtained at a sweep rate of 1 mV·s^{-1} are shown in Fig. 6.6a. The redox peaks are determined as -0.42/-0.70 V vs. Ag/AgCl for VO_2 and 1.56/1.36 V vs. Ag/AgCl for $LiNi_{0.5}Mn_{1.5}O_4$ respectively. The charge/discharge curves of VO_2 and $LiNi_{0.5}Mn_{1.5}O_4$ were collected under the current density of 50 mA·g^{-1}, within the potential range from -0.2 to -0.95 V vs. Ag/AgCl for VO_2 and 0.4 to 1.7 V vs. Ag/AgCl for $LiNi_{0.5}Mn_{1.5}O_4$. The corresponding charge/discharge curves shown in Fig. 6.6b are those after three test cycles, which deliver the average capacities of 19(2)/21(7) mAh·g^{-1} for VO_2 and 11(8) /11(2) mAh·g^{-1} for $LiNi_{0.5}Mn_{1.5}O_4$ respectively. The charge capacity of VO_2 and discharge capacity of $LiNi_{0.5}Mn_{1.5}O_4$ were utilized for determining the mass of active materials which is ~2.0 g·cm^{-2} for anode, ~3.5 g·cm^{-2} for cathode, respectively, determined through the inverse ratio on charge capacity of VO_2 (19(2) mAh·g^{-1}) against discharge capacity of $LiNi_{0.5}Mn_{1.5}O_4$ (11(2) mAh·g^{-1}).

Based on the capacity matching, one full cell with 2.4 mg VO_2 and 3.7 mg $LiNi_{0.5}Mn_{1.5}O_4$, together with $LiNO_3$ OSGE was assembled for GCD cycling tests under 1 C (110 mA·g^{-1}, derived from the discharge capacity of $LiNi_{0.5}Mn_{1.5}O_4$), from 1.1 to 2.5 V within 100 cycles (Fig. 6.6c). The charge/discharge curves of 1st, 10th, 20th, 50th and 100th cycles in Fig. 6.6c, deliver the voltage plateau of ~2.45 V, while the capacity (calculated on the mass of both anode and cathode, dividing the observed capacity by total active mass of anode and cathode) varies from 83.(5)/55.(9) mAh·g^{-1} with 66.(9)% CE at the first cycle to 65.(7)/64.(7) mAh·g^{-1} with 98.(5)% CE at 100th cycle. The discharge capacity reaches a maximum value of 71.(7) mAh·g^{-1} (95.(8)% CE) at 4th cycle, while the relevant energy density is calculated through integrating the discharge curve in Origin software, which is determined as 17(6) Wh·kg^{-1}. 3 C was chosen for the long-term performance test towards another new VO_2 (2.3 mg)//$LiNi_{0.5}Mn_{1.5}O_4$ (3.1 mg) coin cell. Repeated GCD was conducted towards another full cell with active materials of 2.1 mg for anode, 3.4 mg for cathode, which was cycled for 700 cycles (Fig. 6.6d). The discharge capacity is 58.(5) mAh·g^{-1} in the first cycle and 47.(1) mAh·g^{-1} in the last cycle with 80.(5)% capacity retention. Meanwhile, its CE increases with continuous charge/discharge reactions, which reaches above 99.(0)% after 500

cycles. Both the cyclic number and CE are impressive among the published works about the ARBs involving $LiNi_{0.5}Mn_{1.5}O_4$ cathodes [189, 339, 340].

6.2.3 Elevated-temperature performance of ARLiBs based on LiNO$_3$ OSGE

As mentioned above, a practical battery should work smoothly under various extreme circumstances, which usually requires a wide working temperature window. In this work, LiNO$_3$ OSGE retains wide enough ESWs at elevated temperatures, therefore the battery performance of LiNO$_3$ OSGE was further investigated at 40, 60 and 80 °C, respectively. To demonstrate the performance of OSGE-based ARLiBs at elevated temperatures, $LiMn_2O_4$ with higher bulk and surface stability was employed to replace the $LiNi_{0.5}Mn_{1.5}O_4$ cathode. Before the battery performance test, the CV curves of VO_2 anode and $LiMn_2O_4$ cathode with areas of 1 cm^2 were collected at various temperatures (RT to 80 °C) under different sweep rates (0.2 to 1.0 mV·s^{-1}). The CV curves obtained at RT are displayed at Fig. 6.7a for VO_2 and 6.7b for $LiMn_2O_4$. The CV curves at elevated temperatures are shown in Fig. 6.8a-c and 6.8d-f, respectively, in which both thermodynamic and kinetic transition with temperature can be observed. Thermodynamically, the redox couple of VO_2 is changed from -0.45 (II)/-0.67 (I) V at RT to -0.33 (II)/-0.55 (I) V vs. Ag/AgCl at 80 ° C under 1 mV·s^{-1} sweep rate, shifting to the higher potential with the similar tendency under other sweep rates. Likewise, the two redox couples of $LiMn_2O_4$ are shifted from 1.16 (IV)/1.06 (I) and 1.03 (III)/0.93 (II) V at RT to 1.19 (IV)/1.12 (I) and 1.06 (III)/1.01 (II) V vs. Ag/AgCl at 80 °C with a similar trend under other sweep rates. The transition to higher potential of all peaks at elevated temperatures can be easily explained based on the Nernst equation.

Kinetically, the diffusion coefficient of Li$^+$ (D_{Li}) of both VO_2 and $LiMn_2O_4$ electrodes should be improved at higher temperatures. To prove that, the relationship between peak current (i_P) and sweep rate (v) was investigated, which can be summarized according to:

$$i_p = av^b \tag{6.2}$$
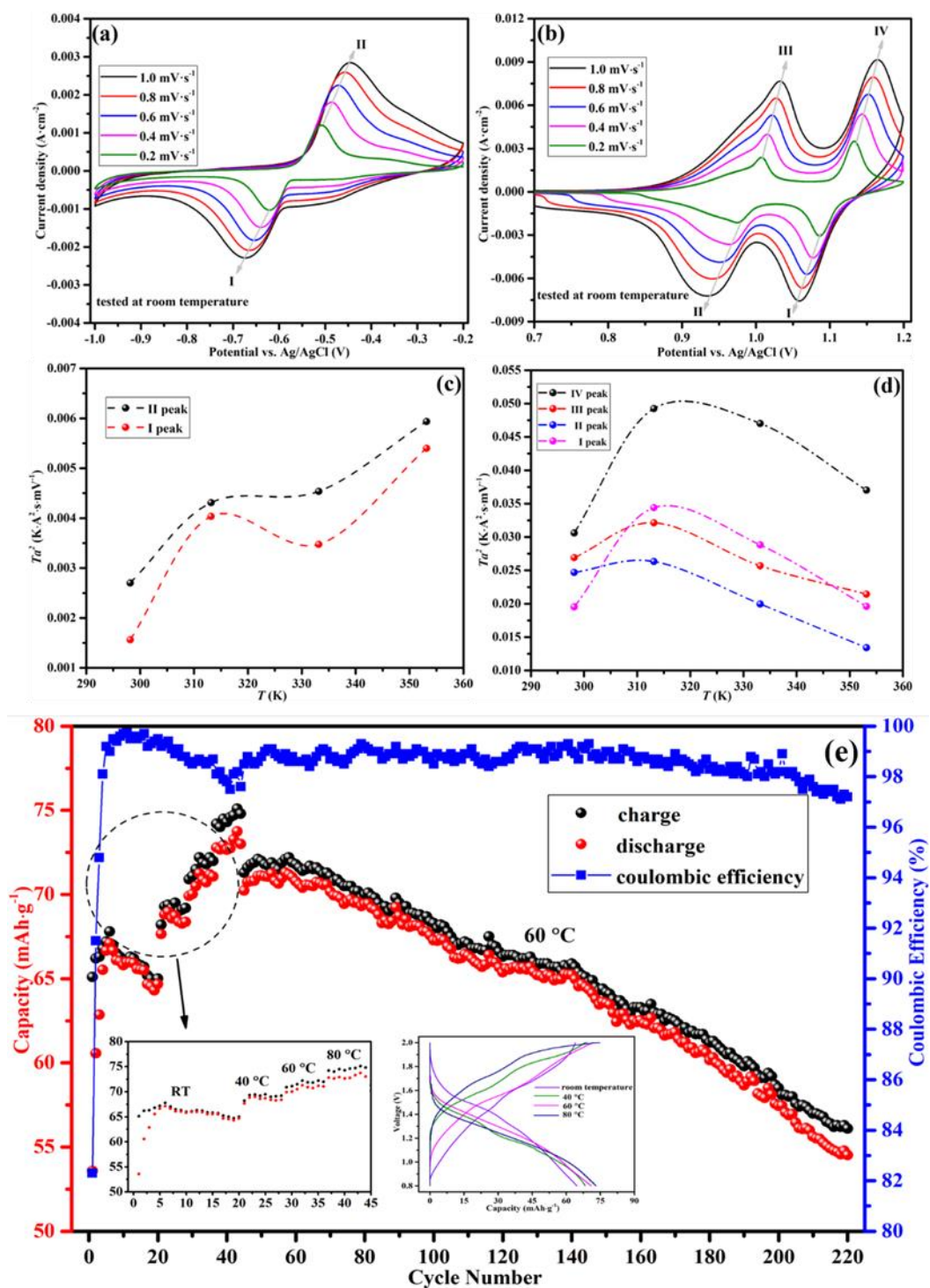
Fig. 6.7 (a) CV curves of VO$_2$ electrode in three-electrode cell with OSGE under various sweep rates at RT; (b) CV curves of LiMn$_2$O$_4$ electrode in three-electrode cell with OSGE under various sweep rates at RT; (c) Relationship between T and a^2T of VO$_2$ electrode; (d) Relationship between T and a^2T of LiMn$_2$O$_4$ electrode; (e) Cyclic performance of VO$_2$//LiMn$_2$O$_4$ full cell under 3 C charge/discharge rate at different temperatures with according charge/discharge curves shown in the inset.

It has been sufficiently demonstrated that the intercalation of battery behaviour is controlled by cation diffusion within the crystalline framework of electrode materials, and the corresponding voltametric response can be summarized as :

$$i_p = nFACD_{Li}^{\frac{1}{2}}v^{\frac{1}{2}}\left(\frac{\alpha nF}{RT}\right)^{\frac{1}{2}}\pi^{\frac{1}{2}}\chi(bt) \tag{6.3}$$

, where C is surface concentration of electrode material (the difference caused by the charge-discharge reaction here is negligible due to super concentration of $LiNO_3$ OSGE), α is the transfer coefficient, n is the number of electrons included in the electrode reaction, F is the Faraday constant, A is the surface area of the electrode material, T is the absolute temperature, R is the molar gas constant, and the function (bt) represents the normalized current [341]. For battery behaviour, the coefficient of b in equation (2) should be 0.5 as diffusion-controlled process [342]. In our system, the parameters of n, F, A, C, α, n and bt should be the same versus the variation of temperature, they can be expressed as a constant k, which is equalled as:

$$k = (nF)^{\frac{3}{2}}AC\alpha R^{-1/2}\pi^{1/2}\chi(bt) \tag{6.4}$$

Depending on the equations (6.2), (6.3) and (6.4), the coefficient a can be expressed as:

$$a = kD_{Li}^{\frac{1}{2}}T^{-1/2} \tag{6.5}$$

Thus, derived from equation (2.5), the relationship between T and D_{Li} can be concluded as:

$$D_{Li} = a^2Tk^{-2} \tag{6.6}$$

, in which a is equalled to the tangent of the straight lines (Fig. 6.8g-l) derived from Fig. 6.7a-b, 6.8a-c and 6.8d-f. Based on equation (2.6), D_{Li} should own the same tendency with a^2T, thus the variation of a^2T against T regarding VO_2 and

LiMn$_2$O$_4$ is shown in Fig. 6.7c and 6.7d, respectively, in which the observed temperature from RT to 80 ℃ is converted into absolute temperature (T) with the unit of Kelvin (K). For VO$_2$, the a^2T of both I and II peaks is basically increased with increasing T except for peak I at 333.15 K (60 ℃), indicating the generally enhanced D_{Li} of VO$_2$ with increased temperature. For LiMn$_2$O$_4$, a^2T of all the peaks (I, II, III and IV) has the same tendency, reaching a maximum value at 313.15 K (40 ℃). The difference between anode and cathode of D_{Li} variation towards temperature induces the question whether Li$^+$ diffusion of anode or cathode affect more in charge/discharge reaction for the whole battery, which will be further discussed in the full cell performance test.
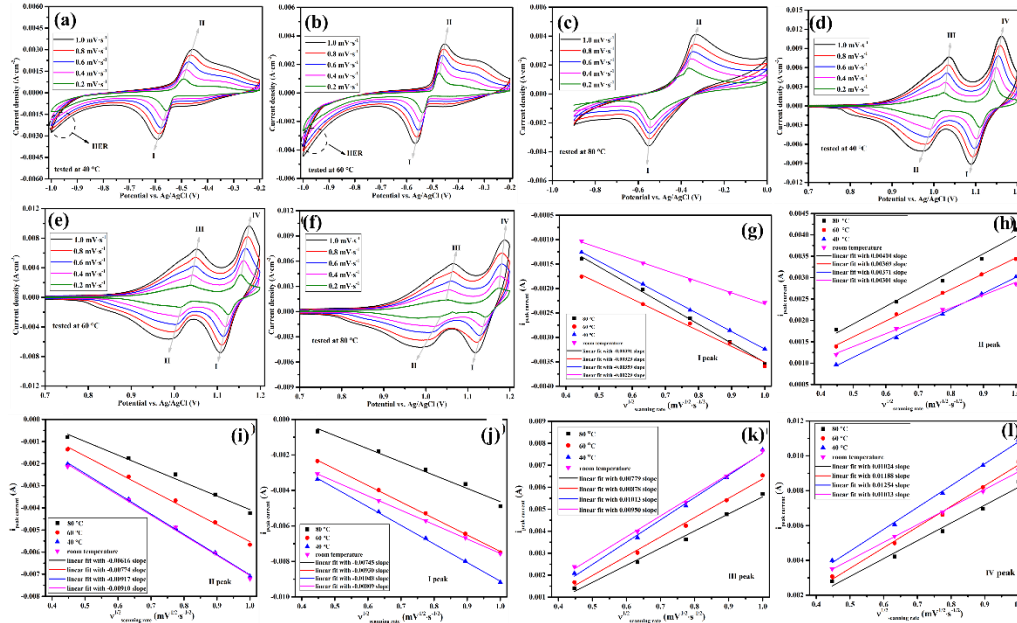
Fig. 6.8 (a-c) CV curves of VO$_2$ electrode in three-electrode cell with OSGE under various sweep rates at 40, 60 and 80 °C; (d-f) CV curves of LiMn$_2$O$_4$ electrode in three-electrode cell with OSGE under various scanning rates at 40, 60 and 80 °C; (g-h) Relationship between i and v of I and II peaks of VO$_2$ electrode at various temperatures. (i-l) Relationship between i and v of I, II, III and IV peaks of LiMn$_2$O$_4$ electrode at various temperatures.
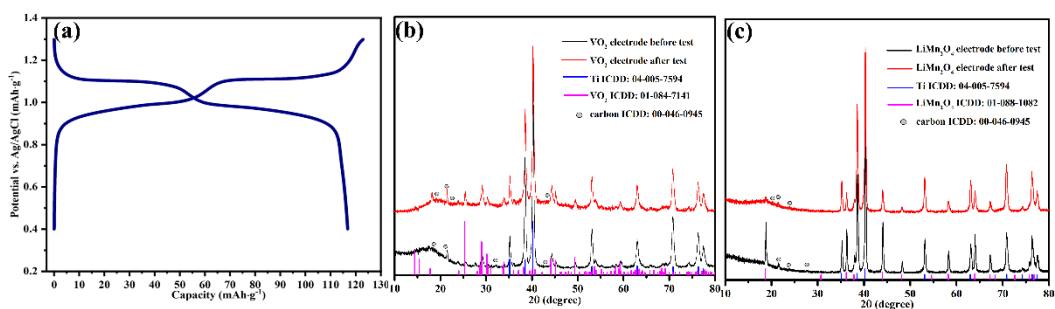
Fig. 6.9 (a) Charge/discharge curves of $LiMn_2O_4$ in three-electrode cell with OSGE under 50 mA·g^{-1} current density; (b-c) XRD plot of VO_2, and $LiMn_2O_4$ electrode before and after elevated-temperature GCD test.

Before being assembled into a full cell, the average practical capacity of $LiMn_2O_4$ is determined through the charge-discharge curve in a three-electrode cell (Fig. 6.9a), which is 12.(3)/11.(7) mAh·g^{-1} under a current density of 50 mA·g^{-1}, thus the mass loading of $LiMn_2O_4$ is still controlled as ~3.5 mg·cm^{-2} as well. The full cell with 1.9 mg anode active matter and 3.4 mg cathode active matter was tested with GCD cycling under 3 C (1 C=110 mA·g^{-1}) at various temperatures from RT to 80 °C (Fig. 6.7e). The capacity of the last cycle within the same tested temperature is elevated from 65.(0)/64.(7) (99.(5)% CE) at room temperature, 69.(2)/68.(4) (98.8% CE) at 40 °C, 72.(0)/71.(1) (98.(7)% CE) at 60 °C, to 74.(8)/73.(0) mAh·g^{-1} (97.(6)% CE) at 80 °C. The relevant charge/discharge curves are displayed in the inserted graph of Fig. 6.7e. The improved capacity is induced by the facilitated electrode kinetics and mass transportation, which owns the similar tendency with D_{Li} vs. T of VO_2 rather than that of $LiMn_2O_4$. While the CE of this cell is slightly decreased with the elevated temperature due to the solvent electrolysis caused by enhanced kinetics of OER and HER. Considering both capacity and CE, 60 °C was selected for long-term performance testing under the same rate and voltage limitation as for RT. The parameter of initial cycle is 72.(1)/71.(1) mAh·g^{-1} (98.(6)% CE), which is transferred into 56.(1)/54.(5) mAh·g^{-1} (97.(2)% CE) after 176 cycles with 76.(6) % capacity retention. The total cycling of this battery at various temperatures is 220 cycles. To best of our knowledge, this elevated-temperature stability is remarkable among the investigated ARBs [184, 196], although the capacity still has room to be improved. The XRD plot of VO_2 and $LiMn_2O_4$ electrodes, before and after elevated temperature test are shown in Fig. 6.9b and 6.9c. The phases are maintained after being tested at elevated temperatures,

demonstrating the good chemical compatibility with OSGE in this ARLiB, while the possibility of amorphous secondary phase cannot be eliminated.
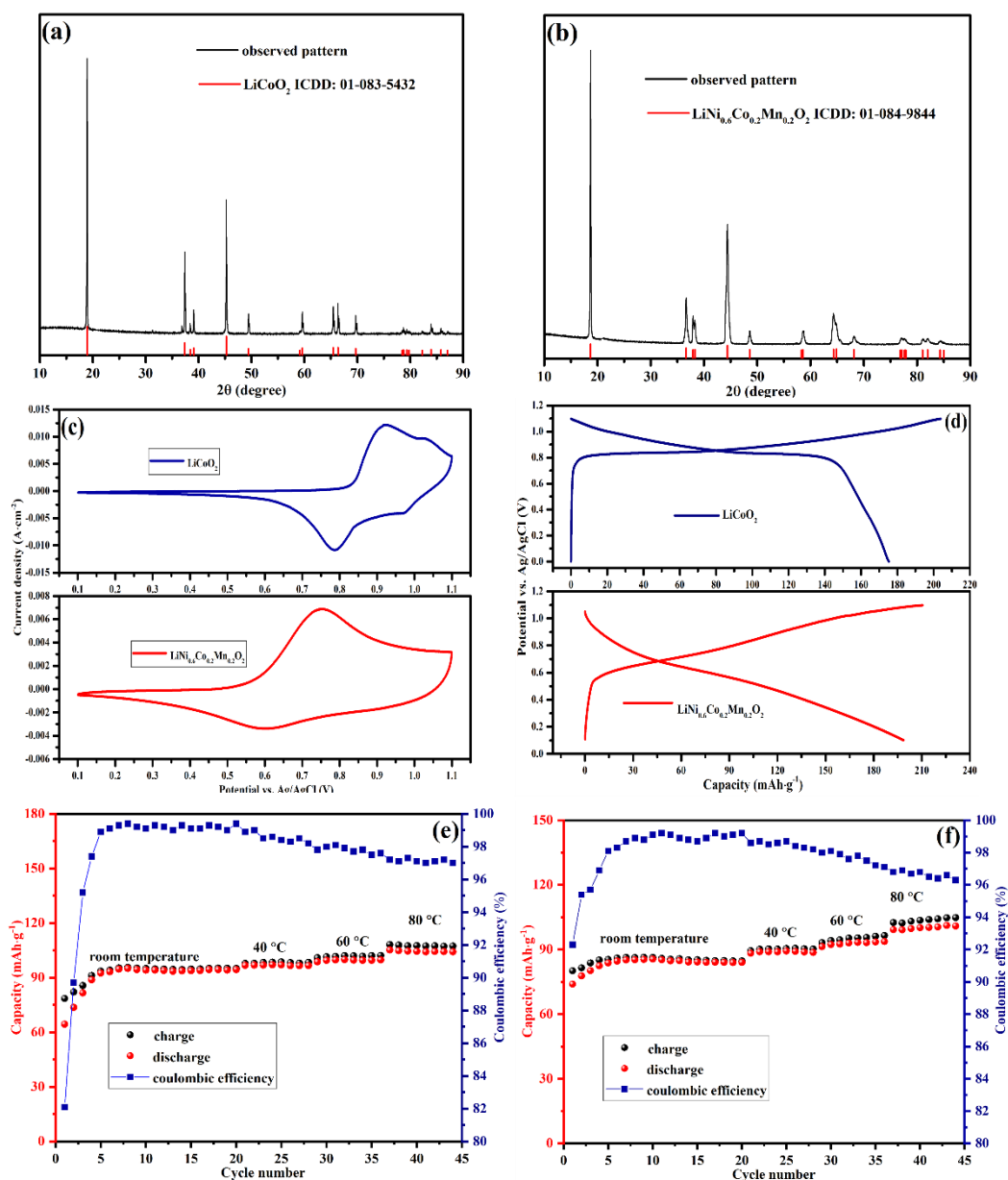
Fig. 6.10 (a) XRD plot of LiCoO$_2$; (b) XRD plot of LiNi$_{0.6}$Co$_{0.2}$Mn$_{0.2}$O$_2$; (c) CV curves of LiCoO$_2$ and LiNi$_{0.6}$Co$_{0.2}$Mn$_{0.2}$O$_2$; (d) Charge/discharge curves of LiCoO$_2$ and LiNi$_{0.6}$Co$_{0.2}$Mn$_{0.2}$O$_2$; (e) Cyclic performance of VO$_2$//LiCoO$_2$ full cell at elevated temperaures; (f) Cyclic performance of VO$_2$//LiNi$_{0.6}$Co$_{0.2}$Mn$_{0.2}$O$_2$ full cell at elevated temperaures.

In order to validate the universality of this OSGE, layered $LiCoO_2$ and $LiNi_{0.6}Co_{0.2}Mn_{0.2}O_2$ electrodes were prepared with pure phase (ICDD: 01-083-5432 for $LiCoO_2$ and ICDD: 01-084-9844 for $LiNi_{0.6}Co_{0.2}Mn_{0.2}O_2$) shown in Fig. 6.10a and 6.10b. The corresponding CV curves demonstrate 0.92/0.79 and 1.03/0.97 V vs. Ag/AgCl redox couples for $LiCoO_2$ and 0.75/0.60 V vs. Ag/AgCl for $LiNi_{0.6}Co_{0.2}Mn_{0.2}O_2$ (Fig. 6.10c). The charge/discharge curves of $LiCoO_2$ and $LiNi_{0.6}Co_{0.2}Mn_{0.2}O_2$ were collected in a three-electrode system with AC as counter electrode, delivering average discharge capacities of 17(5) and 19(9) $mAh \cdot g^{-1}$ (Fig. 6.10d). Based on the discharge capacity, the loading mass of $LiCoO_2$ and $LiNi_{0.6}Co_{0.2}Mn_{0.2}O_2$ were determined as ~2.2 and ~2.0 $mg \cdot cm^{-2}$, then assembled with VO_2 anode and $LiNO_3$ OSGE in the coin cells. The VO_2 (2.3 mg)//$LiCoO_2$ (2.1 mg) and VO_2 (2.2 mg)//$LiNi_{0.6}Co_{0.2}Mn_{0.2}O_2$ (1.8 mg) full cells were tested under 3 C rate, at various temperatures from RT to 80 ℃ as shown in Fig. 6.10e and 6.10f which demonstrate the feasibility to employ these two layered electrodes in OSGE system at elevated temperatures.

6.3 Conclusions

In this chapter, the use of OSGE based on $LiNO_3$ and PVA further expands the ESW of corresponding RTSGE, on the purpose of achieving ARBs with higher energy density and stability. The wider ESW is originated from the contact ion pair and de-solvation in solvation structures, which was demonstrated by the Raman spectra and MD simulation. $LiNi_{0.5}Mn_{1.5}O_4$ was investigated as the cathode with high working potential, which was assembled with a VO_2 anode in a full battery based on $LiNO_3$ OSGE. This 2.5 V ARLiB was successfully operated for 700 cycles with near 99% CE, which is excellent among the published works on ARBs utilising a $LiNi_{0.5}Mn_{1.5}O_4$ cathode. Moreover, the good stability of OSGE at elevated temperature (to 80 °C) has been demonstrated, enabling the impressive 220 cycles of the VO_2//$LiMn_2O_4$ battery at elevated temperatures. Whilst the universality of this OSGE was proved as well via being applied into layered cathode. Compared with perchlorate OSGE, it shows better stability against high working voltage (2.5 V vs. 2.0 V) and elevated temperatures. In summary, this work is significant in three aspects. Firstly, it proves the feasibility of utilizing

inhomogeneous electrolytes only if there are continuous pathways for charged ions and mass transportation. Secondly, this can be a strategy to expand the salts used in salt-concentrated electrolytes from costly, high-solubility organic salts to inexpensive, relatively low-solubility inorganic substitutions. And last but not the least, it provides a strategy to develop aqueous electrolytes with wide ESW at evaluated temperatures to tolerate the over-heating. In next chapter, acetates will be developed as suitable salt for OSGE, which can manipulate the potential challenge from rate capability to OSGE-based ARBs via hybrid charge storage mechanism.

CHAPTER 7 Acetate "oversaturated gel electrolyte" for high-stability aqueous Zn//MnO₂ battery

7.1 Abstract

As a good commercial battery, the ability to work under extreme climates and respond to incidents such as overheating and overcharging is greatly demanded [334, 343]. Thus, herein, acetate OSGE was prepared with 1 m $Zn(OAc)_2$ and 40 m KOAc with PAA at 75 °C. An aqueous Zn//MnO₂ battery based on the OSGE exhibited excellent stability (2000 charge-discharge cycles at a rate of 5 C) and high energy density (38(6) $Wh \cdot kg^{-1}$ based on 2.6 mg MnO₂) at an overcharge working voltage of 2.0 V. At RT, the OSGE could further extend the ESW to 3.45 V (-1.5 to 1.95 V vs. Ag/AgCl), which is 0.2 V wider than that of acetate RTSGE of 1 m $Zn(OAc)_2$+31 m KOAc-PAA). Meanwhile, an ESW of 3.3 V (-1.35 to 1.95 V vs. Ag/AgCl) could be maintained at 80 °C. The wide ESW of OSGE not only suppressed the formation of Zn dendrites at RT, but also enabled good performance of the aqueous Zn//MnO₂ battery at a temperature range between RT to 80 °C (300 cycles at 60 °C with 90.6% capacity retention). The reaction mechanism at the Zn anode in OSGE was determined as stripping/plating, while that of the MnO₂ cathode was deemed as hybrid charge storage consisting of capacitive behaviour and a proton-involved electrode reaction. OSGE expands the range of salts used in a salt-concentrated electrolyte system by breaking through the limitation of solubility.

7.2 Results and discussion

7.2.1 Property of OSGE

The ESW of electrolytes is equal to the difference between the potential of electrolyte reduction at negative potentials and the potential of electrolyte oxidation at positive potentials, whilst eliminating the effect from the charge/discharge process of the double electric layer in electrode-electrolyte interfaces [317, 344]. Therefore, the ESW of OSGE and RTSGE at temperatures of RT, 40, 60 to 80 °C were determined via two different slopes around onset

points for both negative and positive sides of LSV curves (Fig. 7.1a). The ESW of OSGE at RT was 3.45 V (-1.5 to 1.95 V vs. Ag/AgCl) and could be maintained at higher temperatures of 40 and 60 ℃. This value slightly decreased to 3.30 V (-1.35 to 1.95 V vs. Ag/AgCl) at 80 °C. In contrast, the ESW of RTSGE decreased from 3.25 V (-1.35 to 1.9 V vs. Ag/AgCl) at RT to 3.0 V (-1.3 to 1.7 V vs. Ag/AgCl) at 80 °C due to decreased potential of OER at elevated temperatures. It should be noted that the faradic current at negative sides of the LSV curves for both OSGE and RTSGE could be categorized into two parts caused by HER and Zn deposition, as shown in the LSV curves at 40 °C. However, both HER and Zn deposition could be thermodynamically suppressed in OSGE.
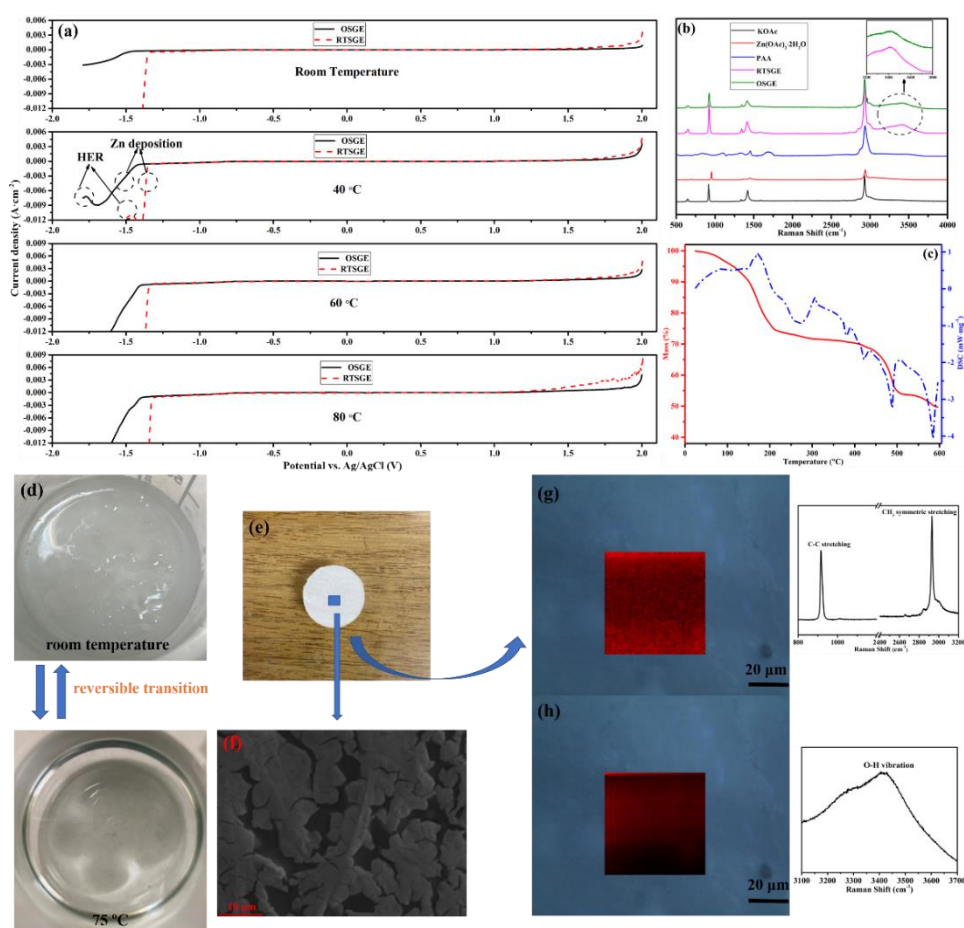
Fig. 7.1 (a) ESW of RTSGE and OSGE at different temperatures; (b) Raman spectra of original chemicals, RTSGE and OSGE; (c) STA analysis on OSGE from RT to 600 °C; (d) Reversible transition between sol and gel state of OSGE; (e) Optical image of OSGE on glass fiber substrate; (f) SEM image of OSGE with 10 µm resolution; (g-h) Raman mappings of OSGE generated by the peak intensity ratio, and peak intensity selection, respectively.
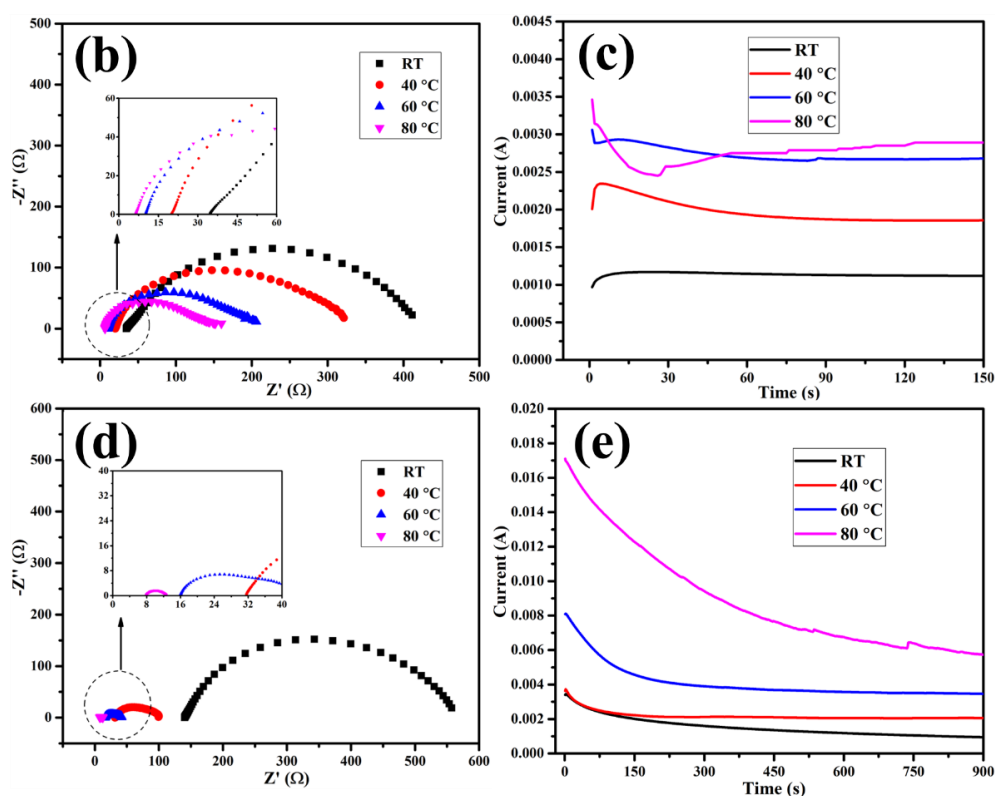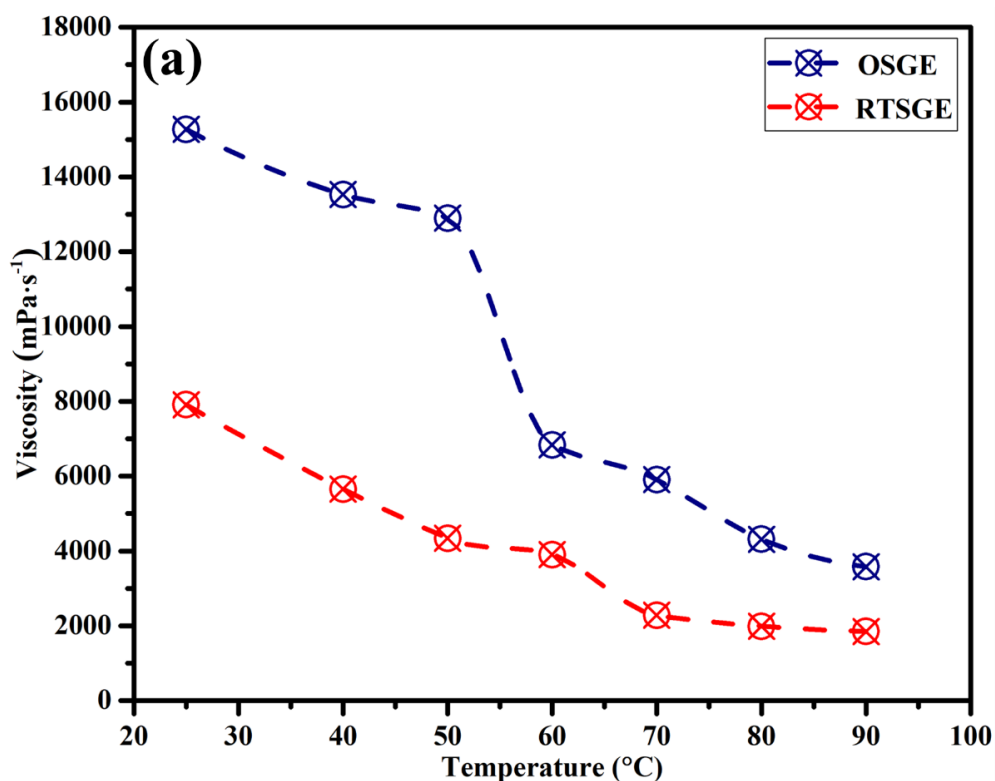
Fig. 7.2 (a) Tendency upon viscosity vs. temperature of RTSGE and OSGE; (b) EIS plot of RTSGE-based Zn//Zn symmetrical cell at various temperatures; (c) RTSGE-based Zn//Zn symmetrical cell at various temperatures. (c) EIS plot of OSGE-based Zn//Zn symmetrical cell at various temperatures. (d) OSGE-based Zn//Zn symmetrical cell at various temperatures.

164

To experimentally identify the reasons behind the widened ESW of OSGE, Raman spectra of OSGE and RTSGE samples were collected (Fig. 7.1b). For comparison, the Raman spectra of the original chemicals (KOAc, $Zn(OAc)_2 \cdot 2H_2O$ and PAA) were also collected. According to previous studies, the peak reflecting the O-H bond (3200-3600 cm^{-1}) from perturbation of the water H-bond network, was weakened due to the crowded hydrated clusters in increased salt concentrations [193, 209]. The corresponding peak of the O-H bond in OSGE was weaker compared to that of RTSGE, indicating a weakened H bond and more aggregated water molecules which lead to reduced activity of water. STA was further employed to study stability and phase transition of acetate OSGE at elevated temperatures (Fig. 7.1c). The mass loss at 100 °C was only ~5%, which indicated desired water retention in OSGE. The glass transition point of OSGE was determined at ~ 60 °C through the cross point of the tangent lines for both the endothermic and exothermic area. After the cross point, the viscosity was significantly lowered, indicating the gel-sol transition (consistent with the viscosity change from 12898 to 4339 $mPa \cdot s^{-1}$ when the temperature increases from 50 to 60 °C (Fig. 7.2a)). The gel-sol transition was recorded in the top-view optical images in Fig. 7.1d, which display the reversible transition between white gel and transparent sol. This is an in-situ solidifying process according to reported work [71], and OSGE can be classified as quasi-solid state.

Other than wide ESW, ionic conductivity is another critical parameter for battery electrolytes. Ionic conductivity can ensure the desired charge and mass transportation within the electrolyte and interface, hence guaranteeing low ohmic polarization and excellent rate capability of batteries. The ionic conductivity of RTSGE and OSGE at various temperatures was measured by EIS using 0.1 M KCl aqueous solution (1.28×10^{-2} S·cm^{-1} at RT) as the calibration solution [80, 207]. The ionic conductivity of RTSGE was higher than that of OSGE (Fig. 7.2b and 7.2d), owed to the viscosity difference between RTSGE and OSGE (Fig. 7.2a). The ionic conductivity of both samples increased at elevated temperatures, from 3.74×10^{-3} at RT to 6.59×10^{-2} S·cm^{-1} at 80 °C for OSGE and from 1.52×10^{-2} at RT to 8.08×10^{-2} S·cm^{-1} at 80 °C for RTSGE. Notably, the conductivity measured is the total conductivity, which included the conductivity of all the charge carriers. Thus, to investigate the effects caused by ions other than Zn^{2+}, the transference

number of Zn^{2+} ($T_{Zn^{2+}}$) of OSGE/RTSGE was measured by the current interrupt method. This was carried out in a Zn//Zn symmetrical cell with OSGE/RTSGE using Zn metal electrodes working as reversible electrodes for Zn^{2+}, whilst also serving as blocking electrodes for other ions. $T_{Zn^{2+}}$ can be determined by the initial current (I_O) and final steady-state current (I_S) of the current interrupt method with the following equation [80, 345]:

$$T_{Zn^{2+}} = I_s/I_O \qquad\qquad (7.1)$$

The recorded currents against time are shown in Fig. 7.2c and 7.2e. The $T_{Zn^{2+}}$ value at various temperatures were determined to be around 0.4 and 0.8 for OSGE and RTSGE respectively. The Zn^{2+} conductivty of OSGE was determined as 1.03×10^{-3} at RT and 2.21×10^{-2} S·cm^{-1} at 80 °C, which was lower than that of RTSGE (1.43×10^{-2} at RT and 6.75×10^{-2} S·cm^{-1} at 80 °C). Parameters regarding the ESW, mixed ionic conductivity and Zn^{2+} conductivity of OSGE and RTSGE at different temperatures are summarized in Table 7.2. Although the Zn^{2+} conductivity of OSGE is lowered by the de-solvated Zn^{2+} in OSGE, it is still high enough to perform as a good electrolyte for Zn//MnO$_2$ batteries. Based on the previous report, the crystallized salt is an ionic insulator, whilst the OSGE remains working if the ion-insulated salt is isolated by the continuous ion-conductor [207]. Therefore, the morphology of OSGE was characterized by SEM and Raman mapping.

Fig. 7.1e and 7.1f show the optical image of OSGE casted on a glass fibre substrate and the SEM image of the selected area respectively. Some micron sized pores are observed, most likely owed to the loss of water under high vacuum during the SEM measurement. A 50×50 μm selected area on the sample was characterized by Raman mapping with a spectrum range from 400 to 4000 cm^{-1} to eliminate the interference of the high vacuum environment of SEM. The Raman mapping images in Fig. 7.1g and 7.1h were generated by peak intensity ratio (between that of C-C stretching(~916 cm^{-1}) and that of -CH$_3$ symmetric stretching (~2930 cm^{-1})) selection [346], and O-H vibration. The intensity ratio range in Fig. 7.1g was from 0.25 to 0.5, and the intensity range in Fig. 7.1h was from 1000 to 3000 counts. The

colours in both samples varied from dark red to bright red, indicating the continuous gel area and dispersed crystallized salt area with different contrast. Although inhomogeneous morphology was observed, OSGE still delivered desired ionic conductivity attributed to the ion-conductive gel (continuous phase) and isolated salts (dispersed phase). The conductivity of OSGE reveals that applying heterogeneous electrolytes into batteries is feasible as long as there exists a continuous pathway for charge carriers.

Table 7.1 Summary on ESWs and ionic conductivity of various electrolytes.

Sample	ESW vs. Ag/AgCl at 1 mV·s^{-1} (V)	Mixed ionic conductivity (S·cm^{-1})	Zn^{2+} conductivity (S·cm^{-1})	Test temperature (°C)
RTSGE	3.25 (-1.35 to 1.9)	1.52×10^{-2}	1.43×10^{-2}	RT
	3.15 (-1.35 to 1.8)	2.61×10^{-2}	2.08×10^{-2}	40
	3.10 (-1.35 to 1.75)	4.03×10^{-2}	3.53×10^{-2}	60
	3.0 (-1.3 to 1.7)	8.08×10^{-2}	6.75×10^{-2}	80
OSGE	3.45 (-1.5 to 1.95)	3.74×10^{-3}	1.03×10^{-3}	RT
	3.40 (-1.45 to 1.95)	1.66×10^{-2}	9.15×10^{-3}	40
	3.35 (-1.4 to 1.95)	3.29×10^{-2}	1.40×10^{-2}	60
	3.30 (-1.35 to 1.95)	6.59×10^{-2}	2.21×10^{-2}	80
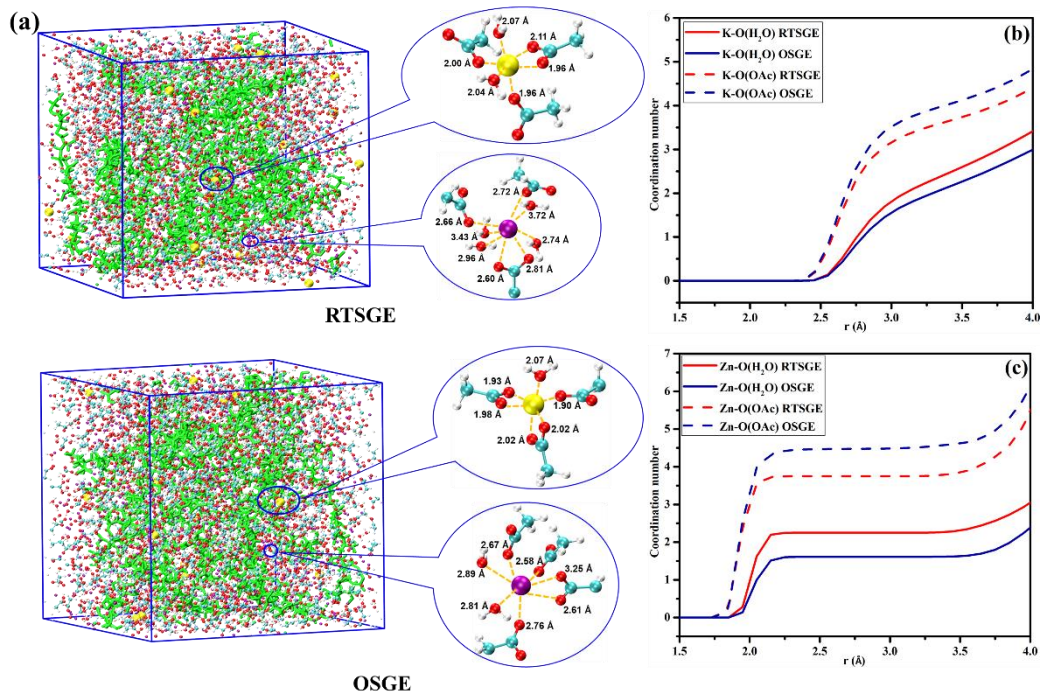
Fig. 7.3 (a) Snapshot of simulation boxes for RTSGE and OSGE, yellow spheres represent Zn^{2+}, purple spheres represent K^+, red spheres represent O atoms, cyan spheres represent C atoms, white spheres represent H atoms, and green sticks represent PAA; (b) Coordination number of K-O(H_2O) and K-O(OAc) in both RTSGE and OSGE; (c) Coordination number of Zn-O(H_2O) and Zn-O(OAc) in both RTSGE and OSGE.

To explore the fundamental explanation behind the wider ESW of OSGE than that of RTSGE, MD simulation was employed. Snapshots of the simulation boxes for RTSGE and OSGE are shown in Fig. 7.3a, in which both K^+ and Zn^{2+} primary solvation sheaths are displayed, and the average coordination number of K-O(H_2O) and Zn-O(H_2O) of OSGE is less than that of RTSGE after 2 Å radius (the difference is no more than 0.5), indicating the reduced number of activated water molecules (Fig. 7.3b and 7.3c). Moreover, in K^+ and Zn^{2+} primary solvation sheaths, the average distance between K^+/Zn^{2+} and (OAc)⁻ is shortened as well, from ~2.7/2.0 Å for RTSGE to ~2.5/1.9 Å for OSGE. According to the reported works, at oversaturated situations, electrolyte configuration can evolve from SSIP-dominated structure to CIP-dominated structure (shown in Fig. 1.14a) [240, 347]. This kind of electrolyte is merely composed of inactive ''frozen-like'' solvent, de-solvated cation constituted crystal-like salt solute. The MD simulation is consisted

with the Raman spectra result as well (Fig. 7.1b), in which O-H bond (3200-3600 cm^{-1}) from perturbation of the water H-bond network was weakened due to the crowded hydrated clusters and solidification. Therefore, a more aggressive electrolyte is achieved with even wider ESW. It should be noted that the CIP structures in Zn^{2+}-involved electrolytes is able to stem Zn depositing from electrolytes as the result shown in Fig. 7.1a, preventing the formation of Zn dendrites and stabilizing Zn metal electrodes [131, 348-350].

7.2.2 Performance of OSGE-based Zn//Zn symmetrical cell and Zn//MnO₂ battery at RT

In order to experimentally demonstrate the enhanced stability and reversibility of Zn metal electrodes, RTSGE/OSGE-based Zn//Ti cells and Zn//Zn symmetrical cells were prepared as CR2032 coin cells. The cells were tested by cyclic CV and GCD cycling (Fig. 7.4). Zn//Ti cells were utilized to confirm the Zn redox mechanism and relevant CE in RTSGE/OSGE through 1 mV·s^{-1} scanned CV curves. In Fig. 7.4a, the redox couple of the RTSGE-based Zn//Ti cell was located at around ±0.3 V vs. Zn/Zn^{2+} during the first cycle then shifted to ±0.20 V vs. Zn/Zn^{2+}, whilst that of OSGE-based Zn//Ti cell was maintained at about ±0.17 V vs. Zn/Zn^{2+} (Fig. 7.4b). According to published papers, the redox potential of Zn stripping/plating is around ±0.20 V vs. Zn/Zn^{2+} [80, 131], which is consistent with the CV results above confirming the stripping/plating mechanism of the Zn metal electrodes in both RTSGE and OSGE. The difference of Zn stripping/plating potential between RTSGE and OSGE was caused by various interfacial resistances. Meanwhile, CE of RTSGE/OSGE-based Zn//Ti cells were confirmed by chronocoulometric curves derived from relevant CV curves. It was found that there was an increase from 83.5 % during the first cycle to 99.3 % on the ninth cycle for the RTSGE-based Zn-Ti cell, and from 97.3 to 99.7 % during the first and ninth cycle respectively for the OSGE-based Zn-Ti cell. Subsequently, better reversibility of the Zn stripping/plating reaction in OSGE than that in RTSGE was observed.
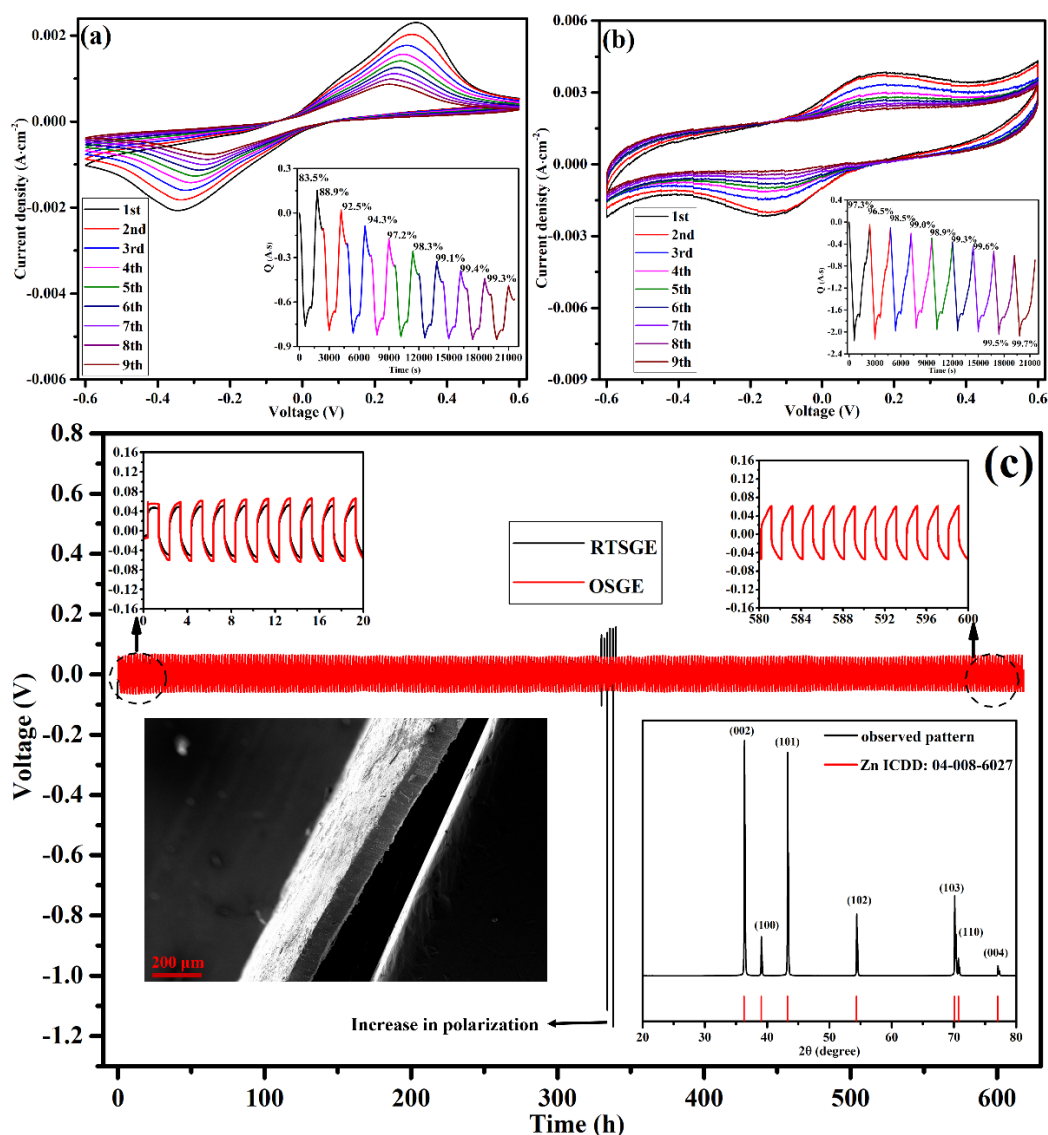
Fig. 7.4 (a) CV curves of RTSGE-based Zn//Ti cell under 1 mV·s^{-1} sweep rate with according chronocoulometry curves as inset; (b) CV curves of OSGE-based Zn//Ti cell under 1 mV·s^{-1} sweep rate with according chronocoulometry curves as inset; (c) Galvanostatic Zn stripping/plating of RTSGE/OSGE-based Zn//Zn symmetrical cells under 0.5 mA·cm^{-2} with cross-section SEM image and XRD plot towards tested Zn metal electrode.

The RTSGE/OSGE-based Zn//Zn symmetrical cells were tested under 0.5 mA·cm^{-2} current density for galvanostatic Zn stripping/plating, with a 0.5 mAh·cm^{-2} capacity limitation. As shown in Fig. 7.4c, both RTSGE and OSGE-based Zn//Zn symmetrical cells deliver the voltage range from ~-0.05 to ~0.05 V, while a sudden increase in polarization of the RTSGE-based one occurs after about 340-hours (~170 cycle). In contrast, the OSGE-based Zn//Zn symmetrical cell runs smoothly

170

within the ~-0.05 to ~0.05 V voltage range for more than 600 hours (300 cycles). The tested Zn metal electrode in the OSGE-based Zn//Zn symmetrical cell was subsequently characterized by SEM and XRD (inset images in Fig. 7.4c). The cross-section SEM image of the tested Zn metal electrode is basically dendrite-free, demonstrating the excellent stability of Zn stripping/plating in OSGE. The corresponding XRD plot reveals a single phase of Zn (ICDD: 04-008-6027), illustrating that the Zn stripping/plating mechanism. The 1 m $Zn(OAc)_2$+31 m KOAc aquoues solution was determined as a mildly alkaline environment (pH = 9.76) beforehand. Zn stripping/plating was formed on the anode side and proton-participated conversion was present on the MnO_2 cathode side [80]. In OSGE, the same reaction mechanisms are present in both the anode and cathode under mildly alkaline conditions, the details of which are provided below.

Before assessing the OSGE-based Zn//MnO_2 battery, CV curves of the Zn metal anode and MnO_2 cathode were collected in a three-electrode system. Redox couples of -0.75/-1.10 V vs. Ag/AgCl for the Zn anode and 0.39/0.16 V vs. Ag/AgCl for the MnO_2 cathode (Fig. 7.5a) were obtained. Following this, an OSGE-based Zn//MnO_2 battery with 2.6 mg MnO_2 was constructed for GCD cycling at a rate of 1 C (308 $mA \cdot g^{-1}$) with a voltage limitation of 0.8-2.0 V (Fig. 7.5b). The charge/discharge curves of the 1st, 10th, 20th, 50th and 100th cycles are shown in Fig. 7.5c. It is revealed that the capacity area at ~1.3 V, which is similar to reported alkaline Zn//MnO_2 batteries [172, 266, 351], whilst the discharge capacity (calculated on 2.6 mg MnO_2) varied from 20(3) $mAh \cdot g^{-1}$ during the first cycle, to 30(4) $mAh \cdot g^{-1}$ with 98.(7)% CE on the 100th cycle. It is worth mentioning that in the first cycle, protons initially need to be inserted into MnO_2 through discharging, then extracted from MnO_2 by charging during the second cycle. The discharge capacity reached a maximum value of 31(2) $mAh \cdot g^{-1}$ (97.(8)% CE) on the 6th cycle, whilst the relevant energy density was determined as 38(6) $Wh \cdot kg^{-1}$ by integrating the discharge curve in Origin. The same Zn//MnO_2 battery was tested under various charge/discharge rates from 1 C to 10 C, as shown in Fig. 7.5d. Generally, the capacity value was maintained until 5 C, then dramatically decreased at 7 C (23(7)/23(6) $mAh \cdot g^{-1}$, 99.(6)%) and 10 C (20(8)/20(7) $mAh \cdot g^{-1}$, 99.(6)%) because of increased ohmic and concentration polarization, although was still at an acceptable level. Based on the results, 5 C was chosen for the long-term

performance test, taking into consideration of both the capacity and rate capability. Repeated GCD tests were conducted towards another OSGE-based Zn//MnO$_2$ battery with 2.2 mg MnO$_2$, which was cycled 2000 times (Fig. 7.5e). The capacity reached a maximum value of 30(2) mAh·g^{-1} on the 368th cycle, then gradully decreased to 24(9) mAh·g^{-1} on the 2000th cycle, with 82.(7)% capacity retention. Meanwhile, the CE increased with continuous charge/discharge reactions, obtaining a value above 99.(5)% after 300 cycles. After GCD cycling, the Zn metal anode was characterized by XRD and SEM/EDX (Fig. 7.6). The major phase of the cylced Zn metal anode confirmed by XRD is Zn (ICDD: 04-008-6027). Weak peaks of ZnO (ICDD: 04-020-0364) are also present, which again indicate Zn stripping/plating at anode despite the slight interaction with OH$^-$ in the mildly alkaline environment of OSGE. The almost dendrite-free morpholgy is confirmed by SEM characterization, demonstrating excellent stability of the Zn metal anode in OSGE.
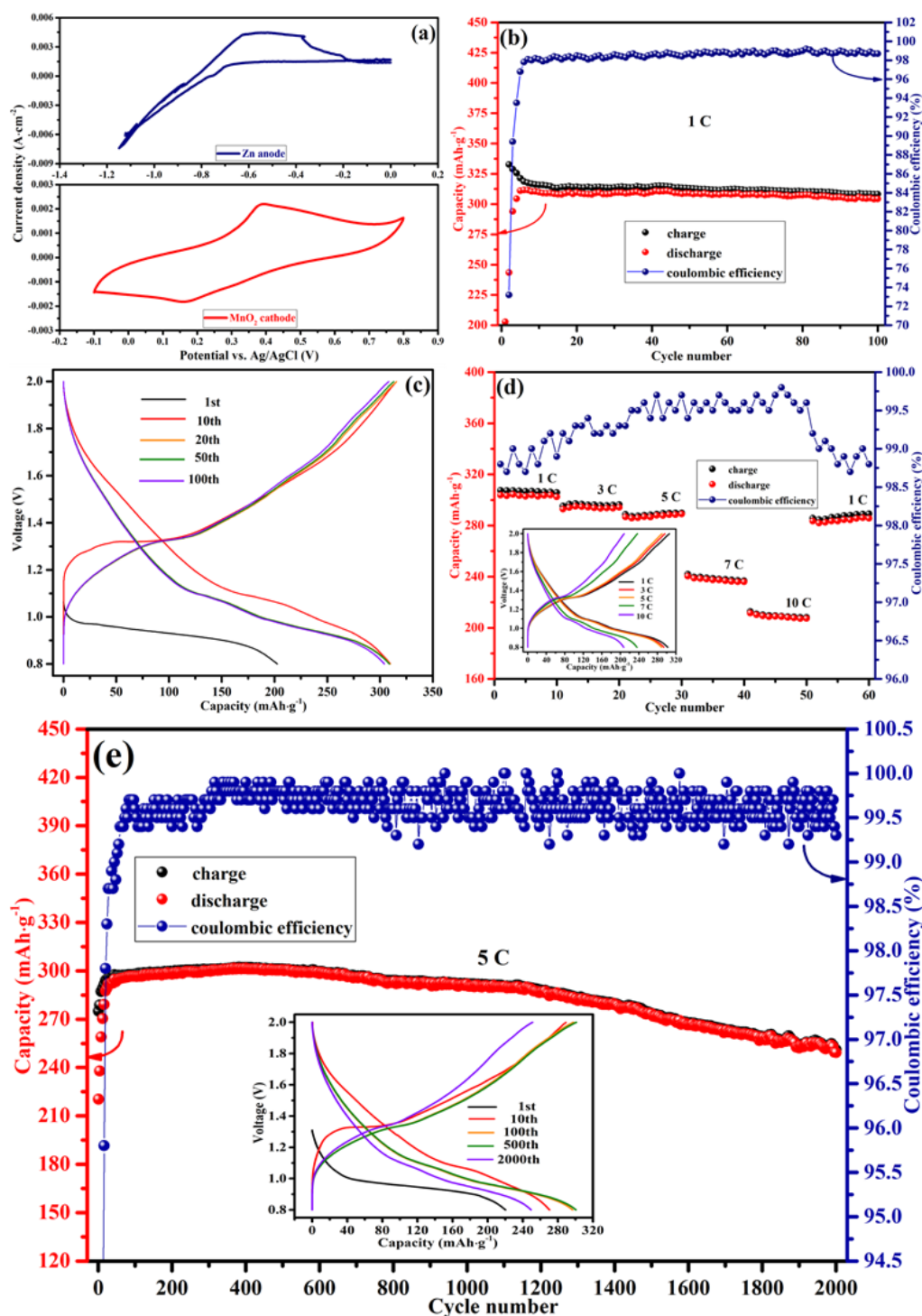
Fig. 7.5 (a) CV curves of Zn and MnO$_2$ electrodes in three-electrode cell with OSGE; (b) GCD cycling of OSGE-based Zn//MnO$_2$ battery under 1 C rate within 100 cycles; (c) GCD cycling of OSGE-based Zn//MnO$_2$ battery under 1 C rate; (d) Rate capability test on OSGE-based Zn//MnO$_2$ battery with according charge/discharge curves as inset; (e) GCD cycling of OSGE-based Zn//MnO$_2$ battery under 5 C rate within 2000 cycles with according charge/discharge curves as inset.
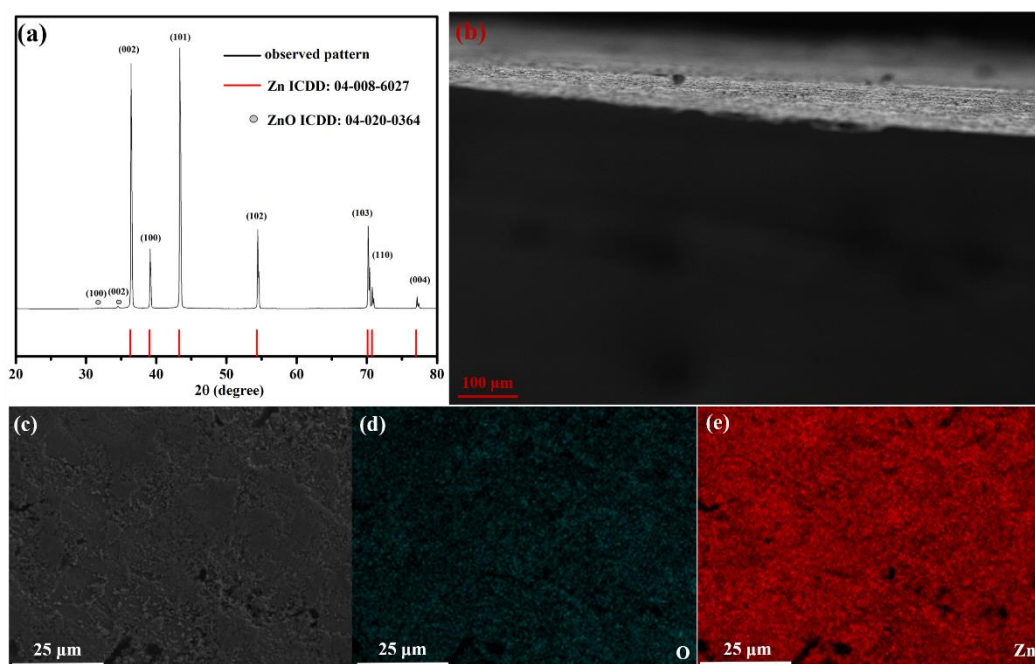
Fig. 7.6 (a) XRD plot of Zn metal anode in OSGE-based $Zn//MnO_2$ battery after GCD test under 5 C, at RT; (b) Cross-section SEM image of Zn metal anode in OSGE-based $Zn//MnO_2$ battery after GCD test under 5 C, at RT with 100 μm resolution; (c) Top-view SEM image of Zn metal anode in OSGE-based $Zn//MnO_2$ battery after GCD test under 5 C with corresponding O (d); Zn (e) EDX mappings, at RT.

7.2.3 Working mechanism of MnO₂ cathode in OSGE

To explore the reaction mechanism of MnO_2 in OSGE, both MnO_2 powder and MnO_2 cathode were studied in detail. According to XRD, the MnO_2 powder is composed of α-MnO_2 (ICDD: 04-005-4884) (insert graph in Fig. 7.7a). Furthermore, the MnO_2 powder was also characterized by SEM/EDX (Fig. 7.7a), which revealed that the power consisted of nanosized particles with a size range of 100 to 200 nm. EDX layered imaging was generated on a selected area of the SEM image, indicating homogeneous distribution of the Mn and O elements. Normally, nanosized particles can introduce pseudocapacitance in electrodes and increase their capacity [352], thus it is necessary to figure out the contribution ratio of diffusion-controlled and capacitive behavior in the capacity of the MnO_2 electrode. Fig. 7.7b shows CV curves the of MnO_2 electrode in a three-electrode system with OSGE collected under different sweep rates from 0.2 to 1.0 mV·s⁻¹.

If the intercalation of battery behaviour is controlled by cation diffusion within the crystalline framework of electrode materials, the relationship between peak current (i_P) and sweep rate (v) can be summarized according to [341]:

$$i_P = av^{0.5} \tag{7.2}$$

Based on this, the slope of the $\log i_P$-$\log v$ curve is around 0.5 for a purely diffusion-controlled electrode reaction. However, the relevant slopes of MnO_2 in Fig. 7.7b are determined as 0.8786 and 0.8535 respectively, indicating that the electrode reaction of MnO_2 is not only controlled by diffusion process. In other words, the MnO_2 electrode exhibits a hybrid charge storage mechanism, and the current response (i) at a fixed potential (V) can be described as the combination of two separate mechanisms, namely capacitive (k_1v) and diffusion-controlled insertion ($k_2v^{1/2}$) according to [353, 354]:

$$i(v) = k_1v + k_2v^{1/2} \tag{7.3}$$

For analytical purposes, equation (4) can be rearranged to [353]:

$$i(v)/v^{1/2} = k_1v^{1/2} + k_2 \tag{7.4}$$

The values of k_1 and k_2 can be determined from the slope and y-intercept of the plot of $i(v)/v^{1/2}$ vs. $v^{1/2}$ respectively. Under these circumstances, the portion of the current arising from the capacitive and diffusion-controlled processes can be distinguished. In the inset image of Fig. 7.7c, this method was used to analyze the charge storage contributed by the diffusion-controlled process (magenta area) and capacitive process (orange area) on the MnO_2 electrode under a sweep rate of 1 mV·s^{-1}. The corresponding contribution ratios of capacity caused by diffusion-controlled and capacitive processes of the MnO_2 electrode under sweep rates from 0.2 to 1 mV·s^{-1} are summarized in Fig. 7.7c. These values varied from 33%/67% to 17%/83%, signifying the enhanced capacitive behavior with increased sweep rates, while MnO_2 electrode demonstrated the hybrid charge storage under all sweep rates.
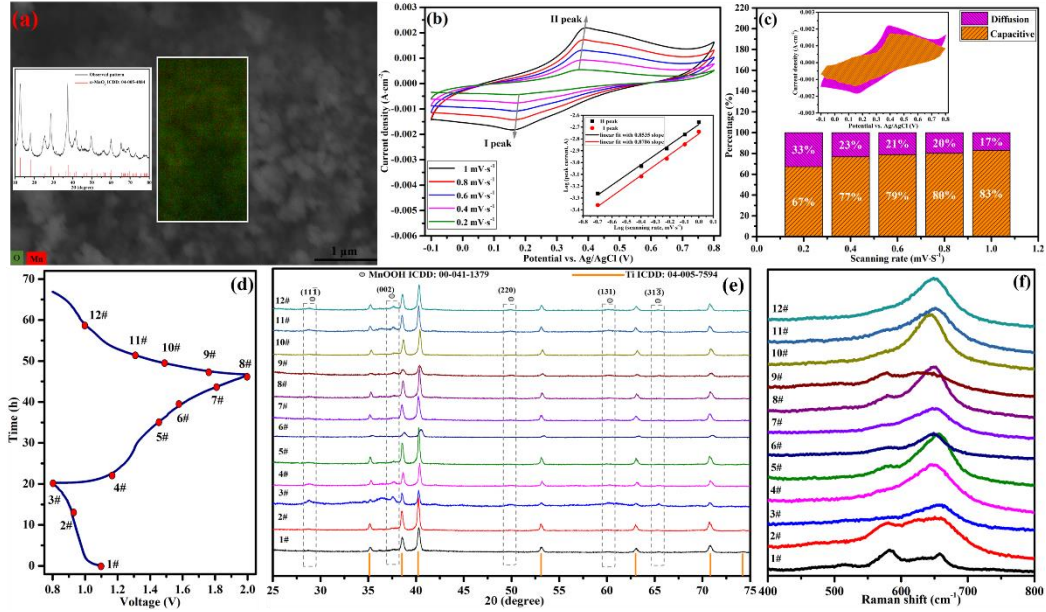
Fig. 7.7 (a) SEM/EDX layered image of MnO$_2$ powder; (b) CV curves of MnO$_2$ electrode in three-electrode system in OSGE under various sweep rates with $\log i_P$ - $\log v$ curve as inset; (c) Contribution ratio of diffusion-controlled and capacitive processes in capacity of MnO$_2$ electrode under various sweep rates with according separation under sweep rates of 0.2 mV·s^{-1}; (d) Charge/discharge curves of OSGE-based Zn//MnO$_2$ batteries for ex-situ characterization; (e) Corresponding ex-situ XRD plots of MnO$_2$ electrodes; (f) Corresponding ex-situ Raman spectra of MnO$_2$ electrodes.

Moreover, to investigate the reaction mechanism of the diffusion-controlled part of the MnO$_2$ electrode in OSGE, ex-situ XRD and ex-situ Raman spectra were utilized towards twelve Zn-MnO$_2$ batteries (Fig. 7.7d). Ex-situ XRD plots revealed that the main phase of the MnO$_2$ electrodes was Ti (ICDD: 04-005-7594), and that γ-MnOOH (ICDD: 00-041-1379) was also present, giving rise to peaks with miller index of (11$\bar{1}$), (002), (220), (131) and (31$\bar{3}$) (Fig. 7.7e). Comparing the ex-situ XRD plots with charge/discharge curves, the peaks of MnOOH were enhanced when discharged to 0.8 V, indicating proton insertion in the MnO$_2$ electrodes. However, the peaks are weakened when charged to 2.0 V, indicating extraction of protons from the electrodes. To get rid of interference from Ti in MnO$_2$ electrodes, ex-situ Raman spectra were collected in the wavenumber range of 400-800 cm^{-1} (Fig. 7.7f). In the spectrum of the original MnO$_2$ electrode (1#), the peaks at ~569 and ~633 cm^{-1} are attributed to the Mn-O symmetric stretching vibration of

[MnO$_6$], and Mn-O stretching vibrations in the basal plane of [MnO$_6$] in α-MnO$_2$ [355] respectively. When MnO$_2$ was discharged to 0.8 V, the left peak disappeared and the right one was slightly shifted (~644 cm^{-1}), indicating the decreased Mn-O bonding and increased Mn-O-Mn bonding, which was probably caused by the formation of γ-MnOOH [355, 356]. On the contrary, peaks at ~569 cm^{-1} and ~633 cm^{-1} occur during the charge process. The combined results of both ex-situ XRD and ex-situ Raman spectra demonstrate the proton-participated reaction for the diffusion-controlled process of the MnO$_2$ electrode in OSGE as described by the following equation [80, 172]:

$$MnO_2 + H_2O + e^- \leftrightarrow MnOOH + OH^- \tag{7.5}$$
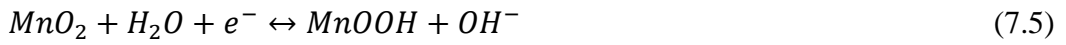
This battery behaviour is quite similar to the reported conversion reaction mechanism, in which the capacity was derived from the electron gain/loss, while protons are originated from water ionization at the cathode. [151] The Zn^{2+} ions worked as charge carrier for the whole cell, transporting between anode and cathode, which were the only carriers for charge transfer between electrodes. The ionized proton/OH$^-$ just generated/consumed locally at cathode, which interacted with Zn^{2+} ions generated at the anode and transfer through the electrolyte to the cathode [16]. Because proton was from water ionization, water can be regarded as active matter as well when calculating the capacity and energy density of this OSGE-based Zn//MnO$_2$ battery. [151] However, calculating pseudocapacitance capacity just takes mass of electrode into consideration due to charge absorption/desorption on electrode surface. [289] Therefore, we utilized both methods for capacity and energy density calculation. The active mass of water and Zn participated in reaction can be estimated as:

$$m_{active\,water} = m_{MnO_2} \times \frac{M_{H_2O}}{M_{MnO_2}} \tag{7.6}$$

$$m_{active\,Zn} = m_{MnO_2} \times \frac{M_{Zn}}{M_{MnO_2}}/2 \tag{7.7}$$

According to the equations (7.6) and (7.7), the maximum capacity and energy density on total mass of active electrode and active water were calculated as 19(7)

mAh·g^{-1} and 24(3) Wh·kg^{-1}, respectively. Whereas those on mass of MnO_2 were 31(2) mAh·g^{-1} and 38(6) Wh·kg^{-1} as above-mentioned.

7.2.4 Performance of OSGE-based Zn//MnO₂ battery at elevated temperature

A commercially mature battery should exhibit excellent cyclic stability as well as stability against extreme climates such as elevated working temperatures. The real operating temperature of a battery is usually higher than RT due to the released heat from the battery during charge/discharge. Therefore, the OSGE-based Zn//MnO$_2$ battery was investigated at 40, 60 and 80 °C. Before GCD measurement, the MnO$_2$ electrode was characterized by CV in a three-electrode system with OSGE at 40, 60 and 80 °C, as shown in Fig. 7.8a, 7.8b and 7.8c, respectively. Compared to the CV curves at RT (Fig. 7.7b), the redox couples of the MnO$_2$ electrode move to higher potentials, whilst maintaining the same electrode reaction mechanism. In the inset graph regarding the $\log i_P$-$\log v$ relationship derived from relevant CV curves, the slope is 0.9877/0.8953 at 40 °C, 0.4493/0.4152 at 60 °C and 0.6634/0.6012 at 80 °C, indicating hybrid charge storage at elevated temperatures. Furthermore, an increased contribution of the diffusion-controlled process in capacity at elevated temperatures could be estimated through a decrease in gradient. The CE of an OSGE-based Zn//MnO$_2$ battery with 2.4 mg MnO$_2$ loading changed from 99.(3)% at RT to 97.(1)% at 80 °C (Fig. 7.8d). The charge/discharge curves at different temperatures are displayed in the inserted graph of Fig. 7.8d, which show 28(9)/28(7) (99.(3)% CE) at RT, 29(4)/29(0) (98.(5)% CE) at 40 °C, 30(2)/29(6) (98.(0)% CE) at 60 °C and 311/302 mAh·g^{-1} (97.(1)% CE) at 80 °C. The CE of the cell slightly decreased with elevated temperatures due to enhanced kinetics of OER and Zn deposition/HER in OSGE, whilst the capacity areas of charge/discharge curves was obviously higher at elevated temperatures, from ~1.3 to ~1.6 V, which is consistent with the trend of CV curves in Fig. 7.8a-c. Considering both capacity and CE, 60 °C was selected for further long-term performance testing using the same cell and test settings. The parameter of the initial cycle was 30(5)/29(9) mAh·g^{-1} (97.(9)% CE), which changed to 27(7)/27(1) mAh·g^{-1} (97.(8)% CE) after 265 cycles, displaying a retention capacity of 90.(6)% (Fig. 7.8d). The total cycling of this battery at various

temperatures was 300 cycles. To the best of our knowledge, this elevated-temperature stability is remarkable compared to investigated ARBs [89, 90, 184]. Compared the elevated-temperature battery performance with nitrate OSGE-based one, the acetate OSGE demonstrates higher stability (330 cycles for acetate one vs. 220 cycles for nitrate one) and higher capacity (29(9) $mAh \cdot g^{-1}$ for acetate one vs. 71.(1) $mAh \cdot g^{-1}$ for nitrate one).
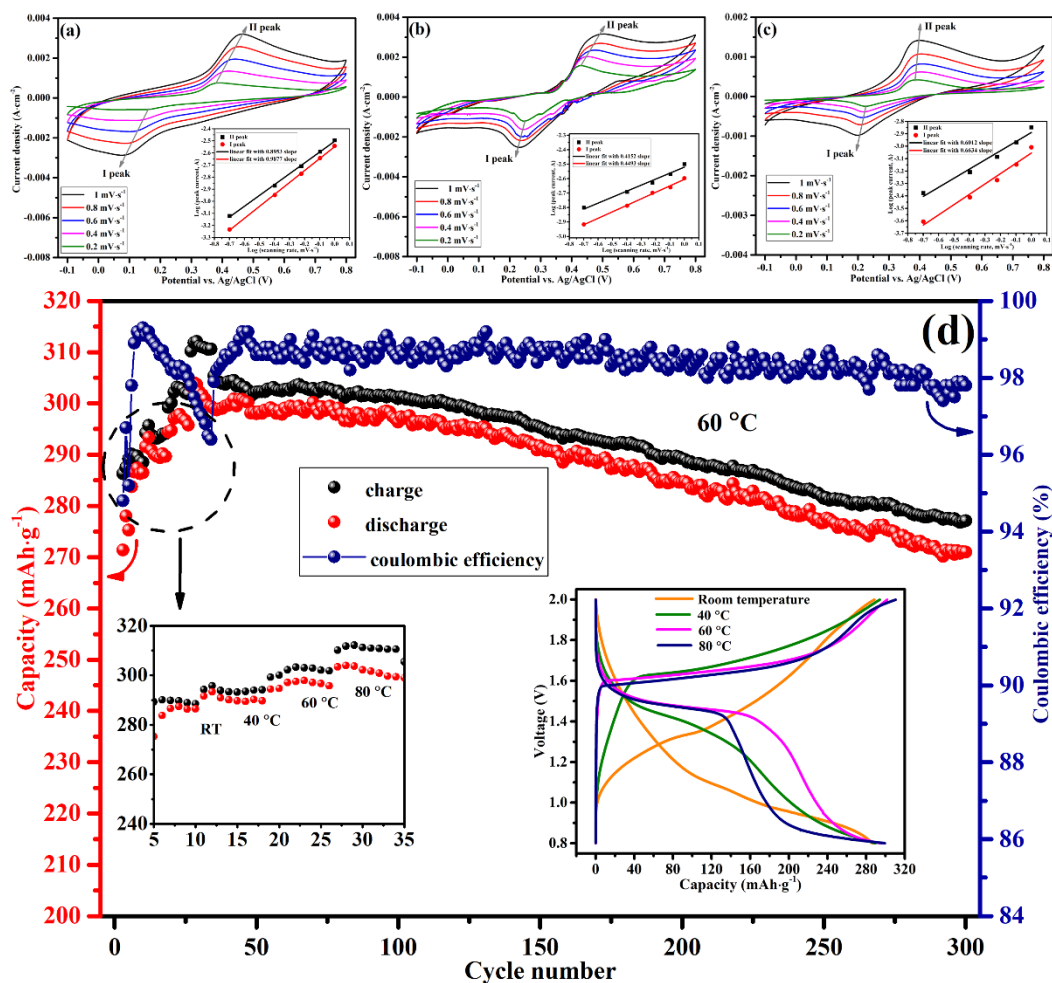
Fig. 7.8 (a-c) CV curves of MnO_2 electrodes in three-electrode cell in OSGE at 40, 60 and 80 °C with $\log i_P$-$\log v$ curve as inset; (d) GCD test towards OSGE-based $Zn//MnO_2$ battery at different temperatures with according charge/discharge curves shown in the inset.

7.3 Conclusions

In this study, the use of OSGE (1m $Zn(OAc)_2$+40 m KOAc-PAA) further expands the ESW compared to that of RTSGE (1 m $Zn(OAc)_2$+31 m KOAc-PAA), from

3.25 to 3.45 V at RT. The wider ESW of OSGE was found to originate from the contacted cation solvation sheath, which was experimentally proven by Raman spectra and theoretically demonstrated by MD simulations. An aqueous $Zn//MnO_2$ battery based on this acetate OSGE exhibited higher reversibility and energy density than the one based on acetate salt-concentrated electrolyte. At an operating voltage of 2.0 V, Zn dendrites were not observed when the battery was cycled at RT. Moreover, the OSGE-based $Zn//MnO_2$ battery was smoothly cycled to 300 cycles at elevated temperatures. The reaction mechanism of the Zn anode was stripping/plating, while that of the MnO_2 cathode was confirmed to be hybrid charge storage, comprised of both diffusion-controlled and capacitive processes. Ex-situ XRD and ex-situ Raman spectra were used to determine the proton insertion/extraction of the diffusion-controlled process in the MnO_2 cathode. Overall, this work facilitates the development of robust ARBs that can tolerate over-charging and over-heating conditions. In the future, we will explore more appropriate salts for OSGEs to develop more robust ARBs suiting real applications.

CHAPTER 8 *N,N*-Dimethylacetamide diluted nitrate concentrated electrolyte for aqueous Zn//LiMn₂O₄ hybrid ion battery

8.1 Abstract

N,N-dimethylacetamide (DMA) solvent along with LiNO₃ salt has previously been utilized in a Li//O₂ battery to stabilize SEI. It was found that DMA showed stability towards the O₂ reaction at the electrode. A Li//O₂ cell with a 1 M LiNO₃ electrolyte in DMA solvent demonstrated a consistent charging profile and good capacity retention [357]. The electrolyte stability toward both the O₂ cathode and Li metal anode was achieved due to the solvent possessing an amide core, with nitrate anions for SEI formation on the Li metal anode [358, 359]. Recently, the DMA electrolyte was further developed with LiF and LiN_xO_y coexisting SEI film using LiNO₃ together with LiTFSI salt. As a result, the cyclic life of the Li//Li symmetrical and Li//O₂ batteries were elongated to 1800 hours and 180 cycles respectively [360].

Herein, we attempted to use DMA to dilute 2.5 m Zn(NO₃)₂+13 m LiNO₃ aqueous electrolyte, on purpose of lessening dissolved salts. Furthermore, it is necessary to eliminate O₂ in electrolytes to improve cyclic stability of ARBs [40], however, the stable nature of DMA in O₂ atmosphere may be utilized to assembling batteries in air directly. The nitrate concentrated electrolytes (NCEs) were diluted by DMA with a volume ratio of 1:1, 1:3, 1:4, 1:5, 1:7 and 1:9, abbreviated as 1, 3, 4, 5, 7 and 9 DDNCEs respectively. Their ESWs, ionic conductivity and Zn//Zn symmetrical cell performance were compared, among which 4 DDNCE was selected as the optimized composition, showing metrics of 3.1 V ESW, 4.14×10^{-3} S·cm⁻¹ ionic conductivity, and 110-hour Zn stripping/plating with dendrite-free morphology. MD simulation was employed to fundamentally explain the optimum performance of 4 DDNCE, through which the solvation structures of Zn^{2+} and Li^+ were found to evolve from water-solvated, to weakly solvated, and finally to DMA-solvated on increasing DMA amount. The 4 DDNCE was assembled with a Zn metal anode and LiMn₂O₄ nanorod cathode to form a Zn-Li hybrid ion battery

without O_2 elimination and delivered a maximum capacity of 121.0 mAh·g^{-1} under 0.2 C rate (1 C=148 mA·g^{-1}, based on the mass of $LiMn_2O_4$) within a working voltage range of 0.8-2.0 V. A desired cyclic lifespan of 200 cycles under 1 C rate with relevant CE approaching 99.0% was achieved. This work demonstrates wide-ESW electrolytes using relatively low salt concentration and shows good cyclic stability of ARBs through solvent-hybridization strategy rather than eliminating O_2 in electrolytes.

8.2 Results and discussion

8.2.1 Property of DMA-diluted electrolytes

The ESW of different DDNCEs were collected by LSV with 1 mV·s^{-1} as sweep rate and Ti foils as inert electrodes (Fig. 8.1a), amongst which 4 DDNCEs delivered widest ESW of 3.1 V (-1.60 to 1.50 V vs. Ag/AgCl), while the pristine NCE delivered ESW of 2.8 V (-1.0 to 1.80 V vs. Ag/AgCl). The high concentration of nitrate can suppress OER [53], moreover $LiNO_3$ was discovered to facilitate formation of CEI on the surface of $LiNiO_2$ cathode in ARLiBs [234], which can account for the high stability towards OER of NCE. However, with the addition of DMA, OER stability of DDNCEs was weakened due to the relatively lower concentration of $LiNO_3$, while the critical stability potential towards HER and Zn deposition was extended to -1.60 V vs. Ag/AgCl for 4 DDNCE. After that, both the positive (OER) and negative (HER/Zn deposition) sides of LSV curves upon DDNCEs were shrunken with the increasing portion of DMA, until 2.4 V (-0.95 to 1.45 V vs. Ag/AgCl) for 9 DDNCE. The observed ESWs are not simply determined by the thermodynamic factors but, more importantly, by kinetic factors as well, such as electrode surface, sweep rate [54], causing the inconsistency of ESW characterization. Nevertheless, the ESW tendency with DMA and NCE portion variation is still of accuracy due to the same kinetic setting. To reveal the reason behind ESW trend of DDNCEs experimentally, Raman spectra was utilized with result shown in Fig. 8.1b, in which the broad peak of 3200-3700 cm^{-1} and peak of ~1042 cm^{-1} signify the H bond and symmetrical stretching vibration of NO_3^- respectively [53]. While the peaks standing for DMA are enhanced with DMA ration increasing, especially the peaks of ~2935 and ~740 cm^{-1} presenting

for CH$_2$ rocking model and CH$_3$ stretching model respectively [361]. It is worth noting that the broad peaks (3200-3700 cm^{-1}) gradually shift to left (from ~3478 to ~3441 cm^{-1}) with DMA ration increasing until 4 DDNCE, indicating the waned interaction between Li$^+$/Zn^{2+} and water molecules. However, the continuous DMA portion increasing after 4 DDNCE, induces right shift (from ~3441 to ~3469 cm^{-1}) of H bond peak, thus the again enhanced interaction between Li$^+$/Zn^{2+} and water molecules. The former waned interaction reveals that the introduction of DMA can break Li$^+$/Zn^{2+}-H$_2$O solvation structures, while the latter enhanced interaction together with the intensified peaks of referring to DMA indicates the strengthened Li$^+$/Zn^{2+}-DMA solvation structures, which will be further demonstrated in the following MD simulations.
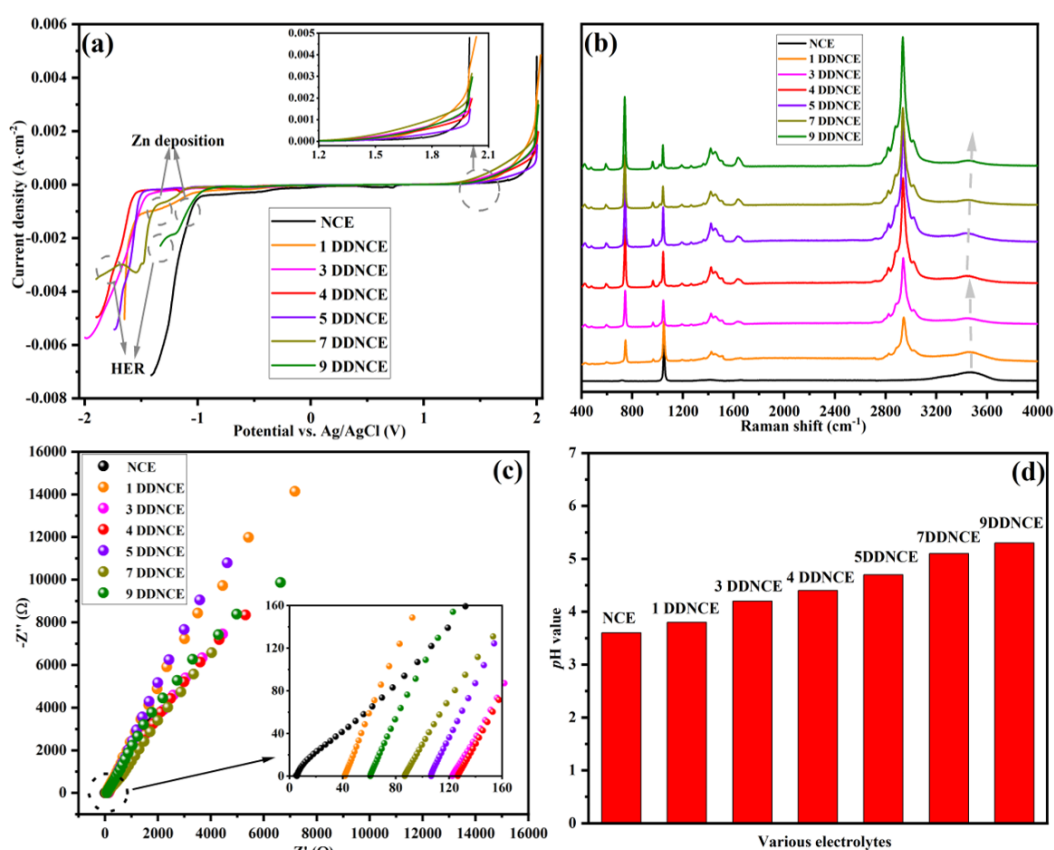
Fig. 8.1 (a) ESWs of various DDNCEs under 1 mV·s^{-1} sweep rate; (b) Raman spectra of various DDNCEs with a spetra range of 400-4000 cm^{-1}; (c) EIS plots of various DDNCEs with a frequecy range of 1 M-0.1 Hz; (d) pH value of various DDNCEs.

Beside ESW, ionic conductivity is an important electrolyte parameter as well. Herein, EIS was employed to determine ionic conductivity of different DDNCEs with same dimensions (Fig. 8.1c), using 0.1 M KCl aqueous solution (1.28×10^{-2} $S \cdot cm^{-1}$ at RT) as calibration sample [207, 362]. The ionic conductivity is decreased from 1.04×10^{-1} $S \cdot cm^{-1}$ for NCE to 4.14×10^{-3} $S \cdot cm^{-1}$ for 4 DDNCE due to the weakened solvation structures (de-solvation) of Li^+/Zn^{2+}, and associatively lowered transference number [45]. Whereas the ionic conductivity is again raised to 8.62×10^{-3} $S \cdot cm^{-1}$ for 9 DDNCE attributing to the re-built Li^+/Zn^{2+} solvation structures, which is still lower than that of NCE and 1 DDNCE because of the lower salt concentration and lower permittivity of DMA [363]. Besides, the ionic conductivity can be influenced by viscosity and salt concentration. The lower salt concentration would decrease ionic conductivity, associated with the variation from NCE to 4 DDNCE, whilst the lower viscosity would enhance ionic conductivity, associated with the change from 4 DDNCE to 9 DDNCE. The solubility variation of $LiNO_3$ with DMA addition was investigated as shown in Fig. 8.2a. The solubility of $LiNO_3$ in water was confirmed as 96.1 g, while that was almost halved to 54.7 g in a mixed solvent of water and DMA (1:1 in volume ratio). After that, the solubility was decreased to that of pure DMA (15.3 g). Notably, the DDNCEs were prepared by diluting NCE (2.5 m $Zn(NO_3)_2$+13 $LiNO_3$) with DMA in different volume ratios (DMA vs. NCE), with no precipitates observed in any volume ratio. The viscosity of NCE was determined as 332.5 mPa·s, while the viscosity was continuously decreased to 58.9 mPa·s^{-1} (9 DDNCE) with increasing volume of DMA (Fig. 8.2b). The transference number of Zn^{2+} in various DDNCEs was determined through current interrupt method as shown in Fig. 8.2c, which was increased from 0.11 (NCE) to 0.31 (5 DDNCE) then decreased to 0.19 (9 DDNCE). This tendency aligns well with the change of solvation structure. When the cation is solvated in a high degree, the anion is relatively "naked" thus can be migrated more freely. However, in DDNCE system, the weakened cation solvation induces contacted cation/anion ion pairs, which can slacken the NO_3^- anion largely then improve the transference number of Zn^{2+}. Overall, the ESWs and ionic conductivity of various DDNCEs are summarized in Table 8.2.
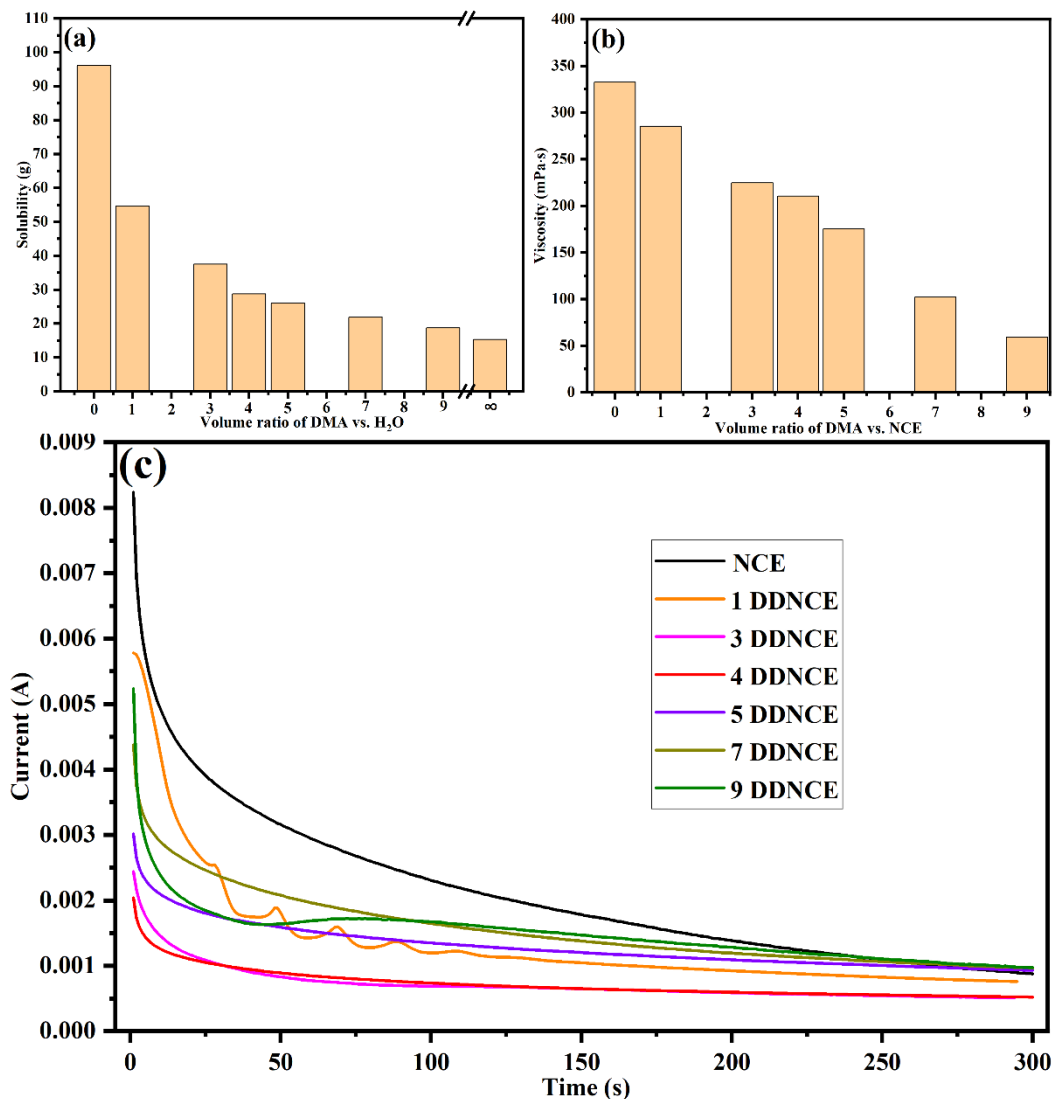
Fig. 8.2 (a) Solubility variation of $LiNO_3$ in various solvents with different volume ratios of DMA and water; (b) Viscosity variation of different DDNCEs; (c) Current interrupt characterization for determining Zn^{2+} transference number of different DDNCEs.
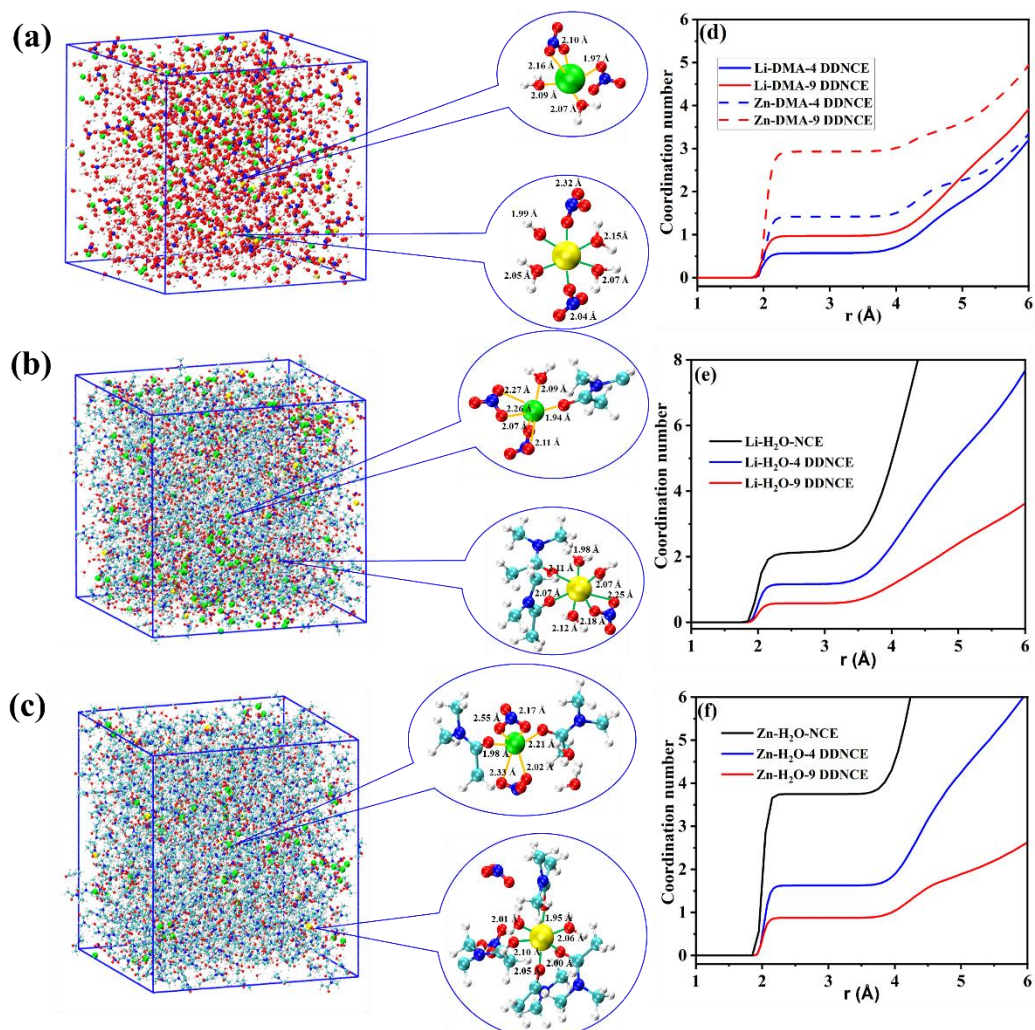
Fig. 8.3 (a) Snapshot of simulation box (green spheres represent Li^+, yellow spheres represent Zn^{2+}, red spheres represent O atoms, blue spheres represent N atoms, white spheres represent H atoms, and cyan spheres represent C atoms) for NCE; (b) 4 DDNCE; (c) 9 DDNCE; (d) Coordination number of Li^+-DMA and Zn^{2+}-DMA in 4 DDNCE and 9 DDNCE; (e) Coordination number of Li^+-H_2O in NCE, 4 DDNCE and 9 DDNCE; (f) Coordination number of Zn^{2+}-H_2O in NCE, 4 DDNCE and 9 DDNCE.

Table 8.1 Summary on ESWs and ionic conductivity of various DDNCEs.

Electrolyte	ESW vs. Ag/AgCl at 1 mV·s^{-1} (V)	Ionic conductivity (S·cm^{-1})
NCE	2.8 (-1.0 to 1.8)	1.04×10^{-1}
1 DDNCE	2.7 (-1.1 to 1.6)	1.25×10^{-2}
3 DDNCE	3.0 (-1.5 to 1.5)	4.28×10^{-3}
4 DDNCE	3.1 (-1.6 to 1.5)	4.14×10^{-3}
5 DDNCE	3.0 (-1.55 to 1.45)	4.92×10^{-3}
7 DDNCE	2.6 (-1.15 to 1.45)	6.05×10^{-3}
9 DDNCE	2.4 (-0.95 to 1.45)	8.62×10^{-3}

The various pH value of electrolytes will cause the different mechanisms in ARZiBs [85, 94, 179], while the mild electrolytes are desired for high reversibility of Zn metal electrodes [151, 364, 365]. Therefore, the pH value of DDNCEs was tested as exhibited in Fig. 8.1d. The pH value of pristine NCE was determined as 3.6, and after diluted by DMA, that was raised to 4.4 for 4 DDNCE and 5.3 for 9 DDNCE, which can be regarded as mildly acid environment. To theoretically explain the evolution of solvation structures with DMA ration increasing, and accordingly varied ESWs of DDNCEs, MD simulations were employed. Snapshots of simulation boxes for NCE, 4 DDNCE and 9 DDNCE are shown in Fig. 8.3a, 8.3b and 8.3c respectively, with both Li$^+$ and Zn^{2+} primary solvation sheaths displayed. The coordination number of Li$^+$/Zn^{2+}-H$_2$O and Li$^+$/Zn^{2+}-DMA in NCE, 4 DDNCE and 9 DDNCE are derived from the simulation boxes as Fig. 8.3d, 8.3e and 8.3f. The coordination number of Li$^+$/Zn^{2+}-H$_2$O is decreased and that of Li$^+$/Zn^{2+}-DMA is increased with DMA added, indicating the weakened Li$^+$/Zn^{2+}-H$_2$O and fortified Li$^+$/Zn^{2+}-DMA solvation sheaths, which are consistent with Raman spectra results. Moreover, in Li$^+$/Zn^{2+} primary solvation sheaths, the distance between Li$^+$/Zn^{2+} and NO$_3^-$ in 4 DDNCE is shortened, indicating the de-

solvation and more aggressive liquid structure owing to low permittivity of DMA solvent, thus the suppressed activity towards HER and Zn deposition. The higher stability towards Zn deposition in 4 DDNCE also prevents the formation of Zn dendrites and stabilizes Zn metal anodes [348, 366]. However, with the continuously added DMA, the distance between Li^+/Zn^{2+} and NO_3^- in 9 DDNCE is elongated again, which together with the fortified Zn^{2+}-DMA solvation sheaths boosts Zn deposition as shown in LSV curve of 9 DDNCE (Fig. 8.1a).

8.2.2 Reversibility of Zn metal anode

In order to experimentally demonstrate the enhanced reversibility of Zn metal electrodes in 4 DDNCE, Zn//Zn symmetrical cells were assembled with NCE, 4 DDNCE and 9 DDNCE in CR2032 coin cells, respectively. Zn//Zn symmetrical cells were tested under 0.5 mA·cm^{-2} current density for galvanostatic Zn stripping/plating, with a 0.5 mAh·cm^{-2} capacity limitation. In Fig. 8.4a, 4 DDNCE and 9 DDNCE deliver the voltage ranges of ±~0.15 and ±~0.2 V, respectively, while that of NCE is ±~0.1 V at the beginning, due to the lower ionic conductivity and transference number of 4 DDNCE and 9 DDNCE than those of NCE. The voltage range of 4 DDNCE can be retained after 110-hour stripping/plating, however that of NCE and 9 DDNCE are increased to ±~0.2 and ±~0.35, respectively, demonstrating the optimum reversibility of Zn metal electrodes in 4 DDNCE. The tested Zn metal electrode in the 4 DDNCE-based Zn//Zn symmetrical cell was subsequently characterized by SEM and XRD (Fig. 8.4b, 8.4c and 8.4d). The cross-section and top-view SEM images of the tested Zn metal electrode are basically dendrite-free, demonstrating the excellent stability of Zn stripping/plating in 4 DDNCE. The corresponding XRD plot reveals a phase of Zn (ICDD: 04-008-6027) with a slight phase of ZnO (ICDD: 04-020-0364). The existence of ZnO is originated from the oxygen in 4 DDNCE, which was not eliminated before coin cell assembly.
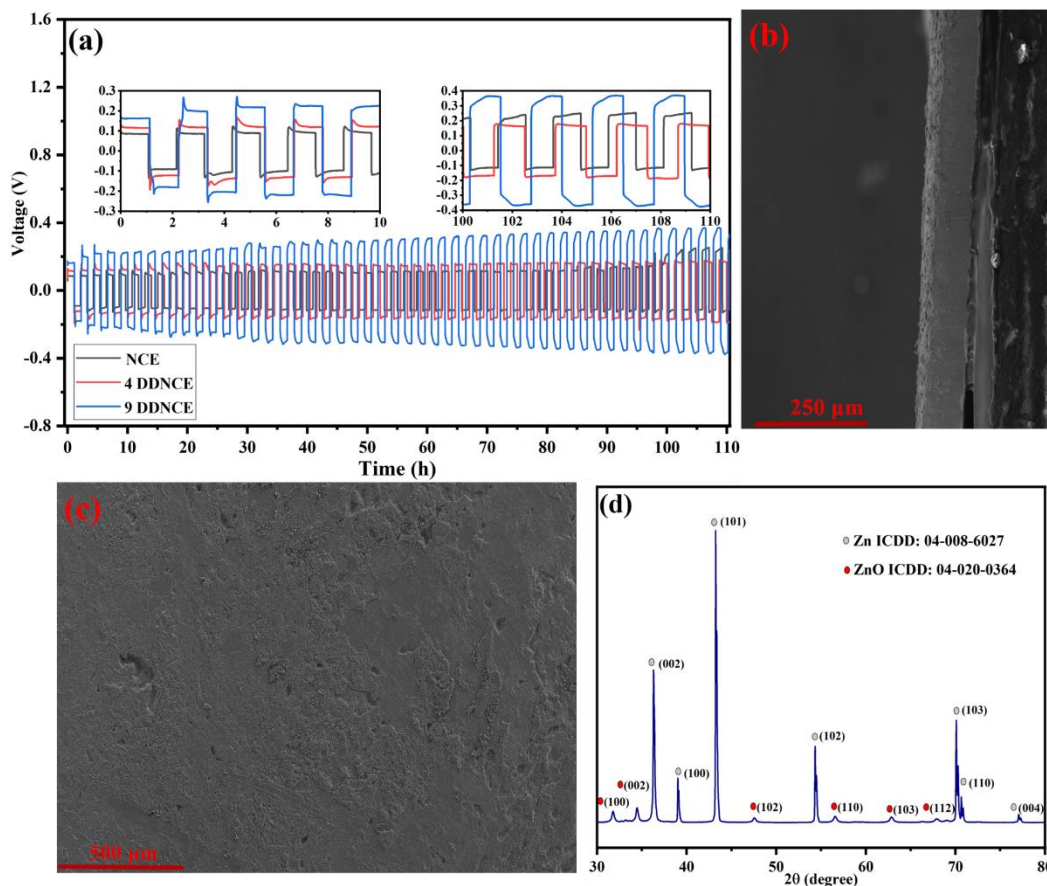
Fig. 8.4 (a) Zn stripping/plating characterization towards Zn//Zn symmetrical cells with NCE, 4 DDNCE and 9 DDNCE in conditions of 0.5 mA·cm^{-2} current density and 0.5 mAh·cm^{-2} capacity limitation; (b) Cross-section SEM image upon Zn metal electrode of symmetrical cell with 4 DDNCE after test; (c) Top-view SEM image upon Zn metal electrode of symmetrical cell with 4 DDNCE after test; (d) XRD plot upon Zn metal electrode of symmetrical cell with 4 DDNCE after test.

8.2.3 Performance of aqueous Zn//LiMn$_2$O$_4$ HiBs based on DMA-diluted electrolyte at RT

To further demonstrate stability of 4 DDNCE, LiMn$_2$O$_4$ nanorods were paired up with Zn metal anodes as HiBs for electrochemical characterization. The nanorod morphology of LiMn$_2$O$_4$ was determined by SEM in Fig. 8.5a, which is beneficial for enhancing electrode kinetics and mass transportation [248, 367]. EDX was further employed with layered EDX image shown in Fig. 8.5b, in which Mn and O are distributed evenly within the nanorods. In Fig. 8.5c, single phase of spinel LiMn$_2$O$_4$ is confirmed (ICDD: 01-070-8342) with cubic crystal system

189

and Fd-3m space group. Before assessing the 4 DDNCE-based Zn//LiMn$_2$O$_4$ HiB, CV curves of the Zn metal anode and LiMn$_2$O$_4$ cathode were collected in a three-electrode cell for determining working voltage. One redox couple of -0.46/-1.04 V vs. Ag/AgCl for the Zn anode, and two redox couples of 0.98/0.89 V and 1.12/1.03 V vs. Ag/AgCl for the LiMn$_2$O$_4$ cathode were obtained respectively as shown in Fig. 8.5d. Following this, a 4 DDNCE-based Zn//LiMn$_2$O$_4$ HiB with 3.2 mg LiMn$_2$O$_4$ active matter was constructed for rate capability characterization with a charge/discharge rate range of 0.2 to 4 C (1 C=148 mA·g^{-1}) under a voltage limitation of 0.8-2.0 V (Fig. 8.5e). The capacity (based on the mass of LiMn$_2$O$_4$) and CE of that Zn//LiMn$_2$O$_4$ HiB were tested as 123.7/120.0 (97.0 %), 119.4/117.0 (98.0 %), 114.9/113.1 (98.4 %), 89.7/88.2 (98.3 %), 76.8/75.6 (98.5 %) and 58.3/57.4 (98.5 %) mAh·g^{-1} under charge/discharge rates of 0.2, 0.5, 1, 2, 3 and 4 C, respectively. The above-mentioned capacity is the metric of last cycle for every charge/discharge rate, while the maximum discharge capacity is 121.0 mAh·g^{-1} under 0.2 C rate with relevant energy density of 165.8 Wh·kg^{-1} by integrating the discharge curve in Origin. In comparison, one NCE and one 9 DDNCE-based Zn//LiMn$_2$O$_4$ HiB with 2.8 and 3.3 mg LiMn$_2$O$_4$ active matter, respectively, were assembled and characterized for rate capability as shown in Fig. 8.5a and 8.5b. The CE of NCE-based one fails to approach 98.0 %, while that of 9 DDNCE-based one is even worse as no more than 88.0 % under every charge/discharge rate, and relevant capacity fades dramatically under 3 C rate.

1 C rate was chosen for long-term performance test, taking into consideration of both the capacity and rate capability. Repeated GCD tests were conducted towards another 4 DDNCE-based Zn//LiMn$_2$O$_4$ HiB with 3.4 mg LiMn$_2$O$_4$, which was cycled 200 times (Fig. 8.5f). Coresponding discharge capacity reached a maximum value of 115.3 mAh·g^{-1} on the 5th cycle, then gradully decreased to 95.1 mAh·g^{-1} on the 200th cycle, with 82.5 % capacity retention. Meanwhile, the CE increases with repeated charge/discharge reactions at first, touching 99.0 % after around 120 cycles, then goes back to grade of 98.0 % after about 150 cycles. Previously, the O$_2$ in electrolytes was exclued by vaccum, bubbling N$_2$ or N$_2$/Ar-fill glove box for guaranteeing cyclic stability of ARBs, [40, 187, 209, 368, 369]. And recently, one ARLiB with open struture was constrcuted, based on WiSE, which delivered 1000 charge/discharge cycles under 2.5 V working volatge [183]. As for this work, the

relatively dilute 4 DDNCE containing O_2 was attempted, showing good cyclic stability as well. After charge/discharge cycling, the Zn metal anode was characterized by SEM and XRD. Both the cross-section and top-view SEM images of Zn metal anode in Fig. 8.5g and 8.5h demonstrate the dendrite-free morphology, while the XRD plot in Fig. 8.5i can be distigushed into the main phase of Zn (ICDD: 04-008-6027) and slight phase of ZnO (ICDD: 04-020-0364). The exsitence of ZnO is attributed to the O_2 in 4 DDNCE, which is propobly account for hindering the further extented cyclic life. In the future, surface coating on the surface of Zn metal anode can be a option to further improve cyclic stability.
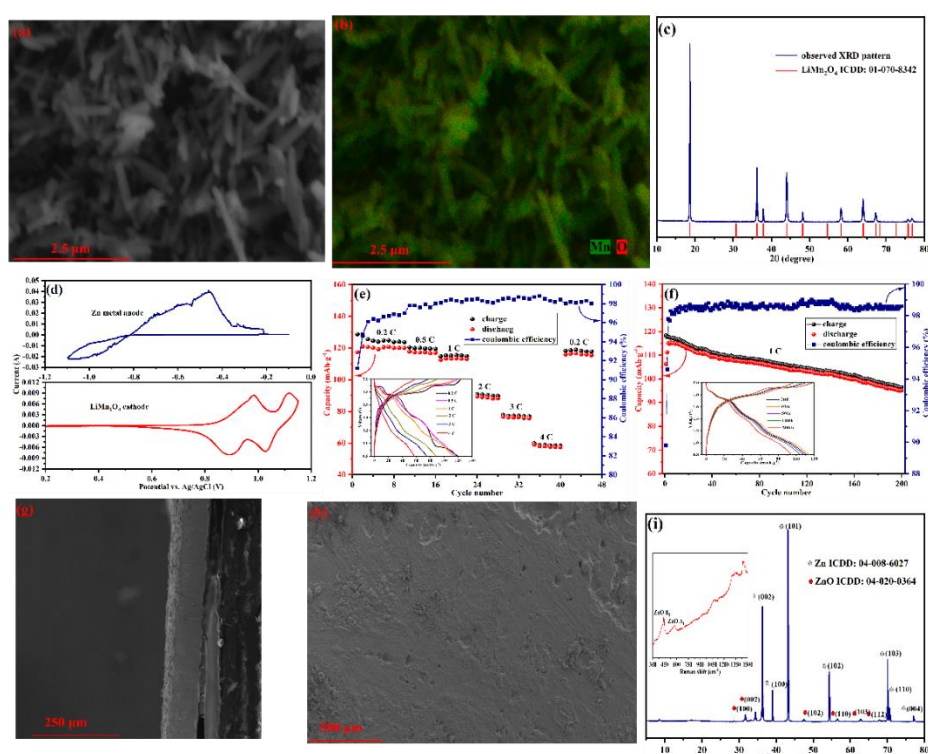
Fig. 8.5 (a) Morphology of $LiMn_2O_4$ nanorods; (b) Layered EDX image of $LiMn_2O_4$ nanorods; (c) XRD plot of $LiMn_2O_4$ nanorods; (d) CV curves of Zn metal anode and $LiMn_2O_4$ nanorod cathode in three-electrode cell with 4 DDNCE under $1\ mV\cdot s^{-1}$ sweep rate; (e) Rate capability characterization upon one $Zn//LiMn_2O_4$ battery based on 4 DDNCE under 0.2 to 4 C charge/discharge rates; (f) Cyclic stability characterization upon one $Zn//LiMn_2O_4$ battery based on 4 DDNCE under 1 C charge/discharge rate; (g) Cross-section SEM image upon Zn metal electrode of $Zn//LiMn_2O_4$ battery with 4 DDNCE after test; (h) Top-view SEM image upon Zn metal electrode of $Zn//LiMn_2O_4$ battery with 4 DDNCE after test; (i) XRD plot upon Zn metal electrode of $Zn//LiMn_2O_4$ battery with 4 DDNCE after test.

191

To prove the ameliorated electrode kinetics and mass transportation in $LiMn_2O_4$ nanorods, the microsized $LiMn_2O_4$ cathode prepared as our previous work [207], was assembled with 4 DDNCE and Zn metal anode in CR2032 coin cell for comparison. Before that, the $LiMn_2O_4$ powder was characterized by SEM/EDX as Fig. 8.6c and 8.6d, which demonstrate the morphology of around ten-micron particle. The capacity (based on 3.5 mg $LiMn_2O_4$) and CE of that $Zn//LiMn_2O_4$ battery were tested as 109.2/106.4 (97.4 %), 103.9/101.8 (98.0 %), 98.8/97.2 (98.4 %), 86.8/85.6 (98.6 %), 73.4/72.4 (98.6 %) and 58.5/57.6 (98.5 %) $mAh \cdot g^{-1}$ under charge/discharge rates of 0.2, 0.5, 1, 2, 3 and 4 C, respectively (Fig. 8.6e). Compared with that with $LiMn_2O_4$ nanorods, the capacity is lower especially under 0.2, 0.5 and 1 C rates, which demonstrates the improved kinetics of $LiMn_2O_4$ nanorods.
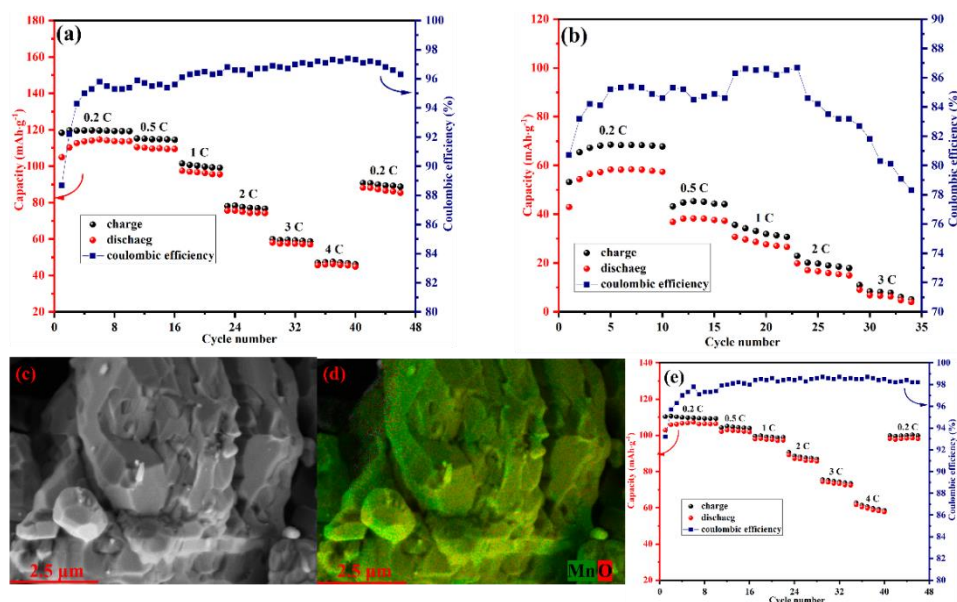
Fig. 8.6 (a) Rate capability characterization upon one $Zn//LiMn_2O_4$ battery based on NCE under 0.2 to 4 C charge/discharge rates ; (b) Rate capability characterization upon one $Zn//LiMn_2O_4$ battery based on 9 DDNCE under 0.2 to 3 C charge/discharge rates; (c) Morphology of $LiMn_2O_4$ microparticles with 2.5 μm resolution; (d) Layered EDX image of $LiMn_2O_4$ microparticles with 2.5 μm resolution; (e) Rate capability characterization upon one $Zn//LiMn_2O_4$ battery based on 4 DDNCE under 0.2 to 4 C charge/discharge rates.

8.3 Conclusions

In this study, the use of DMA in nitrate aqueous system can realize excellent stability towards HER and Zn deposition, whilst guarantee the cyclic stability of Zn//Zn symmetrical cell and Zn//LiMn$_2$O$_4$ HiB without O$_2$ eliminating. Amongst the DMA-diluted electrolytes, 4 DDNCE was chosen as the optimum one due to the widest ESW of 3.1 V and acceptable ionic conductivity of 4.14×10^{-3} S·cm^{-1}. The best electrochemical stability of 4 DDNCE was discovered to originate from the waned Li$^+$/Zn^{2+} solvation sheath, which was experimentally and theoretically proven by Raman spectra and MD simulations, respectively. A Zn//LiMn$_2$O$_4$ HiB with nanorod LiMn$_2$O$_4$ cathode based on 4 DDNCE exhibited high stability of 200 charge/discharge cycles with approaching 99.0 % CE and considerable energy density. The tested Zn metal anode shown the almost dendrite-free morphology, while a slight phase of ZnO could be discovered due to O$_2$ attendance in 4 DDNCE. In the coming similar works, surface coating on Zn metal anode can be opted as the way for further prolonged cyclic life. Overall, this work provides a simple strategy of solvent hybridization to lessen the salt portion while retain the excellent electrochemical stability. Meanwhile, this work also indicates one route of utilizing dilute electrolytes for high stability ARBs without O$_2$ eliminating on purpose of simplifying battery assembly, which can be expanded to more aprotic and water-miscible solvents commonly used in Li//O$_2$ batteries.

CHAPTER 9　Conclusions and future work

9.1 Conclusions

The narrow ESWs, electrode dissolution/side reaction and temperature-variation instability of aqueous electrolytes engender the low energy density, undesired cyclic lifespan and limited working temperature windows of ARBs. Therefore, the strategies of electrolyte additive, pH-management, salt-concentrated electrolyte, gelling, solvent hybridizing, interface tuning and beyond concentrated electrolyte for mitigating the challenges of aqueous electrolyte have been proposed. All these new electrolyte concepts mutually optimized ARBs, while the salt-concentrated electrolytes were massively investigated and well developed due to their simple processing and high effectiveness. This thesis focused on salt-concentrated electrolytes as well, which utilized cost-effective salts such as acetates, perchlorates, and nitrates to suit practical applications, thus improved stability, working voltage and energy density of ARBs. In aqueous $Zn//MnO_2$ system based on acetates, the working voltage could go up to 2.0 V, which was regarded as overcharging in comparison of batteries with same working mechanism. While the mechanism can be determined as hybrid charge storage mechanism, comprised by battery behavior and capacitive behavior. Amongst ARBs, nanosized electrodes would enhance extrinsic pseudocapacitance, which was also observed in $VO_2//LiNi_{0.5}Mn_{1.5}O_4$ redox pair in 45 m CsOAc+7 m LiOAc electrolyte. To break through physical limitation of salt solubility, concept of OSGE was proposed with inhomogeneous morphology while retain ionic conductivity. The OSGEs could further broaden the ESWs of RTSGEs, which basically remained ESWs at elevated temperatures. One $VO_2//LiNi_{0.5}Mn_{1.5}O_4$ battery based on $LiNO_3$ OSGE delivered 2.5 V working voltage with stable GCD cycling, while one $Zn//MnO_2$ battery based on acetate OSGE was cycled to 2000 cycles under overcharging. The elevated-temperature performance of OSGE-based batteries was impressive among ARBs, even working smoothly at 80 °C. The stable operation of ARBs with relatively diluted electrolytes in existence of oxygen was validated by DMA-diluted nitrate concentrated electrolyte, which simplified the ARBs assembly proposing. The relevant metrics of these works are summarized in Table 9.1.

Table 9.1 A summary of battery performance based on the electrolytes in this thesis.

Electrolyte	Electrode	Working voltage	Cyclic stability	Working temperature
1 m $Zn(OAc)_2$+31 m KOAc	$Zn//MnO_2$-TiN/TiO_2	2.0 V	600 cycles (1/3 C)	RT
45 m CsOAc+7 m LiOAc	$VO_2//LiNi_{0.5}Mn_{1.5}O_4$	2.5 V	1200 cycles (3 C)	RT
1 m Zn(OAc)2+40 m KOAc-PAA	$Zn//MnO_2$	2.0 V	2000 cycles (5 C)	RT to 80 °C
1 m $Zn(ClO_4)_2$+10 m $LiClO_4$-PVA	$Zn//LiMn_2O_4$	2.0 V	300 cycles (1 C)	RT
33 m $LiNO_3$-PAA	$VO_2//LiNi_{0.5}Mn_{1.5}O_4$	2.5 V	700 cycles (3 C)	RT
33 m $LiNO_3$-PAA	$VO_2//LiMn_2O_4$	2.0 V	220 cycles (3 C)	RT to 80 °C
DMA diluted 2.5 $Zn(NO_3)_2$+13 m $LiNO_3$	$Zn//LiMn_2O_4$	2.0 V	200 cycles (1 C)	RT

In terms of working voltage, nitrate OSGE-based VO_2//$LiNi_{0.5}Mn_{1.5}O_4$ cell (chapter 6) delivered highest one of 2.5 V. Although the same redox couple (chapter 4) based on acetate salt-concentrated electrolyte demonstrated the same working voltage, it was contributed by capacitive behaviour largely. As for the cyclic lifespan, acetate OSGE-based Zn//MnO_2 (chapter 7) cell showed the best cyclability of 2000 cycles in conditions of 5 C rate and 2 V working voltage (overcharging), as well as most excellent elevated-temperature stability of 300 cycles under same rate and working voltage up to 80 °C. Concerning energy density, the ones in chapters 3, 5, 7 and 8 were only based on the active mass of cathode due to Zn metal anode, while those in chapters 4 and 6 were based on the active mass of both anode and cathode, closer to real applications. Compared with commercialized LiBs with highest energy density of 350 wh·kg^{-1}, the ARBs in this thesis are not winners, while their safety and stability are better, especially the acetate OSGE-based Zn// MnO_2 battery.

9.2 Future work

According to Table 9.1, these electrolytes enabled high-voltage and high-stability ARBs, while relevant works can be enhanced as follows:

- The ESWs of these electrolytes can be extended in HER side by combining the salt-concentrated strategy with additives/interface tuning.
- The low-temperature battery performance based on these electrolytes, especially OSGEs need to be studied in detail.
- The electrode loading mass in ARBs here need to be increased as commercially mature ones.
- The capacitive behaviour of Zn//MnO_2 and VO_2//$LiNi_{0.5}Mn_{1.5}O_4$ redox couples shall be revealed with more fancy characterization.
- The anion-effect towards ESWs and stability of ARBs are unclear, which can be investigated in future.

As for ARBs, attention shall be paid to some potential challenges for further commercialization. The first one is the gap between industry and academics. In fact, reporting the performance based on a limited number of metrics does not give a realistic picture of the battery performance required by practical use. Although

it is not necessary to force the standardization of the electrode and button cell design for fundamental research, it is of paramount importance to understand the influence from button cell design, fabrication, and testing protocol to tested results, providing more reliable results as guidelines for future studies and practices. The second one is about simulation and characterization towards aqueous electrolytes. The parameters of MD simulation for solvation sheath, and DFT calculation for electrode-electrolyte interface should be pre-set conscientiously. As for experimental characterization upon ion solvation structure, Raman, FTIR and NMR are used mostly as indirect methods, while seldom works were reported using direct methods. The third one is about salt-concentrated electrolytes. The necessity of that high concentration shall be re-thought, because too concentrated is as bad as too diluted in some cases. While there is still a long way to practise WiSE, the most popular salt-concentrated specie, because of fragile in-situ grown SEI, and poor elevated-temperature performance. Moreover, suitable concentration and rational interfacial design are more critical than pursuing even more concentrated electrolytes. The most evident benefit induced by salt-concentrated electrolytes is expanded ESWs, thence higher working voltage and higher energy density of ARBs. However, improving capacity is another way for more considerable energy density. ZABs and ARFBs are regarded as effective aqueous chemistries to significantly improve capacity, which are promising alternatives for salt-concentrated strategy.

References

1. Hänsel, M.C., et al., *Climate economics support for the UN climate targets.* Nature Climate Change, 2020.
2. Lambers, J.H.R., *Extinction risks from climate change.* Science, 2015. **348**(6234): p. 501-502.
3. Eskander, S.M.S.U. and S. Fankhauser, *Reduction in greenhouse gas emissions from national climate legislation.* Nature Climate Change, 2020.
4. Babacan, O., et al., *Assessing the feasibility of carbon dioxide mitigation options in terms of energy usage.* Nature Energy, 2020.
5. Bauer, N., et al., *Global energy sector emission reductions and bioenergy use: overview of the bioenergy demand phase of the EMF-33 model comparison.* Climatic Change, 2018.
6. Thomas, C.E., *Fuel cell and battery electric vehicles compared.* International Journal of Hydrogen Energy, 2009. **34**(15): p. 6005-6020.
7. Zeng, X., et al., *Commercialization of Lithium Battery Technologies for Electric Vehicles.* Advanced Energy Materials, 2019. **9**(27): p. 1900161.
8. Tran, M., et al., *Realizing the electric-vehicle revolution.* Nature Climate Change, 2012. **2**(5): p. 328-333.
9. Lu, Y., et al., *Research and development of advanced battery materials in China.* Energy Storage Materials, 2019. **23**: p. 144-153.
10. Yoshino, A., *The Birth of the Lithium-Ion Battery.* Angewandte Chemie International Edition, 2012. **51**(24): p. 5798-5800.
11. Armand, M. and J.M. Tarascon, *Building better batteries.* Nature, 2008. **451**(7179): p. 652-657.
12. Lee, W., et al., *Advances in the Cathode Materials for Lithium Rechargeable Batteries.* Angewandte Chemie International Edition, 2020. **59**(7): p. 2578-2605.
13. Wang, Q., et al., *Progress of enhancing the safety of lithium ion battery from the electrolyte aspect.* Nano Energy, 2019. **55**: p. 93-114.
14. Wang, D., et al., *Quantifying electric vehicle battery degradation from driving vs. vehicle-to-grid services.* Journal of Power Sources, 2016. **332**: p. 193-203.
15. Zhu, G.-L., et al., *Fast Charging Lithium Batteries: Recent Progress and Future Prospects.* Small, 2019. **15**(15): p. 1805389.
16. Girishkumar, G., et al., *Lithium−Air Battery: Promise and Challenges.* The Journal of Physical Chemistry Letters, 2010. **1**(14): p. 2193-2203.
17. Evers, S. and L.F. Nazar, *New Approaches for High Energy Density Lithium–Sulfur Battery Cathodes.* Accounts of Chemical Research, 2013. **46**(5): p. 1135-1143.
18. Parasuraman, A., et al., *Review of material research and development for vanadium redox flow battery applications.* Electrochimica Acta, 2013. **101**: p. 27-40.
19. Zheng, F., et al., *Review on solid electrolytes for all-solid-state lithium-ion batteries.* Journal of Power Sources, 2018. **389**: p. 198-213.
20. Pang, Q., et al., *Tuning the electrolyte network structure to invoke quasi-solid state sulfur conversion and suppress lithium dendrite formation in Li–S batteries.* Nature Energy, 2018. **3**(9): p. 783-791.

21. Bin, D., et al., *The development in aqueous lithium-ion batteries.* Journal of Energy Chemistry, 2018. **27**(6): p. 1521-1535.
22. Famprikis, T., et al., *Fundamentals of inorganic solid-state electrolytes for batteries.* Nature Materials, 2019. **18**(12): p. 1278-1291.
23. Zhao, W., et al., *Solid-State Electrolytes for Lithium-Ion Batteries: Fundamentals, Challenges and Perspectives.* Electrochemical Energy Reviews, 2019. **2**(4): p. 574-605.
24. Janek, J. and W.G. Zeier, *A solid future for battery development.* Nature Energy, 2016. **1**(9): p. 16141.
25. Xin, S., et al., *Solid-State Lithium Metal Batteries Promoted by Nanotechnology: Progress and Prospects.* ACS Energy Letters, 2017. **2**(6): p. 1385-1394.
26. Galiński, M., A. Lewandowski, and I. Stępniak, *Ionic liquids as electrolytes.* Electrochimica Acta, 2006. **51**(26): p. 5567-5580.
27. Liu, J., et al., *Progress in aqueous rechargeable batteries.* Green Energy & Environment, 2018. **3**(1): p. 20-41.
28. Manjunatha, H., G.S. Suresh, and T.V. Venkatesha, *Electrode materials for aqueous rechargeable lithium batteries.* Journal of Solid State Electrochemistry, 2011. **15**(3): p. 431-445.
29. Tang, W., et al., *Aqueous rechargeable lithium batteries as an energy storage system of superfast charging.* Energy & Environmental Science, 2013. **6**(7): p. 2093-2104.
30. Gurung, A., et al., *A review on strategies addressing interface incompatibilities in inorganic all-solid-state lithium batteries.* Sustainable Energy & Fuels, 2019. **3**(12): p. 3279-3309.
31. Yue, L., et al., *All solid-state polymer electrolytes for high-performance lithium ion batteries.* Energy Storage Materials, 2016. **5**: p. 139-164.
32. Manuel Stephan, A., *Review on gel polymer electrolytes for lithium batteries.* European Polymer Journal, 2006. **42**(1): p. 21-42.
33. Wang, Y. and W.-H. Zhong, *Development of Electrolytes towards Achieving Safe and High-Performance Energy-Storage Devices: A Review.* ChemElectroChem, 2015. **2**(1): p. 22-36.
34. Liu, Z., et al., *Voltage issue of aqueous rechargeable metal-ion batteries.* Chemical Society Reviews, 2020. **49**(1): p. 180-232.
35. Alias, N. and A.A. Mohamad, *Advances of aqueous rechargeable lithium-ion battery: A review.* Journal of Power Sources, 2015. **274**: p. 237-251.
36. Pasta, M., et al., *A high-rate and long cycle life aqueous electrolyte battery for grid-scale energy storage.* Nature Communications, 2012. **3**(1): p. 1149.
37. Wu, X. and X. Ji, *Aqueous batteries get energetic.* Nature Chemistry, 2019. **11**(8): p. 680-681.
38. Eftekhari, A., *High-Energy Aqueous Lithium Batteries.* Advanced Energy Materials, 2018. **8**(24): p. 1801156.
39. Suo, L., et al., *"Water-in-salt" electrolyte enables high-voltage aqueous lithium-ion chemistries.* Science, 2015. **350**(6263): p. 938-943.
40. Luo, J.-Y., et al., *Raising the cycling stability of aqueous lithium-ion batteries by eliminating oxygen in the electrolyte.* Nature Chemistry, 2010. **2**(9): p. 760-765.
41. Posada, J.O.G., et al., *Aqueous batteries as grid scale energy storage solutions.* Renewable and Sustainable Energy Reviews, 2017. **68**: p. 1174-1182.

42. Kim, H., et al., *Aqueous Rechargeable Li and Na Ion Batteries.* Chemical Reviews, 2014. **114**(23): p. 11788-11827.

43. Yue, J., et al., *Interface Concentrated-Confinement Suppressing Cathode Dissolution in Water-in-Salt Electrolyte.* Advanced Energy Materials, 2020. **10**(36): p. 2000665.

44. Nian, Q., et al., *Aqueous Batteries Operated at −50 °C.* Angewandte Chemie International Edition, 2019. **58**(47): p. 16994-16999.

45. Xu, K., *Electrolytes and Interphases in Li-Ion Batteries and Beyond.* Chemical Reviews, 2014. **114**(23): p. 11503-11618.

46. Li, M., et al., *New Concepts in Electrolytes.* Chemical Reviews, 2020. **120**(14): p. 6783-6819.

47. Goodenough, J.B., *Design considerations.* Solid State Ionics, 1994. **69**(3): p. 184-198.

48. Mahmood, N., T. Tang, and Y. Hou, *Nanostructured Anode Materials for Lithium Ion Batteries: Progress, Challenge and Perspective.* Advanced Energy Materials, 2016. **6**(17): p. 1600374.

49. Goodenough, J.B. and Y. Kim, *Challenges for Rechargeable Li Batteries.* Chemistry of Materials, 2010. **22**(3): p. 587-603.

50. Ishikawa, M., et al., *Electric double layer capacitors with new gel electrolytes.* Electrochimica Acta, 1995. **40**(13): p. 2217-2222.

51. Xu, K., *Toward Reliable Values of Electrochemical Stability Limits for Electrolytes.* Journal of The Electrochemical Society, 1999. **146**(11): p. 4172.

52. Chen, S.G., et al., *Perchlorate Based "Oversaturated Gel Electrolyte" for an Aqueous Rechargeable Hybrid Zn–Li Battery.* ACS Applied Energy Materials, 2020. **3**(3): p. 2526-2536.

53. Chen, S., et al., *Nitrate-based 'oversaturated gel electrolyte' for high-voltage and high-stability aqueous lithium batteries.* Energy Storage Materials, 2021. **37**: p. 598-608.

54. Xu, K., *Nonaqueous Liquid Electrolytes for Lithium-Based Rechargeable Batteries.* Chemical Reviews, 2004. **104**(10): p. 4303-4418.

55. Kirby, W.B., *Linden's Handbook of Batteries, Fifth Edition.* 5th edition. ed. 2019, New York: McGraw-Hill Education.

56. Kontturi, A.-K., et al., *Effect of preferential solvation on Gibbs energies of ionic transfer.* Journal of the Chemical Society, Faraday Transactions, 1994. **90**(14): p. 2037-2041.

57. Huang, J., et al., *Recent Progress of Rechargeable Batteries Using Mild Aqueous Electrolytes.* Small Methods, 2019. **3**(1): p. 1800272.

58. Li, W., J.R. Dahn, and D.S. Wainwright, *Rechargeable Lithium Batteries with Aqueous Electrolytes.* Science, 1994. **264**(5162): p. 1115-1118.

59. Whitacre, J.F., A. Tevar, and S. Sharma, *Na4Mn9O18 as a positive electrode material for an aqueous electrolyte sodium-ion energy storage device.* Electrochemistry Communications, 2010. **12**(3): p. 463-466.

60. Park, S.I., et al., *Electrochemical Properties of NaTi2(PO4)3 Anode for Rechargeable Aqueous Sodium-Ion Batteries.* Journal of The Electrochemical Society, 2011. **158**(10): p. A1067.

61. Bin, D., et al., *Progress in Aqueous Rechargeable Sodium-Ion Batteries.* Advanced Energy Materials, 2018. **8**(17): p. 1703008.

62. Pu, X., et al., *Recent Progress in Rechargeable Sodium-Ion Batteries: toward High-Power Applications.* Small, 2019. **15**(32): p. 1805427.

63. Wessells, C.D., et al., *Nickel Hexacyanoferrate Nanoparticle Electrodes For Aqueous Sodium and Potassium Ion Batteries.* Nano Letters, 2011. **11**(12): p. 5421-5425.

64. Liu, S., et al., *Aqueous TiO2/Ni(OH)2 rechargeable battery with a high voltage based on proton and lithium insertion/extraction reactions.* Energy & Environmental Science, 2010. **3**(11): p. 1732-1735.

65. Tomai, T., et al., *Metal-free aqueous redox capacitor via proton rocking-chair system in an organic-based couple.* Scientific Reports, 2014. **4**(1): p. 3591.

66. Yang, C., et al., *Aqueous Li-ion battery enabled by halogen conversion–intercalation chemistry in graphite.* Nature, 2019. **569**(7755): p. 245-250.

67. Suo, L., et al., *Advanced High-Voltage Aqueous Lithium-Ion Battery Enabled by "Water-in-Bisalt" Electrolyte.* Angewandte Chemie International Edition, 2016. **55**(25): p. 7136-7141.

68. Jiang, H., et al., *A High-Rate Aqueous Proton Battery Delivering Power Below −78 °C via an Unfrozen Phosphoric Acid.* Advanced Energy Materials, 2020. **10**(28): p. 2000968.

69. Wu, X., et al., *Rocking-Chair Ammonium-Ion Battery: A Highly Reversible Aqueous Energy Storage System.* Angewandte Chemie International Edition, 2017. **56**(42): p. 13026-13030.

70. Rong, Z., et al., *Materials Design Rules for Multivalent Ion Mobility in Intercalation Structures.* Chemistry of Materials, 2015. **27**(17): p. 6016-6021.

71. Li, M., et al., *Design strategies for nonaqueous multivalent-ion and monovalent-ion battery anodes.* Nature Reviews Materials, 2020. **5**(4): p. 276-294.

72. Wu, X., et al., *A Rechargeable Battery with an Iron Metal Anode.* Advanced Functional Materials, 2019. **29**(20): p. 1900911.

73. Wei, L., et al., *An aqueous manganese-copper battery for large-scale energy storage applications.* Journal of Power Sources, 2019. **423**: p. 203-210.

74. Manalastas Jr, W., et al., *Water in Rechargeable Multivalent-Ion Batteries: An Electrochemical Pandora's Box.* ChemSusChem, 2019. **12**(2): p. 379-396.

75. Zeng, X., et al., *Recent progress and perspectives on aqueous Zn-based rechargeable batteries with mild aqueous electrolytes.* Energy Storage Materials, 2019. **20**: p. 410-437.

76. Kundu, D., et al., *A high-capacity and long-life aqueous rechargeable zinc battery using a metal oxide intercalation cathode.* Nature Energy, 2016. **1**(10): p. 16119.

77. Wruck, W.J., *Rechargeable Zn-MnO[sub 2] Alkaline Batteries.* Journal of The Electrochemical Society, 1991. **138**(12): p. 3560.

78. Fang, G., et al., *Recent Advances in Aqueous Zinc-Ion Batteries.* ACS Energy Letters, 2018. **3**(10): p. 2480-2501.

79. Xu, C., et al., *Energetic Zinc Ion Chemistry: The Rechargeable Zinc Ion Battery.* Angewandte Chemie International Edition, 2012. **51**(4): p. 933-935.

80. Chen, S., et al., *Salt-concentrated acetate electrolytes for a high voltage aqueous Zn/MnO2 battery.* Energy Storage Materials, 2020. **28**: p. 205-215.

81.   Zeng, Y., et al., *Achieving Ultrahigh Energy Density and Long Durability in a Flexible Rechargeable Quasi-Solid-State Zn–MnO2 Battery.* Advanced Materials, 2017. **29**(26): p. 1700274.

82.   Jin, Y., et al., *Joint Charge Storage for High-Rate Aqueous Zinc–Manganese Dioxide Batteries.* Advanced Materials, 2019. **31**(29): p. 1900567.

83.   Chao, D., et al., *An Electrolytic Zn–MnO2 Battery for High-Voltage and Scalable Energy Storage.* Angewandte Chemie International Edition, 2019. **58**(23): p. 7823-7828.

84.   Liu, C., et al., *A High Energy Density Aqueous Battery Achieved by Dual Dissolution/Deposition Reactions Separated in Acid-Alkaline Electrolyte.* Advanced Energy Materials, 2020. **10**(12): p. 1903589.

85.   Zhong, C., et al., *Decoupling electrolytes towards stable and high-energy rechargeable aqueous zinc–manganese dioxide batteries.* Nature Energy, 2020. **5**(6): p. 440-449.

86.   Yadav, G.G., et al., *Breaking the 2 V Barrier in Aqueous Zinc Chemistry: Creating 2.45 and 2.8 V MnO2–Zn Aqueous Batteries.* ACS Energy Letters, 2019. **4**(9): p. 2144-2146.

87.   Xie, C., et al., *A highly reversible neutral zinc/manganese battery for stationary energy storage.* Energy & Environmental Science, 2020. **13**(1): p. 135-143.

88.   Li, M., et al., *A Novel Dendrite-Free Mn2+/Zn2+ Hybrid Battery with 2.3 V Voltage Window and 11000-Cycle Lifespan.* Advanced Energy Materials, 2019. **9**(29): p. 1901469.

89.   Li, G., et al., *Membrane-Free Zn/MnO2 Flow Battery for Large-Scale Energy Storage.* Advanced Energy Materials, 2020. **10**(9): p. 1902085.

90.   Mo, F., et al., *Zwitterionic Sulfobetaine Hydrogel Electrolyte Building Separated Positive/Negative Ion Migration Channels for Aqueous Zn-MnO2 Batteries with Superior Rate Capabilities.* Advanced Energy Materials, 2020. **10**(16): p. 2000035.

91.   Li, H., et al., *An extremely safe and wearable solid-state zinc ion battery based on a hierarchical structured polymer electrolyte.* Energy & Environmental Science, 2018. **11**(4): p. 941-951.

92.   Wang, D., et al., *A Nanofibrillated Cellulose/Polyacrylamide Electrolyte-Based Flexible and Sewable High-Performance Zn–MnO2 Battery with Superior Shear Resistance.* Small, 2018. **14**(51): p. 1803978.

93.   Zeng, X., et al., *Toward a Reversible Mn4+/Mn2+ Redox Reaction and Dendrite-Free Zn Anode in Near-Neutral Aqueous Zn/MnO2 Batteries via Salt Anion Chemistry.* Advanced Energy Materials, 2020. **10**(32): p. 1904163.

94.   Chao, D., et al., *Atomic Engineering Catalyzed MnO2 Electrolysis Kinetics for a Hybrid Aqueous Battery with High Power and Energy Density.* Advanced Materials, 2020. **32**(25): p. 2001894.

95.   Song, W.-J., et al., *Stretchable Aqueous Batteries: Progress and Prospects.* ACS Energy Letters, 2019. **4**(1): p. 177-186.

96.   Verma, V., et al., *Progress in Rechargeable Aqueous Zinc- and Aluminum-Ion Battery Electrodes: Challenges and Outlook.* Advanced Sustainable Systems, 2019. **3**(1): p. 1800111.

97. Zečević, S., et al., *Effect of pulsating current on anode polarisation in an aluminium anode battery with a neutral aqueous electrolyte.* Electrochimica Acta, 1981. **26**(11): p. 1625-1631.

98. Liu, S., et al., *Aluminum storage behavior of anatase TiO2 nanotube arrays in aqueous solution for aluminum ion batteries.* Energy & Environmental Science, 2012. **5**(12): p. 9743-9746.

99. Wang, F., et al., *High-Voltage Aqueous Magnesium Ion Batteries.* ACS Central Science, 2017. **3**(10): p. 1121-1128.

100. Zhang, Y., et al., *Preparation of M1/3Ni1/3Mn2/3O2 (M=Mg or Zn) and its performance as the cathode material of aqueous divalent cations battery.* Electrochimica Acta, 2015. **182**: p. 971-978.

101. Mizuno, Y., et al., *Electrochemical Mg2+ intercalation into a bimetallic CuFe Prussian blue analog in aqueous electrolytes.* Journal of Materials Chemistry A, 2013. **1**(42): p. 13055-13059.

102. Chen, L., et al., *Aqueous Mg-Ion Battery Based on Polyimide Anode and Prussian Blue Cathode.* ACS Energy Letters, 2017. **2**(5): p. 1115-1121.

103. Lee, C. and S.-K. Jeong, *A Novel Superconcentrated Aqueous Electrolyte to Improve the Electrochemical Performance of Calcium-ion Batteries.* Chemistry Letters, 2016. **45**(12): p. 1447-1449.

104. Gheytani, S., et al., *An Aqueous Ca-Ion Battery.* Advanced Science, 2017. **4**(12): p. 1700465.

105. Blurton, K.F. and A.F. Sammells, *Metal/air batteries: Their status and potential — a review.* Journal of Power Sources, 1979. **4**(4): p. 263-279.

106. Lee, J.-S., et al., *Metal–Air Batteries with High Energy Density: Li–Air versus Zn–Air.* Advanced Energy Materials, 2011. **1**(1): p. 34-50.

107. Zhang, T., et al., *Li / Polymer Electrolyte / Water Stable Lithium-Conducting Glass Ceramics Composite for Lithium–Air Secondary Batteries with an Aqueous Electrolyte.* Journal of The Electrochemical Society, 2008. **155**(12): p. A965.

108. Zhang, T., et al., *Aqueous Lithium/Air Rechargeable Batteries.* Chemistry Letters, 2011. **40**(7): p. 668-673.

109. Hayashi, K., K. Shima, and F. Sugiyama, *A Mixed Aqueous/Aprotic Sodium/Air Cell Using a NASICON Ceramic Separator.* Journal of The Electrochemical Society, 2013. **160**(9): p. A1467-A1472.

110. Li, Y. and H. Dai, *Recent advances in zinc–air batteries.* Chemical Society Reviews, 2014. **43**(15): p. 5257-5275.

111. Fu, J., et al., *Recent Progress in Electrically Rechargeable Zinc–Air Batteries.* Advanced Materials, 2019. **31**(31): p. 1805230.

112. Liu, S., et al., *A novel rechargeable zinc-air battery with molten salt electrolyte.* Journal of Power Sources, 2017. **342**: p. 435-441.

113. Deyab, M.A. and Q. Mohsen, *Improved battery capacity and cycle life in iron-air batteries with ionic liquid.* Renewable and Sustainable Energy Reviews, 2021. **139**: p. 110729.

114. Chawla, N., *Recent advances in air-battery chemistries.* Materials Today Chemistry, 2019. **12**: p. 324-331.

115. Hang, B.T., et al., *The effect of additives on the electrochemical properties of Fe/C composite for Fe/air battery anode.* Journal of Power Sources, 2006. **155**(2): p. 461-469.

116. Boyjoo, Y., et al., *Engineering nanoreactors for metal–chalcogen batteries.* Energy & Environmental Science, 2021. **14**(2): p. 540-575.

117. Peng, H.-J., J.-Q. Huang, and Q. Zhang, *A review of flexible lithium–sulfur and analogous alkali metal–chalcogen rechargeable batteries.* Chemical Society Reviews, 2017. **46**(17): p. 5237-5288.

118. Yun, S., et al., *Materials and Device Constructions for Aqueous Lithium–Sulfur Batteries.* Advanced Functional Materials, 2018. **28**(38): p. 1707593.

119. Licht, S. and D. Peramunage, *Novel Aqueous Aluminum/Sulfur Batteries.* Journal of The Electrochemical Society, 1993. **140**(1): p. L4-L6.

120. Wu, X., et al., *Rechargeable Iron–Sulfur Battery without Polysulfide Shuttling.* Advanced Energy Materials, 2019. **9**(40): p. 1902422.

121. Li, N., et al., *Integrating a Photocatalyst into a Hybrid Lithium–Sulfur Battery for Direct Storage of Solar Energy.* Angewandte Chemie International Edition, 2015. **54**(32): p. 9271-9274.

122. Gross, M.M. and A. Manthiram, *Development of low-cost sodium-aqueous polysulfide hybrid batteries.* Energy Storage Materials, 2019. **19**: p. 346-351.

123. Zhao, Y., et al., *Initiating a Reversible Aqueous Zn/Sulfur Battery through a "Liquid Film".* Advanced Materials, 2020. **32**(32): p. 2003070.

124. Chen, Z., et al., *Aqueous Zinc–Tellurium Batteries with Ultraflat Discharge Plateau and High Volumetric Capacity.* Advanced Materials, 2020. **32**(42): p. 2001469.

125. Chen, Z., et al., *Zinc/selenium conversion battery: a system highly compatible with both organic and aqueous electrolytes.* Energy & Environmental Science, 2021. **14**(4): p. 2441-2450.

126. Ao, H., et al., *Rechargeable aqueous hybrid ion batteries: developments and prospects.* Journal of Materials Chemistry A, 2019. **7**(32): p. 18708-18734.

127. Yao, H.-R., et al., *Rechargeable dual-metal-ion batteries for advanced energy storage.* Physical Chemistry Chemical Physics, 2016. **18**(14): p. 9326-9333.

128. Chen, L., et al., *New-concept Batteries Based on Aqueous Li+/Na+ Mixed-ion Electrolytes.* Scientific Reports, 2013. **3**(1): p. 1946.

129. Cao, X., et al., *A low-cost Mg2+/Na+ hybrid aqueous battery.* Journal of Materials Chemistry A, 2018. **6**(32): p. 15762-15770.

130. Yan, J., et al., *Rechargeable hybrid aqueous batteries.* Journal of Power Sources, 2012. **216**: p. 222-226.

131. Wang, F., et al., *Highly reversible zinc metal anode for aqueous batteries.* Nature Materials, 2018. **17**(6): p. 543-549.

132. Placke, T., et al., *Perspective on Performance, Cost, and Technical Challenges for Practical Dual-Ion Batteries.* Joule, 2018. **2**(12): p. 2528-2550.

133. Zhang, L., et al., *A Review of Emerging Dual-Ion Batteries: Fundamentals and Recent Advances.* Advanced Functional Materials, 2021. **n/a**(n/a): p. 2010958.

134. Wu, X., et al., *Reverse Dual-Ion Battery via a ZnCl2 Water-in-Salt Electrolyte.* Journal of the American Chemical Society, 2019. **141**(15): p. 6338-6344.

135. Ding, J., et al., *Review of Hybrid Ion Capacitors: From Aqueous to Lithium to Sodium.* Chemical Reviews, 2018. **118**(14): p. 6457-6498.

136. Wang, Y.-g. and Y.-y. Xia, *A new concept hybrid electrochemical surpercapacitor: Carbon/LiMn2O4 aqueous system.* Electrochemistry Communications, 2005. **7**(11): p. 1138-1142.

137. Zheng, J.P., *The Limitations of Energy Density of Battery/Double-Layer Capacitor Asymmetric Cells.* Journal of The Electrochemical Society, 2003. **150**(4): p. A484.

138. Athouël, L., et al., *Variation of the MnO2 Birnessite Structure upon Charge/Discharge in an Electrochemical Supercapacitor Electrode in Aqueous Na2SO4 Electrolyte.* The Journal of Physical Chemistry C, 2008. **112**(18): p. 7270-7277.

139. Dong, L., et al., *Extremely safe, high-rate and ultralong-life zinc-ion hybrid supercapacitors.* Energy Storage Materials, 2018. **13**: p. 96-102.

140. Yao, Y., et al., *Assessment methods and performance metrics for redox flow batteries.* Nature Energy, 2021.

141. Li, Z. and Y.-C. Lu, *Material Design of Aqueous Redox Flow Batteries: Fundamental Challenges and Mitigation Strategies.* Advanced Materials, 2020. **32**(47): p. 2002132.

142. Sum, E. and M. Skyllas-Kazacos, *A study of the V(II)/V(III) redox couple for redox flow cell applications.* Journal of Power Sources, 1985. **15**(2): p. 179-190.

143. Ma, D., et al., *Highly active nanostructured CoS2/CoS heterojunction electrocatalysts for aqueous polysulfide/iodide redox flow batteries.* Nature Communications, 2019. **10**(1): p. 3367.

144. Schmidt-Rohr, K. and Q. Chen, *Parallel cylindrical water nanochannels in Nafion fuel-cell membranes.* Nature Materials, 2008. **7**(1): p. 75-83.

145. Singh, P. and B. Jonshagen, *Zinc   bromine battery for energy storage.* Journal of Power Sources, 1991. **35**(4): p. 405-410.

146. Li, B., et al., *Ambipolar zinc-polyiodide electrolyte for a high-energy density aqueous redox flow battery.* Nature Communications, 2015. **6**(1): p. 6303.

147. Price, A., et al., *A novel approach to utility scale energy storage [regenerative fuel cells].* Power Engineering Journal, 1999. **13**(3): p. 122-129.

148. Li, Z., et al., *A high-energy and low-cost polysulfide/iodide redox flow battery.* Nano Energy, 2016. **30**: p. 283-292.

149. Xu, Y., et al. *Novel organic redox flow batteries using soluble quinonoid compounds as positive materials.* in *2009 World Non-Grid-Connected Wind Power and Energy Conference.* 2009.

150. Feng, R., et al., *Reversible ketone hydrogenation and dehydrogenation for aqueous organic redox flow batteries.* Science, 2021. **372**(6544): p. 836.

151. Pan, H., et al., *Reversible aqueous zinc/manganese oxide energy storage from conversion reactions.* Nature Energy, 2016. **1**(5): p. 16039.

152. Chao, D., et al., *Roadmap for advanced aqueous batteries: From design of materials to applications.* Science Advances, 2020. **6**(21): p. eaba4098.

153. Zhang, S.S., *A review on electrolyte additives for lithium-ion batteries.* Journal of Power Sources, 2006. **162**(2): p. 1379-1394.

154. Guo, S., et al., *Fundamentals and perspectives of electrolyte additives for aqueous zinc-ion batteries.* Energy Storage Materials, 2021. **34**: p. 545-562.

155. Hou, Z., et al., *Surfactant widens the electrochemical window of an aqueous electrolyte for better rechargeable aqueous sodium/zinc battery.* Journal of Materials Chemistry A, 2017. **5**(2): p. 730-738.

156. Hoang, T.K.A., et al., *Sustainable gel electrolyte containing Pb2+ as corrosion inhibitor and dendrite suppressor for the zinc anode in the rechargeable hybrid aqueous battery.* Materials Today Energy, 2017. **4**: p. 34-40.

157. Xu, W., et al., *Diethyl ether as self-healing electrolyte additive enabled long-life rechargeable aqueous zinc ion batteries.* Nano Energy, 2019. **62**: p. 275-281.

158. Hao, J., et al., *Toward High-Performance Hybrid Zn-Based Batteries via Deeply Understanding Their Mechanism and Using Electrolyte Additive.* Advanced Functional Materials, 2019. **29**(34): p. 1903605.

159. Cao, L., et al., *Fluorinated interphase enables reversible aqueous zinc battery chemistries.* Nature Nanotechnology, 2021.

160. An, Y., et al., *Stable Aqueous Anode-Free Zinc Batteries Enabled by Interfacial Engineering.* Advanced Functional Materials, 2021. **n/a**(n/a): p. 2101886.

161. Wang, F., et al., *Stabilizing high voltage LiCoO2 cathode in aqueous electrolyte with interphase-forming additive.* Energy & Environmental Science, 2016. **9**(12): p. 3666-3673.

162. Nian, Q., et al., *Designing Electrolyte Structure to Suppress Hydrogen Evolution Reaction in Aqueous Batteries.* ACS Energy Letters, 2021: p. 2174-2180.

163. Cui, J., et al., *Improved electrochemical reversibility of Zn plating/stripping: a promising approach to suppress water-induced issues through the formation of H-bonding.* Materials Today Energy, 2020. **18**: p. 100563.

164. Sun, T., et al., *High Power and Energy Density Aqueous Proton Battery Operated at −90 °C.* Advanced Functional Materials, 2021. **31**(16): p. 2010127.

165. Yue, F., et al., *An Ultralow Temperature Aqueous Battery with Proton Chemistry.* Angewandte Chemie International Edition, 2021. **n/a**(n/a).

166. Li, W., W.R. McKinnon, and J.R. Dahn, *Lithium Intercalation from Aqueous Solutions.* Journal of The Electrochemical Society, 1994. **141**(9): p. 2310-2316.

167. Li, W. and J.R. Dahn, *Lithium‐Ion Cells with Aqueous Electrolytes.* Journal of The Electrochemical Society, 1995. **142**(6): p. 1742-1746.

168. Bai, L., et al., *Reducing hydrated protons co-intercalation to enhance cycling stability of CuV2O5 nanobelts: a new anode material for aqueous lithium ion batteries.* Journal of Materials Chemistry, 2012. **22**(33): p. 16957-16963.

169. Xie, Z., et al., *High performance of zinc-ferrum redox flow battery with Ac−/HAc buffer solution.* Journal of Energy Chemistry, 2016. **25**(3): p. 495-499.

170. Demir-Cakan, R., et al., *An aqueous electrolyte rechargeable Li-ion/polysulfide battery.* Journal of Materials Chemistry A, 2014. **2**(24): p. 9025-9029.

171.	Wang, F., et al., *A Stimulus-Responsive Zinc–Iodine Battery with Smart Overcharge Self-Protection Function.* Advanced Materials, 2020. **32**(16): p. 2000287.

172.	Cheng, F.Y., et al., *High-power alkaline Zn–MnO$_2$ batteries using γ-MnO$_2$ nanowires/nanotubes and electrolytic zinc powder.* Advanced Materials, 2005. **17**(22): p. 2753-2756.

173.	Zhang, N., et al., *Cation-Deficient Spinel ZnMn2O4 Cathode in Zn(CF3SO3)2 Electrolyte for Rechargeable Aqueous Zn-Ion Battery.* Journal of the American Chemical Society, 2016. **138**(39): p. 12894-12901.

174.	Sun, W., et al., *Zn/MnO2 Battery Chemistry With H+ and Zn2+ Coinsertion.* Journal of the American Chemical Society, 2017. **139**(29): p. 9775-9778.

175.	Guo, X., et al., *Zn/MnO2 battery chemistry with dissolution-deposition mechanism.* Materials Today Energy, 2020. **16**: p. 100396.

176.	Dai, L., et al., *Jahn–Teller Distortion Induced Mn2+-Rich Cathode Enables Optimal Flexible Aqueous High-Voltage Zn-Mn Batteries.* Advanced Science, 2021. **n/a**(n/a): p. 2004995.

177.	Li, C., et al., *A high-voltage aqueous lithium ion capacitor with high energy density from an alkaline–neutral electrolyte.* Journal of Materials Chemistry A, 2019. **7**(8): p. 4110-4118.

178.	Fan, W., et al., *A high voltage aqueous zinc–manganese battery using a hybrid alkaline-mild electrolyte.* Chemical Communications, 2020. **56**(13): p. 2039-2042.

179.	Yuan, X., et al., *A Fully Aqueous Hybrid Electrolyte Rechargeable Battery with High Voltage and High Energy Density.* Advanced Energy Materials, 2020. **10**(40): p. 2001583.

180.	Yamada, Y., et al., *Advances and issues in developing salt-concentrated battery electrolytes.* Nature Energy, 2019. **4**(4): p. 269-280.

181.	Dong, Q., et al., *Cathodically Stable Li-O2 Battery Operations Using Water-in-Salt Electrolyte.* Chem, 2018. **4**(6): p. 1345-1358.

182.	Yang, C., et al., *Unique aqueous Li-ion/sulfur chemistry with high energy density and reversibility.* Proceedings of the National Academy of Sciences, 2017. **114**(24): p. 6197-6202.

183.	Chen, L., et al., *Enabling safe aqueous lithium ion open batteries by suppressing oxygen reduction reaction.* Nature Communications, 2020. **11**(1): p. 2638.

184.	Jiang, L., et al., *Building aqueous K-ion batteries for energy storage.* Nature Energy, 2019. **4**(6): p. 495-503.

185.	Reber, D., R.-S. Kühnel, and C. Battaglia, *Suppressing Crystallization of Water-in-Salt Electrolytes by Asymmetric Anions Enables Low-Temperature Operation of High-Voltage Aqueous Batteries.* ACS Materials Letters, 2019. **1**(1): p. 44-51.

186.	Zhang, C., et al., *A ZnCl2 water-in-salt electrolyte for a reversible Zn metal anode.* Chemical Communications, 2018. **54**(100): p. 14097-14099.

187.	Lukatskaya, M.R., et al., *Concentrated mixed cation acetate "water-in-salt" solutions as green and low-cost high voltage electrolytes for aqueous batteries.* Energy & Environmental Science, 2018. **11**(10): p. 2876-2883.

188.	Leonard, D.P., et al., *Water-in-Salt Electrolyte for Potassium-Ion Batteries.* ACS Energy Letters, 2018. **3**(2): p. 373-374.

189. Yamada, Y., et al., *Hydrate-melt electrolytes for high-energy-density aqueous batteries.* Nature Energy, 2016. **1**(10): p. 16129.

190. Zheng, Q., et al., *Sodium- and Potassium-Hydrate Melts Containing Asymmetric Imide Anions for High-Voltage Aqueous Batteries.* Angewandte Chemie International Edition, 2019. **58**(40): p. 14202-14207.

191. Wu, S., et al., *Clean Electrocatalysis in a Li2O2 Redox-Based Li–O2 Battery Built with a Hydrate-Melt Electrolyte.* ACS Catalysis, 2018. **8**(2): p. 1082-1089.

192. Chen, C.-Y., et al., *A Room-Temperature Molten Hydrate Electrolyte for Rechargeable Zinc–Air Batteries.* Advanced Energy Materials, 2019. **9**(22): p. 1900196.

193. Chen, S., et al., *Effect of cation size on alkali acetate-based 'water-in-bisalt' electrolyte and its application in aqueous rechargeable lithium battery.* Applied Materials Today, 2020. **20**: p. 100728.

194. Zheng, J., et al., *Understanding Thermodynamic and Kinetic Contributions in Expanding the Stability Window of Aqueous Electrolytes.* Chem, 2018. **4**(12): p. 2872-2882.

195. Tang, X., et al., *A universal strategy towards high–energy aqueous multivalent–ion batteries.* Nature Communications, 2021. **12**(1): p. 2857.

196. Zhang, Q., et al., *Modulating electrolyte structure for ultralow temperature aqueous zinc batteries.* Nature Communications, 2020. **11**(1): p. 4463.

197. Bi, H., et al., *A Universal Approach to Aqueous Energy Storage via Ultralow-Cost Electrolyte with Super-Concentrated Sugar as Hydrogen-Bond-Regulated Solute.* Advanced Materials, 2020. **32**(16): p. 2000074.

198. Liu, H., et al., *A Zinc–Dual-Halogen Battery with a Molten Hydrate Electrolyte.* Advanced Materials, 2020. **32**(46): p. 2004553.

199. Wu, S., et al., *Hybrid high-concentration electrolyte significantly strengthens the practicability of alkaline aluminum-air battery.* Energy Storage Materials, 2020. **31**: p. 310-317.

200. Suo, L., et al., *"Water-in-Salt" Electrolyte Makes Aqueous Sodium-Ion Battery Safe, Green, and Long-Lasting.* Advanced Energy Materials, 2017. **7**(21): p. 1701189.

201. Chen, L., et al., *A 63 m Superconcentrated Aqueous Electrolyte for High-Energy Li-Ion Batteries.* ACS Energy Letters, 2020. **5**(3): p. 968-974.

202. Lee, M.H., et al., *Toward a low-cost high-voltage sodium aqueous rechargeable battery.* Materials Today, 2019. **29**: p. 26-36.

203. Yang, W., et al., *Hydrated Eutectic Electrolytes with Ligand-Oriented Solvation Shells for Long-Cycling Zinc-Organic Batteries.* Joule, 2020. **4**(7): p. 1557-1574.

204. Wang, Z., et al., *Hydrogel Electrolytes for Flexible Aqueous Energy Storage Devices.* Advanced Functional Materials, 2018. **28**(48): p. 1804560.

205. Liu, Z., et al., *Towards wearable electronic devices: A quasi-solid-state aqueous lithium-ion battery with outstanding stability, flexibility, safety and breathability.* Nano Energy, 2018. **44**: p. 164-173.

206. Wang, G., et al., *LiCl/PVA Gel Electrolyte Stabilizes Vanadium Oxide Nanowire Electrodes for Pseudocapacitors.* ACS Nano, 2012. **6**(11): p. 10296-10302.

207. Chen, S., et al., *Perchlorate Based "Oversaturated Gel Electrolyte" for an Aqueous Rechargeable Hybrid Zn–Li Battery.* ACS Applied Energy Materials, 2020. **3**(3): p. 2526-2536.

208. Yang, C., et al., *Flexible Aqueous Li-Ion Battery with High Energy and Power Densities.* Advanced Materials, 2017. **29**(44): p. 1701972.

209. Xie, J., Z. Liang, and Y.-C. Lu, *Molecular crowding electrolytes for high-voltage aqueous batteries.* Nature Materials, 2020. **19**(9): p. 1006-1011.

210. Pan, W., et al., *High-Performance Aqueous Na–Zn Hybrid Ion Battery Boosted by "Water-In-Gel" Electrolyte.* Advanced Functional Materials, 2021. **31**(15): p. 2008783.

211. Dai, C., et al., *Maximizing Energy Storage of Flexible Aqueous Batteries through Decoupling Charge Carriers.* Advanced Energy Materials, 2021. **11**(14): p. 2003982.

212. Yang, J., et al., *Antifreezing Zwitterionic Hydrogel Electrolyte with High Conductivity of 12.6 mS cm−1 at −40 °C through Hydrated Lithium Ion Hopping Migration.* Advanced Functional Materials, 2021. **31**(18): p. 2009438.

213. Chen, M., et al., *Anti-freezing flexible aqueous Zn–MnO2 batteries working at −35 °C enabled by a borax-crosslinked polyvinyl alcohol/glycerol gel electrolyte.* Journal of Materials Chemistry A, 2020. **8**(14): p. 6828-6841.

214. Wang, F., et al., *Hybrid Aqueous/Non-aqueous Electrolyte for Safe and High-Energy Li-Ion Batteries.* Joule, 2018. **2**(5): p. 927-937.

215. Wrogemann, J.M., et al., *Development of Safe and Sustainable Dual-Ion Batteries Through Hybrid Aqueous/Nonaqueous Electrolytes.* Advanced Energy Materials, 2020. **10**(8): p. 1902709.

216. Zhu, J., et al., *Hybrid Aqueous/Nonaqueous Water-in-Bisalt Electrolyte Enables Safe Dual Ion Batteries.* Small, 2020. **16**(17): p. 1905838.

217. Zhang, H., et al., *Aqueous/Nonaqueous Hybrid Electrolyte for Sodium-Ion Batteries.* ACS Energy Letters, 2018. **3**(7): p. 1769-1770.

218. Zhao, J., et al., *"Water-in-deep eutectic solvent" electrolytes enable zinc metal anodes for rechargeable aqueous batteries.* Nano Energy, 2019. **57**: p. 625-634.

219. Dou, Q., et al., *"Water in salt/ionic liquid" electrolyte for 2.8 V aqueous lithium-ion capacitor.* Science Bulletin, 2020. **65**(21): p. 1812-1822.

220. Chen, J., et al., *Improving Electrochemical Stability and Low-Temperature Performance with Water/Acetonitrile Hybrid Electrolytes.* Advanced Energy Materials, 2020. **10**(3): p. 1902654.

221. Chang, N., et al., *An aqueous hybrid electrolyte for low-temperature zinc-based energy storage devices.* Energy & Environmental Science, 2020. **13**(10): p. 3527-3535.

222. Hao, J., et al., *Boosting Zinc Electrode Reversibility in Aqueous Electrolytes by Using Low-Cost Antisolvents.* Angewandte Chemie International Edition, 2021. **60**(13): p. 7366-7375.

223. Zhang, L. and G. Yu, *Hybrid Electrolyte Engineering Enables Safe and Wide-Temperature Redox Flow Batteries.* Angewandte Chemie International Edition, 2021. **n/a**(n/a).

224. Shang, Y., et al., *An "Ether-In-Water" Electrolyte Boosts Stable Interfacial Chemistry for Aqueous Lithium-Ion Batteries.* Advanced Materials, 2020. **32**(40): p. 2004017.

225. He, X., et al., *Fluorine-free water-in-ionomer electrolytes for sustainable lithium-ion batteries.* Nature Communications, 2018. **9**(1): p. 5320.

226. Liu, C., et al., *Engineering Fast Ion Conduction and Selective Cation Channels for a High-Rate and High-Voltage Hybrid Aqueous Battery.* Angewandte Chemie Internatinal Edition, 2018. **57**(24): p. 7046-7050.

227. Suo, L., et al., *How Solid-Electrolyte Interphase Forms in Aqueous Electrolytes.* Journal of the American Chemical Society, 2017. **139**(51): p. 18670-18680.

228. Li, D., et al., *Design of a Solid Electrolyte Interphase for Aqueous Zn Batteries.* Angewandte Chemie International Edition, 2021. **60**(23): p. 13035-13041.

229. Yang, C., et al., *4.0 V Aqueous Li-Ion Batteries.* Joule, 2017. **1**(1): p. 122-132.

230. Zhang, Q., et al., *Interfacial Design of Dendrite-Free Zinc Anodes for Aqueous Zinc-Ion Batteries.* Angewandte Chemie International Edition, 2020. **59**(32): p. 13180-13191.

231. Deng, C., et al., *A Sieve-Functional and Uniform-Porous Kaolin Layer toward Stable Zinc Metal Anode.* Advanced Functional Materials, 2020. **30**(21): p. 2000599.

232. Kang, L., et al., *Nanoporous CaCO3 Coatings Enabled Uniform Zn Stripping/Plating for Long-Life Zinc Rechargeable Aqueous Batteries.* Advanced Energy Materials, 2018. **8**(25): p. 1801090.

233. Zhang, L., et al., *An In Situ Artificial Cathode Electrolyte Interphase Strategy for Suppressing Cathode Dissolution in Aqueous Zinc Ion Batteries.* Small Methods, 2021. **n/a**(n/a): p. 2100094.

234. Lee, C., et al., *Cathode-Electrolyte-Interphase Film Formation on a LiNiO2 Surface in Conventional Aqueous Electrolytes: Simple Method to Improve the Electrochemical Performance of LiNiO2 Electrodes for Use in Aqueous Li-Ion Batteries.* Advanced Energy Materials, 2021. **n/a**(n/a): p. 2100756.

235. Hou, Z., et al., *Passivation effect for current collectors enables high-voltage aqueous sodium ion batteries.* Materials Today Energy, 2019. **14**: p. 100337.

236. Wang, S.-B., et al., *Lamella-nanostructured eutectic zinc–aluminum alloys as reversible and dendrite-free anodes for aqueous rechargeable batteries.* Nature Communications, 2020. **11**(1): p. 1634.

237. Zheng, J., et al., *Reversible epitaxial electrodeposition of metals in battery anodes.* Science, 2019. **366**(6465): p. 645-648.

238. Li, J., et al., *Tunable stable operating potential window for high-voltage aqueous supercapacitors.* Nano Energy, 2019. **63**: p. 103848.

239. Yan, C., et al., *Architecting a Stable High-Energy Aqueous Al-Ion Battery.* Journal of the American Chemical Society, 2020. **142**(36): p. 15295-15304.

240. Chang, Z., et al., *A Liquid Electrolyte with De-Solvated Lithium Ions for Lithium-Metal Battery.* Joule, 2020. **4**(8): p. 1776-1789.

241. Chang, Z., et al., *Beyond the concentrated electrolyte: further depleting solvent molecules within a Li+ solvation sheath to stabilize high-energy-density lithium metal batteries.* Energy & Environmental Science, 2020. **13**(11): p. 4122-4131.

242. Sun, Y., et al., *Salty Ice Electrolyte with Superior Ionic Conductivity Towards Low-Temperature Aqueous Zinc Ion Hybrid Capacitors.* Advanced Functional Materials, 2021. **n/a**(n/a): p. 2101277.

243. Cai, S., et al., *Water–Salt Oligomers Enable Supersoluble Electrolytes for High-Performance Aqueous Batteries.* Advanced Materials, 2021. **33**(13): p. 2007470.

244. Shbeh, M.M. and R. Goodall, *Open pore titanium foams via metal injection molding of metal powder with a space holder.* Metal Powder Report, 2016. **71**(6): p. 450-455.

245. Yan, D., et al., *MnO₂ film with three-dimensional structure prepared by hydrothermal process for supercapacitor.* Journal of Power Sources, 2012. **199**: p. 409-412.

246. Zhang, Y., et al., *Synthesis and characterization of belt-like VO2(B)@carbon and V2O3@carbon core–shell structured composites.* Colloids and Surfaces A: Physicochemical and Engineering Aspects, 2012. **396**: p. 144-152.

247. Zhou, L., D. Zhao, and X. Lou, *LiNi0.5Mn1.5O4 Hollow Structures as High-Performance Cathodes for Lithium-Ion Batteries.* Angewandte Chemie International Edition, 2012. **51**(1): p. 239-241.

248. Kim, D.K., et al., *Spinel LiMn2O4 Nanorods as Lithium Ion Battery Cathodes.* Nano Letters, 2008. **8**(11): p. 3948-3952.

249. Wang, X. and Y. Li, *Selected-Control Hydrothermal Synthesis of α- and β-MnO2 Single Crystal Nanowires.* Journal of the American Chemical Society, 2002. **124**(12): p. 2880-2881.

250. Toby, B.H., *EXPGUI, a graphical user interface for GSAS.* Journal of Applied Crystallography, 2001. **34**: p. 210-213.

251. Larson, A.C. and R.B. Von Dreele, *General Structure Analysis System (GSAS).* General Structure Analysis System (GSAS), Los Alamos National Laboratory Report, LAUR-86, 2004.

252. Hess, B., et al., *GROMACS 4: Algorithms for Highly Efficient, Load-Balanced, and Scalable Molecular Simulation.* Journal of Chemical Theory and Computation, 2008. **4**(3): p. 435-447.

253. Damm, W., et al., *OPLS all-atom force field for carbohydrates.* Journal of Computational Chemistry, 1997. **18**(16): p. 1955-1970.

254. Jorgensen, W.L., et al., *Comparison of simple potential functions for simulating liquid water.* The Journal of Chemical Physics, 1983. **79**(2): p. 926-935.

255. Wahab, A., et al., *Ultrasonic Velocities, Densities, Viscosities, Electrical Conductivities, Raman Spectra, and Molecular Dynamics Simulations of Aqueous Solutions of Mg(OAc)2 and Mg(NO3)2: Hofmeister Effects and Ion Pair Formation.* The Journal of Physical Chemistry B, 2005. **109**(50): p. 24108-24120.

256. Tesei, G., G. Paradossi, and E. Chiessi, *Poly(vinyl alcohol) Oligomer in Dilute Aqueous Solution: A Comparative Molecular Dynamics Simulation Study.* The Journal of Physical Chemistry B, 2012. **116**(33): p. 10008-10019.

257. Gross, A.S., A.T. Bell, and J.-W. Chu, *Preferential Interactions between Lithium Chloride and Glucan Chains in N,N-Dimethylacetamide Drive Cellulose Dissolution.* The Journal of Physical Chemistry B, 2013. **117**(12): p. 3280-3286.

258. Feller, S.E., et al., *Constant pressure molecular dynamics simulation: The Langevin piston method.* The Journal of Chemical Physics, 1995. **103**(11): p. 4613-4621.

259. Darden, T., D. York, and L. Pedersen, *Particle mesh Ewald: An N·log(N) method for Ewald sums in large systems.* The Journal of Chemical Physics, 1993. **98**(12): p. 10089-10092.

260. Cisneros, G.A., et al., *Classical Electrostatics for Biomolecular Simulations.* Chemical Reviews, 2014. **114**(1): p. 779-814.

261. Spalding, D.B., *The Molecular Theory of Gases and Liquids.J. O. Hirschfelder, C. F. Curtiss and R. B. Bird. John Wiley,New York. Chapman & Hall, London, 1954. 1,219 pp.Diagrams. 160s.* The Journal of the Royal Aeronautical Society, 1955. **59**(531): p. 228-228.

262. Schulten, D.K., *VMD: Visual molecular dynamics.* Journal of Molecular Graphics, 1996.

263. Ghosh, A., C. Wang, and P. Kofinas, *Block Copolymer Solid Battery Electrolyte with High Li-Ion Transference Number.* Journal of The Electrochemical Society, 2010. **157**(7): p. A846-A849.

264. Zheng, J.X., et al., *Understanding Thermodynamic and Kinetic Contributions in Expanding the Stability Window of Aqueous Electrolytes.* Chem, 2018. **4**(12): p. 2872-2882.

265. Xu, C., et al., *Energetic Zinc Ion Chemistry: The Rechargeable Zinc Ion Battery.* Angewandte Chemie Internatinal Edition, 2012. **51**(4): p. 933-935.

266. Hertzberg, B.J., et al., *Effect of Multiple Cation Electrolyte Mixtures on Rechargeable Zn–MnO2 Alkaline Battery.* Chemistry of Materials, 2016. **28**(13): p. 4536-4545.

267. Kakiuchi, T., T. Yoshimatsu, and N. Nishi, *New Class of Ag/AgCl Electrodes Based on Hydrophobic Ionic Liquid Saturated with AgCl.* Analytical Chemistry, 2007. **79**(18): p. 7187-7191.

268. Zheng, X., et al., *Electronic Structure Engineering of LiCoO2 toward Enhanced Oxygen Electrocatalysis.* Advanced Energy Materials, 2019. **0**(0): p. 1803482.

269. Biswick, T., et al., *Evidence for the formation of anhydrous zinc acetate and acetic anhydride during the thermal degradation of zinc hydroxy acetate, Zn5(OH)8(CH3CO2)2·4H2O to ZnO.* Solid State Sciences, 2009. **11**(2): p. 330-335.

270. Yang, C.-C. and S.-J. Lin, *Improvement of high-rate capability of alkaline Zn–MnO2 battery.* Journal of Power Sources, 2002. **112**(1): p. 174-183.

271. Pratt, K.W., et al., *Molality-based primary standards of electrolytic conductivity (IUPAC Technical Report)*, in *Pure and Applied Chemistry*. 2001. p. 1783.

272. Younesi, R., et al., *Lithium salts for advanced lithium batteries: Li–metal, Li–O2, and Li–S.* Energy & Environmental Science, 2015. **8**(7): p. 1905-1922.

273. Zhou, T., et al., *Twinborn TiO2–TiN heterostructures enabling smooth trapping–diffusion–conversion of polysulfides towards ultralong life lithium–sulfur batteries.* Energy & Environmental Science, 2017. **10**(7): p. 1694-1703.

274. Guo, Y.G., J.S. Hu, and L.J. Wan, *Nanostructured materials for electrochemical energy conversion and storage devices.* Advanced Materials, 2008. **20**(15): p. 2878-2887.

275. Maier, J., *Nanoionics: ion transport and electrochemical storage in confined systems.* Nature Materials, 2005. **4**(11): p. 805-815.

276. Wruck, W.J., et al., *Rechargeable Zn ‐ MnO2 Alkaline Batteries.* Journal of the Electrochemical Society, 1991. **138**(12): p. 3560-3567.

277. Liu, M., et al., *Tuning phase evolution of β-MnO2 during microwave hydrothermal synthesis for high-performance aqueous Zn ion battery.* Nano Energy, 2019. **64**: p. 103942.

278. Li, Y., et al., *Reaction Mechanisms for Long-Life Rechargeable Zn/MnO2 Batteries.* Chemistry of Materials, 2019. **31**(6): p. 2036-2047.

279. Alfaruqi, M.H., et al., *Electrochemically Induced Structural Transformation in a γ-MnO2 Cathode of a High Capacity Zinc-Ion Battery System.* Chemistry of Materials, 2015. **27**(10): p. 3609-3620.

280. Chen, L., et al., *New-concept Batteries Based on Aqueous Li+/Na+ Mixed-ion Electrolytes.* Scientific Reports, 2013. **3**: p. 1946.

281. Sharma, P.K. and M.S. Whittingham, *The role of tetraethyl ammonium hydroxide on the phase determination and electrical properties of γ-MnOOH synthesized by hydrothermal.* Materials Letters, 2001. **48**(6): p. 319-323.

282. Yang, R., et al., *Synthesis and characterization of single-crystalline nanorods of α-MnO2 and γ-MnOOH.* Materials Chemistry and Physics, 2005. **93**(1): p. 149-153.

283. Kohler, T., T. Armbruster, and E. Libowitzky, *Hydrogen Bonding and Jahn–Teller Distortion in Groutite,α-MnOOH, and Manganite,γ-MnOOH, and Their Relations to the Manganese Dioxides Ramsdellite and Pyrolusite.* Journal of Solid State Chemistry, 1997. **133**(2): p. 486-500.

284. Lin, D., Y. Liu, and Y. Cui, *Reviving the lithium metal anode for high-energy batteries.* Nature Nanotechnology, 2017. **12**: p. 194.

285. Wagner, F.S., *Rubidium and Rubidium Compounds*, in *Kirk ‐ Othmer Encyclopedia of Chemical Technology*.

286. Liang, X., et al., *A facile surface chemistry route to a stabilized lithium metal anode.* Nature Energy, 2017. **2**: p. 17119.

287. Wu, H., et al., *Improving battery safety by early detection of internal shorting with a bifunctional separator.* Nature Communications, 2014. **5**(1): p. 5193.

288. Simon, P. and Y. Gogotsi, *Materials for electrochemical capacitors.* Nature Materials, 2008. **7**(11): p. 845-854.

289. Simon, P., Y. Gogotsi, and B. Dunn, *Where Do Batteries End and Supercapacitors Begin?* Science, 2014. **343**(6176): p. 1210-1211.

290. Kundu, D., et al., *A high-capacity and long-life aqueous rechargeable zinc battery using a metal oxide intercalation cathode.* Nature Energy, 2016. **1**: p. 16119.

291. Mähler, J. and I. Persson, *A Study of the Hydration of the Alkali Metal Ions in Aqueous Solution.* Inorganic Chemistry, 2012. **51**(1): p. 425-438.

292. Kiefer, E.F. and W. Gericke, *Nuclear magnetic resonance investigation of secondary valence forces. II. Intramolecular mercury-halogen coordination in 3-halopropylmercury compounds.* Journal of the American Chemical Society, 1968. **90**(19): p. 5131-5136.

293. Zhou, P.-P., et al., *Halogen as halogen-bonding donor and hydrogen-bonding acceptor simultaneously in ring-shaped H3N·X(Y)·HF (X = Cl, Br*

and Y = F, Cl, Br) Complexes. Physical Chemistry Chemical Physics, 2011. **13**(16): p. 7408-7418.

294. Lide, D.R., *CRC Handbook of Chemistry and Physics*. Vol. 85. 2004: CRC press.

295. Wang, Y.-H., et al., *In situ Raman spectroscopy reveals the structure and dissociation of interfacial water*. Nature, 2021. **600**(7887): p. 81-85.

296. Quilès, F. and A. Burneau, *Infrared and Raman spectra of alkaline-earth and copper(II) acetates in aqueous solutions*. Vibrational Spectroscopy, 1998. **16**(2): p. 105-117.

297. Zhang, J., et al., *"Water-in-salt" polymer electrolyte for Li-ion batteries*. Energy & Environmental Science, 2020. **13**(9): p. 2878-2887.

298. Sidgwick, N.V. and J.A.H.R. Gentle, *CCXXI.—The solubilities of the alkali formates and acetates in water*. Journal of the Chemical Society, Transactions, 1922. **121**(0): p. 1837-1843.

299. Yamada, Y., et al., *Hydrate-melt electrolytes for high-energy-density aqueous batteries*. Nature Energy, 2016. **1**: p. 16129.

300. Armstrong, G., et al., *The synthesis and lithium intercalation electrochemistry of VO2(B) ultra-thin nanowires*. Journal of Power Sources, 2008. **178**(2): p. 723-728.

301. Chabi, S., et al., *Ideal Three-Dimensional Electrode Structures for Electrochemical Energy Storage*. Advanced Materials, 2014. **26**(15): p. 2440-2445.

302. Lou, X.W., et al., *Self-Supported Formation of Needlelike Co3O4 Nanotubes and Their Application as Lithium-Ion Battery Electrodes*. Advanced Materials, 2008. **20**(2): p. 258-262.

303. Pasero, D., et al., *Oxygen nonstoichiometry and phase transitions in LiMn1.5Ni0.5O4-delta*. Journal of the Electrochemical Society, 2008. **155**(4): p. A282-A291.

304. Jiang, J.W. and J.R. Dahn, *Dependence of the heat of reaction of Li0.81C6 (0.1 V), Li7Ti5O12, (1.55 V), and Li0.5VO2 (2.45 V) reacting with nonaqueous solvents or electrolytes on the average potential of the electrode material*. Journal of the Electrochemical Society, 2006. **153**(2): p. A310-A315.

305. Oka, Y., et al., *PHASE-TRANSITION AND V4+-V4+ PAIRING IN VO2(B)*. Journal of Solid State Chemistry, 1993. **105**(1): p. 271-278.

306. Umar, Z.A., et al., *Substrate temperature effects on the structural, compositional, and electrical properties of VO2 thin films deposited by pulsed laser deposition*. Surface and Interface Analysis, 2018. **50**(3): p. 297-303.

307. Tao, S.W., J. Canales-Vazquez, and J.T.S. Irvine, *Structural and electrical properties of the perovskite oxide Sr2FeNbO6*. Chemistry of Materials, 2004. **16**(11): p. 2309-2316.

308. Tao, S.W. and J.T.S. Irvine, *Phase transition in perovskite oxide La0.75Sr0.25Cr0.5Mn0.5O3-δ observed by in situ high-temperature neutron powder diffraction*. Chemistry of Materials, 2006. **18**(23): p. 5453-5460.

309. Liu, X., et al., *A facile method for preparing VO2 nanobelts*. Materials Letters, 2008. **62**(12): p. 1878-1880.

310. Armstrong, G., et al., *TiO2(B) Nanowires as an Improved Anode Material for Lithium-Ion Batteries Containing LiFePO4 or LiNi0.5Mn1.5O4*

Cathodes and a Polymer Electrolyte. Advanced Materials, 2006. **18**(19): p. 2597-2600.

311. Sun, W., et al., *"Water-in-Salt" electrolyte enabled LiMn2O4/TiS2 Lithium-ion batteries.* Electrochemistry Communications, 2017. **82**: p. 71-74.

312. Suo, L., et al., *"Water-in-Salt" electrolytes enable green and safe Li-ion batteries for large scale electric energy storage applications.* Journal of Materials Chemistry A, 2016. **4**(17): p. 6639-6644.

313. Li, Q., et al., *Extra storage capacity in transition metal oxide lithium-ion batteries revealed by in situ magnetometry.* Nature Materials, 2021. **20**(1): p. 76-83.

314. Wei, J., et al., *Dissolution–Crystallization Transition within a Polymer Hydrogel for a Processable Ultratough Electrolyte.* Advanced Materials, 2019. **31**(30): p. 1900248.

315. Veith, G.M., et al., *Influence of Lithium Salts on the Discharge Chemistry of Li–Air Cells.* The Journal of Physical Chemistry Letters, 2012. **3**(10): p. 1242-1247.

316. Younesi, R., M. Hahlin, and K. Edström, *Surface Characterization of the Carbon Cathode and the Lithium Anode of Li–O2 Batteries Using LiClO4 or LiBOB Salts.* ACS Applied Materials & Interfaces, 2013. **5**(4): p. 1333-1341.

317. Xu, K., S.P. Ding, and T.R. Jow, *Toward Reliable Values of Electrochemical Stability Limits for Electrolytes.* Journal of The Electrochemical Society, 1999. **146**(11): p. 4172-4178.

318. Nagarale, R.K., V.K. Shahi, and R. Rangarajan, *Preparation of polyvinyl alcohol–silica hybrid heterogeneous anion-exchange membranes by sol–gel method and their characterization.* Journal of Membrane Science, 2005. **248**(1): p. 37-44.

319. Zheng, J., R. Garcia-Mendez, and L.A. Archer, *Engineering Multiscale Coupled Electron/Ion Transport in Battery Electrodes.* ACS Nano, 2021.

320. Chen, S., et al., *Acetate-based 'oversaturated gel electrolyte' enabling highly stable aqueous Zn-MnO2 battery.* Energy Storage Materials, 2021. **42**: p. 240-251.

321. Luo, J.-Y., et al., *Raising the cycling stability of aqueous lithium-ion batteries by eliminating oxygen in the electrolyte.* Nature Chemistry, 2010. **2**: p. 760.

322. Sheela, T., et al., *Ionic conductivity and free volume related microstructural properties of LiClO4/PVA/NaAlg polymer composites: Positron annihilation spectroscopic studies.* Journal of Non-Crystalline Solids, 2016. **454**: p. 19-30.

323. Luo, J.-Y. and Y.-Y. Xia, *Aqueous Lithium-ion Battery LiTi2(PO4)3/LiMn2O4 with High Power and Energy Densities as well as Superior Cycling Stability**.* Advanced Functional Materials, 2007. **17**(18): p. 3877-3884.

324. Lin, Z., et al., *Aligning academia and industry for unified battery performance metrics.* Nature Communications, 2018. **9**(1): p. 5262.

325. Hoang, T.K.A., et al., *Sustainable Gel Electrolyte Containing Pyrazole as Corrosion Inhibitor and Dendrite Suppressor for Aqueous Zn/LiMn2O4 Battery.* ChemSusChem, 2017. **10**(13): p. 2816-2822.

326. Hoang, T.K.A., et al., *Performance of Thixotropic Gel Electrolytes in the Rechargeable Aqueous Zn/LiMn2O4 Battery.* ACS Sustainable Chemistry & Engineering, 2017. **5**(2): p. 1804-1811.

327. Xiong, W., et al., *Controlling the sustainability and shape change of the zinc anode in rechargeable aqueous Zn/LiMn2O4 battery.* Energy Storage Materials, 2018. **15**: p. 131-138.

328. Chung, K.Y., et al., *Studies of LiMn2O4 Capacity Fading at Elevated Temperature Using In Situ Synchrotron X-Ray Diffraction.* Journal of The Electrochemical Society, 2006. **153**(4): p. A774-A780.

329. Thangadurai, V., S. Narayanan, and D. Pinzaru, *Garnet-type solid-state fast Li ion conductors for Li batteries: critical review.* Chemical Society Reviews, 2014. **43**(13): p. 4714-4727.

330. Bachman, J.C., et al., *Inorganic Solid-State Electrolytes for Lithium Batteries: Mechanisms and Properties Governing Ion Conduction.* Chemical Reviews, 2016. **116**(1): p. 140-162.

331. Chen, N., et al., *Ionogel Electrolytes for High-Performance Lithium Batteries: A Review.* Advanced Energy Materials, 2018. **8**(12): p. 1702675.

332. James, D.W. and W.H. Leong, *Structure of Molten Nitrates. III. Vibrational Spectra of LiNO3, NaNO3, and AgNO3.* The Journal of Chemical Physics, 1969. **51**(2): p. 640-646.

333. Lin, X., et al., *Rechargeable Battery Electrolytes Capable of Operating over Wide Temperature Windows and Delivering High Safety.* Advanced Energy Materials, 2020. **n/a**(n/a): p. 2001235.

334. Nakhanivej, P., et al., *Transport and Durability of Energy Storage Materials Operating at High Temperatures.* ACS Nano, 2020. **14**(7): p. 7696-7703.

335. Wang, T., D. Mantha, and R.G. Reddy, *Thermal stability of the eutectic composition in LiNO3–NaNO3–KNO3 ternary system used for thermal energy storage.* Solar Energy Materials and Solar Cells, 2012. **100**: p. 162-168.

336. Kausar, A., *Innovations in Poly(Vinyl Alcohol) Derived Nanomaterials.* Advances in Materials Science, 2020. **20**(3): p. 5-22.

337. Mai, L., et al., *One-Dimensional Hetero-Nanostructures for Rechargeable Batteries.* Accounts of Chemical Research, 2018. **51**(4): p. 950-959.

338. Yu, L., H.B. Wu, and X.W.D. Lou, *Self-Templated Formation of Hollow Structures for Electrochemical Energy Applications.* Accounts of Chemical Research, 2017. **50**(2): p. 293-301.

339. Wang, F., et al., *Spinel LiNi0.5Mn1.5O4 Cathode for High-Energy Aqueous Lithium-Ion Batteries.* Advanced Energy Materials, 2017. **7**(8): p. 1600922.

340. Arun, N., et al., *Importance of nanostructure for reversible Li-insertion into octahedral sites of LiNi0.5Mn1.5O4 and its application towards aqueous Li-ion chemistry.* Journal of Power Sources, 2015. **280**: p. 240-245.

341. Wang, Y., Y. Song, and Y. Xia, *Electrochemical capacitors: mechanism, materials, systems, characterization and applications.* Chemical Society Reviews, 2016. **45**(21): p. 5925-5950.

342. Das, S.R., S.B. Majumder, and R.S. Katiyar, *Kinetic analysis of the Li+ ion intercalation behavior of solution derived nano-crystalline lithium manganate thin films.* Journal of Power Sources, 2005. **139**(1): p. 261-268.

343. Lin, X., et al., *Rechargeable Battery Electrolytes Capable of Operating over Wide Temperature Windows and Delivering High Safety.* Advanced Energy Materials, 2020. **10**(43): p. 2001235.

344. Peljo, P. and H.H. Girault, *Electrochemical potential window of battery electrolytes: the HOMO–LUMO misconception.* Energy & Environmental Science, 2018. **11**(9): p. 2306-2309.

345. Ghosh, A., C. Wang, and P. Kofinas, *Block Copolymer Solid Battery Electrolyte with High Li-Ion Transference Number.* Journal of The Electrochemical Society, 2010. **157**(7): p. A846.

346. Nickolov, Z., et al., *Raman and IR study of cobalt acetate dihydrate.* Journal of Molecular Structure, 1995. **354**(2): p. 119-125.

347. Yao, Y.-X., et al., *Regulating Interfacial Chemistry in Lithium-Ion Batteries by a Weakly Solvating Electrolyte**.* Angewandte Chemie International Edition, 2021. **60**: p. 4090-4097.

348. Tian, Y., et al., *Recent Advances and Perspectives of Zn-Metal Free "Rocking-Chair"-Type Zn-Ion Batteries.* Advanced Energy Materials, 2021. **11**(5): p. 2002529.

349. Song, J., et al., *Crossroads in the renaissance of rechargeable aqueous zinc batteries.* Materials Today, 2021. **45**: p. 191-212.

350. Yi, Z., et al., *Strategies for the Stabilization of Zn Metal Anodes for Zn-Ion Batteries.* Advanced Energy Materials, 2021. **11**(1): p. 2003065.

351. Seo, J.K., et al., *Intercalation and Conversion Reactions of Nanosized β-MnO2 Cathode in the Secondary Zn/MnO2 Alkaline Battery.* The Journal of Physical Chemistry C, 2018. **122**(21): p. 11177-11185.

352. Gogotsi, Y. and R.M. Penner, *Energy Storage in Nanomaterials – Capacitive, Pseudocapacitive, or Battery-like?* ACS Nano, 2018. **12**(3): p. 2081-2083.

353. Bard, A.J. and L. Faulkner. *Electrochemical Methods: Fundamentals and Applications*. 1980.

354. Du, D.W., et al., *Preparation of nanoporous nickele-copper sulfide on carbon cloth for high-performance hybrid supercapacitors.* Electrochimica Acta, 2018. **273**: p. 170-180.

355. Tian, L., et al., *Morphology and phase transformation of α-MnO2/MnOOH modulated by N-CDs for efficient electrocatalytic oxygen evolution reaction in alkaline medium.* Electrochimica Acta, 2020. **337**: p. 135823.

356. Smith, P.F., et al., *Coordination Geometry and Oxidation State Requirements of Corner-Sharing MnO6 Octahedra for Water Oxidation Catalysis: An Investigation of Manganite (γ-MnOOH).* ACS Catalysis, 2016. **6**(3): p. 2089-2099.

357. Walker, W., et al., *A Rechargeable Li–O2 Battery Using a Lithium Nitrate/N,N-Dimethylacetamide Electrolyte.* Journal of the American Chemical Society, 2013. **135**(6): p. 2076-2079.

358. Bryantsev, V.S., et al., *The Identification of Stable Solvents for Nonaqueous Rechargeable Li-Air Batteries.* Journal of The Electrochemical Society, 2012. **160**(1): p. A160-A171.

359. Giordani, V., et al., *Synergistic Effect of Oxygen and LiNO3 on the Interfacial Stability of Lithium Metal in a Li/O2 Battery.* Journal of The Electrochemical Society, 2013. **160**(9): p. A1544-A1550.

360. Yu, Y., et al., *A renaissance of N,N-dimethylacetamide-based electrolytes to promote the cycling stability of Li–O2 batteries.* Energy & Environmental Science, 2020. **13**(9): p. 3075-3081.

361. Edwards, H.G.M., A.F. Johnson, and E.E. Lawson, *A Raman spectroscopic study of N,N-dimethylacrylamide.* Spectrochimica Acta Part A: Molecular Spectroscopy, 1994. **50**(2): p. 255-261.

362. Wu, Y.C., W.F. Koch, and K.W. Pratt, *Proposed New Electrolytic Conductivity Primary Standards for KCl Solutions.* Journal of research of the National Institute of Standards and Technology, 1991. **96**(2): p. 191-201.

363. Świergiel, J. and J. Jadżyn, *Static Dielectric Permittivity and Electric Conductivity of N-Methylacetamide + N,N-Dimethylacetamide Mixtures.* Journal of Chemical & Engineering Data, 2009. **54**(8): p. 2296-2300.

364. Jin, Y., et al., *Stabilizing Zinc Anode Reactions by Polyethylene Oxide Polymer in Mild Aqueous Electrolytes.* Advanced Functional Materials, 2020. **30**(43): p. 2003932.

365. Pan, H., et al., *Electrolyte Effect on the Electrochemical Performance of Mild Aqueous Zinc-Electrolytic Manganese Dioxide Batteries.* ACS Applied Materials & Interfaces, 2019. **11**(41): p. 37524-37530.

366. Song, J., et al., *Crossroads in the renaissance of rechargeable aqueous zinc batteries.* Materials Today, 2021. **45**: p. 191-212.

367. Wei, Q., et al., *Porous One-Dimensional Nanomaterials: Design, Fabrication and Applications in Electrochemical Energy Storage.* Advanced Materials, 2017. **29**(20): p. 1602300.

368. Wang, Y., et al., *A Novel High Capacity Positive Electrode Material with Tunnel-Type Structure for Aqueous Sodium-Ion Batteries.* Advanced Energy Materials, 2015. **5**(22): p. 1501005.

369. Liu, L., et al., *Viologen radical stabilization by molecular spectators for aqueous organic redox flow batteries.* Nano Energy, 2021. **84**: p. 105897.